UNIVERSITÀ DEGLI STUDI DI UDINE
Dottorato di Ricerca in Fisica – Ciclo XIX
Linea di Ricerca in Fisica Sperimentale

Ph.D. Dissertation

INDIRECT SEARCH OF DARK MATTER IN THE HALOS OF GALAXIES.

Role of substructures on the signals from dark matter annihilation and prospects for detection of single dark matter clumps with the MAGIC Telescope

Erica Bisesi

February 2007

supervised by
Prof. A. de Angelis & **Prof. M. Persic**

A David, mio amore meraviglioso

Contents

Introduction

What is the Universe made of?

The question about the nature of dark matter (DM) is one of the greatest puzzles in our present understanding of Nature. During the last decades, remarkable progress has been made in cosmology, both observational and theoretical. These rapid developments have led to the consciousness that ordinary matter, baryons and electrons we are used to see around us in our everyday world, do not account for most of the mass in the Universe: we appear to live in a flat Universe composed primarly of new, unfamilar and unidentified forms of matter and energy. This conclusion is supported by some astrophysical and cosmological observations: primordial nucleosyntesis (the very successful theory of the nuclear origin of the lightest elements in the periodic table), as well as recent measurements of the amount of deuterium, limit the baryonic content of the Universe to only 4% of its critical density, so the nature of the remaining 23% has yet to be identified, the further 73% being in some form with negative pressure, a cosmological constant Λ or dark energy. In this sense, most of the mass of our Universe is *dark*.

In the theory of structure formation, not only is the amount of DM important, but so is the type of particle it is made up. The great watershed rests on the heaviness of the DM candidate: very light particles, like massive but light neutrinos, will be relativistic when structure starts to form, will be hot and free-stream out of galaxy-sized overdense regions, so that only very large structures can form early. Consequently, *hot dark matter* (HDM) particles populate a scenario where structure forms top-down by the fragmentation of larger objects into smaller ones. The main problem with this behavior is that the high speeds of the particles in the early Universe could not have allowed small density fluctuations to clump together in order to create the large fluctuations we see now. We believe galaxies are distributed throughout the Universe as it is now due to the growth of small initial fluctuations. Since HDM particles

would have been moving so fast that these tiny initial fluctuations would have been smoothed out, such a kind of theory cannot account for the observed distribution of galaxies at very high redshift. On the other hand, massive (GeV or heavier) particles were moving with non-relativistic velocities when they decoupled and could therefore clump also on smaller scales. This is the *cold dark matter* (CDM) scenario, where structure typically forms in a hierarchical fashion, with smaller objects forming first, and bigger ones originating from the progressive clustering and merging of the smaller units. Inbetween HDM and CDM there may exist *warm dark matter* (WDM), which could be made up of keV scale neutral particles (like the supersymmetric partner of the graviton, the gravitino, in some models of supersymmetry breaking). Within this picture, the inverse of the mass scale of the particle defines a length scale of structure formation below which early structure is suppressed. WDM is not currently favoured, both for particle physics and structure formation reasons - but this possibility should be kept in mind. Another possibility involves non-thermally produced particles, like the axion, which behave like CDM although they most likely are very light particles. Among the different DM theories, in the present work we will adopt the paradigm of CDM with a cosmological constant (ΛCDM), given its remarkable success in describing large-scale structure formation.

In spite of this, the Standard Model of particle physics does not contain any suitable DM candidate. Therefore, as a strong indication of physics beyond the Standard Model, the DM problem needs to be addressed not only from the original astrophysical standpoint, but also as a strong necessity to extend the current standard theory of elementary particles. In this sense, one of the most promising frameworks consistent with the ΛCDM paradigm is represented by supersymmetry (SUSY). Although SUSY was introduced as an extension of the Standard Model without any reference to the DM problem, it was soon recognized that in its minimal formulation it could provide a natural and suitable DM particle candidate, i.e. the lightest among the SUSY partners of Standard Model particles, the *neutralino*. Many theoretical arguments have been put forward as motivations for a realization of SUSY at energy scales not far from the electroweak symmetry breaking scale: SUSY provides an elegant solution to the hierarchy problem and a mechanism for radiative electro-weak symmetry breaking; it yields the unification of gauge couplings; it predicts a heavy top quark and indicates a correct value for $sin^2\theta_W$ long before experimental programs managed to perform the actual measurements; moreover, consistently with the latest Standard Model global fits from LEP, it implies a light Higgs boson. Finally, on purely theoretical grounds, it has been realized that SUSY is an essential ingredient of any attempt

to unify gravity with the other Standard Model interactions [162].

With the lighting of the CERN Large Hadron Collider (LHC), scheduled for November 2007, we are going to enter in a new era when particle physics experiments will investigate an energetic range where physics beyond the Standard Model is expected to show up. Furtherly, the problem of the detection of DM particles is one of the main targets included into the extensive experimental program began in the early Eighties. In addition to collider experiments and direct neutralino searches, neutralino annihilation into gamma rays, antimatter particles, neutrinos produced by pair annihilations in the center of the Sun and synchrotron emission from the charged products represent a reliable way of detecting these intriguing particles.

The main aim of the present Thesis is to substantiate a phenomenological analysis of DM physics within SUSY theories, by considering the issue of the indirect detection of a given SUSY DM candidate with the Major Atmospheric Gamma-Ray Imaging Čerenkov (MAGIC) Telescope. MAGIC has been operating since March 2004. Its 17 m diameter dish makes it the world's largest single-dish Čerenkov telescope. It is situated at The Roque de Los Muchachos on the Canary island of La Palma (Spain), a volcanic island off the African coast. With this device we are able to detect cosmic gamma-rays above the threshold of 50 GeV. Observations in this region of the electromagnetic spectrum are expected to provide very important issues for the understanding of a wide variety of astrophysical phenomena. Among them, (i) searching for astrophysical signatures of the lightest stable SUSY particle and (ii) interpreting some unidentified EGRET sources may play a primary role.

(i) One of the biggest problems in the current understanding of structure formation involves the DM distribution inside galactic halos. Recently, very high resolution numerical simulations confirmed that the dark halos are not structureless objects, but rather are clumpy systems characterized by the presence of a wide population of subhalos. Although the current standard ΛCDM paradigm has been very successful in matching the observational data on large scale, it has been noted that the ΛCDM model overpredicts the abundance of substructures compared with that of observed Galactic satellites. This ΛCDM problem on sub-galactic scale is regarded as a fundamental issue that has to be addressed. It was suggested that the ΛCDM problem on sub-galactic scale could be resolved by radically changing the nature of DM. Less dramatically, the problem may be addressed also accounting for astrophysical processes

such as the presence of a photoionizing background and inefficient star formation in small mass halos. In these pictures the observed number of satellite galaxies is small because only the most massive substructures contain stars, while most substructures are *dark*. To detect these small dark substructures, indirect detection of DM can be a very powerful tool.

(ii) In the third EGRET catalog, 271 sources with E > 100 MeV are included, 74 out of which have been identified as known astrophysical sources (e.g. pulsars, blazars and a solar flare), 170 remaining unidentified till now. A detailed analysis of the spectra of some of these sources indicate that a plausible solution to the question concerning their nature may be obtained assuming that they are DM clumps in the Milky Way halo. In this investigation, however, a caveat is that the result does depend on the spatial distribution of subhalos. Despite the importance of substructures to understand the structure formation in the Universe, most previous work had to resort to numerical approaches in studying the mass and spatial distributions of substructures. However, N-body simulations need high force and mass resolution to overcome the 'overmerging' problem, this makes the large number of calculations cumbersome. By contrast, the analytic approach has the advantage that it allows to compute distributions for a wide range of parameters.

In this spirit, the first step of the present work has been the implementation of a realistic semi-analytic model for the spatial mass function of subhalos into `DarkSUSY` [1] , incorporating effects that may influence the distribution and evolution of satellites in presence of a baryonic core, such as mass loss due to tidal stripping and orbital decay due to dynamical friction.
In a subsequent step, assuming the lightest neutralino in the Minimal Supersymmetric Standard Model (MSSM) as the main DM costituent, we applied the formalism discussed above to the EGRET unidentified gamma-ray source $3EG\_J1835 + 5918$ and compared predictions of the emitted gamma-ray flux in some relevant cosmolog-

[1] `DarkSUSY` is a publicly-available advanced numerical package for neutralino dark matter calculations. In this code one can compute the neutralino density in the Universe today, using precision methods which include resonances, pair production thresholds and coannihilations. Masses and mixings of supersymmetric particles can be computed within DarkSUSY or with the help of external programs such as `FeynHiggs`, `ISASUGRA` and `SUSPECT`. Accelerator bounds can be checked to identify viable DM candidates. `DarkSUSY` also computes a large variety of astrophysical signals from neutralino dark matter, such as direct detection in low-background counting experiments and indirect detection through antiprotons, antideuterons, gamma-rays and positrons from the Galactic halo or high-energy neutrinos from the center of the Earth or of the Sun [98].

ical scenarios with observational data. This investigation is well motivated by the proposal of observation of some of these sources during the cycle II of the MAGIC Telescope, observation whose main aspects have also been object of the present search.

An important part of this work has been dedicated to the discussion of the main tasks of the data analysis chain for the MAGIC Telescope, involving the many aspects of calibration, imaging, data reduction, gamma-hadron separation and production of spectra. This detailed study has been performed on a well known standard candle source, the Crab Nebula, and subsequently applied to the source of the present interest. The discussion and interpretation of results obtained from the analysis of the data of the unidentified gamma-ray source $3EG\_J1835 + 5918$ fulfills this part.

Another excellent candidate to seek for gamma-rays from neutralino annihilations is the Draco dwarf spheroidal satellite. This object is located off the Galactic plane, it has a large M/L ratio hence a large DM fraction, it is the largest Milky Way satellite and is relatively nearby. There are no known very high energy (VHE) gamma-ray emitters near the dynamical center of Draco, where the DM-related gamma-ray luminosity is expected to be highest; additionally, there is no evidence for stars beyond the tidal radius, so no strong tidal effects are present. The CACTUS collboration, operating with a ground-based Air Čerenkov Telescope at the Solar Two facility in California, recently announced a gamma-ray signal from the direction to this source, invoking the annihilation of DM particles in its halo as a possible explanation. Given the need of an indipendent confirmation and the compatibility of the CACTUS and MAGIC energy ranges, several hours of observation time devoted to the Draco dwarf spheroidal satellite (hereafter: 'Draco', for short) were planned for MAGIC's cycle II. In a dedicated section of this Thesis, we will discuss the observation of Draco, as well as the status of the subsequent data analysis carried out by the MAGIC Dark Matter Working Group [2] .

Finally, we have addressed the problem of the cumulative gamma-ray signal from the halos of star-forming galaxies. In the framework of this Thesis, the VHE gamma-ray emission from a star-forming galaxy is due to mainly three contributions:

★ a non-baryonic contribution originating from the radiation of self-annihilating

[2]H. Bartko, W. Wittek (Max-Planck-Institut für Physik, München), E. Bisesi (Università di Udine and INFN, Italy), A. Biland, S. Stark, P. Häfliger (Institute for Particle Physics, Swiss Federal Institute of Technology (ETH), Zürich), J. Flix (Institut de Física d'Altes Energies, Barcelona).

DM, consisting of two separate components: the signal from the smooth DM halo distribution, and the enhanced signal from the halo substructures;

★ a first baryonic component due to the collective emission from TeV-point sources - which are evolutionary end-products of massive, bright, short-lived progenitor stars: these TeV sources are immediate products of the ongoing star formation activity;

★ a second baryonic component which mainly results from the hadronic illumination of interstellar gas by the SN-accelerated cosmic-ray protons.

We will give an approximate recipe to estimate the relative weigths of these different components. This will be applied to a suitable Local Group target, the Andromeda galaxy. In this spirit, some attention will be devoted to discussing the main DM TeV-emission scenarios in the SUSY parameter space. This estimate may turn out of some use to upcoming observational campaigns by current Čerenkov telescopes.

In the case of the Milky Way, some emphasis will be given to neutralino searches through antimatter detection, in view of the imminent results of space-based experiments which will greatly further our knowledge of the physics of cosmic antiprotons and positrons.

"Lo giorno se n'andava, e l'aere bruno
toglieva li animai che sono in terra
dalle fatiche loro; e io sol uno

m'apparecchiava a sostener la guerra
sì del cammino e sì della pietate,
che ritrarrà la mente che non erra."

(*Inf., II, 1-6*)

The plan of this Thesis is the following.

In **Chapter 1,** the general framework of modern cosmology is briefly reviewed; this introductory part is integrated by a detailed discussion of the main astrophysical and cosmological evidences for the presence of dark matter. The DM distribution in galaxies is the subject of **Chapter 2.** After an overview on the status of the literature about the picture of our Galactic halo, we will hereby expose our personal contribution to the study of the mass and spatial distribution function of subhalos, focusing on the most important effects that may influence the distribution and evolution of DM clumps inside their progenitors. In **Chapter 3,** we will threat the particle physics models for non-baryonic dark matter, reviewing the presently most discussed models for Weakly Interacting Massive Particles ('WIMP's), namely the supersymmetric models, as well as the alternative scenario represented by Kaluza-Klein (KK) particles. Afterwards, in **Chapter 4** we will briefly discuss the main methods of detection of the lightest electrically neutral supersymmetric particle, the neutralino, concluding this part with a prediction for the enhancement in the gamma, antiproton and positron signals due to the presence of clumps in the halo of the Milky Way. An application of these results is outlined in **Chapter 5,** where we finally enter in the 'hot' part of this work. Devoted to the discussion of the unidentified EGRET gamma-ray sources, this chapter contains the proposal of identification of the $3EG\_J1835+5918$ source with a DM clump, in the light of the predictions put forward about the gamma-ray signal from annihilating neutralino DM inside Milky Way satellites. **Chapter 6** and **7** are respectively devoted to the presentation of the main features of the MAGIC Telescope and data analysis methods. A certain interest is given in the last one to the explanation of the technique applied for the reduction of MAGIC data, and particularly on a developed analysis method to study extended emissions, as the emission from neutralino annihilation is in most scenarios not likely expected to come from point-like sources. After a preliminar investigation reviewing in **Chapter 8** results from the analysis of a MAGIC data sample of the Crab Nebula, study aimed to give a reference for the other source analysed in this Thesis, in **Chapter 9** we will hold up the proposal of observation for some unidentified EGRET sources during the cycle II of the MAGIC Telescope; the data analysis and discussion of the main results for $3EG\_J1835+5918$ conclude the part of this dissertation devoted to Galactic DM gamma-ray sources. In a similar way, moving outside the Milky Way, the proposal of observation and the status of data analysis for the Draco dwarf spheroidal galaxy are handled in **Chapter 10.** The third subject of interest of the present work, the esti-

mation of the cumulative TeV gamma-ray emission from some star-forming galaxies in and nearby the Local Group, is covered in **Chapter 11.** Finally, **Chapter 12** ends the Thesis with some concluding remarks and an outlook.

The book is structured into **three main parts:** at first, we discuss all the DM evidences and properties, like its distribution, particle physics models and indirect detection methods with the current generation of telescopes, as well as our personal contributions on the phenomenology, embracing Chapters from 1 to 5. At a subsequent step, in a second part including the following two chapters, we illustrate the main features of the MAGIC experiment, getting into the heart of the observations and data analysis of some possible galactic and extragalactic DM sources respectively in Chapters 8, 9 and 10, 11 respectively.

Part I

Supersymmetric DM in Galaxies and its Indirect Detection with the Current Generation Telescopes

Chapter 1

The Dark Matter in the Universe

1.1 Basics of standard cosmology

The only broadly accepted theory for the origin and evolution of the Universe is the *Big Bang model*. This template postulates that our Universe has been and still is expanding from a compressed and hot phase, started about 10^{10} years ago. This picture is supported by a number of observational cornerstones – the Hubble-type expansion in the redshifts of galaxies, the abundance of light elements sythesized during the first few minutes, and the existence still today of the cosmic microwave background (CMB), a thermal radiation field being originated just at the epoch when first atoms formed, 400.000 years after the Big Bang. Moreover, the excellent fit with the observed correlation function of large-scale structure of the Universe makes this picture more solid than ever, particularly after the recent results of the third years Wilkinson Microwave Anisotropy Probe (WMAP) data. Cosmology has been entered an era of precision measurements, when information from all these important processes has become accurate enough that it can be used to clarify the detailed structure and evolution of the Universe [33, 39, 143].

The Big Bang model is a very sophisticated theory which has its deep theoretical foundation in Einstein's general theory of relativity and has been tested on many different length scales. In order to simplify the mathematical analysis, one assumes that the Universe is isotropic and homogeneous on the average. Such properties are confirmed by many observations: in particular, CMB radiation measurements have proved on the largest scale that the observed temperature anisotropies, which are related to the density fluctuations at the time of recombination, are smaller than one part in 10^4 (once subtracted the dipole component ($\sim 10^{-3}$), interpreted as due to the Earth motion with respect to the CMB frame) [33]. One can show that every isotropic, homogeneous three-dimensional space can be parametrized by coordinates

which give a line element (squared distance between points at a fixed time) of the form:

$$ds^2 = -c^2\,dt^2 + a^2\left(\frac{dr^2}{1-kr^2} + r^2 d\Omega^2\right), \tag{1.1}$$

where *a(t)* is the so-called *scale factor* and the constant k describes the spatial curvature, taking one of the three values $k = -1,\ 0,\ +1$, depending on whether the geometry is open, flat or closed. These are the Friedmann-Lemăitre-Robertson-Walker (FLRW) models. For the simplest case $k = 0$, we see that the spatial part of Eq. 1.1 reduces to the metric of ordinary, flat, Euclidean three-dimensional space, with the scale factor a giving the overall normalization of physical distances. As a consequence of the observed expansion of the Universe, the scale factor depends on time ($a = a(t)$ with $\dot{a}/a > 0$ at the present time $t = t_0$), so that the basic aim of observational cosmology are the determination of k and the computation of $a(t)$, both in the past and in the future.

The Friedmann equations. The solution of one of the components of the Einstein's tensor equations gives the dependence of the scale factor a contained into the Friedmann equations:

$$\left(\frac{\dot{a}}{a}\right)^2 + \frac{k}{a^2} = \frac{8\pi G_N}{3}\rho_{tot}, \tag{1.2}$$

where G_N is Newton's gravitational constant and ρ_{tot} is the total average energy density of the Universe. The latter gets contributions at least from matter, radiation and perhaps vacuum energy (cosmological constant),

$$\rho_{tot} = \rho_M + \rho_R + \rho_\Lambda. \tag{1.3}$$

In particle physics units, $\hbar = c = 1$, G_N has the dimension of the inverse of a squared mass, the Planck mass ($m_P \sim 1.22 \cdot 10^{19}$ GeV). From the particle physics viewpoint, this means that gravity is governed by some still unknown theory at superhigh energy, whose low-energy limit is Einstein's general theory of relativity. The prime candidate for such a fundamental theory is string theory or one of its related versions, but this is an active, on-going field of research [32].
As the overall value of the scale factor is arbitrary, it is common to introduce the Hubble constant:

$$H(t) = \frac{\dot{a}(t)}{a(t)}, \tag{1.4}$$

which governs the local expansion according to Hubble's law, $v = Hd$, being v the recession velocity and d the physical distance. The present value of this parameter, uncertain to around 5%, is $H_0 = 73 \pm 3$ km s^{-1} Mpc^{-1}. One usually writes:

$$H_0 = h \cdot 100 \text{ km s}^{-1} \text{ Mpc}^{-1}, \tag{1.5}$$

with $h = 0.73 \pm 0.03$ for a flat Universe (1 Mpc is $3.08 \cdot 10^{24}$ m) [178].
Consequently, the linear length scale of the Universe is presently being stretched by a fraction of $3.24 \cdot 10^{-18}h$ per second. The inverse of this expansion rate defines a time, the Hubble time $t_H = 9.79\ h^{-1}$ Gyr. In standard cosmology, the present age of the Universe is by a numerical factor slightly less than this value, reflecting the fact that the expansion rate should have been larger in past than today. The first observational evidence for this was Hubble's detection of a cosmological redshift of the light emitted by distant galaxies. For an emitted wavelength λ_{emit} and an observed wavelength λ_{obs}, the redshift parameter z is defined by:

$$1 + z \equiv \frac{\lambda_{obs}}{\lambda_{emit}}. \tag{1.6}$$

In the standard FLRW model of cosmology, the redshift is related to the change in scale factor $a(t)$ through the relation:

$$1 + z = \frac{a(t_{obs})}{a(t_{emit})}. \tag{1.7}$$

In particle physics units ($\hbar = c = 1$), the expansion rate has the dimension of mass, the numerical value being $2.1 \cdot 10^{-42}h$ GeV. The large value of the Planck mass compared to the expansion mass scale (and all other other fundamental mass scales in nature) is one of the unsolved problems of theoretical physics [33].
We see from Eq. 1.2 that the Universe is flat ($k = 0$) when the energy density equals the *critical density* ρ_c, given by:

$$\rho_c \equiv \frac{3H^2}{8\pi G_N}. \tag{1.8}$$

From Eq. 1.5, the present numerical value of this parameter is computed to be $\rho_c^0 = 1.88 \cdot 10^{-29}h^2$ g cm^{-3}.
By defining the quantity Ω_i of a substance of species i as:

$$\Omega_i \equiv \frac{\rho_i}{\rho_c}, \tag{1.9}$$

the Friedmann equation Eq. 1.2 can then be written in the equivalent form:

$$\frac{k}{H^2a^2} + 1 = \frac{\rho}{\left(\frac{3H^2}{8\pi G_N}\right)} \equiv \Omega = \sum_i \Omega_i. \tag{1.10}$$

We thus see that Ω is the energy density in units of the critical density, so that a flat Universe is descripted by $\Omega = 1$.
Following [39], we give the following expression of the expansion rate:

$$\frac{H^2(z)}{H_0^2} = \Big[\Omega_M(1+z)^3 + \Omega_R(1+z)^4 + \Omega_\Lambda\Big], \tag{1.11}$$

the various contributions Ω_i to the energy density evolving with time differently, according to the equation of state of each component.

1.2 The DM in the Universe

Ordinary matter, the one we deal with in our everyday life, turns out to be nothing but a very subdominant fraction of the overall energy density of the Universe. Moreover, and no less remarkably, the observational evidences pointing to this overall picture are (increasingly) accurate and independent.
Despite the fact that most of our information about the Universe comes from electromagnetic radiation at different wavelengths, the history of astronomical discoveries of objects whose presence can only be inferred from the resulting gravitational effects on luminous matter is longstanding. For instance, in 1846 this method led to the discovery of Neptune from unexplained residuals in the motion of Uranus. In a similar way, in 1933 Zwicky pointed out that the very existence of the Coma cluster of galaxies would be impossible unless its dynamics was dominated by some kind of unseen (dark) matter (DM). It took however a few decades to realize that DM differs drastically from ordinary baryonic matter, and even longer to pin down a quantitative statement about the actual amount of this exotic form of matter. The determination of cosmological parameters, made possible by the combination of the latest data on CMB anisotropies, of Lyman-α forest and of Supernovae Ia surveys, is of extraordinary accuracy when compared with previous estimates. What is however most striking about these measurements is the apparent concordance of sets of very different observational pieces of evidences towards a minimal model, commonly dubbed ΛCDM or concordance model. The observed structure of galaxies and clusters of galaxies, their motions, the anisotropies of the CMB, the abundance of light elements, the large scale structure and the theory of structure formation, to a satisfactory extent, all nicely fit into this relatively simple single model. This does not mean of course that there are

no marginal discrepancies between the ΛCDM predictions and some astronomical or cosmological observations, and that the model is, in itself, theoretically complete and exhaustive: nevertheless it constitutes a sound framework which, unless differently specified, we will hereafter refer to.

1.3 DM Evidences

The DM existence has been established on a huge variety of scales, from the internal structures of galaxies to the large-scale structure of the Universe. In this section, we will describe how recent progress in both observational astrophysics and experimental cosmology led to a picture of the Universe where the need of a non-luminous component of matter is clearly outstanding.

1.3.1 Astrophysical scales

The first reasoning to invoke the presence of DM rests on the rotational curves of *spiral galaxies*. Combining optical surface photometry with 21 cm line observations makes it possible to measure the circular velocities of disk galaxies out to large Galactocentric distances. The observed behavior is strongly the same for all spirals, remarkably turning out to be a universal property of them: circular velocities linearly rise with the Galactocentric distance in the inner region until a maximum value around $R = 2\,R_d$, with $R_d \sim 2$–4 kpc the scale lenght of the disk where luminous matter is contained, and stay flat at large distances, e.g. out towards the edge of the visible disk (see Fig. 1.1).

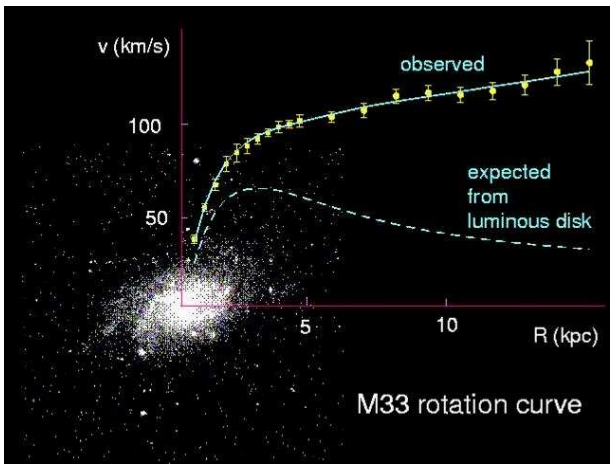

Figure 1.1: An optical image of the nearby spiral galaxy M33, with its rotation curve. Figure by [33].

The flatness beyond the distance where no more star are observed indicates a DM distribution that extents well farther out than that of the visible matter. The dashed falling line corresponds, on the other hand, to the case of absence of DM. On the other side, in Newtonian dynamics the circular velocity of a given object at a distance R from the Galactic Center is expected to be:

$$v_c(R) = \sqrt{\frac{G\,M(R)}{R}}, \tag{1.12}$$

where $M(R) \equiv 4\,\pi\,\int_V \rho(R)\,R^2\,dR$ and $\rho(R)$ is the mass density profile. This implies $v \propto R^{-1/2}$ for $R \geq 3\,R_d$. The dramatic disagreement between the observational data and the theoretical predictions indicates a dominant DM contribution in the halo, where asimptotically $M(R) \propto R$ and $\rho(R) \propto R^{-2}$.

The situation is nearly different for galaxies with different morphologies, as the *elliptical galaxies*. In that case it is not easy to derive the rotation curves, because the highly chaotic motion of stars. The technique adopted for these objects involves a dynamical analysis of stellar orbits, and may be not straightforward in some cases, relying on strong assumptions on a consistent number of observables. Anyway, very precise measurements of strong gravitational lensing effects recently confirmed analytical predictions for ellipticals, supporting the claim that there exists more mass than we can see in galaxies of all types.

1.3.2 Clusters scales

At the scale of galaxy clusters, the object mass determination is based on several methods: application of the virial theorem, obervations of weak gravitational lensing on background galaxies images, and study of the profile of X–ray emission tracing the distribution of hot emitting gas. The virial theorem states that any isolated self-gravitating system reaches the equilibrium state where gravity is balanced by kinetic pressure, e.g.:

$$2K + U = 0, \tag{1.13}$$

where K and U respectively are the cluster kinetic and the potential energies. Both quantities depend on both the mean effective radius and mean squared velocity which allow (under suitable isotropicity assumptions) a precise determination of the cluster overall mass. From separate analysis of the hot gas content of galaxy clusters, as well as strong and weak gravitational lensing results, we derive that the DM content

of regular clusters lies inbetween that of spiral and ellipticals, $30\,M_{lum}$ and $45\,M_{lum}$ respectively [162].

1.3.3 Cosmological scales

A further independent argument in favour of a non-baryonic matter component in the Universe comes from cosmology, in particular by the strong constraints on the abundances of baryons and matter placed by WMAP. The existence of a background radiation originating from the propagation of photons in the early Universe was predicted by G. Gamow in 1948 and discovered by A. Penzias and R. Wilson in 1965. After many decades of experimental effort, the CMB has been measured to be a highly isotropic black body radiation with a temperature $T_0 \simeq 2.726$ K. Anisotropies corresponding to temperature $\Delta T/T \sim 10^{-5}$ have been discovered in 1992 by the COBE mission. Today, the analysis of CMB anisotropies carried out by the WMAP experiment enables an accurate test of cosmological models and puts stringent constraints on cosmological parameters.
The physics of the CMB reflects the acoustic oscillations of the matter-radiation at the time of recombination, driven by the interplay of gravity and radiation pressure. The observed temperature anisotropies in the sky are usually expanded as:

$$\frac{\delta T}{T}(\theta,\phi) = \sum_{\ell=2}^{+\infty} \sum_{m=-\ell}^{+\ell} a_{\ell m} Y_{\ell m}(\theta,\phi), \tag{1.14}$$

where $Y_{\ell m}(\theta,\phi)$ denote spherical harmonics, providing the coefficients c_l of the variance of a_{lm}:

$$c_\ell \equiv \langle |a_{\ell m}|^2 \rangle \equiv \frac{1}{2\ell+1} \sum_{m=-\ell}^{\ell} |a_{\ell m}|^2. \tag{1.15}$$

If the temperature fluctuations are assumed to be Gaussian, as appears to be the case, all of the information contained in CMB maps can be compressed into the *power spectrum*, essentially giving the behavior of c_ℓ as a function of ℓ, $\ell(\ell+1)C_\ell/2\pi$. This quantity reflects the acoustic oscillations in terms of acoustic peaks, whose location and height provides the required information on the geometry and composition of the Universe. More in detail, the position of the first acoustic peak is fixed by the angle θ_1. This quantity is very sensitive to the geometry of the Universe, described by the Ω_{tot} parameter. WMAP measurements give:

$$\Omega_{tot} = 1.02 \pm 0.02, \tag{1.16}$$

that means a *flat* Universe. From the analysis of the WMAP data alone, abundances of baryons and matter respectively are:

$$\Omega_B h^2 = 0.024 \pm 0.001, \qquad \Omega_M h^2 = 0.14 \pm 0.02. \tag{1.17}$$

The obtained value of $\Omega_B h^2$ is consistent with predictions from Big Bang nucleosynthesis:

$$0.018 < \Omega_B h^2 < 0.023. \tag{1.18}$$

An independent estimate of this quantity, remarkably consistent with the range of Eq. 1.18, arises from the features of high-redshift Lyman-α forest neutral hydrogen absorption lines observed in the spectra of background quasars. The piece of information stemming from the determination of the overall baryonic matter content of the Universe may be used to quantify the amount of non-baryonic DM, once the total amount of matter has been determined.

According to Sec. 1.1, the energy budget of a Universe is the sum of the contributions from matter (Ω_M), radiation (Ω_R) and vacuum energy (cosmological constant, Ω_Λ). As currently $\Omega_M >> \Omega_R$, Eq. 1.16 may be rewritten:

$$\Omega_M + \Omega_\Lambda = 1. \tag{1.19}$$

To solve the degeneracy in the $(\Omega_M, \Omega_\Lambda)$ plane, a powerful technique rests on measurements of standard candles luminosities. Standard candles are astronomical objects of known absolute luminosity, located at cosmological distances, a primary role being played by distant Type-Ia supernovae. Once their apparent – and absolute – luminosities L_{app} and L_{abs} are known, this yields to a unique determination of the distance, which depends in a known way on the cosmological parameters Ω_M and Ω_Λ (as a function of the redshift z of the object). Given a point in the (Ω_M, Ω_Λ) plane, this yields to a a curve in the (L–z) plane (the so-called *'Hubble diagram'*). Fig. 1.2, 1.3 and 1.4 collect results from the WMAP analysis of CMB data on the $(\Omega_M, \Omega_\Lambda)$ plane. From a best-fit to data, Eq. 1.19 implies that the Universe contains a large fraction of dark energy. By *'dark energy'* we mean a generic fluid contributing to the Universe energy density featuring negative pressure, and which does not cluster gravitationally, at least up to the galactic cluster scales. The most favourable candidate is the cosmological constant, but alternative explanations, such

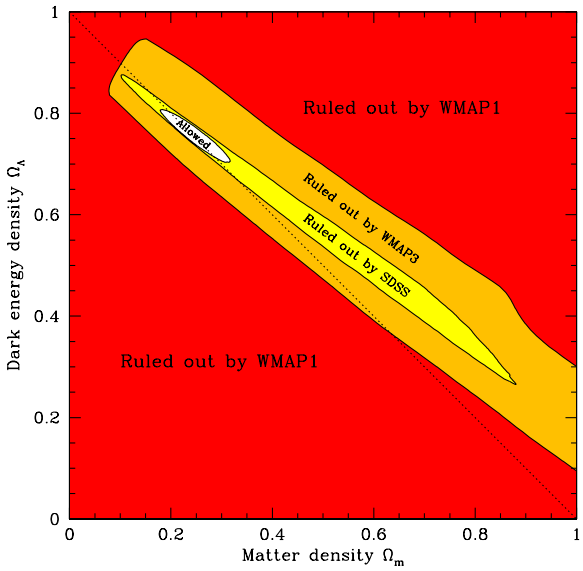

Figure 1.2: Constraints on the geometry of the Universe in the (Ω_M, Ω_Λ) plane from the CMB anisotropies as measured by the WMAP satellite.

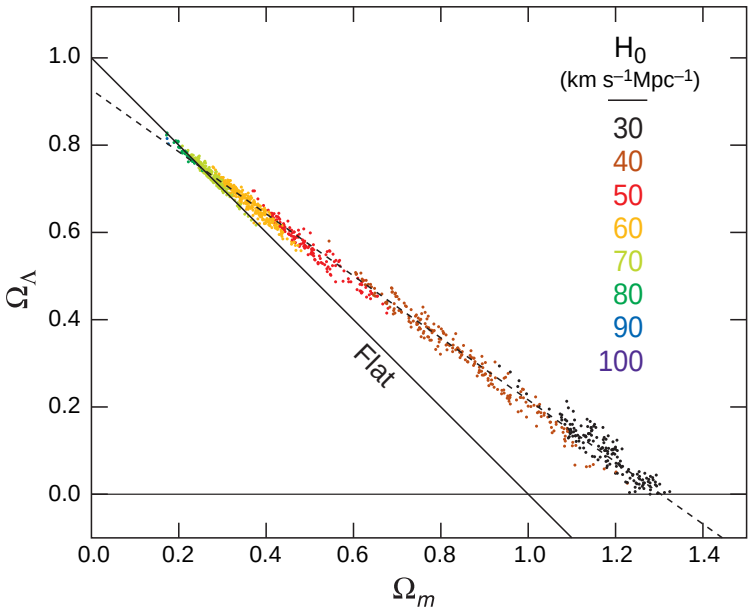

Figure 1.3: Range of non-flat cosmological models consistent with the WMAP data only. The models in the figure are all power-law CDM models with dark energy and dark matter, but without the constraint that $\Omega_M + \Omega_\Lambda = 1$. Figure by [178].

a dynamical scalar fiels (*quintessence*) have also been pursued.

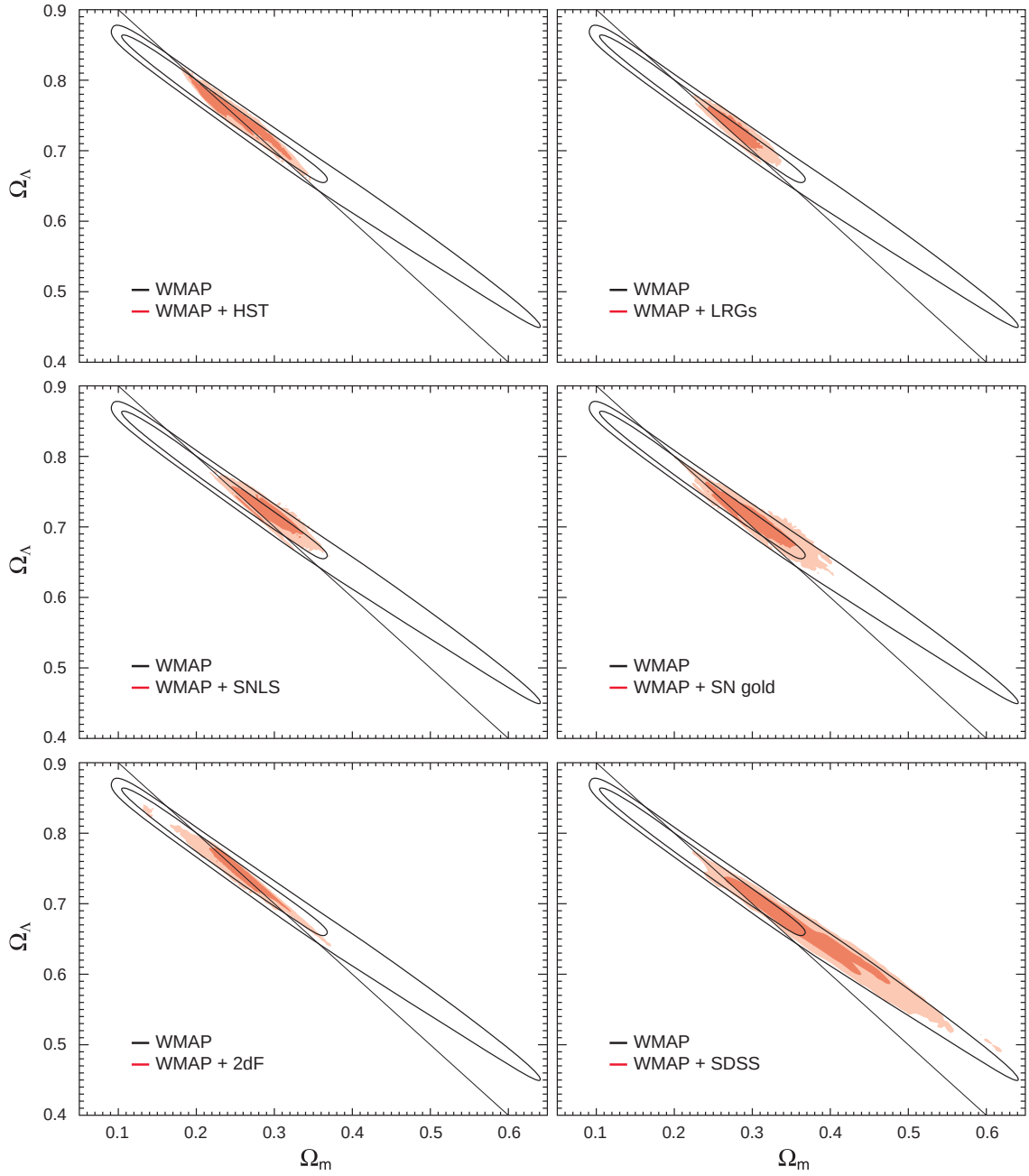

Figure 1.4: Joint two-dimensional marginalized contours (68% and 95%) for matter density, Ω_M, and vacuum energy density, Ω_Λ for power-law CDM models with dark energy and dark matter, but without the constraint that $\Omega_M + \Omega_\Lambda = 1$. The panels show various combinations of WMAP and other data sets. While models with $\Omega_M = 0.415$ and $\Omega_\Lambda = 0.630$ are a better fit to the WMAP three year data alone than the flat model, the combination of WMAP three year data and other astronomical data favors nearly flat cosmologies. *Upper left*: WMAP+HST key project measurement of H_0. *Upper right*: WMAP+SDSS LRG measurement of the angular diameter distance to $z = 0.35$. *Middle left*: WMAP+SNLS data. *Middle right*: WMAP+SNGold. *Lower left*: WMAP+2dFGRS. *Lower right*: WMAP+SDSS. Figure by [178].

Chapter 2

Modeling the DM Distribution

'The distribution of dark matter bears no relationship to anything you will have read in the literature up to now... These are the first properties other than existence that we've been able determine'.

Gerry Gilmore

2.1 Introduction

Modeling the mass distribution within the Milky Way (MW) Galaxy is a classical problem which has been addressed many times. Because of the unique capability to observe the MW in great detail, this problem has always been a productive testing ground for theories of galactic structure and galaxy formation. In the absence of a coherent halo formation theory, early models were plagued by the arbitrary structure parameters of the dark halos. More recent developments in the theory of DM halo formation make this sort of modeling much more meaningful because the halo parameters (such as total mass, peak rotation speed and concentration parameter) may no longer be considered free parameters but are correlated, and these correlations are specified within the context of a given CDM cosmology [55].

While very successful on large scales, the standard cosmological theory introduces some difficulties on the scales of galaxies and dwarf galaxies. The so-called *substructure problem*, i.e. the predicted over-abundance of subhalos relative to observed dwarf satellites of the MW [122, 139], may have been successfully resolved by invoking the presence of a photoionizing background that 'squelches' star-formation in small halos [31, 56, 177]. However, there are problems which remain thorny, mainly related to the

halo cusp and concentration. Their manifestations are mainly encountered in objects which are DM dominated - namely, the central parts of low surface brightness and dwarf galaxies [89, 139, 141, 187]. For example, the high central density of ΛCDM DM halos appears to be inconsistent with the observed rotation curves of dwarf and low surface brightness galaxies [18, 47, 48, 67, 68].

It is interesting to ask how ΛCDM models fare in their predictions for luminous, high surface brightness galaxies, such as the MW and M 31. These systems probe the DM properties on mass scales of 10^{12} $M_{\odot}$, which are significantly larger than the $10^{8}-10^{9}$ $M_{\odot}$ scales tested by inner rotation curves of dwarf galaxies. The MW is particularly interesting for constraining the central DM cusp because the inner $3-10$ kpc region is well studied. Apart from the rotation curve and integrated light distribution, the MW offers many more opportunities to study very detailed data which are not generally available for extragalactic systems, i.e. individual stellar radial velocities and proper motions in the solar neighbourhood, and recently, Galactic bulge microlensing events.

It is likely that the halo of our Galaxy consists mostly of weakly interacting elementary particles (WIMPs), rather than black holes or failed stars (MACHOs), a necessary condition to apply the standard cosmological approach. The very low microlensing counts by MACHOs in the inner 50 kpc halo of the MW imply that elementary particles make up more than $80-90\%$ of the halo [21, 124, 195]. Therefore it should be valid to apply halo formation models to our Galaxy, which predict an outer DM profile of the form $\rho \propto r^{-3}$.

Modeling the Milky Way turns out to be challenging because of its complex formation process. The present-day DM halos can have density profiles very different from those predicted in numerical simulations. They are squeezed and deformed by the gravitational force of the baryons, which collapse out of the original halo to form heavy disks and dense nuclear bulges. The amount of squeezing also depends on the angular momentum transfer between the baryons and the DM halo. The DM cusp is elusive to detection because the gravitational force at the center is dominated by the baryons.

Apart from detailed data, the MW provides a good laboratory for studying most of the main features of galactic dynamics and formation history.

In the present chapter, we will breast to describe the main features of the MW halo, deferring the discussion about other representative systems, like M 31 or the dwarf galaxies, to the continuation of this Thesis.

2.2 The picture of the Milky Way

According with the standard cosmological picture, galaxies and clusters of galaxies form within CDM halos by trapping and cooling of the baryonic gas inside the DM potential wells. The underlying paradigm of this theory is that formation and evolution of structures occur in a hierarchical framework: small objects are the first to form, while bigger structures originate from their progressive collapsing and merging, leading to self-similar configurations. More in general, the DM halos rise from the gravitational amplification of primeval fluctuations, generated at the epoch of inflation with a primordial power spectrum [153]. Recently, very high resolution numerical simulations confirmed that the dark halos are not smooth structureless objects, but clumpy systems characterized by the presence of a wide population of subhalos [71, 72, 192].

Three ingredients are needed for an actual prediction of the gamma, antiproton and positrons fluxes from annihilating DM. We are required to specify the WIMP pair annihilation cross section and estimate the number of photons emitted per annihilation, as well as the energy distribution of these photons: the choice of the particle physics model fixes this element. The second element needed is then the DM density profile in a generic halo of mass M at redshift z. Finally, we need to know the distribution of sources, i.e. we need an estimate of the subhalo mass function. Some insight on the latter two ingredients comes from the ΛCDM model for structure formation: we outline here hypotheses and results entering the prediction for the DM induced flux. We start this section discussing the main features of DM halos, dealing afterwards with the subject of substructure distribution and properties, as well as with their role on the WIMP induced signals.

Henceforth, we will refer to the concordance cosmological model suggested by WMAP 3yr [178]; namely, we assume that the present matter energy density is $\Omega_{M,0} = 0.266$, that the Hubble constant in units of 100 km s^{-1} Mpc^{-1} is $h = 0.71$, that the present mean energy density in baryons is $\Omega_{B,0} = 0.0233/h^2$, with the only other significant extra matter term in CDM $\Omega_{CDM} = \Omega_M - \Omega_B$, that our Universe has a flat geometry and a cosmological constant Λ, i.e. $\Omega_\Lambda = 1 - \Omega_M$, and, finally, that the primordial power spectrum is scale invariant and is normalized to the value $\sigma_8 = 0.772$.

2.2.1 The properties of halos

N-body simulations seem to indicate that DM density profiles can be described in the form:

$$\rho(r) = \rho' \, g(r/r_s) \, , \tag{2.1}$$

where r_s is a length scale and ρ' the corresponding density. The function $g(x)$ is found to be more or less universal over the whole mass range of the simulated halos, although different functional forms have been claimed in different simulations: we will consider the result originally proposed by Navarro, Frenk and White [147] (hereafter NFW profile),

$$g_{NFW}(x) = \frac{1}{x^\gamma \, (1+x)^{3-\gamma}}, \quad \gamma = 1, \tag{2.2}$$

supported also by more recent simulations performed by the same group, and the result found in the higher resolution simulation (but with fewer simulated halos) by Diemand et al. [72] (hereafter M05 profile),

$$g_{M05}(x) = \frac{1}{x^\gamma \, (1+x)^{3-\gamma}}, \quad \gamma = 1.2. \tag{2.3}$$

The two functional forms have the same behavior at large radii and they are both singular towards the center of the halo, but the M05 profile increases much faster than the NFW profile (non-universal forms, with central cusp slopes depending on evolution details have been claimed as well [121]).

There have been a number of reports in the literature arguing that the rotation curves of many small-size disk galaxies rule out divergent DM profiles (note however that this issue is not settled yet), while they can be fitted by profiles with a flat density core. We consider then here a second picture, where the choice of the initial density distribution is deduced supposing that a large transfer of angular momentum between the luminous and the dark components of the cosmic structure has been occurred due to the baryon infall, so that the shape of the DM profile in the inner region of the galaxy has been significantly modified. This leads to the alternative functional form of the Burkert profile [57], which has also been shown to be adequate to reproduce a large catalogue of rotation curves of spiral galaxies:

$$g_B(r) = \frac{1}{(1+x)\,(1+x^2)}. \tag{2.4}$$

While this empirical profile may be justified for the distribution of clumps inside the halo, keeping into accont some global dynamical effects which may have modified the density distribution of the DM, it will not realistic to introduce it for the internal distribution of subhalos, which we will consistently describe by a cuspy profile.

To fully specify the radial density profile, two parameters are needed. While the classical approach involves the lenght scale r_s and the normalization factor ρ' mentioned above, it may however be useful to adopt other two parameters, the virial mass m_{vir} of the object and its concentration parameter c_{vir}. For the latter, we adopt here the definition by Bullock et al. [55]: let the virial radius R_{vir} of a halo of mass M at redshift z be defined as the radius within which the mean density of the halo is Δ_{vir} times the mean background density $\bar{\rho}(z)$ at that redshift:

$$M \equiv \frac{4\pi}{3}\Delta_{vir}\bar{\rho}(z)\, R_{vir}^3. \tag{2.5}$$

We take the virial overdensity to be approximated by the following expression, valid in a flat cosmology,

$$\Delta_{vir} \simeq \frac{(18\pi^2 + 82x - 39x^2)}{\Omega_M(z)}, \tag{2.6}$$

with $x \equiv \Omega_M(z) - 1$, ($\Delta_{vir} \simeq 337$ for $\Omega_M = 0.3$ at $z = 0$). The concentration parameter is then defined as:

$$c_{vir} = \frac{R_{vir}}{r_{-2}}, \tag{2.7}$$

with r_{-2} the radius at which the effective logarithmic slope of the profile is -2, i.e. it is the radius set by the equation $d/dr\ (r^2 g(r))|_{r=r_{-2}} = 0$. This means that $r_{-2} = r_s$ for the NFW profile, while $x_{-2} \equiv r_{-2}/r_s$ is equal to about 0.63 for the M05 profile and to 1.52 for the Burkert profile. Note that these definitions of R_{vir} and c_{vir} differ from those adopted in Ref. [147] and Ref. [80].

After identifying the behavior in Eq. 2.1, Navarro et al. noticed also that, for a given cosmology, the halos in their simulation at a given redshift show a strong correlation between c_{vir} and M [147], with larger concentrations in lighter halos. This trend may be intuitively explained by the fact that low-mass halos typically collapsed earlier, when the Universe was denser. Bullock et al. [55] confirmed this behavior with a larger sample of simulated halos and propose a toy model to describe it, which improves on the toy model originally outlined in [147]: on average, a collapse redshift z_c is assigned to each halo of mass M at the epoch z through the relation $M_\star(z_c) \equiv FM$, where the typical collapsing mass $M_\star$ is defined implicitly by $\sigma\,(M_\star(z)) = \delta_c(z)$, and is postulated to be a fixed fraction F of M (we choose $F = 0.015$). In the last expression, $\sigma(M)$ is the present, linear theory, rms density fluctuations in spheres containing a mean mass M and $\delta_c(z)$ is the critical overdensity required for collapse in the spherical model (see Sec. 2.3.1 for a mathematical definition of these quantities). The density

of the Universe at z_c is then associated with a characteristic density of the halo at z; it follows that, on average, the concentration parameter is given by:

$$c_{vir}(M,z) = K\frac{1+z_c}{1+z} = \frac{c_{vir}(M,z=0)}{(1+z)}, \tag{2.8}$$

where K is a constant i.e. independent of M and cosmology) to be fitted to the results of the simulations. Bullock et al. [55] show that this toy model reproduces rather accurately the dependence of c_{vir} found in the simulations on both M and z. We reproduce this fit at $z = 0$ in Fig. 2.1; 'data' points and relative error bars are taken from [55] and just represent a binning in mass of results in their simulated halos: in each mass bin, the marker and the error bars correspond, respectively, to the peak and the 68% width in the c_{vir} distribution. We determine K with a best fitting procedure in the cosmology $\Omega_{M,0} = 0.3$, $\Omega_{\Lambda,0} = 0.7$, $h = 0.7$ and $\sigma_8 = 1$ adopted in the N-body simulation referred to, and then use this value to estimate the mean c_{vir} in other cosmologies; we find $K = 4.4$. Finally, following again Bullock et al. [55], we assume that, for a given M, the distribution of concentration parameters $\mathcal{P}$ is log-normal with a 1σ deviation $\Delta(\log_{10} c_{vir})$ around the mean, independent of M and cosmology; we take $\Delta(\log_{10} c_{vir}) = 0.2$.

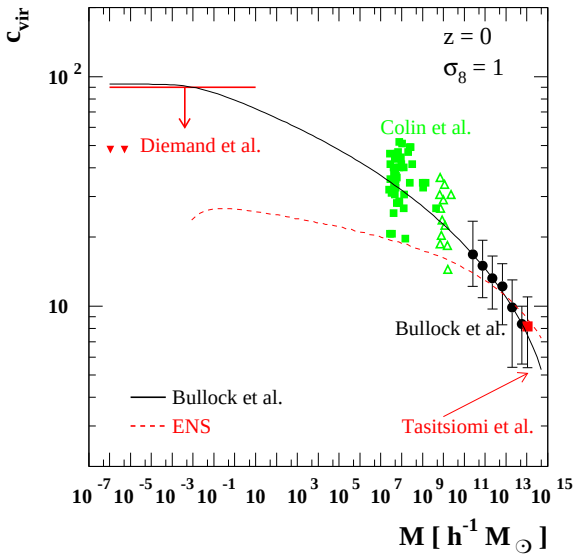

Figure 2.1: Dependence of c_{vir} on mass, at $z = 0$, as in the Bullock et al. toy model (solid line) and in the ENS toy model (dashed line); predictions are comparated to a few sets of simulation results in different mass ranges.

An alternative toy model to describe the relation between c_{vir} and M has been discussed by Eke, Navarro and Steinmetz [80] (hereafter ENS model): the relation they propose has a similar scaling in z, with however a different definition of the collapse redshift z_c and a milder dependence of c_{vir} on M. In our notation, they define z_c through the equation:

$$D(z_c)\sigma_{\rm eff}(M_p) = \frac{1}{C_\sigma}, \tag{2.9}$$

where $D(z) = g(z)/[g(0)(1+z)]$ represents the linear growth rate of the density field,

$$g(z) \approx \frac{5}{2}\,\Omega_M\,[\Omega_M^{4/7} - \Omega_\Lambda + (1+\Omega_M/2)(1+\Omega_\Lambda/70]^{-1}, \tag{2.10}$$

$$\Omega_M \equiv \Omega_M(z) = \frac{\Omega_{M,0}\,(1+z)^3}{E^2(z)}, \tag{2.11}$$

$$\Omega_\Lambda \equiv \Omega_\Lambda(z) = \frac{\Omega_{\Lambda,0}}{E^2(z)}, \tag{2.12}$$

$$E(z) = [\Omega_{\Lambda,0} + (1-\Omega_0)\,(1+z^2) + \Omega_{M,0}\,(1+z^3)]^{1/2} \tag{2.13}$$

and $\sigma_{\rm eff}$ is an 'effective' amplitude of the power spectrum on scale M:

$$\sigma_{\rm eff}(M) = \sigma(M)\,\left(-\frac{d\ln(\sigma)}{d\ln(M)}(M)\right) = -\frac{d\sigma}{dM}M, \tag{2.14}$$

which modulates $\sigma(M)$ and makes z_c dependent on both the amplitude and the shape of the power spectrum, rather than just on the amplitude as in the toy model of Bullock et al. Finally, in Eq. 2.9, M_p is assumed to be the mass of the halo contained within the radius at which the circular velocity reaches its maximum, while C_σ is the parameter (independent on M and cosmology) which has to be fitted to the simulations. With this definition of z_c it follows that, on average, c_{vir} can be expressed as:

$$c_{vir}(M,z) = \left(\frac{\Delta_{vir}(z_c)\,\Omega_M(z)}{\Delta_{vir}(z)\,\Omega_M(z_c)}\right)^{1/3}\frac{1+z_c}{1+z}\,. \tag{2.15}$$

As we already mentioned, the dependence of c_{vir} on M as given in the equation above is weaker than in the Bullock et al. toy model. Our best fitting procedure gives $C_\sigma = 76$ and the behavior in Fig. 2.1 (dashed line), which reproduces the N-body 'data' fairly well, with values not very far from those obtained in the Bullock et al. model within the range of simulated masses, and possibly just a slight underestimate of the mean value in the lighter mass end. On the other hand, the extrapolation outside the simulated mass range can give much larger discrepancies. When going to

small M, c_{vir} increases in both cases, but the growth in the model of Bullock et al. is much faster than in the ENS model; in the next chapter, we will show explicitly how this uncertainty propagates to the prediction of the DM induced gamma-ray flux. The sensitivity of our results to the choice of cosmological parameters is generally much weaker: the largest effect is given by the overall linear scaling of $c_{vir}(M, z)$ with σ_8. There is also the possibility to change the cosmological model by including other dark components; we are not going to discuss any such case in detail, we just mention that a neutrino component at the level of current upper limits is not going to change severely our picture, while a substantial WDM component may play a crucial role if z_c is indeed defined according to the ENS prescription.

2.2.2 Baryonic components

As already mentioned, the high central density of ΛCDM halos appears to be inconsistent with the observed rotation curves of some galaxies [172]. Indeed, in the past years a wealth of observations led to a serious discrepancy with the cuspy density distribution predicted by N-body simulations in ΛCDM cosmology. More in detail, rotation curves in spirals follow an Universal profile (URC) that can be described in terms of an exponential thin stellar disk and a dark halo with a constant density core, whose relative importance increases with galaxy luminosity (see Fig. 2.2 and [159, 174, 173]). To solve this awkward disagreement, a solution for the existence of a region of constant density is that DM halos formed with a cuspy profile, but interactions with baryons during the early stages of galaxy formation smoothed out the original cusp (see Sec. 2.2.1 and [57]). As a consequence, the actual dynamical evolution of DM halos, including their baryonic content, is more complex than that resulting from numerical simulations. In order to provide a more realistic description of the inner distribution and evolution of DM in the Milky Way, we perform a self-treatment of the baryons and DM components.

In traditional mass models of the MW one decomposes the baryons into several descriptive components: the nucleus, the bulge, the bar, the spheroid, the thin disk, the thick disk, and the cold interstellar medium in the disk. It is somewhat problematic to determine where a component starts and ends, and this invariably adds to confusion of terminology. For example, the bar sits in the overlap region between the bulge and the disk, and most stars in this region rotate in the same sense with similar angular speed.

Following [69] and [120], we take a different approach. We divide up the mass of the Galaxy into only two components: a dark halo component and a summed-up baryonic

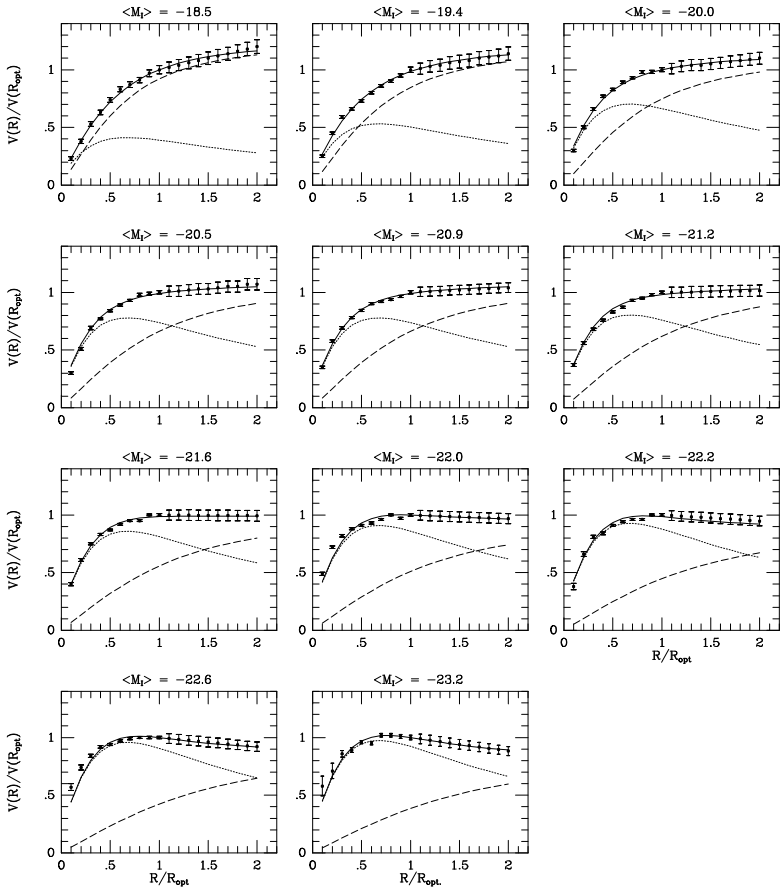

Figure 2.2: Synthetic rotation curves (circles) and the Universal Rotation Curve (solid line). The dark/luminous contributions are indicated with a dashed/dotted line. Figure by [172].

component. We describe this baryonic sum by a function M_B $(< r)$, which is the combined mass of baryons inside the radius r. It is understood that the mass distribution is far from spherical. In fact it is highly flattened, and triaxial inside ~ 3.5 kpc. We incorporate some minimal modeling of the dynamical effects of flattening and triaxiality, but without repeating earlier more rigorous 3-dimensional triaxial dynamical models [196, 101]. Our models for the bulge/bar are motivated by the [196] model of the galactic bulge/bar. That model used COBE DIRBE de-reddened infrared maps [191] and a collection of stellar kinematics data in the direction of the central parts of the galactic bulge. The fit to the data indicated that the bar has an elongated boxy triaxial shape [196] added a steep oblate nucleus to the best-fit so-called 'G2' model of [76]. The nucleus and a massive central black hole are important for modeling the compressed density of the DM within 100 pc. The total mass of the bulge, the bar,

and the nucleus was $(2.2 \pm 0.2) \times 10^{10}\, M_\odot$. No DM was explicitly included in the model of [196]. A massive Miyamo-Nagai analytic disk potential was used to make the rotation curve flat within 8 kpc. Here, instead of the Miyamo-Nagai disk, we use a double-exponential disk as in [118]. The combined density of nucleus, bulge/bar, and disk are modeled by the following three components:

$$\rho_{\rm B} = \rho_n + \rho_{bb} + \rho_d, \tag{2.16}$$

$$\rho_n = \rho_{n0}\,(s_n)^{-1.85} \exp\left(-s_n\right), \tag{2.17}$$

$$\rho_{bb} = \rho_{bb0} \exp\left(-s_{bb}^2/2\right), \tag{2.18}$$

$$\rho_d = \rho_{d0} \exp\left(-s_d\right), \tag{2.19}$$

where ρ_{n0}, ρ_{bb0} and ρ_{d0} are characteristic densities, determined by the corresponding total masses M_n, M_{bb} and M_d of the components ρ_n, ρ_{bb} and ρ_d. The dimensionless radii s_n, s_{bb} and s_d are given by:

$$s_n^2 = \frac{0.6^2(x^2+y^2)+z^2}{z_0^2}, \tag{2.20}$$

$$s_{bb}^4 = \frac{\left[(0.26x)^2+(0.42y)^2\right]^2+z^4}{z_0^4}, \tag{2.21}$$

$$s_d = \frac{\sqrt{x^2+y^2}+12|z|}{r_d}. \tag{2.22}$$

The above aspect ratios in the components $\rho_n(s_n)$, $\rho_{bb}(s_{bb})$ and $\rho_d(s_d)$ are taken from [196] to reproduce the shape of the COBE bar and the disk of [118]. We take the vertical scale height $z_0 = 400$ pc from [196], and take the disk scale-length to be $r_d = 3$ or 3.5 kpc, and the distance to the Galactic Center to be $R_0 = 8$ or 8.5 kpc. These parameter combinations produce acceptable fits to the light distribution of the Milky Way after proper normalization of the three components. [196] normalizes the ρ_n and ρ_{bb} components so that they have equal strength at about a distance $z = 0.75\, z_0$ on the minor axis. This fixes the ratio $\rho_{n0} : \rho_{bb0}$ so that $\rho_n + \rho_{bb}$ joins smoothly from an observed power-law nucleus to the observed COBE bar. The ratio $\rho_{bb0} : \rho_{d0}$ is fixed so that $(M_n + M_{bb}) : M_d = 1 : 5$, approximately matching the bulge-to-disk K-band luminosity ratio $1.1 \times 10^{10}\, L_\odot : 4.9 \times 10^{10}\, L_\odot$ of [118]. Kent et al. in fact introduced a linear tapering of their disk scale length from 250 pc at the solar radius to 167 pc at the center for better matching of the observed surface brightness map. This makes their disk less massive than our double-exponential disk if both are normalized to the

surface density and the volume density at the solar radius. The same is true of the triaxial models of [90], where the axisymmetric disk is tailored into a triaxial hole inside 3.5 kpc. We do not introduce this fine tailoring of the disk, instead favoring the mathematical simplicity of a ρ_{bb} bar and a ρ_d disk, rather than a true bar or disk. The extra mass contained in our ρ_{bb} disk is at the price of reducing the mass of our ρ_d bar given the same budget of mass or light within the central 3.5 kpc. Given the uncertain truncations of the three components ρ_n, ρ_{bb} and ρ_d, they should be treated as convenient functions to describe the overall distribution of baryons. When computing the rotation curve, we approximate ρ_d as a razor-thin disk, and ρ_n and ρ_{bb} as spherical. The enclosed baryonic mass is computed by spherically averaging ρ_B:

$$M_B(< r) = m_{BH} + 4\pi \int_0^r \langle \rho_B \rangle \, r^2 dr \,, \tag{2.23}$$

where

$$\langle \rho_B \rangle \equiv \int \rho_B \frac{d\Omega}{4\pi} \tag{2.24}$$

and we include a central black hole of mass $m_{BH} = 2.7 \times 10^6 \, M_\odot$.
The total mass of the Galaxy inside a radius r is computed as:

$$M(r) = M_{\rm B}(r) + M_{\rm DM}(r), \tag{2.25}$$

where $M_{\rm DM}(r)$ is the DM mass profile. In our Milky Way models the parameters of the bulge are kept close to those of the original [196] bulge. This is done to preserve the agreement with the COBE data and with estimates of stellar radial velocities. Another reason is the microlensing counts, which may be a problem for models of the Milky Way [197]. The rate of microlensing events was estimated for the [196] bulge and was found to be consistent with the constraints on the counts [154].

2.3 Substructures in galactic halos

In the outcoming scenario in which the most promising candidates for DM are WIMPs, supercomputer simulations of the formation history of galactic halos found that the first objects to form should have mass of $10^{-6} M_\odot$ and half mass radii of 10^{-2}pc [72]. Fig. 2.3 shows the numerical simulations of the abundance of collapsed and virialised DM halos of a given mass performed by Diemand, Moore and Stadel in

2005. As described in their paper [72], the same region was simulated twice using different types of intial fluctuations: (A) SUSY-CDM with a 100 GeV neutralino (stars) and (B) an additional model with no small scale cut-off to the power spectrum (open circles), as might be produced by an axion DM candidate. Densities are given in co-moving units, masses in $h^{-1}\,M_\odot = 1.41\,M_\odot$. Model (B) has a steep mass function down to the resolution limit, whereas run (A) has many fewer halos below a mass of about $5 \times 10^{-6}\ h^{-1}\,M_\odot = 3.5 \times 10^{-6}\ h^{-1}\,M_\odot$. Simulations do not probe the mass range from about $3 \times 10^{-4}\ h^{-1}\,M_\odot$ to $2 \times 10^{-1}\ h^{-1}\,M_\odot$.

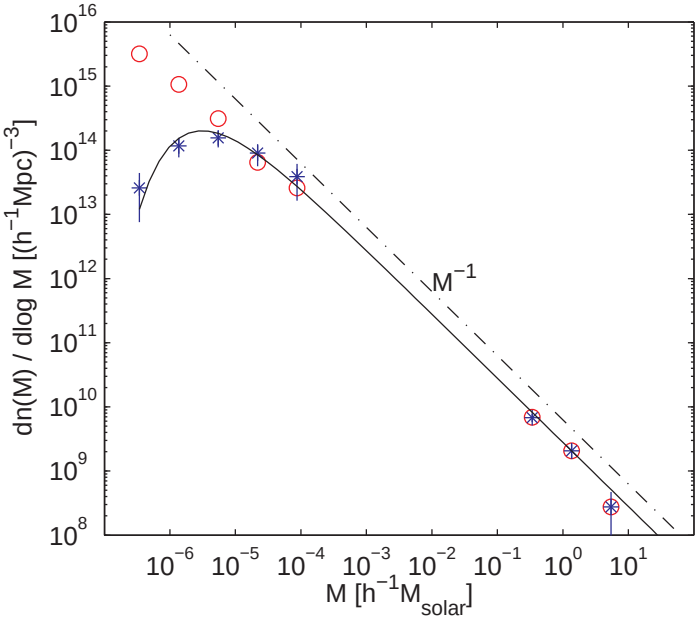

Figure 2.3: Diemand et al. numerical simulations of the abundance of collapsed and virialised DM halos of a given mass. The dashed-dotted line shows an extrapolation of the number density of galaxy halos (from [164]), assuming $dn(M)/d\log M \propto M^{-1}$. The solid line is the function $dn(M)/d\log M = 2.8 \times 10^9\,(M/h^{-1}\,M_\odot)^{-1} \exp -(M/M_{\rm cutoff})^{-2/3}\ h^{-1}\ {\rm Mpc}^{-3}$, with a cutoff mass $M_{\rm cutoff} = 5.7 \times 10^{-6}\ h^{-1}\,M_\odot$. The power spectrum cutoff is $P(k) \propto \exp -(k/{k_{fs}}^2)$, where k_{fs} is the free streaming scale and assuming $k \propto M^{-1/3}$ motivates the exponent of $-2/3$ in fitting function. Figure by [72].

In what follows we will suppose that the same models introduced above for the density profile and concentration parameter consistently hold for both the host halo and the subhalos, capital letters and small letters being used for the notation of the former and the latter respectively.

We also note that when looking inside subhalos, other options are possible to mod-

ify a posteriori the adopted concentration model. For instance, we can scale up the concentration parameter of some factor independent of the mass of the substructure, meaning that we are taking it to be more concentrated than the halo. This assumption is supported by results of numerical simulations [55], where a mapping of mass to concentration is derived for both isolated halos and subhalos. Indeed, c_{vir} is an environmental parameter which depends on the total amount of matter, so that in the case of subhalos it is quite unrealistic to correlate it to the cosmological concentration only. Therefore, in what follows we will furthemore specify our model by the paramaeter F_s, i.e. the ratio of the concentration inside substructures and that of halos of equal mass:

$$F_s \equiv \frac{\langle c_{sub} \rangle}{\langle c_{halo} \rangle}. \tag{2.26}$$

2.3.1 The subhalo spatial mass function

As the astrophysical signals produced by DM WIMP pair annihilation scale with the square of the WIMPs density, in the computation of the subhalo mass function it is crucial to accurately model the spatial distribution of the substructures inside the halo of the progenitor. More in detail, one cannot ignore the effect of spatial correlation on the mass distribution function because these substructures originated from density fluctuations that were close to one another. In the last years, a number of authors introduced a modified formalism to extend the Press & Schecther theory (PS) [161], to include the fact the subhalos grew from spatially correlated density fluctuations in high-density regions, deriving a mass and spatial distribution function which is intermediate between the original PS and the classical extended theory (EPS), where a conditional mass distribution function was introduced to take account of the presence of substructures inside the host halo [91, 125, 149, 194].
This spatially-extended Press & Schecther theory (SPS) postulates that the initial number density of the subhalos of mass m_i formed at redshift z_i at a distance R_i inside a host halo of mass M and redshift z is given by the product of the probability of a substructure of being found in a spherical shell of radius R_i and thickness dR_i and the conditional mass distribution function that, when located at a given position inside the halo, it has an initial mass between m_i and $m_i + dm_i$:

$$\frac{d^2 N_{M,z,z_i}(R_i, m_i)}{dR_i\, dm_i} = P_{M,z}(R_i) \cdot C_{M,z,z_i}(R_i, m_i). \tag{2.27}$$

For the first term on the right size of Eq. 2.27, we make the a priori assumption that it has the form of the halo profile $g(R_i/R_s)$, expecting that subhalos initially follow the distribution of DM particles:

$$P_{M,z}(R_i) = 4\,\pi\,Ri^2\,A\,g(R_i/R_s)\,dR_i, \tag{2.28}$$

where R_s is the lenght scale for the host halo and the normalization factor A is determined by the condition:

$$\int_0^{R_{vir}} P_{M,z}(R_i)dR_i = 1. \tag{2.29}$$

The conditional distribution is obtained following [91, 125, 149, 194]:

$$C_{M,z,z_i}(m_i, R_i) = \frac{M}{m_i}\,f(\sigma_s^2, \delta_c(z_i)|\sigma_h^2, \delta_c(z))\,\Big|\frac{\partial\sigma_s^2}{\partial m_i}\Big|dm_i, \tag{2.30}$$

$$f(\sigma_s^2, \delta_c(z_i)|\sigma_h^2, \delta_c(z)) = \frac{1}{\sqrt{2\,\pi}}\,\Big|\frac{\partial\alpha}{\partial\sigma_s}\Big|\,\frac{1}{\sigma_s}\,\exp\Big(-\frac{\alpha^2}{2}\Big), \tag{2.31}$$

$$\alpha \equiv \alpha(R_i) = \frac{\Big(\delta_c(z_i) - \delta_c(z)\,\frac{\sigma_c^2}{\sigma_h^2}\Big)}{\sqrt{\sigma_s^2 - \frac{\sigma_c^4}{\sigma_h^2}}}, \tag{2.32}$$

where the quantities $\sigma_{s,h}$ and σ_c are respectively the mass variances of the linear density field on the mass scales m_i, M and the linear density cross-correlation, and are related to the dimensionless fluctuation power spectrum $P(k)$ as in [155]:

$$\sigma_s^2 = \int_{-\infty}^{ln\,k(m_i)} P(k)\,\mathrm{d}\,\ln k, \tag{2.33}$$

$$\sigma_h^2 = \int_{-\infty}^{ln\,k(M)} P(k)\,\mathrm{d}\,\ln k, \tag{2.34}$$

$$\sigma_c^2 = \int_{-\infty}^{ln\,k(M)} P(k)\,\tilde{W}_1(k\,R_i)\,\mathrm{d}\,\ln k, \tag{2.35}$$

$\tilde{W}_1 = \sin(kR_i)/kR_i$ being a top-hat window function on the scale R_i and $k(M)$ the wave number:

$$k(M) = \Big(\frac{6\,\pi\,\bar{\rho}}{M}\Big)^{1/3}, \tag{2.36}$$

with $\bar{\rho}$ the comoving DM background density, $\bar{\rho} \simeq \rho_c\Omega_{M,0}$ with ρ_c being the critical density at $z = 0$; $\delta_c(z) = 1.68/D(z)$ is the dimensionless density threshold for a spherical perturbation to collapse by the redshift z. We parametrize the power spectrum

as $P(k) \sim k^n T^2(k)$ in terms of the primordial power-spectrum shape $\propto k^n$ and of the transfer function $T^2(k)$ associated to a the specific DM scenario, fixing the spectral index $n = 1$ and taking the transfer function $T^2(k)$ as given in the fit of Bardeen & al. [27] for an adiabatic CDM model, with the shape parameter modified to include baryonic matter according to the prescription in [153], Eq. (15.84) and (15.85), and an exponential cutoff at large k corresponding to the free-streaming scale for WIMPs [59, 73, 99, 108]. We note that the fit we use agrees within 10% with other analytic results obtained for large k, hence it holds to the accuracy we are concerned about for the small scales we will consider below. We normalize P and σ by computing σ in spheres of a radius of $8/h$ Mpc and setting the result equal to the parameter σ_8. Following [119], we furthemore consider the subhalo formation epoch distribution, i.e. the probability that a subhalo of mass m_{fin} which exists at redshift z has a mass greater than $m_{fin}/2$ at redshift z_i:

$$\frac{dp}{dz_i}(m_{fin}, z)\, dz_i = \frac{dp}{dw_i}(m_{fin}, w_i) \cdot \frac{dw_i}{dz_i}\, dz_i, \tag{2.37}$$

with

$$w_i(m_{fin}, z, z_i) = \frac{\delta_c(z_i) - \delta_c(z)}{\sqrt{\sigma^2(m_{fin}/2) - \sigma^2(m_{fin})}}, \tag{2.38}$$

$$\sigma^2(m_{fin}) = \frac{1}{(2\,\pi)^3} \int_0^\infty P(k)\, \tilde{W}_2^2(k\, R_m)\, 4\,\pi\, k^2\, dk, \tag{2.39}$$

$$\tilde{W}_2 = (3/(kR_i)^3) \cdot (\sin(kR_i) - kR_i \cos(kR_i)), \tag{2.40}$$

$$R_m = \Big(\frac{3\, m_{fin}}{4\,\pi\,\bar{\rho}}\Big)^{1/3}, \tag{2.41}$$

and adopting for $\frac{dp}{dw_i}\,(m_{fin}, w_i)$ the parametrization of Eq. (C4–C7) in Appendix C of [119].

When applied to subhalos, however, the outlined approach does not seem satisfactory at all, as it is based on the oversimplified assumption of mass conservation, considering only the gravitationl merging of substructures, without taking account of the effects of a number of important dynamical processes that mark the evolution of dark halo substructures leading to their final distributions. Among them, in the present work we consider the mass loss caused by the tidal stripping and the orbital decay due to the dynamical frictions. We neglect here the heating due to the close encounters of DM halos on their orbits.

2.3.2 Dynamical evolution of Milky Way satellites

Tidal stripping. The most dominant force that drive the dynamical evolution of the dark halo substructures are the global tides from host halos [150]. These forces strip the outer parts of subhalos, resulting in the subhalo total disruption or at least significant amount of subhalo mass loss.
Considering a subhalo of mass m and maximum rotational velocity v_{max}, moving in a circular orbit of radius R from the center of a host halo with mass $M(R)$ and maximum rotational velocity V_{max}, its tidal radius r_t is the minimum between these two radii: *i)* the radius at which the gravity force of the subhalo equals the tidal force of the host halo and *ii)* the radius defined by the resonances between the force that the small halo exerts on the DM particles and the tidal force by the progenitor.

These two conditions are respectively expressed by [40, 91, 149]:

$$\left(\frac{R}{r_t}\right)^3 \frac{m(r_t)}{M(R)} = 2 - \frac{R}{M}\frac{\partial M}{\partial R} \qquad \text{and} \tag{2.42}$$

$$\Omega(r)|_{small} = \Omega(R)|_{large}, \tag{2.43}$$

where $\Omega(r)$ and $\Omega(R)$ are the orbital frequencies of the host halo and of the satellite. By solving these equations numerically, some plots are given in literature to show the behavior of the tidal stripping radius with the distance from the center of the Milky Way, for subhalos of different mass [44, 91, 121]. In the left panel of Fig. 2.4 we plot the tidal stripping radius versus the distance from the center of the Milky Way for different choices of the progenitor profile and concentration model, while in the right panel of the picture we show the effect of baryons of the same observable.

For the realistic treatment of the mass-loss caused by the global tides, it is necessary to assign the density profiles to both the host halos and the subhalos. The halo mass confined within the radius of R can be computed from the following relation:

$$M(R) = M_{\rm vir}\frac{f(X)}{f(C)}, \tag{2.44}$$

where $f(X) = f(R/R_{\rm s})$ is a function dependent on the DM halo profile and M_{vir} is its virial mass. If the initial density distributions of both the host halo and the subhalos are described by a NFW profile [147], Eqs. 2.42 and 2.43 become:

$$\frac{f(x)}{f(X)} = \left(\frac{x}{X}\right)^3 \left(\frac{r_{\rm s}V_{\rm max}}{R_{\rm s}v_{\rm max}}\right)^2 \left[2 - \frac{X^2}{(1+X)^2 f(X)}\right], \tag{2.45}$$

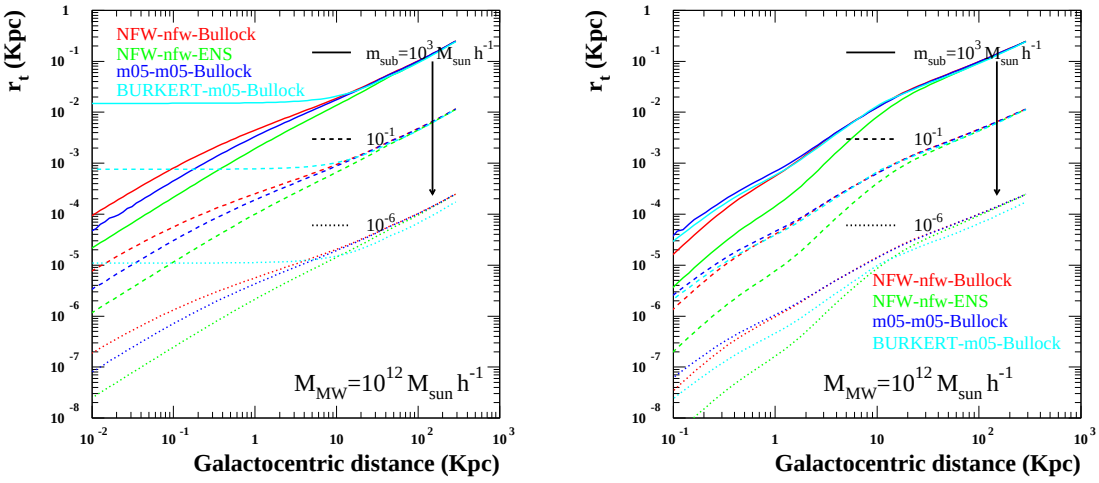

Figure 2.4: *Left panel*: behavior of the tidal stripping radius with the distance from the center of the Milky Way for different choices of the progenitor profile and concentration model. *Right panel*: the same picture in presence of a baryonic component. Figure by Bisesi & Ullio, 2006 [42].

$$\frac{f(x)}{f(X)} = \left(\frac{x}{X}\right)^3 \left(\frac{r_{\rm s} V_{\rm max}}{R_{\rm s} v_{\rm max}}\right)^2, \tag{2.46}$$

where $x \equiv r/r_{\rm s}$ and $X \equiv R/R_{\rm s}$. Here $V_{\rm max}$ and $v_{\rm max}$ represent the maximum circular velocity of the host halo and the subhalo respectively. We approximate that the maximum circular velocity occurs at twice the scale radius [121], $V_{\rm max} = V(2R_{\rm s})$ and $v_{\rm max} = v(2r_{\rm s})$, where the rotation velocities are derived by:

$$V^2(R) = \frac{GM_{\rm vir}}{R}\frac{f(X)}{f(C)}, \tag{2.47}$$

$$v^2(r) = \frac{Gm_{\rm vir}}{r}\frac{f(x)}{f(c)}. \tag{2.48}$$

Once the tidal radius is determined through the above equations 2.45-2.48, the final subhalo mass $m_{\rm f}$, after the tidal stripping effect from the global tides, is computed as:

$$m_{\rm f} = m_{\rm vir}\frac{f(r_{\rm t}/r_{\rm s})}{f(c)}, \tag{2.49}$$

for $r_{\rm t} < r_{\rm vir}$ and $m_{\rm f} = m_{\rm vir}$ otherwise.

Fig. 2.5 shows the masses within the tidal radius against their distance from the center of the Milky Way, for the same models of Fig. 2.4. As the distance from the halo center decreases, the tidal radius of the subhalo and the mass within the tidal

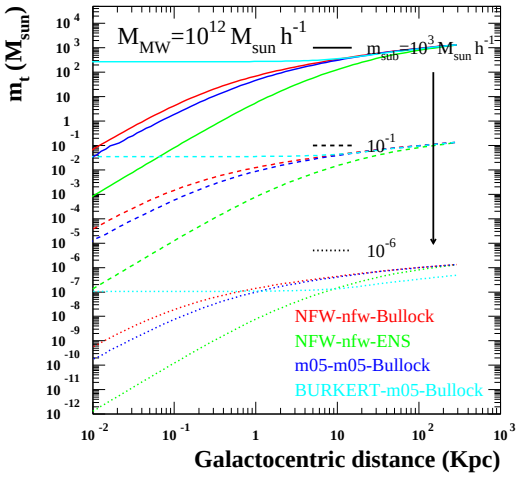

Figure 2.5: Masses within the tidal radius against the distance from the center of the Milky Way, for the same models of Fig. 2.4. Figure by Bisesi & Ullio, 2006 [42].

radius decrease accordingly. Even at large distances from the halo center ($R \simeq R_{vir}$), the subhalo radius changes significantly. Note that the central cusp is not important for survival of subhalos at large distances: r_s is smaller than the tidal radius r_t. At smaller distances ($R \lesssim 2.2\,R_s$), the mass within the tidal radius decreases faster ($m \propto R$) and the orbital-internal resonance defines the tidal stripping. At the same time, whether subhalos survive or not, they already have lost a very large fraction of their mass ($\sim 90\%$, exact number depends on parameters of the subhalo itself) when they get to $R \lesssim R_s$.

Dynamical friction. The dynamical friction effect causes the orbital decay of the subhalos, making tidal forces longer efficient on them. For a substructure moving on a circular orbit of radius R around the host halo, the rate of the orbital radius decay due to this effect is given by the friction time-scale t_{df}:

$$\frac{dR}{dt} = -\frac{R}{t_{\rm df}}, \tag{2.50}$$

which can be estimated by the Chandrasekhar's formula [40]:

$$t_{\rm df}(m_{\rm vir}, R) = \frac{1}{2}\left[\frac{\partial \ln M(R)}{\partial \ln R} + 1\right]^{-1} \cdot \cdot \frac{V^3_{\rm circ}(R)}{4\pi G^2 (\ln\Lambda) m_{\rm vir}\rho(R) g(V_{\rm circ}(R)/\sqrt{2}\sigma_r)}, \tag{2.51}$$

where

$$g(\xi) \equiv \mathrm{erf}(\xi) - \frac{2}{\sqrt{\pi}}\xi e^{-\xi^2}, \tag{2.52}$$

$$\ln\Lambda = 8, \tag{2.53}$$

$$\sigma_r^2 = V_{\max}^2 \frac{2X(1+X)^2}{f(2)} \int_X^\infty \frac{f(x)}{x^3(1+x)^2} dx. \tag{2.54}$$

Here we assume that the initial circular velocities of the subhalos follow the Maxwellian distributions [40, 121], and the Coulomb logarithm Λ has a constant value of 8, since this value is found to give the best result in simulations [183]. Since the dynamical friction timescale is approximately proportional to the radius R [121], the final decayed radius $R_{\rm f}$ of the subhalo during the time interval Δt can be estimated as:

$$R_{\rm f} = R_{\rm i}\left(1 - \frac{\Delta t}{t_{\rm df}(m_{vir}, R_{\rm i})}\right), \tag{2.55}$$

where $R_{\rm i}$ is the initial orbital radius of the subhalo before the orbital decay, and $m_{\rm vir}$ is the initial virial mass of the subhalo before the tidal stripping effect. The model we adopt here is rather simple, and differs from the ones used in the recent comprehensive studies of these dynamical effects. For instance, [104] showed that the effects of tides may be underestimated in the model described above, and that the impulse approximation results in better agreement with the numerical simulations. [30] considered the improved dynamical friction model which incorporates non-circular motions and more complicated Coulomb logarithm Λ. Nevertheless, we keep this simple model so as to be analytically tractable.

The behavior of the dynamical friction time with the distance from the center of the halo of the Milky Way, for different masses of subhalos inside the Galaxy, is shown in Fig. 2.6. For a given subhalo, the dynamical friction time decreases as the subhalo moves into the halo, because the density of the halo increases. Note, however, that this decrease is countered by the subhalo mass decrease due to tidal stripping. The dynamical friction time is thus a varying quantity that depends on the halo mass, the distance from its center and the subhalo's gravitationally bound mass.

The analytic steps to reach the final subhalo spatial and mass distributions with taking account of tidal mass loss and orbital decay caused by dynamical friction are summarized as follows:

1. we determine the final position $R_{\rm f}$ of a subhalo after the dynamical friction effect through equations 2.50-2.55.

2. we determine the tidal radius $r_{\rm t}$ of the subhalo at the final position $R_{\rm f}$ through equations 2.45-2.48;

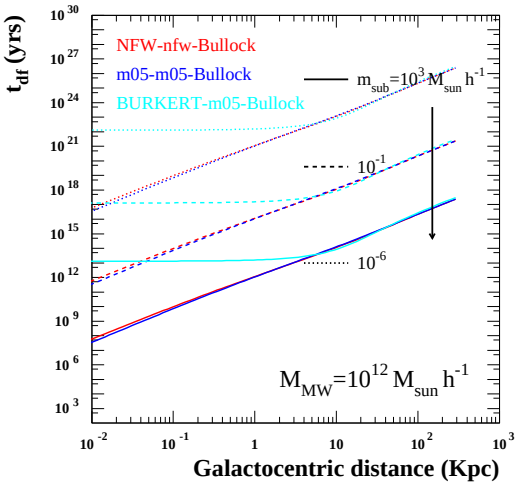

Figure 2.6: Behavior of the dynamical friction time with the distance from the center of the Milky Way, for different subhalo masses and models considered in Fig. 2.4 and 2.5. Figure by Bisesi & Ullio, 2006 [42].

3. we abandon those subhalos whose tidal radius $r_{\rm t}$ is larger than its final orbital radius $R_{\rm f}$, assuming that they will get completely disrupted by the tidal stripping effect;

4. for the survived subhalos with $r_{\rm t} < R_{\rm f}$, we determine the final mass $m_{\rm f}$ through equation 2.49.

The above procedure, represented by the following condition:

$$
\begin{aligned}
m_{\rm f}(m_{\rm i}, R_{\rm i}, z_{\rm i}) &> m, && (2.56)\\
R_{\rm f}(m_{\rm i}, R_{\rm i}, z_{\rm i}) &> R, && (2.57)\\
R_{\rm vir} &> R_{\rm f}(m_{\rm i}, R_{\rm i}, z_{\rm i}), && (2.58)\\
R_{\rm f}(m_{\rm i}, R_{\rm i}, z_{\rm i}) &> r_{\rm t}(m_{\rm i}, R_{\rm i}, z_{\rm i}) && (2.59)
\end{aligned}
$$

define the region shown in Fig. 2.7.
In each picture, we plot contours of the mass and spatial distribution function of Eq. 2.27, times the subhalo formation epoch distribution defined in Eqs. 2.37–2.41. As seen, the regions have a simple topology, and this is easily understandable: the more massive substructures tend to sink faster, thus they should be in the outer regions of the host halo; when $z_{\rm i}$ is larger the typical value of $R_{\rm i}$ also becomes larger because

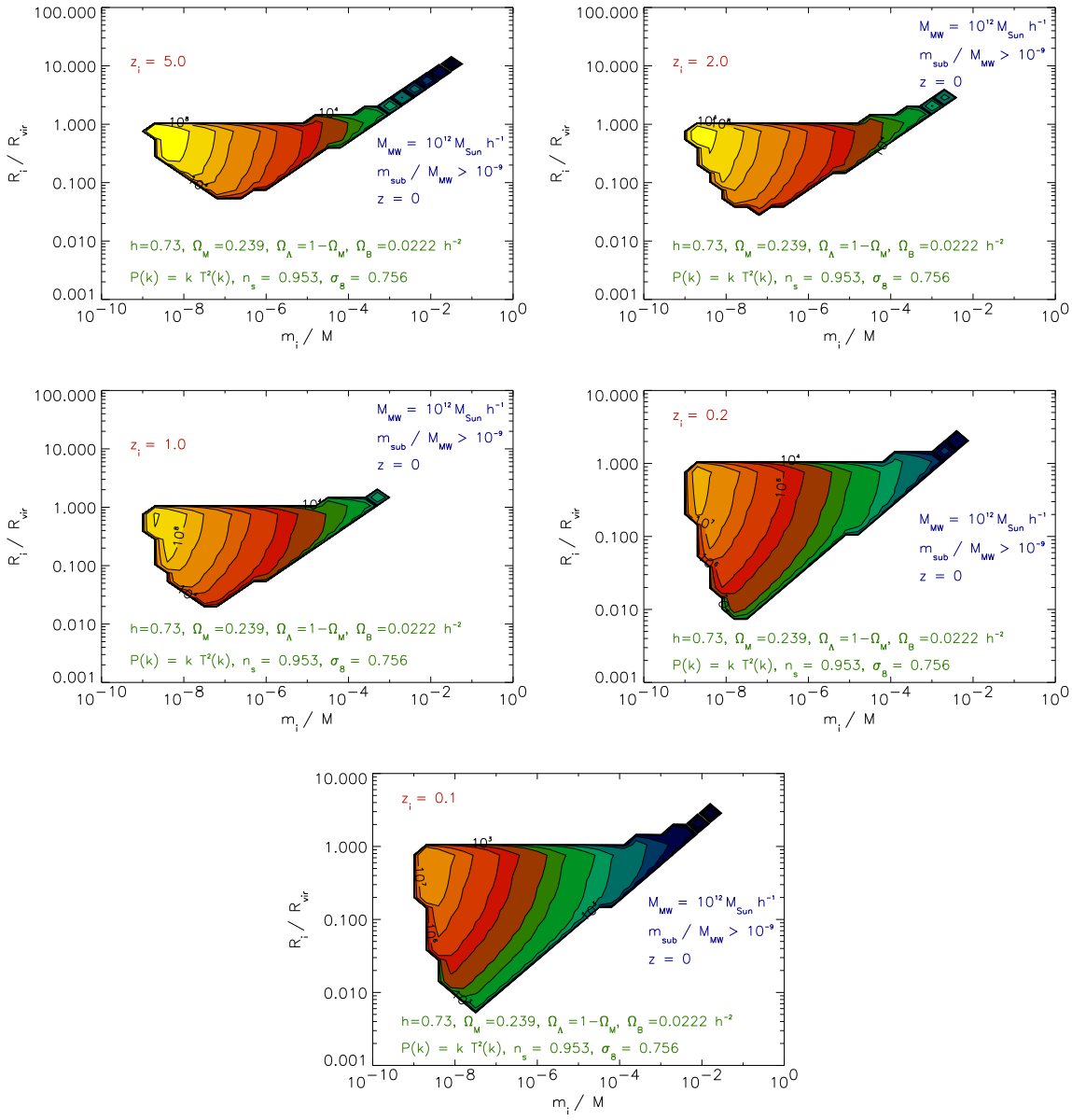

Figure 2.7: The MW subhalo population final configuration region, in the $(m_i,\ R_i)$ plane, for fixed values of z_i; $z_i = 5$ (*upper left*), $z_i = 2$ (*upper right*), $z_i = 1$ (*middle left*), $z_i = 0.2$ (*middle right*), and $z_i = 0.1$ (*lower*). We plot contours of the mass and spatial distribution function of subhalos, weighted on their formation epoch distribution, $(dp/dz_i)\, d^2N_{M,z,z_i}/dR_i\, dm_i$, in a logarithmic space. Yellowish contours mean larger values, thus corresponding regions contribute to the distribution function more. The adopted cosmological parameters, as well as the slope of the power spectrum, are shown on the bottom of each panel (Erica Bisesi, 2006).

substructures experience dynamical friction more. However, we also find that the contribution of massive substructures to the cumulative distribution is rather minor. This is simply because of the small number of massive substructures. Too small $R_{\rm i}$ is not allowed because final sizes of substructures should be smaller than the final distances from the center (Eq. 2.59).

Chapter 3

Dark Matter Candidates

3.1 The DM problem

Given the compelling evidence of a non-baryonic DM component at every observed astrophysical scale, an important task of cosmology and particle physics is to provide a viable candidate of its elementary constituent.
At a first remark, we point out that one cannot a-priori exclude that the general relativity theory of gravity might be modified outside the scales where it has been satisfactory tested by experiments, in order to accomodate some of the evidences for DM into a standard baryonic scenario. Anyway, such a new theory is not available at the moment, making this framework hard to be dealt with.
A suitable particle physics candidate for DM χ should fulfill a list of requirements, dictated by cosmology, astrophysical observations and DM detection experiments. First of all, the cosmological abundance of the species χ must lie in the range dictated by Eq. (1.31):

$$0.119 < \Omega_\chi \, h^2 < 0.135 \ \ [178]. \tag{3.1}$$

Moreover, we require that the species χ must be stable, as well as electrically and color neutral. Finally, if our DM particle candidate would be strongly or electromagnetically interacting with normal matter, it should form anomalously heavy ipotopes, with an abundance $n/n_H \lesssim 10^{-10}$, in strong contrast with existing upper limits on the abundances of hydrogen nuclear isotopes [162]:

$$n/n_H \lesssim 10^{-15} \div 10^{-29} \quad \text{for} \ \ 1 \text{ GeV} \lesssim m_\chi \lesssim 1 \text{ TeV}. \tag{3.2}$$

Therefore, a good DM candidate must be, over a wide mass range, at most *weakly interacting* with matter.

This set of requirements entails that the only plausible DM candidate *within the Standard Model* is the neutrino, which, at least, features the 'undisputed virtue to exist'. However, combining the well-known estimate of the neutrino relic abundance:

$$\Omega_\nu\, h^2 = \sum_{i=1}^{3} \frac{m_i}{93 \text{ eV}}, \tag{3.3}$$

with upper limits on the neutrino masses from tritium β-decay:

$$m_\nu < 2.05 \text{ eV (95\% C.L.)}, \tag{3.4}$$

shows that neutrinos may at best be a subdominant DM component. Moreover, combined CMB and large scale structure data further restrict the possible amount of HDM composed by neutrinos all the way down to [162]:

$$\Omega_\nu\, h^2 < 0.0067. \tag{3.5}$$

The bottom line is therefore that *the existence of DM requires physics beyond the Standard Model.* We will not enter here into the blooming garden of more or less exotic particle DM candidates; we simply state that the minimal supersymmetric extension of the Standard Model is perhaps the best motivated particle physics framework, and provides an ideal candidate for CDM, *the lightest neutralino*, to whom the remining part of this Thesis is devoted to.

3.2 Weakly interacting massive particles

In the context of the non-baryonic scenario, very interesting and plausible candidates for DM are Weakly Interacting Massive Particles (WIMPs). Long-lived or stable WIMPs can be a thermal leftover from the Big Bang, as they were in thermal equilibrium with the Standard Model particles in the early Universe, and decoupled when they were non-relativistic. Moreover, WIMPs have the important merit of accounting for the right fraction of relic matter density. In fact, by solving the Boltzmann equation, which describes the time evolution of the number density $n(t)$ of WIMPs, one find:

$$\Omega_\chi\, h^2 \simeq \frac{3 \times 10^{-27} \text{ cm}^3 \text{ s}^{-1}}{\langle \sigma_{ann}\, v \rangle}, \tag{3.6}$$

where $\Gamma = \langle \sigma_{ann}\, v \rangle\, n$ is the WIMP annihilation rate. If a new particle with weak interactions exists in Nature, its cross section will be $\sigma \simeq \alpha^2 / M^2_{\rm weak}$, where $\alpha \simeq \mathcal{O}(10^{-2})$ is the weak coupling and $M_{\rm weak} \simeq \mathcal{O}(100\ {\rm GeV})$ is a mass of the order of the W gauge boson. Thus one obtains $\sigma \approx 10^{-9}\ {\rm GeV}^{-2} \approx 1$ pb. Since at the freeze-out temperature T_F the velocity v is a significant fraction of the speed of light ($v^2 \approx c^2/20$), this means $\langle \sigma_{ann}\ v \rangle \approx 10^{-26}\ {\rm cm}^3\ {\rm s}^{-1}$. Remarkably, this number is close to the value that we need in Eq. 3.1, in order to obtain the observed density of the Universe.
We will now concentrate on the leading candidate for WIMP, the lightest supersymmetric particle (LSP). Supersymmetry (SUSY) is a new type of symmetry which allows for a possible candidate for DM, so we are required to discuss this question more deeply.

3.3 Basics of SUSY

In this section, we follow [39], in reviewing the basics concepts of SUSY.
In the Standard Model of particle physics there is a fundamental distinction between bosons and fermions: while bosons are the mediators of interactions, fermions are the constituents of matter. It is therefore natural to ask whether a symmetry exists which relates them, thus providing a sort of 'unified' picture of matter and interactions.

There are some major reasons for interest in SUSY. One reason is its role in understanding the *hierarchy problem*. The hierarchy problem is linked to the enormous difference between the electroweak and Planck energy scales. This problem arises in the radiative corrections to the mass of the Higgs boson. All particles get radiative corrections to their mass, but while fermion masses increase only logarithmically, scalar masses increase quadratically with energy, giving corrections at 1-loop of

$$\delta m_s^2 \sim \left(\frac{\alpha}{2\pi}\right) \Lambda^2, \tag{3.7}$$

where Λ is a high-energy cut-off where new physics is expected to play an important role. The radiative corrections to the Higgs mass (which is expected to be of the order of the electroweak scale $M_{weak} \sim 100$ GeV) will destroy the stability of the electroweak scale if Λ is higher than $\sim$ TeV, e.g if Λ is near the Planck mass. An appealing, though not the only, solution to this problem is to postulate the existence of new particles with similar masses but with spin different by one half. Then, since the contribution of fermion loops to δm_s^2 have opposite sign to the corresponding bosonic loops, at the 1-loop level, Eq. 3.7 becomes:

$$\delta m_s^2 \sim \left(\frac{\alpha}{2\pi}\right)\left(\Lambda^2 + m_B^2\right) - \left(\frac{\alpha}{2\pi}\right)\left(\Lambda^2 + m_F^2\right) = \left(\frac{\alpha}{2\pi}\right)\left(m_B^2 - m_F^2\right). \tag{3.8}$$

Furthermore, the SUSY algebra insures that (provided $|m_B^2 - m_F^2| \lesssim 1$ TeV) the quadratic divergence to the Higgs mass is cancelled at all orders of perturbation theory. The SUSY algebra naturally guarantees the existence of new particles, with the required properties, associating to all of the particles of the Standard Model superpartners with the same mass and opposite spin-type (boson or fermion). Another reason for interest in SUSY theories comes from the unification of gauge couplings at a scale $M_U \sim 2 \times 10^{16}$ GeV. Although extrapolation of the coupling constants using only Standard Model particles fails to unify them to a common value, by introducing SUSY at the TeV scale, it was shown that these forces naturally unify at a scale $M_U \sim 2 \times 10^{16}$ GeV. This has been taken as a strong hint in favor of a Grand Unified Theory (GUT), which predicts gauge coupling unification below the Planck scale (see Fig. 3.1).

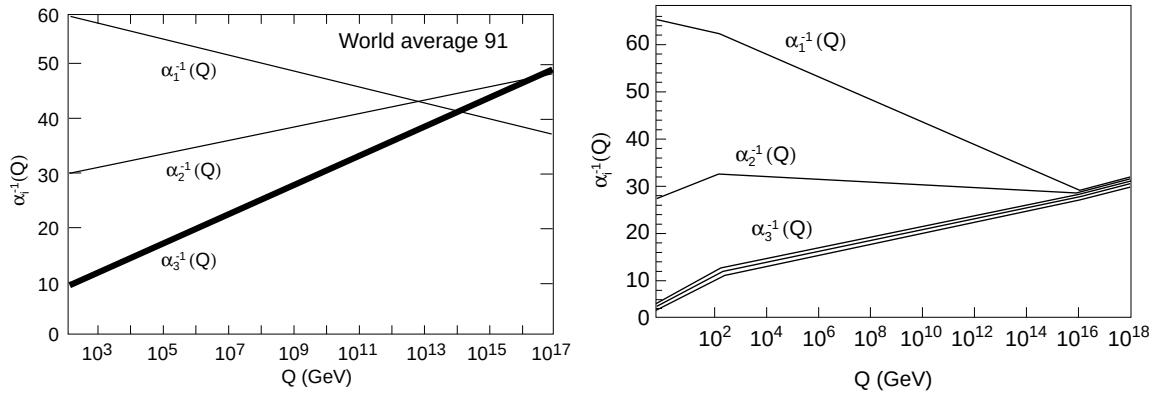

Figure 3.1: The measurements of the gauge coupling strengths at LEP do not (*left panel*) evolve to a unified value if there is no SUSY, but do (*right panel*) if SUSY is included. Figure and text from [39].

The new generators introduced with SUSY change fermions into bosons and vice-versa, e.g.:

$$Q|\text{fermion} >= |\text{boson} >; \qquad Q|\text{boson} >= |\text{fermion} > . \tag{3.9}$$

Because of their fermionic nature, the operators Q must carry spin 1/2, which implies that SUSY must be a spacetime symmetry. The question then arises of how to extend the Poincaré group of spatial translations and Lorentz transformations to include this new boson-fermion symmetry. For realistic theories, the operators Q, which we choose by convention to be Majorana spinors, must satisfy:

$$\{Q_a, \overline{Q}_b\} = 2\gamma^\mu_{ab} P_\mu \tag{3.10}$$

$$\{Q_a, P_\mu\} = 0 \tag{3.11}$$

$$[Q_a, M^{\mu\nu}] = \sigma^{\mu\nu}_{ab} Q^b, \tag{3.12}$$

where

$$\overline{Q}_a \equiv \left(Q^\dagger \gamma_0\right)_a \tag{3.13}$$

and

$$\sigma^{\mu\nu} = \frac{i}{4}[\gamma^\mu, \gamma^\nu] \tag{3.14}$$

are the structure constants of the theory.

Just as Lorentz invariance is manifest in Minkowski space-time, SUSY is manifest in the so-called *superspace* formalism, where a superspace is defined as a set of coordinates $\{x, \theta, \overline{\theta}\}$, where $x = x^\mu$ are the usual coordinate of Minkowski spacetime, and $\theta, \overline{\theta}$ are anti-commuting Weyl spinors. A *superfield* is then a function, $\Phi(x, \theta, \overline{\theta})$, defined on a superspace; it is common to introduce *chiral fields* representing matter and *vector fields* representing gauge fields.

3.3.1 Minimal Supersymmetric Standard Model

To continue this brief introduction to SUSY, we consider the minimal supersymmetric extension of the Standard Model (MSSM). The MSSM is minimal in the sense that it contains the smallest possible field content necessary to give rise to all the fields of the Standard Model. This can be done as follows:

- we associate fermionic superpartners to all gauge fields. Gluons, $W^\pm$ and B bosons then get fermionic partners called *gluinos* ($\tilde{g}$), *winos* ($\tilde{W}^i$) and *binos* ($\tilde{B}$), respectively. The common name for all partners of gauge fields is the *gaugino*;

- we associate scalar partners to the fermions, e.g. quarks and leptons get scalar partners called *squarks* and *sleptons*;

- we introduce one additional Higgs field (for a total of two Higgs doublets, corresponding to five physical Higgs states) and associate one spin 1/2 *higgsino* to each Higgs boson. This is done to give masses to both up and down-type quarks upon electroweak symmetry breaking and also preserve SUSY.

The resulting particle content of the theory is shown in Tables 3.1 and 3.2. One additional ingredient of the MSSM is the conservation of R-parity. R-parity is a

Superfield	SM particles	Spin	Superpartners	Spin
Q	$\begin{pmatrix} u_L \\ d_L \end{pmatrix}$	1/2	$\begin{pmatrix} \tilde{u_L} \\ \tilde{d_L} \end{pmatrix}$	0
U^c	$\bar{u}_R$	1/2	$\tilde{u}^*_R$	0
D^c	$\bar{d}_R$	1/2	$\tilde{d}^*_R$	0
L	$\begin{pmatrix} \nu_L \\ e_L \end{pmatrix}$	1/2	$\begin{pmatrix} \tilde{\nu_L} \\ \tilde{e_L} \end{pmatrix}$	0
E^c	$\bar{e}_R$	1/2	$\tilde{e}^*_R$	0
H_1	H_1	0	$\tilde{H}_1$	1/2
H_2	H_2	0	$\tilde{H}_2$	1/2
G^a	g	1	$\tilde{g}$	1/2
W_i	W_i	1	$\tilde{W}_i$	1/2
B	B	1	$\tilde{B}$	1/2

Table 3.1: Field content of the MSSM.

multiplicative quantum number defined as

$$R \equiv (-1)^{3B+L+2s}. \tag{3.15}$$

All of the Standard Model particles have R-parity $R = 1$ and all sparticles (e.g. superpartners) have $R = -1$. Thus, as a consequence of R-parity conservation, sparticles can only decay into an odd number of sparticles (plus Standard Model particles). The lightest SUSY particle (the LSP) is, therefore, stable and can only be destroyed via pair annihilation, making it an excellent DM candidate.

Among different candidates, sneutrino LSPs have been excluded by direct DM detection experiments. Although axinos and gravitinos cannot be a prori excluded, they arise only in a subset of SUSY scenarios and have some unattractive properties. In particular, gravitinos and axinos have very weak interactions and would be practically impossible to detect, making them less interesting from a phenomenological perspective. The lightest *neutralino* remains an excellent DM candidate, and is further discussed in the next Section.

3.3.2 The lightest neutralino

In the MSSM, the superpartners of the B, W_3 gauge bosons (or the photon and Z, equivalently) and the neutral Higgs bosons, H^0_1 and H^0_2, are called binos ($\tilde{B}$), winos ($\tilde{W}_3$), and higgsinos ($\tilde{H}^0_1$ and $\tilde{H}^0_2$), respectively. These states mix into four Majorana

Standard Model particles and fields		SUSY partners			
		Interaction eigenstates		Mass eigenstates	
Symbol	Name	Symbol	Name	Symbol	Name
$q = d, c, b, u, s, t$	quark	$\tilde{q}_L$, $\tilde{q}_R$	squark	$\tilde{q}_1$, $\tilde{q}_2$	squark
$l = e, \mu, \tau$	lepton	$\tilde{l}_L$, $\tilde{l}_R$	slepton	$\tilde{l}_1$, $\tilde{l}_2$	slepton
$\nu = \nu_e, \nu_\mu, \nu_\tau$	neutrino	$\tilde{\nu}$	sneutrino	$\tilde{\nu}$	sneutrino
g	gluon	$\tilde{g}$	gluino	$\tilde{g}$	gluino
$W^\pm$	W-boson	$\tilde{W}^\pm$	wino	$\tilde{\chi}^\pm_{1,2}$	chargino
H^-	Higgs boson	$\tilde{H}_1^-$	higgsino		
H^+	Higgs boson	$\tilde{H}_2^+$	higgsino		
B	B-field	$\tilde{B}$	bino	$\tilde{\chi}^0_{1,2,3,4}$	neutralino
W^3	W^3-field	$\tilde{W}^3$	wino		
H_1^0	Higgs boson	$\tilde{H}_1^0$	higgsino		
H_2^0	Higgs boson	$\tilde{H}_2^0$	higgsino		
H_3^0	Higgs boson				

Table 3.2: Standard Model particles and their superpartners in the MSSM (adapted from [78]).

fermionic mass eigenstates, called neutralinos. The four neutralino mass eigenstates are typically labelled $\tilde{\chi}^0_1$, $\tilde{\chi}^0_2$, $\tilde{\chi}^0_3$ and $\tilde{\chi}^0_4$, ordered with increasing mass neutralino. In the following we will refer to $\tilde{\chi}^0_1$, e.g. the lightest of the four neutralinos, as *the* neutralino, and denote it simply as $\chi \equiv \tilde{\chi}^0_1$.

In the basis $(\tilde{B}, \tilde{W}_3, \tilde{H}_1^0, \tilde{H}_2^0)$, the neutralino mass matrix can be expressed as:

$$\mathcal{M}_N = \begin{pmatrix} M_1 & 0 & -M_Z \cos\beta \sin\theta_W & M_Z \sin\beta \sin\theta_W \\ 0 & M_2 & M_Z \cos\beta \cos\theta_W & -M_Z \sin\beta \cos\theta_W \\ -M_Z \cos\beta \sin\theta_W & M_Z \cos\beta \cos\theta_W & 0 & -\mu \\ M_Z \sin\beta \sin\theta_W & -M_Z \sin\beta \cos\theta_W & -\mu & 0 \end{pmatrix}, \tag{3.16}$$

where M_1 and M_2 are the bino and wino mass parameters, respectively, θ_W is the Weinberg angle and $\tan\beta$ is the ratio of the vacuum expectation values of the Higgs bosons and μ is the higgsino mass parameter. The lightest neutralino is a linear combination of $\tilde{B}$, $\tilde{W}_3$, $\tilde{H}_1^0$ and $\tilde{H}_2^0$:

$$\chi = N_{11}\tilde{B} + N_{12}\tilde{W}_3 + N_{13}\tilde{H}_1^0 + N_{14}\tilde{H}_2^0. \tag{3.17}$$

We then define the gaugino fraction, f_G, and the higgsino fraction, f_H, as

$$f_G = N_{11}^2 + N_{12}^2 \tag{3.18}$$

and

$$f_H = N_{13}^2 + N_{14}^2 \, . \tag{3.19}$$

3.3.3 Most relevant annihilation channels

The neutralino interactions most relevant for the purposes of dark matter are self-annihilation and elastic scattering off of nucleons. At low velocities, the leading channels for neutralino annihilation are annihilations to fermion-antifermion pairs (primarily heavy fermions, such as top, bottom and charm quarks and tau leptons), gauge bosons pairs (W^+W^- and Z^0Z^0) and final states containing Higgs bosons. In particular, Fig. 3.2 shows the production of two fermions $f\,\tilde{f}$ in the final state through the exchange of boson Z^0 or the pseudo-scalar Higgs A, in the $s-$channel, or through the exchange of sfermions $\tilde{f}$, in the $t-$channel. In mSUGRA (see next), the lightest neutralino $\tilde{\chi}_1^0$ is mainly a bino, so the contributions of these diagrams will be typically small, except for the $\tilde{f}$ $t-$channel, that is highly suppressed by the high $\tilde{f}$ masses. Only the $s-$channels are favored for the (unprovable in mSUGRA) higgsino-like neutralinos. There exist other less favorable channels, like the mentioned W^+W^- production via exchange of chargino in $t-$channel, and many others, but less important.

3.3.4 SUSY models

Although relatively simple in many respects, the MSSM has a huge number of free parameters. Most of these parameters represent masses and mixing angles, much as in the case of the Standard Model. To allow for the practical phenomenological study of the MSSM, the number of parameters which are considered must be reduced. This can be done by making (theoretically well motivated) assumptions which reduce the free parameters from more than 100 to a more tractable quantity. Depending on the used assumptions, one obtains different SUSY models. In this subsection, we will describe a few of the most widely considered SUSY scenarios, including mSUGRA (often called the constrained MSSM) and a phenomenologically simplified MSSM (called the phenomenological, or pMSSM).

mSUGRA. The mSUGRA, or constrained MSSM, scenario is a simple phenomenological model based on a series of theoretical assumptions (see e.g. [115]). The number of free parameters is reduced in this scenario, by assuming that the MSSM parameters obey a set of boundary conditions at the GUT scale:

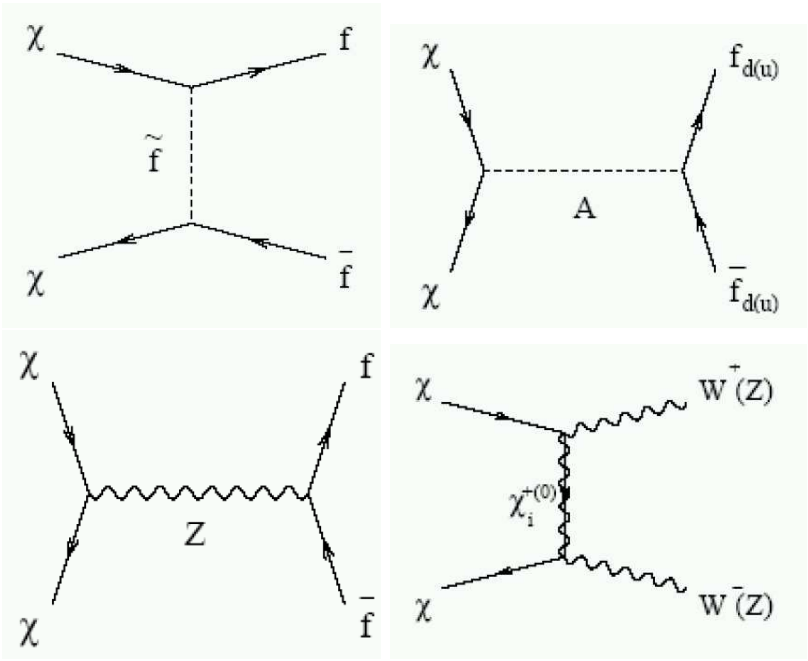

Figure 3.2: Dominant neutralino annihilation diagrams.

- gauge coupling unification:

$$\alpha_1(M_U) = \alpha_2(M_U) = \alpha_3(M_U) \equiv \alpha_U, \tag{3.20}$$

  with $\alpha_i = g_i^2/4\pi$;

- unification of the gaugino masses:

$$M_1(M_U) = M_2(M_U) = M_3(M_U) \equiv m_{1/2}; \tag{3.21}$$

- universal scalar sfermion and Higgs boson masses:

$$M_{\tilde{Q}}(M_U) = M_{\tilde{u}_R}(M_U) = M_{\tilde{d}_R}(M_U) = M_{\tilde{L}}(M_U) = M_{\tilde{l}_R}(M_U) = \\ = M_{H_u}(M_U) = M_{H_d}(M_U) \equiv m_0; \tag{3.22}$$

- universal trilinear couplings:

$$A_u(M_U) = A_d(M_U) = A_l(M_U) \equiv A_0. \tag{3.23}$$

By requiring the minimization of the Higgs potential (in order to recover electroweak symmetry breaking), we are left with five (four continuous and one discrete) free parameters:

$$\tan\beta \ , \ m_{1/2} \ , \ m_0 \ , \ A_0 \ , \ \ \mathrm{sign}(\mu), \tag{3.24}$$

where $\tan\beta$ is the ratio of the vacuum expectation values of the two Higgs fields and μ is the higgsino mass parameter. A discussion of mSUGRA parameters and the definition of SUSY *benchmarks* points may be found in Ref. [29].

Accelerator constraints. In addition to constraints on models in mSUGRA which come from the WMAP measurements, strong limitations can also be placed by collider data. In particular, constraints arise from the absence of new particles at LEP below $\sim$ 100 GeV and the agreement of $b \to s\gamma$ decays with predictions of the Standard Model. Measurements of the anomalous magnetic momentum of the muon, $g_\mu - 2$ also provide a possible constraint. These constraints have been studied in the context of mSUGRA in great detail [24, 81, 169]. We apply here the following conservative cuts on our models:

- Higgs mass: $m_h > 113.5$ GeV [62];
- chargino mass: $m_{\chi^+} > 103.5$ GeV [63];
- $b \to s\,\gamma$ constraint [64];
- the muon anomalous magnetic moment [85]: $8.1\times10^{-10} < \delta_\mu^{\mathrm{SUSY}} = \delta_\mu^{\mathrm{exp}} - \delta_\mu^{\mathrm{SM}} < 44.1\times10^{-10}$ $[2\,\sigma]$.

Once accelerators constraints have been imposed, it is possible to scan the parameter space to obtain the boundaries of its allowed regions. Some examples of this kind are given in Fig. 4.9 of the next chapter. As it is clearly visible, neutralinos with masses from some tens of GeV to some TeV are allowed.

The reach of future collider experiments.

- **Tevatron:** the reach of the Tevatron extends to higher energies than any other accelerator until the time at which the Large Hadron Collider (LHC) becomes operational. The range of masses which can be searched for colored particles (squarks, gluinos and KK quarks, for example), heavy gauge bosons and other new physics will be increased significantly at the Tevatron IIb [39].

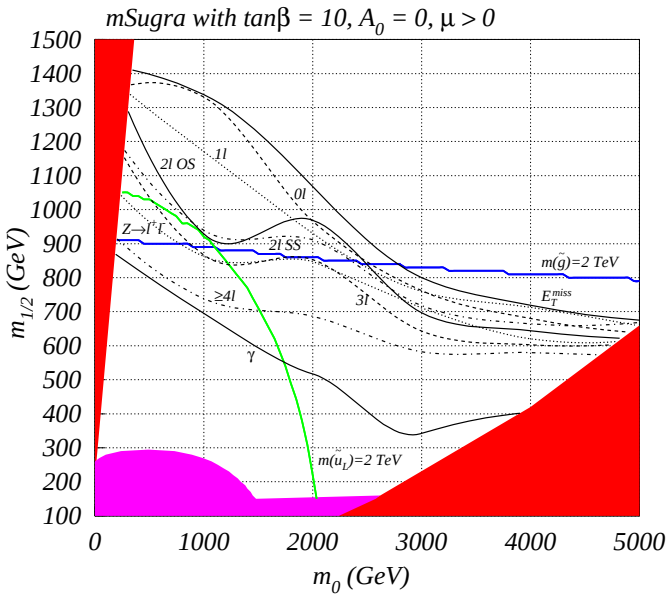

Figure 3.3: An example of the reach of the Large Hadron Collider (LHC) to new TeV-scale physics. The red regions are excluded by theoretical constraints, while the magenta region is excluded experimentally. 100 fb^{-1} of integrated luminosity is assumed. Figure by [39].

- **Large Hadron Collider:** LHC is expected to begin operation around 2007 with proton-proton collisions at 14 TeV center-of-mass energy. A luminosity of 300 inverse femtobarns is expected to be achieved, making the prospects for discovering new physics at the LHC excellent. Numerous classes of models which provide interesting DM candidates will be tested at this very important experiment, searching at scales of up to several TeV. In addition to the Higgs boson(s), the LHC will be sensitive to most SUSY scenarios, models with TeV-scale universal extra dimensional, little Higgs models, etc. Fig. 3.3 shows an example of the reach of the LHC to new TeV-scale physics. As a function of m_0 and $m_{1/2}$ in the mSUGRA (or constrained MSSM) scenario, with $\tan\beta = 10$, $A_0 = 0$ and positive μ, the reach is shown for a variety of channels. Also shown are the 2 TeV up squark and 2 TeV gluino mass contours [39].

The mSUGRA regions. A recent study of mSUGRA parameter space in light of the WMAP measurement of the DM relic density can be found in [82, 77]. We show in Fig. 3.4 and Fig. 3.5 the regions of the $(m_{1/2}, m_0)$ plane consistent with CMB and accelerator data. It is worth mentioning that neutralino models with relic densities lower than the WMAP measurement are not ruled out, although evidently

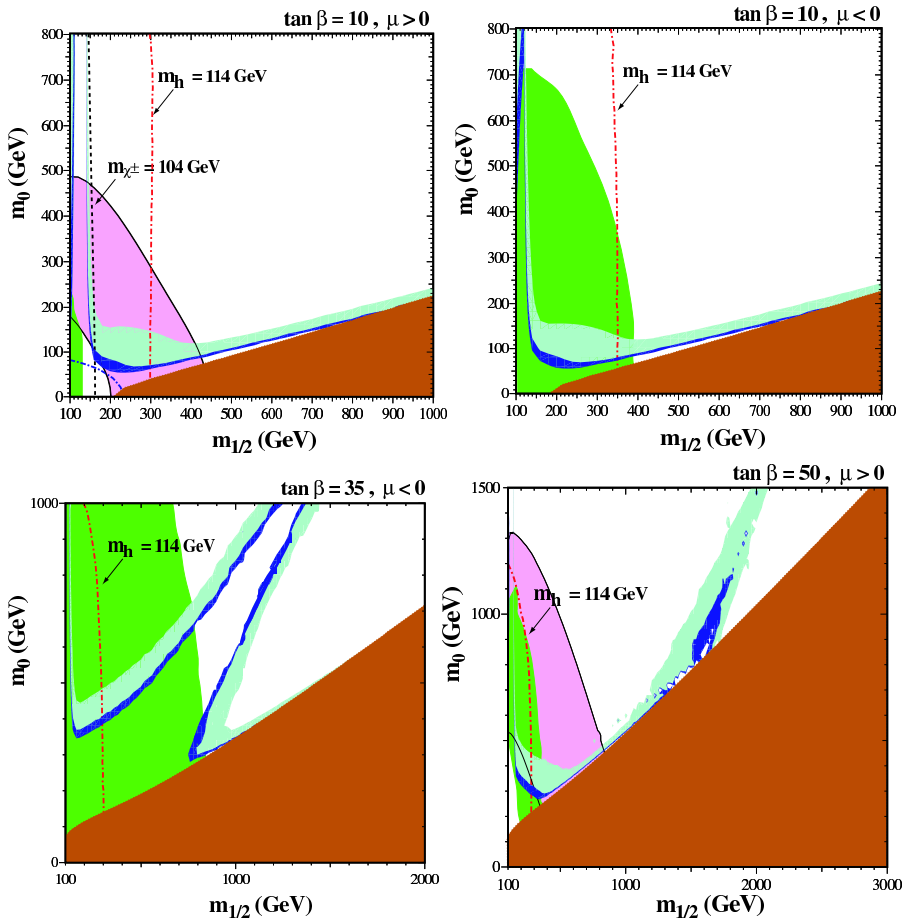

Figure 3.4: The $(m_{1/2}, m_0)$ planes for mSUGRA with (a) $\tan\beta = 10, \mu > 0$, (b) $\tan\beta = 10, \mu < 0$, (c) $\tan\beta = 35, \mu < 0$, and (d) $\tan\beta = 50, \mu > 0$. In each panel, the region allowed by the older cosmological constraint $0.1 \leq \Omega_\chi h^2 \leq 0.3$ has cyan shading, and the region allowed by the 'middle-age' cosmological constraint [176] $0.094 \leq \Omega_\chi h^2 \leq 0.129$ has dark blue shading. Figure taken from [39]. For more details, see Ref. [82].

they cannot make up all the DM. More in detail, it is possible to sample the 5-dimensional mSUGRA parameter space choosing a few values of $\tan\beta$ and A_0, and varying $m_{1/2}$ and m_0, for both $sign(\mu)$. There exist three different regimes:

i) **Slepton coannihilations region (bulk region):** $m_0 \sim m_{1/2}$ and $A_0 = 0$. Here the lightest neutralino is a quasi-pure bino with mass set essentially by $m_{1/2}$ alone; the parameter m_0 sets the sfermion mass scale, with the slepton sector lighter than the squark sector and with the lightest stau always being the lightest sfermion, possibly lighter than the lightest neutralino if $m_0 \ll m_{1/2}$.

ii) **Chargino coannihilations region (focus point region):** $m_0 \gg m_{1/2}$. Close

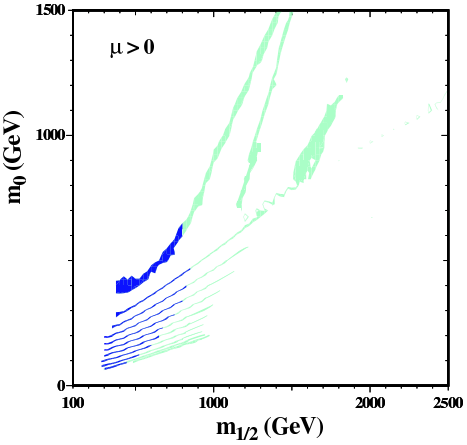

Figure 3.5: Regions of the $(m_{1/2}, m_0)$ plane in mSUGRA that are compatible with $0.094 < \Omega_\chi h^2 < 0.129$ and laboratory constraints for $\mu > 0$ and $\tan\beta = 5, 10, 15, 20, 25, 30, 35, 40, 45, 50, 55$. The parts of the strips compatible with $g_\mu - 2$ at the 2σ level have darker shading. Figure by [82].

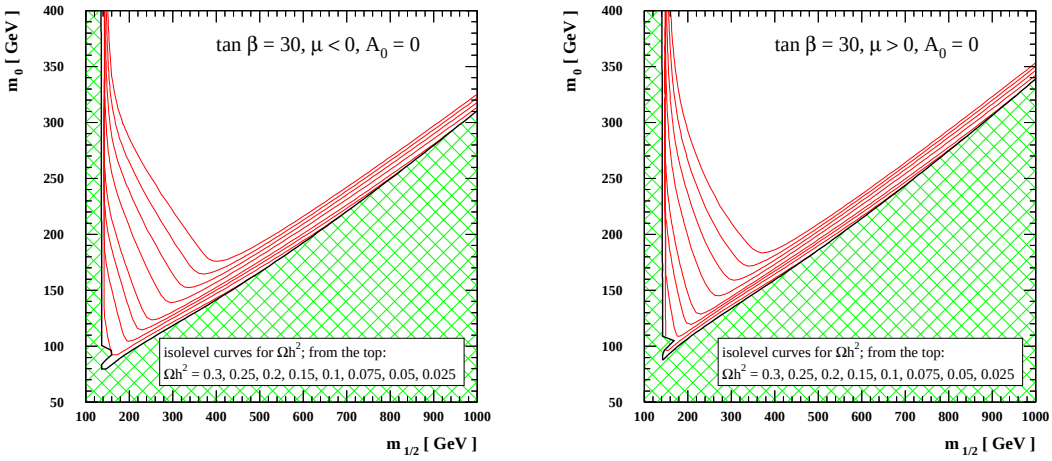

Figure 3.6: Results for $\tan\beta = 30$ and $A_0 = 0$. The isolevel curves for the relic density $\Omega_\chi h^2 = 0.103$ are shown. Figure by [77].

to this region, where there is no radiative electro-weak symmetry breaking, the parameter m is driven to small values and forces a mixing between the gaugino and higgsino sectors; furthemore, the lightest neutralino may contain a large higgsino fraction and the next-to-lightest SUSY particle is a chargino.

iii) Stop coannihilations[1] region: small $m_{1/2}$, moderate m_0 and large A_0. In

[1]Coannihilations are particle processes in the early Universe with any two SUSY particles in the

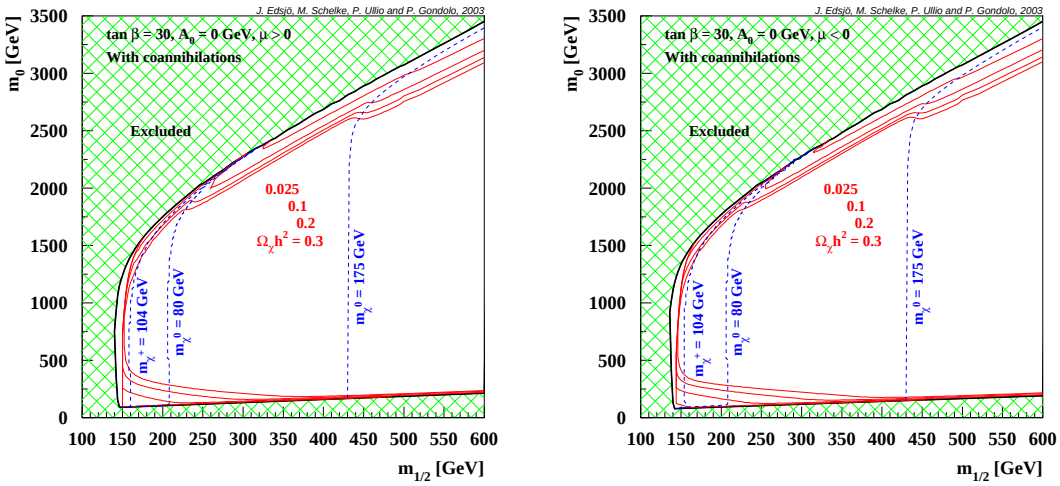

Figure 3.7: The relic density contours for models in the focus point region. Figure by [77].

this region the lightest stop is driven to masses smaller than the mass of the lightest stau or even the mass of the lightest neutralino.

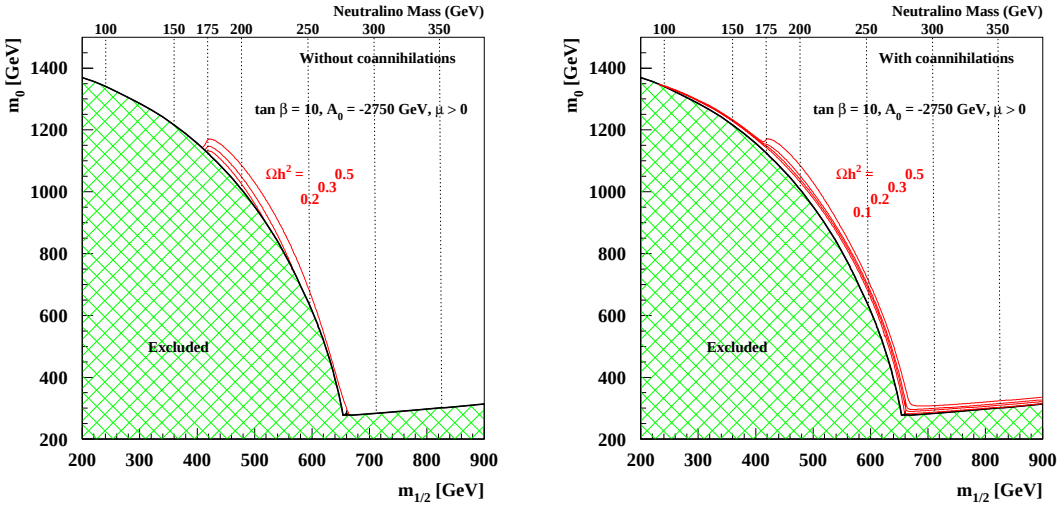

Figure 3.8: Isolevel curves for the relic density a) without coannihilations and b) with coannihilations for an example of mSUGRA parameters where stop coannihilations are important. Figure by [77].

For each of these regimes, Fig. 3.6, 3.7 and 3.8 show the isolevel curves for $\Omega_\chi h^2 = 0.103$, selecting the parts of these curves that fulfill the accelerator constraints.

initial state and any two Standard Model particles in the final state. The role of coannihilations in the mSUGRA framework is deeply discussed in [77].

The phenomenological MSSM. The scenario presented in this section is not necessarily motivated by any theoretical arguments, but rather is justified by focusing on the aspects of SUSY phenomenology which are the most interesting for neutralino DM. The phenomenological MSSM, or pMSSM, is an adaptable framework which can be described by as many as tens of parameters, or as few as five or seven. It is not a model, but rather a convenient description of the phenomenology most relevant to SUSY DM. Common choices in defining a phenomenological MSSM include a) no new sources of CP violation (all the phases in the SUSY breaking terms are set to zero), b) no flavor-changing neutral currents and c) first and second generation universality.

One example of a phenomenological MSSM is used in the `DarkSUSY` program package. In this scheme, in addition to the common features described above, gaugino unification is assumed (similar to Eq. 3.21). The remaining inputs are defined by seven free parameters:

$$\mu,\ M_2,\ \tan\beta,\ M_A,\ m_0,\ A_b,\ A_t, \tag{3.25}$$

where M_A is the mass of the pseudo-scalar Higgs boson, m_0 is the common scalar mass, and $A_{b,t}$ are trilinear couplings appearing in SUSY breaking terms. Unlike in the case of the mSUGRA scenario, the input parameters are chosen at the electroweak scale without making use of renormalization group equations. The inputs used in `DarkSusy` can be expanded beyond these seven to include other parameters, thus representing a more general MSSM. We note that these scenarios are less theoretically motivated in comparison to mSUGRA. Various combinations of theoretically and phenomenologically-based descriptions for SUSY are often considered in the literature, often maintaining some of the theoretically motivated constraints of mSUGRA, while relaxing other requirement.

3.4 Kaluza-Klein particles

Another interesting alternative to these models, whithout the requirement of pushing masses up to ten of TeV range to produce VHE gamma-rays, is that of extra dimensions (UED). In these models, all SM fields propagate in the higher dimensional bulk; for the effective four-dimensional theory, this means that all particles are accompanied by a tower of increasingly more massive Kaluza-Klein (KK) states. The *lightest KK particle (LKP)* is neutral and non-baryonic and, under appropriate conditions, it may be stable, so it is a potential good candidate for non-baryonic DM.

Chapter 4

The Impact of Subhalos on Indirect DM Detection

The subject of this chapter is DM detection. After a brief introduction on the main techniques employed to search signatures of the lightest electrically neutral SUSY particle, the neutralino, we hereby present one of the original contributions developed during this Thesis work, the prediction for the enhancement in the gamma, antiproton and positron signals due to the presence of clumps in the halo of the Milky Way.

4.1 DM detection techniques

The identification of a non-baryonic DM component in the Universe is one of the most pressing tasks in today's research. As just outlined in the previous chapter, a natural solution to the puzzle invokes a new elementary particle appearing as a thermal leftover from the early Universe; in this context, weakly interacting massive particles (WIMPs) have been, over the last three decades or so, the most popular working framework, since there are numerous examples of extensions to the Standard Model of particle physics embedding such DM candidates [33, 39, 144]. From a more pragmatic point of view, since WIMPs are (weakly) coupled to ordinary matter, there is, at the very basis of the framework, a (tiny) open window for testing this hypothesis.

Considerable efforts have been carried out on the experimental side, mainly with focus on direct detection in underground labs, but with significant results as well implementing indirect detection techniques.

4.2 Direct DM detection

Direct detection experiments appear today as one of the most promising techniques for DM detection. The idea is the following: if the Galaxy is filled with WIMPs, then many of these particles should pass through the Earth, making it possible to look for the interaction of such particles with matter, e.g. by recording the recoil energy of nuclei, as WIMPs scatter off them [39]. In such a kind of experiment, the expected events rate per unit time and per unit detector material mass is approximately given by:

$$R \approx \sum_i N_i n_\chi < \sigma_{i\chi} >, \tag{4.1}$$

where the index, i, runs over nuclei species present in the detector,

$$N_i = \frac{\text{Detector mass}}{\text{Atomic mass of species } i}$$

is the number of target nuclei in the detector,

$$n_\chi \equiv \frac{\text{WIMP energy density}}{\text{WIMP mass}}$$

is the local WIMP density and $< \sigma_{i\chi} >$ is the cross section for the scattering of WIMPs off nuclei of species i, averaged over the relative WIMP velocity with respect to the detector.
In the previous chapter, we have discussed the main constraints on the SUSY parameter space, coming from both WMAP and collider experiments. Additionally, direct measurements put the following upper limits on the WIMP-nucleon cross sections (Fig. 4.1 and [17]):

- the combined result for Ge limits the WIMP-nucleon cross-section to $\lesssim 1.6 \times 10^{-43}\,\text{cm}^2$ at the 90% C.L. at a WIMP mass of 60 GeV; this limit constrains some MSSM parameter space and for the first time excludes some parameter space relevant to constrained models (CMSSM);

- the Si result limits the WIMP-nucleon cross-section to $\lesssim 3{\times}10^{-42}\,\text{cm}^2$ at the 90% C.L. at a WIMP mass of 60 GeV, excluding new parameter space for low-mass WIMPs and including a region compatible with interpretation of the DAMA signal as scattering on Na.

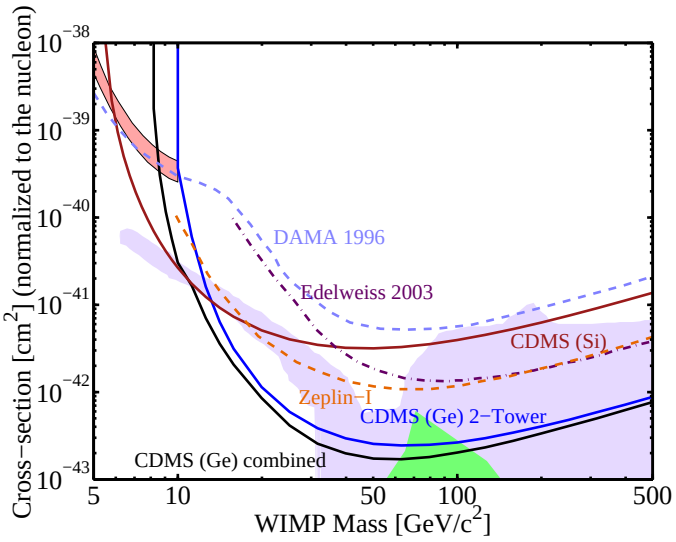

Figure 4.1: WIMP-nucleon cross section upper limits (90% C.L.) versus WIMP mass. Supersymmetric models allow the largest shaded (gray) region, and the smaller shaded (green) region. The shaded region in the upper left is from DAMA, and experimental limits are from DAMA, EDELWEISS, and ZEPLIN. Figure by [17].

4.3 Indirect DM detection

Indirect search for WIMPs through the identification of their annihilation products in the Galactic halo may be carried out via gamma-rays, neutrinos and emission, mainly syncrotron and inverse Compton, from their charged annihilation products. As charged particles do not travel in straight lines, the entire Galactic halo can contribute to the flux of such particles. In the present section, we discuss the collective effects of substructures on DM signals coming from annihilations into gamma-rays and cosmic antiprotons and positrons.

Gamma rays from self-annihilating dark matter.
Neutralino annihilation in the Galactic halo produces both a gamma-ray flux with a continuum energy spectrum and monochromatic gamma-ray lines. Considering a detector with an angular acceptance $\Delta\Omega$ pointing in a direction of Galactic longitude and latitude (l, b), the continuum gamma-ray flux from neutralino annihilation at a given energy E is:

$$\Phi_\gamma(E, \Delta\Omega, l, b) \;=\; \frac{1}{8\,\pi} \sum_F \frac{\langle \sigma\, v_F \rangle}{m_\chi^2} \frac{dN_\gamma^F}{dE} \langle J(l,b) \rangle \, (\Delta\Omega) \;\; \mathrm{cm}^{-2} \;\; \mathrm{s}^{-1} \;\; \mathrm{sr}^{-1}. \tag{4.2}$$

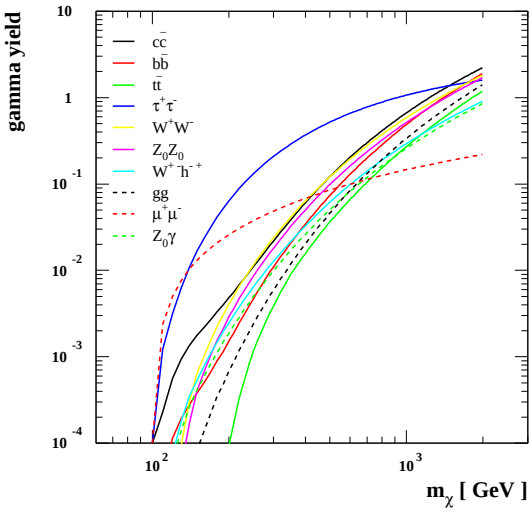

Figure 4.2: Gamma yield per neutralino annihilation with $E_\gamma > 100$ GeV. Different final states are indicated in the legend.

The summation term involves particle physics aspects of the DM candidates, being $\langle \sigma\, v_F \rangle$ the WIMP's annihilation cross section, m_χ its mass and $\frac{dN_\gamma^F}{dE}$ the differential energy distribution of produced photons. Fig. 4.2 shows the gamma yield per annihilation into different final states, which, for an assumed energy threshold of 100 GeV, ranges between 10^{-4} and 1.

The $\langle J(l,b)\rangle(\Delta\Omega)$ term contains informations on the DM astrophysical properties, being connected with its spatial distribution.
If we assume a spherical DM halo in the form of a perfectly smooth distribution of neutralinos, this term is equal to:

$$\langle J(l,b)\rangle_{smooth} = \frac{1}{\Delta\Omega} \int_{\Delta\Omega} d\Omega' \int_{los} \rho^2(L,\psi')dL, \tag{4.3}$$

where L is the distance from the detector along the line of sight, ψ is the angle between the direction of observation and that of the center of the Galaxy and the integration over $d\Omega'$ is performed over the solid angle $\Delta\Omega$ centered on ψ [33, 39, 144] (see Fig. 4.3).
On the other hand, to obtain the subhalos contribution to the gamma-ray flux from neutralino annihilation we should weight the signal on the clump distribution function, i.e. evaluate Eq. 2.27 in the subhalos final state and integrate that function on the (m_i, R_f) region marking clumps once the dynamical evolution processes have led

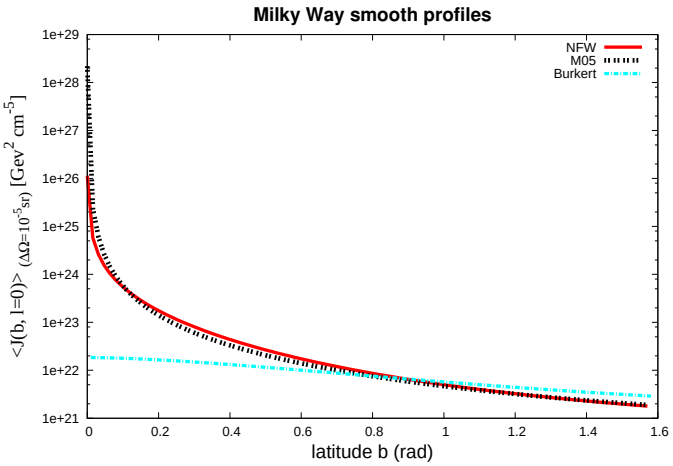

Figure 4.3: Behavior of the $\langle J(l,b)\rangle_{smooth}$ term with the Galactic latitude b, for different halo profiles and the instrumental PSF of the MAGIC experiment ($\Delta\Omega = 10^{-5}$ sr).

them into their final configurations. The corresponding expression is:

$$\langle J(l,b)\rangle_{clump} = \frac{1}{\Delta\Omega}\int_{\Delta\Omega} d\Omega' \int_{los} dL \cdot \tag{4.4}$$

$$\int_{z_i}^{z_f} dz \; \frac{dp}{dz} \int_{m_{min}}^{m_{max}} dm_i \frac{d^2N}{dR_f\, dm_i}\, \rho_{cl}^2(R_f, m_i, z),$$

where dp/dz is the formation epoch distribution of substructures as defined in Sec. 2.3.1.

Gamma rays from antiprotons and positrons.

Charged particles, such as antiprotons and positrons, which are generated in DM annihilations do not travel in straight lines due to the presence of Galactim magnetic field. Therefore, rather than observing a single region, such as the Galactic Center or the Sun, the entire galactic halo can contribute to the flux of such particles.

According to [53], cosmic primary antiprotons can originate from the hadronization of quarks and gluons produced in WIMP self-annihilation processes. Once antiprotons are produced in the dark halo, they diffuse and propagate throughout the Galaxy. The propagated antiproton differential flux at a generic point of coordinates (r, z) in the Galactic rest frame (r is the radial distance from the Galactic Center in the Galactic plane and z is the vertical coordinate) is:

$$\Phi_{\bar{p}}(r,z,E) = \frac{v_{\bar{p}}}{4\,\pi}\,\Upsilon\,\frac{dN_{\bar{p}}}{dT_{\bar{p}}} S^{\bar{p}}_{\text{astro}}(r,z,E), \tag{4.5}$$

with

$$\Upsilon = \frac{1}{2}\xi^2 \frac{\langle \sigma\, v_F \rangle}{m_\chi^2}. \tag{4.6}$$

Notations are as follows: $v_{\bar{p}}$ is the antiproton velocity, $\langle \sigma\, v_F \rangle$ is the average, over the Galactic velocity distribution, of the WIMP annihilation cross-section multiplied by the relative velocity, m_χ is the neutralino mass, ξ represents the fractional local density ρ_χ of the generic WIMP as compared to the total local DM density ρ_0 (0.3 GeV cm^{-3}), i.e. $\xi = \rho_\chi/\rho_0$, and $dN_{\bar{p}}/dT_{\bar{p}}$ is the differential antiproton spectrum per annihilation event:

$$\frac{dN_{\bar{p}}}{dT_{\bar{p}}} = \sum_F BR(\chi\chi \to \bar{p} + X)\frac{dN_{\bar{p}}^F}{dT_{\bar{p}}}, \tag{4.7}$$

where F denotes the different annihilation final states, $BR(\chi\chi \to \bar{p} + X)$ the branching ratios and $dN_{\bar{p}}^F/dT_{\bar{p}}$ stands for the antiproton energy spectra in the F channel. $S_{\rm astro}^{\bar{p}}$ is a function which takes into account all the effects of propagation in the Galaxy [53].
A detailed description of the propagation of cosmic antiprotons in the halo of the Milky Way can be found in [34].

According to [39], positrons can be produced in a variety of dark matter annihilation modes. Direct annihilation to e^+e^- is suppressed for neutralinos, but occurs frequently for Kaluza-Klein DM. Also, annihilations to ZZ or W^+W^- can produce positrons with energy of half of the WIMP mass. A continuum of positrons, extending to much lower energies, will in most cases also be produced in the cascades of annihilation products such as heavy leptons, heavy quarks, Higgs bosons and gauge bosons. The spectrum of positrons produced in DM annihilations can vary significantly depending on the mass and annihilation modes of the WIMP (see Fig. 4.4).

As positrons propagate, they move under the influence of the tangled Galactic magnetic fields, travelling in a random walk, and losing energy via inverse Compton and synchrotron processes. The diffusion-loss equation describing this process is given by:

$$\begin{aligned} \frac{\partial}{\partial t}\frac{dn_{e^+}}{dE_{e^+}} &= \vec{\bigtriangledown} \cdot \Big[K(E_{e^+}, \vec{x})\vec{\bigtriangledown}\frac{dn_{e^+}}{dE_{e^+}}\Big] \\ &+ \frac{\partial}{\partial E_{e^+}}\Big[b(E_{e^+}, \vec{x})\frac{dn_{e^+}}{dE_{e^+}}\Big] + Q(E_{e^+}, \vec{x}), \end{aligned} \tag{4.8}$$

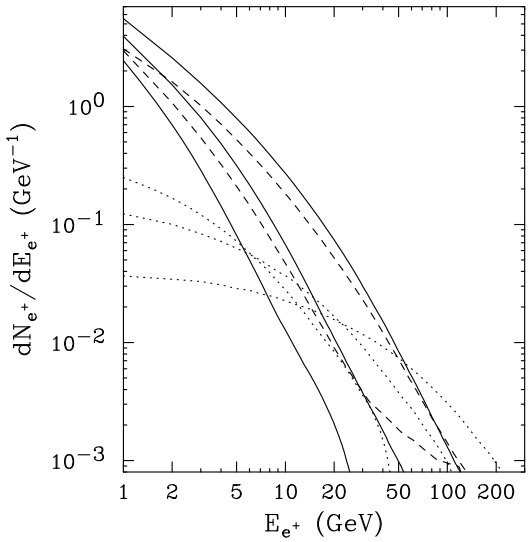

Figure 4.4: The positron spectrum from neutralino annihilations for the most important annihilation modes. Solid lines represent the positron spectrum, per annihilation, for $\chi^0\chi^0 \to b\bar{b}$, for LSPs with masses of 50, 150 and 600 GeV. The dotted lines are the same, but from the process $\chi^0\chi^0 \to \tau^+\tau^-$. Dashed lines represent positrons from the process $\chi\chi \to W^+W^-$ for LSPs with masses of 150 and 600 GeV. The spectrum from $\chi\chi \to ZZ$ is very similar. Figure by [39].

where dn_{e^+}/dE_{e^+} is the number density of positrons per unit energy, $K(E_{e^+}, \vec{x})$ is the diffusion constant, $b(E_{e^+}, \vec{x})$ is the rate of energy loss and $Q(E_{e^+}, \vec{x})$ is the source term. The diffusion constant and rate of energy loss can be parameterized by:

$$K(E_{e^+}) = 3 \times 10^{27} \left[3^{0.6} + E_{e^+}^{0.6}\right] \mathrm{cm}^2\,\mathrm{s}^{-1} \tag{4.9}$$

and

$$b(E_{e^+}) = 10^{-16} E_{e^+}^2\ \mathrm{s}^{-1}, \tag{4.10}$$

respectively. $b(E_{e^+})$ is the result of inverse Compton scattering on both starlight and the cosmic microwave background. The diffusion parameters are constrained from analyzing stable nuclei in cosmic rays (primarily by fitting the boron to carbon ratio).

In equations 4.9 and 4.10, there is no dependence on location. This is due to the assumption of a constant diffusion zone. For our Galaxy, the diffusion zone is best approximated as a slab of thickness $2L$, where L is chosen to be 4 kpc, the best fit to observations. The radius of the slab is unimportant, as it is much larger than the distances which positrons can propagate at these energies. Outside of the diffusion zone, the positron density is assumed to be (nearly) zero (free escape boundary conditions) [39]. For detailed descriptions of the diffusion model, see also [26].

4.4 Collective effects of substructures on dark matter signals

Having specified the distribution of DM particles and set the reference particle physics framework, we are now able to calculate the enhancement in the signals induced by neutralino annihilations. In the left panel of Fig. 4.5 we show the number density in neutralino pairs due to subhalos normalized to the local density $\rho_0(r_0) = 0.3$ GeV cm^{-3}, $N_{pairs}(r) = \rho^2(r) \langle \sigma v_F \rangle / m_\chi^2$, as a function of the distance from the center of the Milky Way for some representative halo profiles introduced here and a sample configuration for the subhalo parameters. For the M05 profile, our best model predicts a local enhancement of about an order of magnitude with respect to the smooth component, while the greatest enhancement of the annihilation signal from subhalos comes from larger radii. What should be pointed out at this stage is that, when computing the impact of dynamical friction, a downside in the followed approach occurs when we make use of the present mass of the parent halo. Actually, this is a very crude simplification of the problem, as the host halo evolves as well, increasing its mass due to merging and accretion with subhalos. This means that, as already observed in [186], the impact of dynamical friction might be strongly underestimated, leading to a final configuration with an overamount of small structures in the inner part of the Galaxy, also thanks to the ineffectiveness of the tidal disruption condition, Eq. 2.59, in that region. We were therefore overestimating the enhancement to the signal from subhalos at the inside of the halo, but this does not affect appreciably our result because it is there dominated by the smooth component; on the other hand, we argue that the signal is not underestimated at the border, although the population might be here impoverished of a considerable fraction of objects, as those should have in any case been destroyed by tidal forces during the formation history of the halo. In the right panel of the same figure, the number density in neutralino pairs is plotted versus the ratio F_s between the concentration inside subhalos and that of halos of equal mass.

Fig. 4.6 shows the high latitude gamma-ray flux for two sample WIMP models with given annihilation rate (simplified scaling with the inverse of the relic density value), dominant annihilation final state into $b\bar{b}$ and mass $M_\chi = 50$ GeV or 100 GeV. The configuration for the substructure distribution is the one obtained assuming a NFW universal shape profile and concentration parameter in substructures being twice the concentration in halos of equal mass (parameter $F_s = 2$), as extrapolated with the Bullock et al. prescription. A dashed-dotted line is used for the contribution

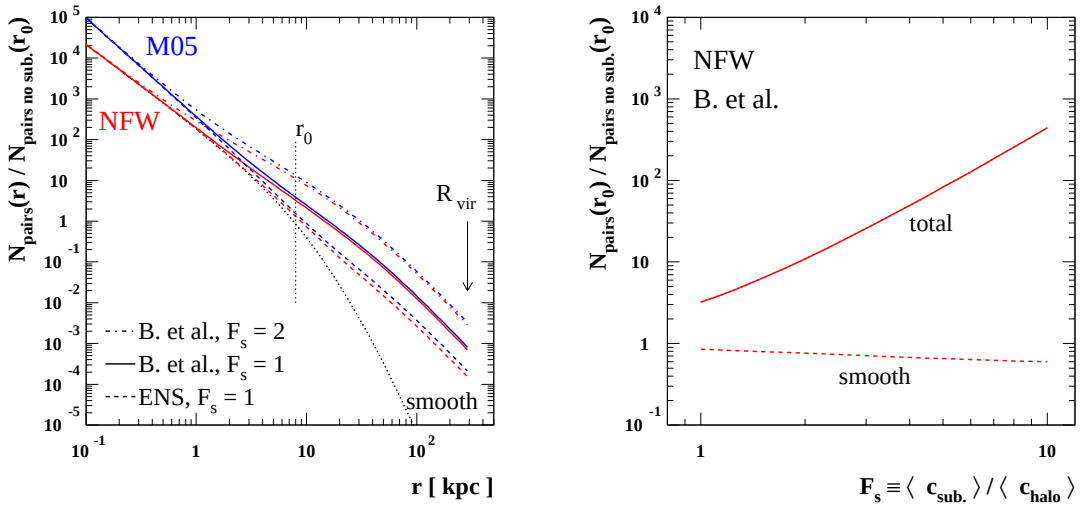

Figure 4.5: *Left panel*: number density in neutralino pairs as a function of the distance for some representative halo profiles and a sample configuration for the subhalo parameters. *Right panel*: the same quantity plotted versus the ratio F_s between the concentration inside substructures and that of halos of equal mass. Figure by Bisesi & Ullio, 2007 [42].

from the smooth halo component only, while a solid line for the total flux from WIMP annihilations; data for the high latitude flux collected by the EGRET experiment are shown for comparison.

The two panels of Fig. 4.7 respectively show the antiproton and positron fluxes for the same SUSY models and cosmological setups of Fig. 4.6. In each case, a dashed-dotted line is used for the contribution from the smooth halo component only, a dashed line for the total flux from WIMP annihilations, while a solid line for the sum of the signal and background contributions; all fluxes displayed are solar modulated and data taken at the corresponding phase of the solar cycle are plotted.

In the left panel of Fig. 4.8 we show the upper limit on the annihilation rate $\langle \sigma v_F \rangle$ obtained by comparing the predicted flux from WIMP annihilations, in the configuration for substructures assumed for the plots in Fig. 4.6 and 4.7, against the full set of available data on cosmic-ray antiproton and positron fluxes (3σ limits; propagation parameters and backgrounds are assumed to be known) and the high latitude gamma-ray flux measured by EGRET (ratio signal over measured flux assuming negligible background). The dominant annihilation final state is assumed to be either $b\bar{b}$ (lower curves) or $\tau^+\tau^-$ (upper curves, no antiproton yield in this case).

Finally, the right panel of Fig. 4.8 shows the rescaling in the flux of antiprotons,

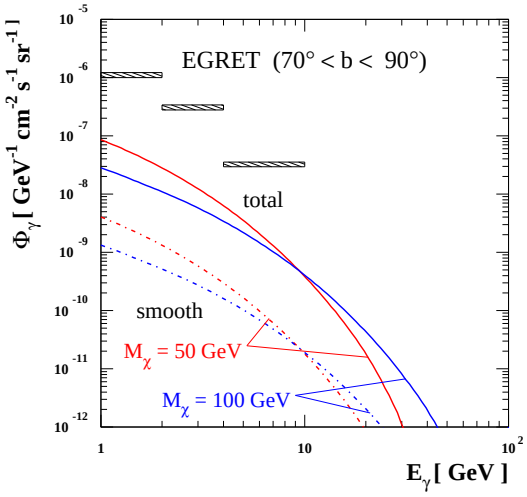

Figure 4.6: The high latitude gamma-ray flux for two sample WIMP models with given annihilation rate (simplified scaling with the inverse of the relic density value), dominant annihilation final state into $b\bar{b}$ and mass $M_\chi = 50$ GeV or 100 GeV; in this plot as well the configuration for the substructure distribution is the one obtained assuming a NFW universal shape profile and concentration parameter in substructures being twice the concentration in halos of equal mass (parameter $F_s = 2$), as extrapolated with the Bullock et al. prescription. A dashed-dotted line is used for the contribution from the smooth halo component only, while a solid line for the total flux from WIMP annihilations; data for the high latitude flux collected by the EGRET experiment are shown for comparison. Figure by Bisesi & Ullio, 2007 [42].

positrons and gamma-rays from WIMP annihilations, as compared to the smooth halo scenario, in case of substructure distribution obtained assuming a NFW universal shape profile and concentration parameter in substructures scaled by the factor F_s with respect to the concentration in halos of equal mass, as extrapolated with the Bullock et al. prescription. No analogous estimates have been found in literature, involving DM candidates of different, more exotic nature.

4.5 Minimum detectable flux

The minimum detectable flux of gamma rays at the $n\,\sigma$ detection level from a telescope is determined by the following condition:

$$\frac{\Phi_\gamma \, A_{eff} \, t_{obs} \, \Delta\Omega}{\sqrt{N_b}} \geq n, \tag{4.11}$$

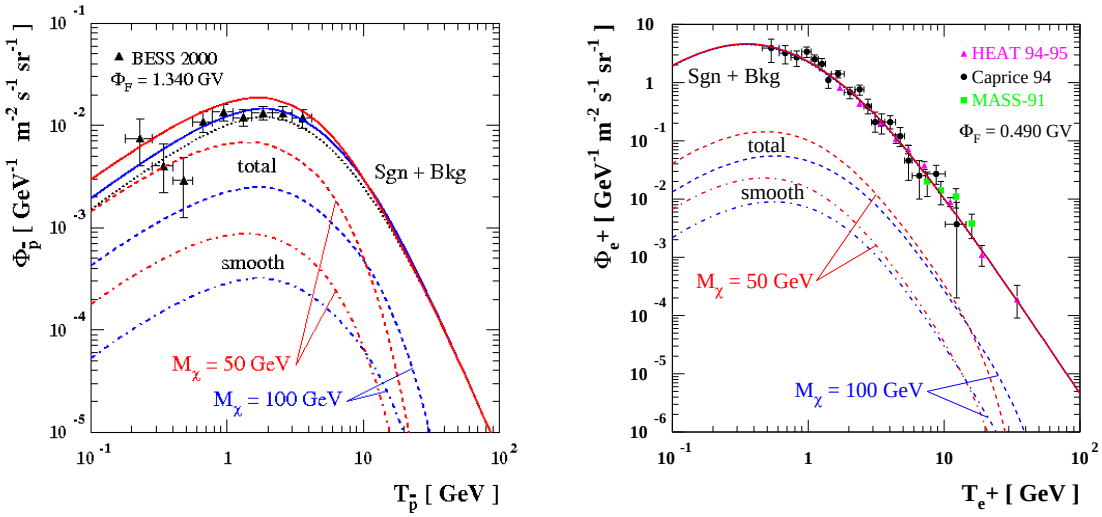

Figure 4.7: The antiproton (*left panel*) and positron (*right panel*) fluxes for two sample WIMP models with given annihilation rate (simplified scaling with the inverse of the relic density value), dominant annihilation final state into $b\bar{b}$ and mass $M_\chi =$ 50 GeV or 100 GeV. The configuration for the substructure distribution is the one obtained assuming a NFW universal shape profile and concentration parameter in substructures being twice the concentration in halos of equal mass (parameter $F_s = 2$) as extrapolated with the Bullock et al. prescription. In each case, a dashed-dotted line is used for the contribution from the smooth halo component only, a dashed line for the total flux from WIMP annihilations, while a solid line for the sum of the signal and background contributions; all fluxes displayed are solar modulated and data taken at the corresponding phase of the solar cycle are plotted. Figure by Bisesi & Ullio, 2007 [42].

where N_b is the number of background counts, hadrons and electrons (follows a poissonian statistics) integrated over the telescope threshold E_{th}, A_{eff} is the effective area, t_{obs} the exposure time and $\Delta\Omega$ the point-spread-function (PSF) of the instrument. Plotting inequality 4.11 with the equality sign onto the SUSY parameter space, one draws a line which divides this space into the detectable (above the line) and undetectable (below the line) regions.

We give an example of minimum detectable flux calculation in Fig. 4.9, comparing MSSM and mSUGRA events in the $m_\chi - \langle\sigma\, v\rangle_{cont}$ space with sensitivity curves for the Galactic Center (panels on the left side) and substructure-enhanced Milky Way halo (panels on the right side). In all plots, referring to three representative annihilation modes ($b\bar{b}, \tau^+\,\tau^-$ and W^+W^-) and to the three halo profiles considered in this work, the following MAGIC specification are assumed (definitions and more detailed

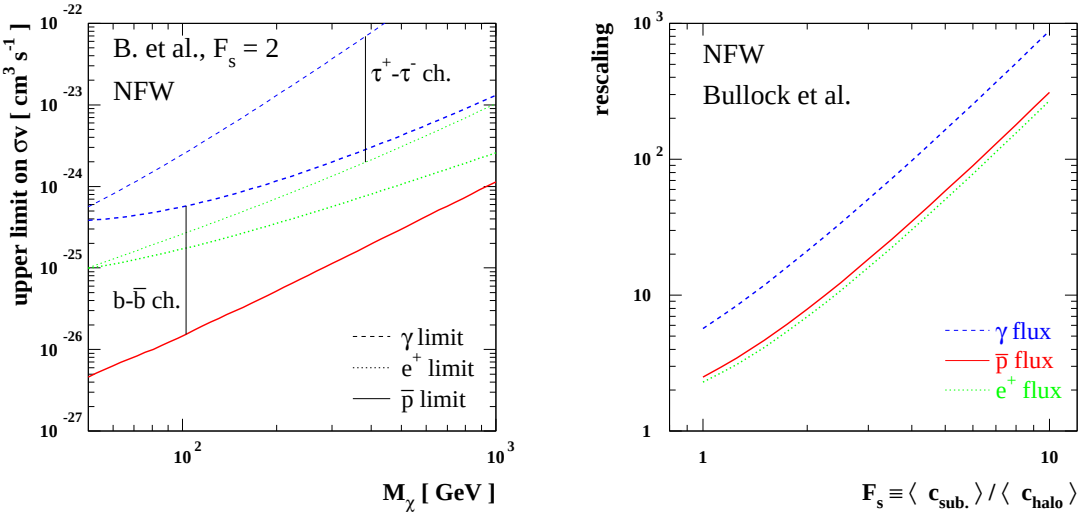

Figure 4.8: *Left panel*: upper limit on the annihilation rate $\langle \sigma v_F \rangle$ obtained by comparing the predicted flux from WIMP annihilations, in the configuration for substructures assumed for the plots in Fig. 4.6 and 4.7, against the full set of available data on cosmic ray antiproton and positron fluxes (3σ limits; propagation parameters and backgrounds are assumed to be known) and the high latitude gamma-ray flux measured by EGRET (ratio signal over measured flux assuming negligible background). The dominant annihilation final state is assumed to be either $b\bar{b}$ (lower curves) or $\tau^+\tau^-$ (upper curves, no antiproton yield in this case). *Right panel*: rescaling in the flux of antiprotons, positrons and gamma-rays from WIMP annihilations, as compared to the smooth halo scenario, in case of substructure distribution obtained assuming a NFW universal shape profile and concentration parameter in substructures scaled by the factor F_s with respect to the concentration in halos of equal mass, as extrapolated with the Bullock et al. prescription. Figure by Bisesi & Ullio, 2007 [42].

discussion in Chapter 6):

- effective area $A_{eff} = 5 \times 10^8$ cm^2;
- energy threshold $E_{th} = 100$ GeV;
- MAGIC PSF $\Delta\Omega = 10^{-5}$ sr;
- observation time $t_{obs} = 20$ hours;
- hadronic and electronic backgrounds as modeled in [66]:

$$\frac{dN_{\rm had}}{d\Omega}(E > E_0) = 6.1 \times 10^{-3} \epsilon_{\rm had} \left(\frac{E_0}{1 \text{ GeV}} \right)^{-1.7} \text{ cm}^{-2} \text{ s}^{-1} \text{ sr}^{-1}; \qquad (4.12)$$

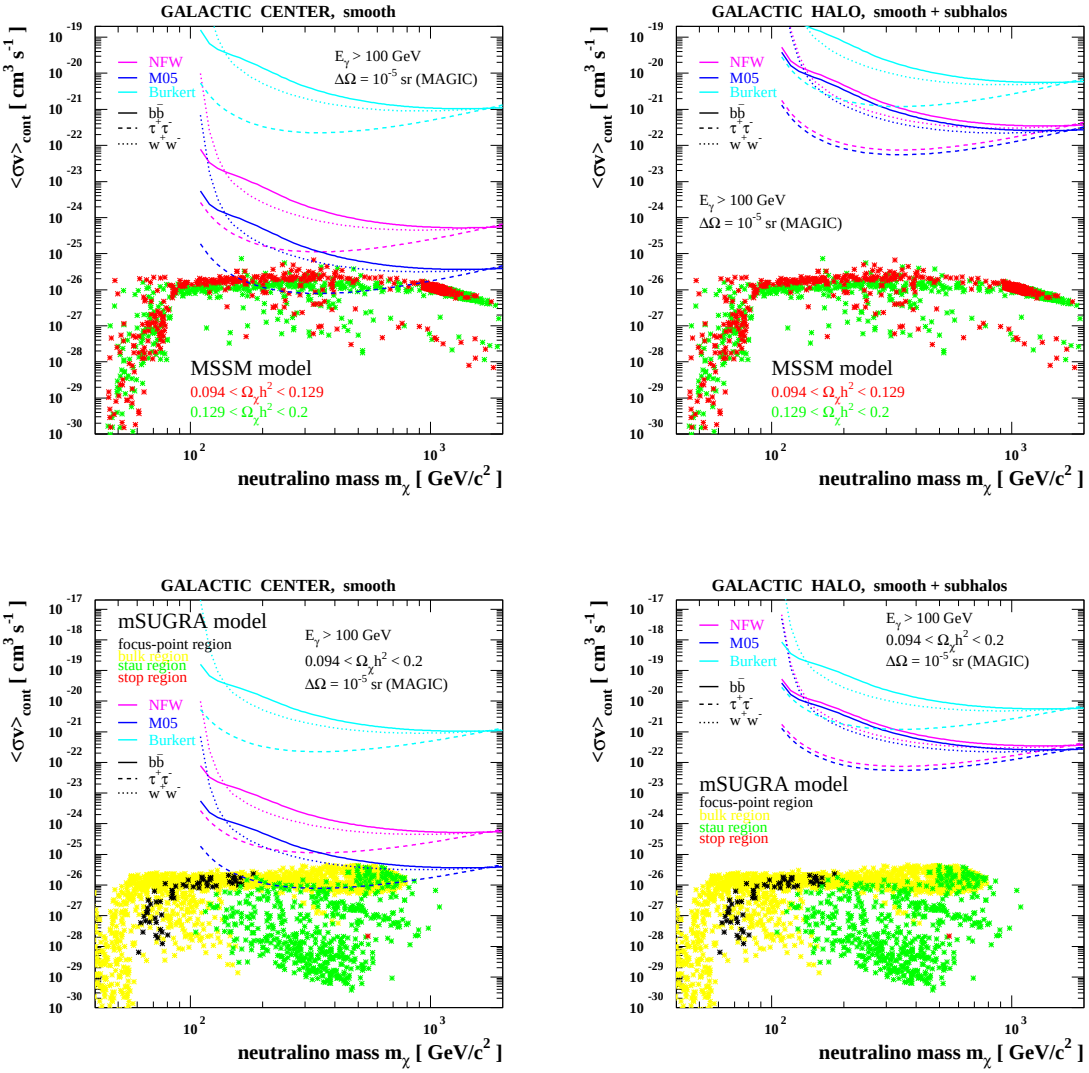

Figure 4.9: Minimum detectable flux calculation for the Galactic Center (*left-side set of plots*) and the Milky Way halo (*right-side set of plots*), for the MSSM and the mSUGRA scenarios. We consider representative annihilation modes $b\bar{b}, \tau^+\tau^-$ and W^+W^- (solid, dashed and dot-dashed lines respectively) and halo profiles as discussed in the text. MAGIC specifications are: $A_{eff} = 5 \times 10^8$ cm^2, $E_{th} = 100$ GeV, $\Delta\Omega = 10^{-5}$ sr, $t_{obs} = 20$ hours, hadronic and electronic backgrounds according to [66].

$$\frac{dN_{\rm el}}{d\Omega}(E > E_0) = 3.0 \times 10^{-2} \left(\frac{E_0}{1\ {\rm GeV}}\right)^{-2.3}\ {\rm cm}^{-2}\ {\rm s}^{-1}\ {\rm sr}^{-1}, \tag{4.13}$$

where ϵ is the fraction of hadronic showers which are misidentified as electromagnetic (of the order of 1% for MAGIC).

As we can see, exclusion plots for the Galactic Center suggest to constrain the anni-

hilation model (among selected ones) to the $\tau^+ \tau^-$ channel. In that case, a neutralino of mass between 100 GeV and 1 TeV should be detectable if DM would be distributed according to a M05 profiles. On the contrary, the detection of a signal from neutralino annihilation in the Galactic halo is excluded for MAGIC in both particle physics scenarios, also in case the DM distribution is enhanced by the subhalo component.
Another example of exclusion plot will be given in Chapter 10, where we discuss MAGIC detection of Draco.

4.6 Discussion

We have implemented a semi-analytical model for the spatial mass function of subhalos in the halo of the Milky Way and introduced some of the most important effects of dynamical evolution of substructures. The model is sensitive to the choice of the density profile and concentration parameter for both the halo and the subhalos. We have performed an accurate analysis of the main configuration setups for neutralino annihilations in the Milky Way and given an estimate of the enhancement in N_{pairs} due to subhalos for the most relevant models. We have found that within the virial radius of the Milky Way about 30−34% of the mass is in the form of DM clumps, a value lightly higher with respect to previous results [35, 180]. The range of variability of this number is set by the choice of the ratio F_s between the concentration inside substructures and that of an halo of equal mass. We have computed the enhancement in the neutralino induced gamma-ray, antiproton and positron signals in the best configuration models which came out from our previous analysis for some sample WIMPs models with given annihilation rate. Our results for the setup defined by the M05 profile, the Bullock et al. concentration model and a rescaling factor $F_s = 2$ predict a local enhancement of about an order of magnitude with respect to the smooth component, while the greatest contributions to the annihilation signal from subhalos come from larger radii.

Chapter 5

Detection of a Possible Dark Matter Signal from EGRET Unidentified Gamma-Ray Sources

We study the prospects that some EGRET unidentified gamma-ray sources (EUS) may be DM satellites in the Milky Way, outlining a new signature of annihilating DM in our halo. In this picture, EUS might be bright sources of gamma rays which could be detected by the present generation of telescopes like GLAST, MAGIC or HESS.

5.1 The Third EGRET Catalog

Statistical studies indicate that the unidentified EGRET sources belong to two groups, namely a galactic and an isotropic extragalactic population of sources. The interpretation of the UES is made more difficult from the large typical error circle in the position estimation which is a hindrance to the association of the observed gamma radiation with signals in other wavelenghts.
For each possible source, the EGRET catalog lists the following informations:

- **EGRET source name.** The name is based on the J2000 (the Julian day corresponding to year 2000), following the IAU naming convention. Due to uncertainties in the position, the name coding could not be definitively matching with the source position itself.
- **RA and DEC.** The J2000 convention of Ra and Dec.
- **Galactic Coordinates.** The same as above.
- θ_{95}**:** The 3EG catalog defines this measure as *'the radius in degrees of the circle containing the same solid angle as the* 95% *confidence contour'*. This means that

the source is situated in a circle with a radius θ_{95} around the mean position with 95% probability.

- **Flux.** There are different flux values for different observation periods (each with a defined name type). P1234 means all EGRET periods. The EGRET catalog provides then a most significant flux (mostly corresponding to P1234), which has been used in the following analysis. The flux is calculated above 100 MeV, with an assumed spectral index of -2 for most sources. However, the authors of the 3EG catalog are quite unclear about the systematic uncertainty of the thus calculated flux: *'if the spectral index differs substantially from 2.0, some additional error should be assumed for the flux F'*. The flux is given in units of 10^{-8} ph cm^{-2} s^{-1}.

- **Statistical uncertainties in the flux.** At this item, there is the 1σ statistical uncertainty in the flux. An additional systematic error of roughly 10% should be added in quadrature, correction which is important only for very strong detections.

- γ**.** The photon spectral index in $F(E) \sim E^{-\gamma}$ derived from the P1234 sum period.

- **Counts.** The number of photons with energy $E > 100$ MeV, as represented by the flux or upper limit. The fractional uncertainty in the photon count is the same as that in F, $\Delta F/F$.

- $\sqrt{\mathbf{TS}}$**.** The statistical significance of the $E > 100$ MeV observation.

- **VP.** The Viewing Period.

- **ID.** P, pulsar; G, galaxy (LMC only); S, solar flare; A, AGN; a, possible AGN.

- **Notes.** E, extended source (only for LMC); em, possibly extended source (because some source location maps are inconsistent with a single point source or poor fit to the calibrated PSF, from the observation presented in the first entry for the source); C, possible source confusion (it may affect flux, significance, or position). If no entry is given in this column, corresponding sources are consistent with the EGRET PSF for a single source.

- **References.**

5.2 EGRET unidentified sources as DM clumps?

A detailed analysis of the spectra of some unidentified EGRET sources indicate that a plausible solution to the question about their nature may be addressed invoking the proposal that they are DM clumps in the Galaxy halo.

In the present section, we investigate the possibility that some of these objects might be MW substructures undergoing annihilations at their center. These sources have not been observed below 100 MeV, thus the turnover expected for π^0 photons at $m_{\pi^0/2} = 67.5$ MeV could not have been observed. However, the spectrum of an annihilating source should be closer to flat around 100 MeV [25], thus the EGRET point sources are typically not very good candidates for annihilation radiation. However, they do set the scale of possible annihilation quite well. The yield of gamma rays predominantly from π^0 decays in the hadronization of annihilation products is typically $dN/d\ln E \sim 2$ annihilation^{-1} at energies of 0.1 GeV. As EUS typically have fluxes of order of $E\,\frac{d\Phi}{dE} \sim 10^{-8}\Big(\frac{E}{\mathrm{GeV}}\Big)^{-1}$ cm^{-2} sec^{-1}, this means that the inferred rate of annihilations for these sources is 5×10^{-8} cm^{-2} s^{-1}.

In such a kind of investigation, a caveat is that the result is dependent on the spatial distribution of substructures. More in detail, once the distance of the clump from the center of the halo is assigned, the requirement that EGRET fluxes are to entirely be connected to the annihilation of DM inside the satellite univocally sets its mass. This section is structured as follows: in Sec. 5.2.1, we discuss the followed criteria to select those sources which are the best targets for DM clumps in the halo of our Galaxy, while in Sec. 5.2.2 we will make use of the EGRET data to constrain the mass of a subhalo at a given distance.
Finally, in the conclusive part of the chapter, we will ascribe to each of these configurations a fulfilment probability, in the light of the predictions put forward about the signal from annihilating neutralino DM inside Milky Way substructures.

5.2.1 Selection of the candidates

When studying the unidentified sources, there are several observables which one might use to determine their nature. One can look at the *spatial distribution* to estimate what fraction of the population is galactic in nature, and what scale height the galactic fraction has, or one can look at *positional correlations* with other object types and galactic structures. The *energy spectrum* is another characteristic which can be used to classify sources as 'PSR-like', 'AGN-like', or 'other'. In this same vein, one can examine the EGRET catalog sources for evidence of *time variability*, in hopes

of distinguishing the various source classes.
The known pulsars are seen to have a fairly constant flux ($\pm$ 10% when averaged over many pulse periods, consistently with the systematic uncertainties in EGRET flux measurements), as is expected from the nature of their energy production. Many AGN are seen to flare dramatically, which makes their identification easier. DM clumps are expected to show no variability, so they should behave as 'pulsar-like' objects.
In order to select those sources in the 3EG which may be good candidates for DM clumps in the Galactic halo, we followed the analysis of time variability outlined in [148]. In this work the EGRET data are re-analyzed to calculate a likelihood function for the flux of each source in each observation, both for detections and upper limits. These functions are combined in a uniform manner with a simple model of the flux distribution to characterize the flux variation by a confidence interval for the relative standard deviation of the flux. The *fractional variability* δ is defined as:

$$\delta = \frac{\sigma}{\mu}, \tag{5.1}$$

where μ and σ are the average and standard deviation, respectively, of the true flux of the source. Similar sources are grouped together, and Tab. (5.1) shows the results for the various source classes. It contains a description of each class, the number of sources in the class, the mean of δ, and an estimate of the intrinsic RMS dispersion of δ in excess of the statistical errors.

When trying to individuate the best candidates for signals from DM clumps, we performed the following selection over the catalog:

- all entries with ID 'A' (AGN), 'a' (possible AGN) or 'S' (solar flare), have been filtered out;
- minimum Galactic latitude of 15°: this reduces the probability that the putative source may be misinterpreted as of different type, especially those confined on the Galactic plane, like PSRs or SNRs;
- steady source: we used the variability indexes δ and their minimum values δ_{min} from [148]; all sources incompatible with steadiness (variability indexes $\delta_{min} > 0$) have been rejected.

These prescriptions allowed us to a preliminary selection of good candidates, including about ten sources. In a subsequent step, we searched the best SUSY model to

Source Class	Members	$< \delta >$	RMS(δ)	Symbol
3EG Classification:				
pulsars	6	0.11 ± 0.02	< 0.07	PSR
supernova remnant associations	10	0.27 ± 0.09	< 0.19	SNR
active galactic nuclei	67	0.70 ± 0.08	0.27 ± 0.05	AGN
quasars	51	0.77 ± 0.09	0.25 ± 0.08	QSO
BL Lac objects	15	0.49 ± 0.16	< 0.32	BLL
unidentified, $\|b\| < 5°$	47	0.42 ± 0.06	0.17 ± 0.08	U0
unidentified, $5° < \|b\| < 15°$	37	0.56 ± 0.12	0.23 ± 0.09	U5
unidentified, $15° < \|b\| < 30°$	45	0.42 ± 0.12	< 0.16	U15
unidentified, $\|b\| > 30°$	29	0.84 ± 0.15	< 0.27	U30
Possible isolated neutron stars:				
Geminga-like objects	3	0.13 ± 0.11	< 0.16	Gem
pulsars without PWN	7	0.21 ± 0.15	< 0.15	noPWN
pulsars with PWN	6	0.66 ± 0.29	0.28 ± 0.16	PWN
Gould's Belt, unidentified, $\|b\| > 5°$	33	0.49 ± 0.13	< 0.26	G
persistent, unidentified [96]	88	0.32 ± 0.05	0.10 ± 0.05	Per
steady, unidentified [100]	120	0.35 ± 0.05	0.11 ± 0.04	St
Associations from [168]:				
supernova remnants	17	0.28 ± 0.10	< 0.17	RSN
WR stars	6	0.45 ± 0.22	< 0.27	WR
Of stars	4	0.26 ± 0.15	< 0.19	Of
OB associations	22	0.40 ± 0.10	0.17 ± 0.08	OB

Table 5.1: Variability of EGRET gamma-ray sources.

fit their spectra among a selection of some benchmark MSSM parameter space configurations. We found that the best matching between theory and experiment occurred for the source $3EG\_J1835{+}5916$, the gamma-ray flux being supposed to be originated by the annihilation of a neutralino of $m_\chi = 46.17$ GeV/c^2, $\langle \sigma\, v \rangle = 6.38 \times 10^{-26}$ cm^3 s^{-1} in the b$\bar{b}$ channel (hereafter, model A). The WIMP-proton and WIMP-neutron spin-independent cross sections are respectively $2.09{\cdot}10^{-43}$ cm^2 and $2.16{\cdot}10^{-43}$ cm^2. Comparing these values with constraints from direct measurements in Fig. 4.1, we see that this model employes a set of parameters which are rather extreme, but still within the allowed range. In Tab. (5.2) we resume the main observational properties of this selected source, while Tab. (5.3) lists the particle physics setup its flux has been modeled with. In Fig. 5.1 we plot the EGRET measured flux data for the source under investigation, as fitted with the SUSY model A. The plot does not include the two lower energy measured values, consistently with that our modeling of the sig-

nal does not consider the soft-energy contribution to the gamma-ray emission due to inverse Compton scattering of monochromatic electrons produced from annihilating neutralinos on the photon cosmic background.

m_χ (GeV/c^2)	46.17
$\langle \sigma\, v \rangle$ (cm^3 s^{-1})	6.38×10^{-26}
$\Omega_\chi\, h^2$	0.048
μ (GeV/c^2)	926.5
m_2 (GeV/c^2)	92.4
$tg\beta$	19.0
m_A (GeV/c^2)	79.8
m_0 (GeV/c^2)	922.5
A_b/m_0	0.95
A_t/m_0	-2.1

Table 5.2: Best fit model (model A) for the source in Fig. 5.1. The neutralino mass m_χ, the annihilation rate $\langle \sigma\, v \rangle$ and the relic density $\Omega_\chi\, h^2$ are shown, as well the MSSM parameter space setup for this model.

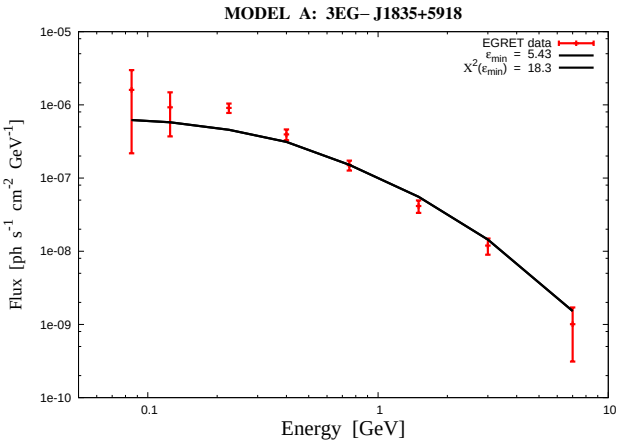

Figure 5.1: EGRET measured differential fluxes (red) for the unidentified gamma-ray source $3EG\_J1835+5918$. Data taken from $http://heasarc.gsfc.nasa.gov/db-perl/W3Browse/w3browse.pl$. Fit with the SUSY model as in Table (5.3).

Tab. 5.2. Selection of possible candidates for DM clumps from the Third EGRET Catalog [103, 148].

Name	R.A.(°)	Decl.(°)	l	b	θ_{95}	$F \pm \Delta F$	γ	Counts	$\sqrt{\text{TS}}$	VP	δ_{min}	δ_{max}	δ	ID	Note	Ref.
J1835+5918	278.87	59.32	88.74	25.07	0.15	60.6 ± 4.4	1.69	452	19.0	P1234	0	0.47	0.15	—		[181]
						55.0 ± 14.6	± 0.07	44	4.8	2.0						
						45.1 ± 14.3		23	4.4	9.2						
						32.5 ± 10.0		31	4.1	22.0						
						81.0 ± 22.8		26	5.1	201.0						
						85.6 ± 19.6		42	6.3	202.0						
						83.7 ± 14.9		69	8.1	201.+						
						78.0 ± 11.9		96	9.3	203.0						
						55.9 ± 8.1		118	9.6	212.0						
						57.0 ± 33.4		6	2.5	302.0						
						84.1 ± 16.4		56	7.5	303.2						
						76.2 ± 32.8		11	3.3	303.4						
						< 85.5		< 7	0.3	303.7						
						75.1 ± 13.9		64	7.8	302.+						
						< 72.4		< 2	0.0	403.0						
						41.3 ± 7.2		93	7.5	P1						
						66.9 ± 6.1		279	15.4	P2						
						58.6 ± 4.7		376	17.1	P12						
						74.0 ± 12.6		76	8.4	P34						

Table 5.3: Selected best candidate for DM clump from the Third EGRET Catalog. We show values of the equatorial and Galactic coordinates, the 95% confidence contour angle, the flux F with its error bar ΔF, the photon spectral index in $F(E) \sim E^{-\gamma}$ derived from the P1234 sum period, the number of photons with energy $E > 100$ MeV, the statistical significance $\sqrt{\text{TS}}$ of the $E > 100$ MeV observation, the viewing period VP and the fractional variability δ of the source. The blank space in the ID column indicate that there exist no firm identification with known sources.

Unidentified EGRET source **3EG_J1835+5918:**

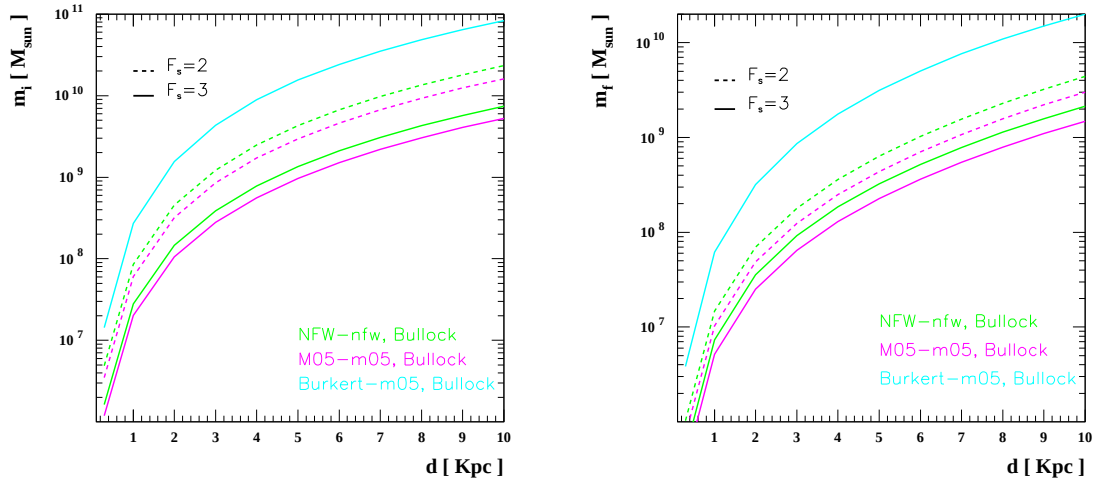

Figure 5.2: Initial (*left panel*) and final (*right panel*) subhalo mass versus the heliocentric distance for the unidentified EGRET source $3EG\_J1835+5918$ for different choices of the progenitor profile and concentration model. Figure by Bisesi & Ullio, 2007 [42].

A careful analysis of the literature drives to the observation that the source has been deeply investigated at many wavelengths (optical photometry, X-ray, radio) by [136, 137, 135] in 2000. These authors state that in case of an AGN, its beamed emission is at least suppressed by a factor 100, and in case of an isolated neutron star, it lacks the steady thermal X-ray flux from a cooling surface. In case of a pulsar, it would show very atypical emission features. For these reasons, authors define the source as belonging to a new class of high–energy gamma-ray emitters. Thus, even in case of a different origin, a counterpart search above 50 GeV would be of outstanding importance. Additionally, this source shows the highest flux among the other EGRET candidates and is the only candidate with a good position estimate (θ_{95}=0.15°).

5.2.2 Is there any chance to identify single DM clumps?

By now we are ready to address the question of the probability that the selected objects may be identified as single MW satellites.
Supposing that our candidate source is located at a heliocentric distance d, we determine its mass $m_i^\star(d)$ by assigning to the cosmological contribution to the signal its minimum value resulting from the χ^2 test in the fit with the EGRET data:

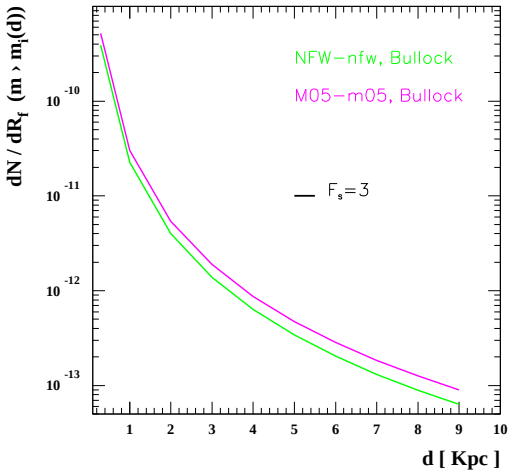

Figure 5.3: Probability of finding a clump of mass m_i at the final distance d according to subhalo distribution model discussed in Chapter 2. Figure by Bisesi & Ullio, 2007 [42].

$$\frac{\int_0^{r_t(R_f(d),m_i^\star)} \rho^2(r, m_i^\star)\, 4\,\pi\, r^2\, dr}{d^2} - \epsilon_{min} = 0, \tag{5.2}$$

where $\rho(r,\, m_i^\star)$ is the profile function inside the clump, the integration is performed on its volume truncated at the tidal radius r_t, and the subscripts i and f denote that the quantities are evaluated in their intial and final states respectively.
In Fig. 5.2, we plot the masses required to fit the signal as a function of the heliocentric distance for the $3EG\_J1835 + 5918$ EGRET source, for some suitable choices of the DM profile and concentrations for the halo and the subhalo as well. As we can see from the right panel of the figure, we find that the source is constrained to exibit quite big masses, the reason of that being due to the largeness of the observed signal with respect to the predictions of the most popular SUSY scenarios. In order to select those configurations for our candidate DM clump which are the most probable in the light of the prediction made in the first part of this work, we should compare results of Fig. 5.2 with the mass and spatial distribution function of Eq. 2.27. To this aim, we evaluate the cumulative mass function up to masses $m_i^\star$ at their corresponding final distances, as set by the mapping of Fig. 5.2, and compare this result with the total number of substructures detectable by the telescope at the same distance:

$$\mathcal{P}_{R_f}(m_i^\star) = \frac{dN(m > m_i^\star(d))}{dR_f} \Big/ \frac{dN(m > m_{min})}{dR_f}, \tag{5.3}$$

being $m_{min} = 10^{-6}$ $M_\odot$ the minimum clump mass resulting from simulations [72]. Eq. 5.3 provides the probability $\mathcal{P}_{R_f}$ of finding a clump of mass $m_i^\star$ at the final distance d. The results are shown in Fig. 5.3.

5.3 Discussion

We have used the probability function of finding a subhalo of a given mass at a given Galactocentric distance to constrain the hypothesis that at least some EGRET unidentified gamma-ray sources may be DM clumps. Restricting our analysis to the particular object $3EG\_J1835 + 5918$, we find that, based on our simulations, it is extremely unlikely that the flux from this source could be due to neutralino annihilation. We therefore rule out this possibility, and suggest a more conventional nature for this source, i.e. a stellar remnant (pulsar, SNR, PWN, etc.).

Part II

The MAGIC Telescope and Data Analysis Method

Chapter 6

The Čerenkov Technique and the MAGIC Telescope

"Maraviglia sarebbe in te se, privo
d'impedimento, giù ti fossi assiso,
com'a terra quiete in foco vivo".
Quinci rivolse inver' lo cielo il viso.

(*Par., I, 139-142*)

6.1 Introduction

MAGIC (*Major Atmospheric Gamma-Ray Imaging Čerenkov*) (Fig. 6.1) is an Imaging Atmospheric Čerenkov Telescope or IACT that has been inaugurated on October 2003, starting measuring since the commissioning ended in late 2004.

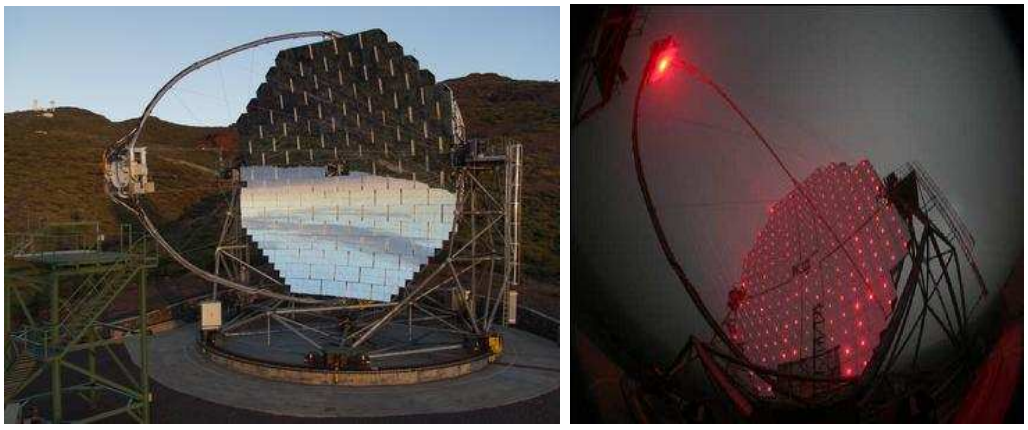

Figure 6.1: The MAGIC Telescope.

The project is funded primarily by the agencies BMFB (Germany), MPG (Ger-

many), INFN (Italy) and CICYT (Spain). It is located at the *Roque de los Muchachos* site (see Fig. 6.2), on the Canary island of La Palma, a volcanic island off the African coast at 28° N and 17° W and at an altitude above sea level from 2200 to 2500 m. The site has excellent conditions for optical observations, and is run by the IAC. With its 17 m diameter reflecting surface and 236 m^2 mirrors installed, MAGIC is the greatest Čerenkov telescope in the world. Its main peculiarities are:

- a low energetic threshold of 30 GeV;
- a stiff and light structure, allowing the complete repositioning of the telescope in a very short time, less than one minute;
- a high quality reflecting surface;
- the *Active Mirror Control* (AMC), a calibration system based on the laser technique;
- a high quantum efficiency detector with photomultipliers, the *Camera*;
- a very efficient *Trigger System*, whose potentiality is to subtract the largest part of the background noise;
- a *Data Acquisition System* (DAQ), based on 300 MHz operating Flash-ADC, able to follow the temporal evolution of the showers.

A detailed description of the MAGIC Telescope in given in Sec. 6.4. Anyway, before entering into these technical details, let us spend some words on the current picture of the gamma-ray sky and the way people has been able to get into its understanding.

6.2 The gamma-ray sky

At present the knowledge of the Universe and its evolution is pursued using informations derived from observations with every kind of radiation, in particular electromagnetic waves. The observable electromagnetic spectrum extends from radio waves (at wavelengths of several tens of meters, or energies of some 0.00001 eV) to ultra-high energy gamma quanta (wavelengths of picometers or energies of 100 TeV). Observations at visible wavelengths (0.5 to 1 μm) have a history of centuries, while gamma astronomy by satellites (keV to few GeV) and ground-based telescopes (above 300 GeV) are end-of-20^{th} century newcomers.
An important contribution to the knowledge of the gamma-ray sky came during the

Figure 6.2: The Roque de Los Muchachos site.

last decade thanks to the work of EGRET (*Energetic Gamma-Ray Experiment Telescope*) that, on board of the CGRO (*Compton Gamma-Ray Observatory*) satellite, provided a detailed sky map covering the energy range from 30 MeV to over 20 GeV. This telescope recorded gamma-ray photons individually as electron-positron pair production events, which were authomatically processed to provide the arrival detection and energy of each photon. The Third EGRET Catalog (3EG) [103] of high-energy gamma-ray sources includes data detected from 1991 April, 22$^{\text{nd}}$ to 1995 October, 3$^{\text{rd}}$ (cycles 1, 2, 3 and 4 of the mission). It includes 271 sources on the whole, with energy E $>$ 100 MeV; of them, 74 have been identified as a solar flare, the Large Magellanic Cloud, five rotation powered pulsars, a probable radio galaxy detection (Cen A), and 66 high-confidence identifications of blazars (BL Lac objects, flat-spectrum radio quasars, or unidentified flat-spectrum radio sources); additionally, there are 27 lower confidence potential blazars. This means that the 3EG contains 170 sources with no firmly identification with known objects, although potential candidates have been associated to a number of them. A map of the sources detected by the EGRET Telescope, shown in Galactic coordinates, is presented in Fig. 6.3.

Contrary to the lowest energy gamma-ray band, detection of photons in the TeV region requires instruments with a bigger collection area, like the ground-based telescopes with *Imaging Atmospheric Čerenkov Technique* (IACT). Although a considerable effort has been applied to the development of alternative techniques, like solar arrays (STACEE, see [102]) and air-shower particle detectors (MILAGRO, see [23]), these experiments are not yet very competitive.
The present understanding of the TeV gamma-ray sky is partly due to the joint efforts

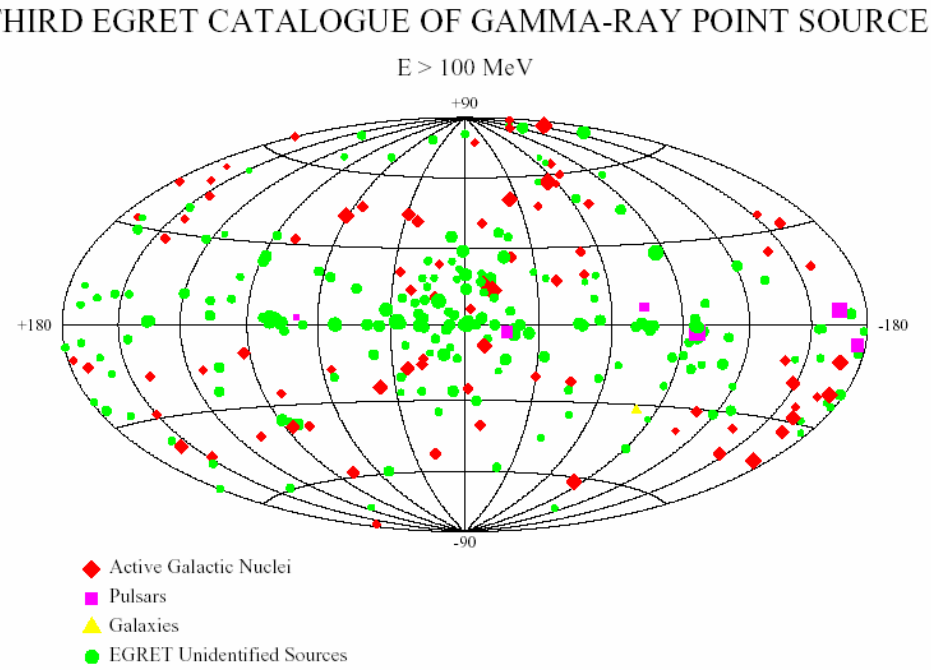

Figure 6.3: Map of the EGRET sources, shown in Galactic coordinates.

of the first generation of IACTs operating in the 1990s, the 10 m diameter WHIPPLE Telescope on Mount Hopkins in Arizona, the HEGRA array at La Palma, Canary Islands, and CAT at Themis (France), having been strongly improved thanks to a new generation of instruments that since the beginning of the new century have been able to perform observations from an energy threshold of $\sim$ 100 GeV up to several TeV. The first of such an experiment was the HESS Telescope [106], an array of four instruments located in Namibia, each of them with a diameter of 12 m. HESS main features are the energy threshold of about 150 GeV with an unprecedented 5σ flux sensitivity around 0.5 Crab for a 50 hour observation, an angular resolution around 0.07° and a wide field of view, which turn it into an excellent instrument for sky scans. The 17 m diameter single MAGIC Telescope [20], the lowest energy threshold IACT in the world, was commissioned one year later at La Palma. Two more telescope systems are well on their way (see Fig. 6.4). They are the VERITAS array in Kitt Peak, USA [109], and an upgrade of the existing CANGAROO array in Australia [116].

Both HESS and MAGIC have recently announced plans for an extension. HESS is to build a gigantic 28 m diameter single telescope at the center of the existing array and MAGIC is already installing a second 17 m telescope to be operated in coincidence

with the first one, which will be commissioned in 2007.

Figure 6.4: The new generation of IACTs.

After the Crab Nebula was established as the standard candle at very high energies (VHE) by WHIPPLE, several years elapsed until the discovery of a second source. An Active Galactic Nucleus (AGN) – Mrk 421 – was claimed in 1994 again by the WHIPPLE collaboration, that subsequently discovered a second AGN also of the BL Lac type, Mrk 501. Although during the 1990s the progress was quite slow, by 2003 the number of confirmed VHE sources had crept up to 12. Thanks to the new generation of IACTs, during the last two years the GeV–TeV astronomy has been going through a phase transition, getting the number of sources almost tripled. HESS performed a 112 hour scan of the Galactic plane in the range of Galactic longitude [-30°, 30°] and ± 3° latitude [2]. New sources were detected above 6σ (see Fig. 6.5) and seven tentative ones above 4σ have been recently released. Four of the eight high significance sources are potentially associated with supernova remnants (SNRs) and two ones with EGRET sources. In three cases they could be associated with pulsar wind nebulae (PWNs). In one case the source has no counterpart at other wavelengths. Along with two other unidentified sources in this energy band, this suggests the possibility of a new class of dark particle accelerators in our galaxy. Two

of the objects in the scan have been recently confirmed by MAGIC [19]. Fig. 6.6 shows

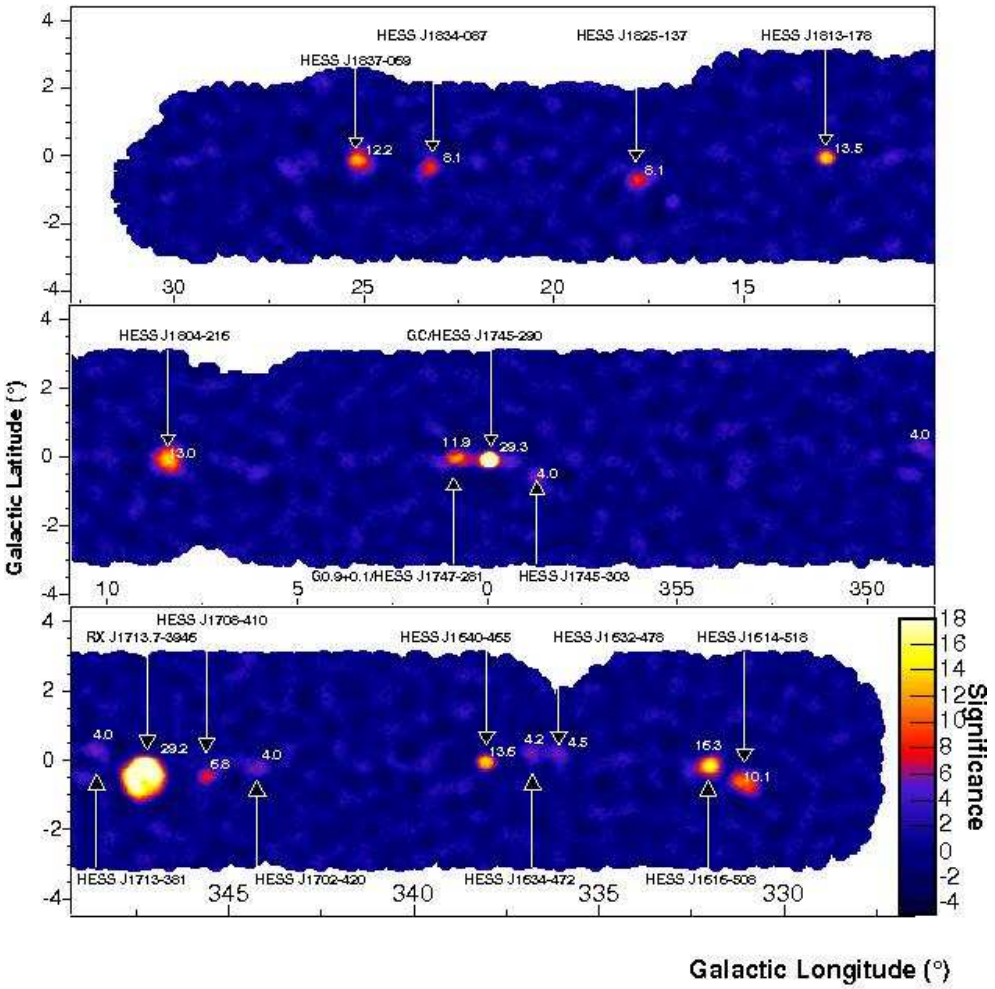

Figure 6.5: HESS scan of the Galactic plane between ±30° in longitude and ±3° in latitude. The sources indicated are detected at a significance level greater than 4σ. Figure by [188].

how the number of detected sources in the TeV energy domain has increased in the last two years, as soon as the last generation of ground-based Čerenkov telescopes have started operating. The most recent catalogue of sources claims 32 sources, including six unidentified objects. There are now two consolidated populations of galactic VHE emitters (PWNs and SNRs). The VHE catalogue lists six PWNs, six SNRs, one binary pulsar (PSR), one microquasar (mQSO), a region of diffuse emission and eleven AGNs. In the last months MAGIC and HESS have detected several new AGNs with redshifts up to 0.19, at distances almost a factor 10 larger than the two first ones detected at TeV energies.

For a more detailed discussion of the recent results in VHE gamma-ray astronomy, we refer to Chapter 11.

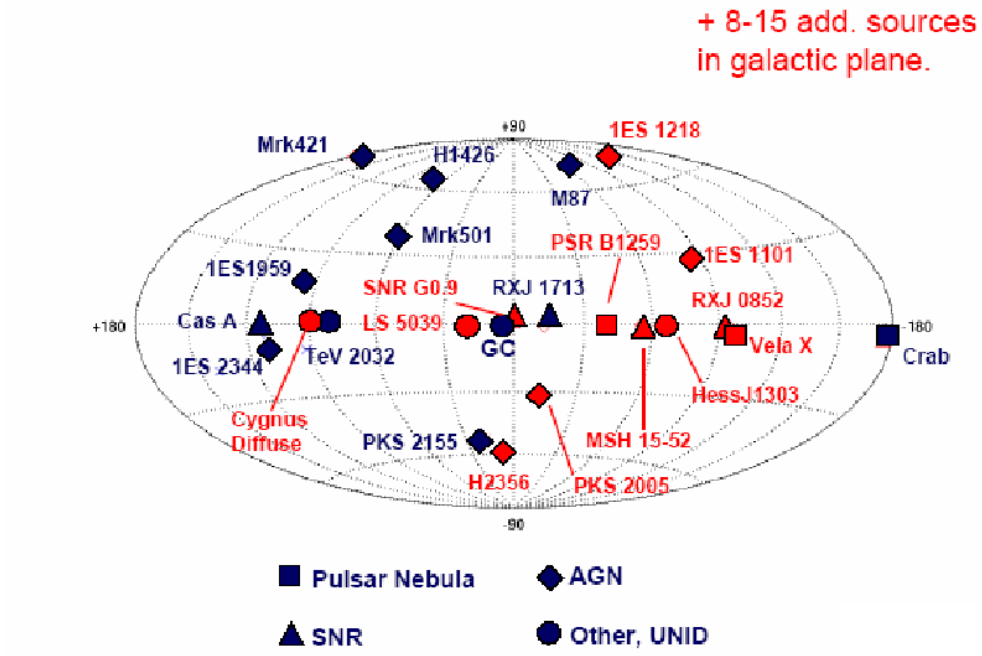

Figure 6.6: The VHE gamma-ray sky in 2005. Not shown are eight more sources discovered by HESS in a survey of the Galactic plane. Red symbols indicate the most recent detections, brought during 2004 and 2005 by the last generation of IACTs: HESS and MAGIC. Figure by [151].

6.3 Imaging Atmospheric Čerenkov Telescopes

IACTs are ground-based telescopes for the detection of VHE electromagnetic particles, in particular gamma rays. Having no electric charge, VHE gammas are not affected by magnetic fields, and can, therefore, act as messengers of distant cosmic events, allowing straight extrapolation to the source. Although high-energy gamma quanta get absorbed in the atmosphere, they can be observed indirectly. The absorption process proceeds by creation of a cascade or shower of high-energy secondary particles. When these charged secondary particles pass through a dielectric and transparent medium at a speed higher than the speed of light in that medium, they emit radiation at the characteristic angle θ_c which widens as the atmosphere thickens:

$$\theta_c = \arccos(1/\beta\, n), \tag{6.1}$$

being the threshold condition for Čerenkov radiation:

$$\beta \geq \beta_{min} = \frac{1}{n}, \tag{6.2}$$

with n is the refraction index of the medium. The Čerenkov photons have energies in the visible and UV range, and pass through the atmosphere; thus they can be observed on the surface of the earth by sufficiently sensitive instruments. A sketch of the principle of the Čerenkov technique is illustrated in Fig. 6.7.

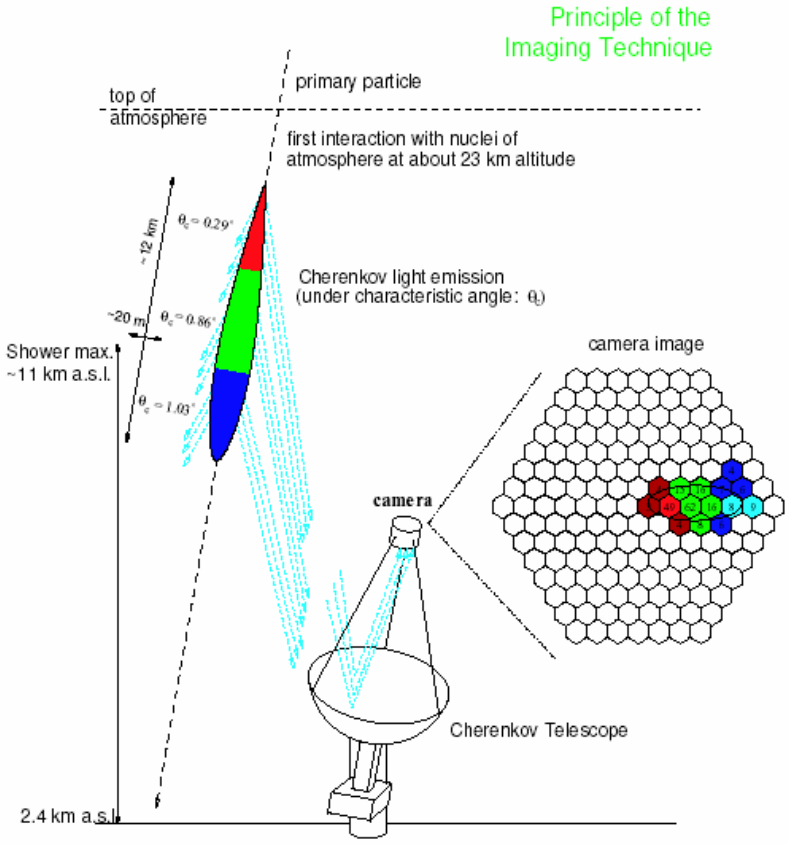

Figure 6.7: The Čerenkov technique, through the formation of the image of an electromagnetic air shower in an IACT pixelized camera for a typical 1 TeV gamma-ray induced shower.

6.3.1 Extensive Air Showers

An *Extensive Air Shower* (EAS) (Fig. 6.8) is a particle cascade originating by the interaction of a cosmic or a gamma ray with the atmosphere. There exist two different kinds of EAS, depending on the nature of the primary particle which they have been originated from, photons or hadrons. The numerous secondary charged particles

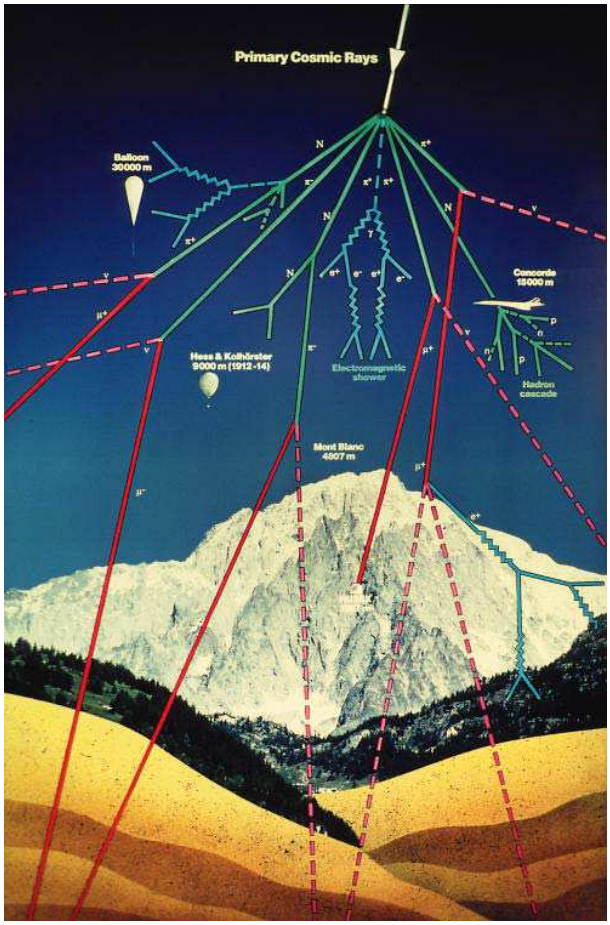

Figure 6.8: An example of EAS originated by a cosmic ray.

in an *electromagnetic shower*, for an incident gamma rather exclusively electrons and positrons, all radiate low-energy (visible to ultraviolet) photons, the Čerenkov radiation. Most of the shower development happens at an altitude above sea level from 20 to below 10 km. The radiated photons have an energy corresponding to a window of penetration, and arrive in large enough numbers on the surface of the Earth to become an indirect image of the shower, allowing identification against backgrounds and reconstruction of the original particle's direction and energy. The showering process and the generation of Čerenkov light in a forward cone have two immediate experimental consequences: the light is spread over a large area, typically a circle with a diameter of 250 m, and hence the light intensity per unit area on ground is low. This allows detection of a gamma impinging anywhere inside this disk, e.g. an effective area of 30 to 100 000 m^2, as long as the initial energy is high enough to produce enough Čerenkov light. Conversely, the signals are weak, marginally detectable; hence, the instrumental sensitivity must be pushed as far as possible:

the collection area (mirror surface) must be maximized, and the camera elements (photomultipliers) must respond to single photons with high efficiency. To further improve sensitivity, experiments are installed on mountain tops far from background light and with observation time lost due to clouds as little as possible.
Gammas of the high energies that can be recorded by IACTs are relatively rare events. They have to be discriminated against a cosmic ray background, several orders of magnitude more abundant. These are mostly protons or light ionized atoms, producing (more dissipated) *hadronic showers*, in which the charged particles also radiate Čerenkov photons. However, hadronic showers do not typically come from the direction in which the telescope is trying to observe a gamma source. The main aspect which distinguishes between electromagnetic and hadronic showers is their lateral distribution, being the latter partially more extended than the former. Also, hadronic showers are much less concentrated: the hadrons interact via the strong interaction, producing hadrons and leptons as secondary particles, so multiple electromagnetic and hadronic secondary showers appear, with large fluctuations in relative energy, spread over a volume much larger than for an electromagnetic shower. The image that hadrons produce in the detector, therefore, has different characteristics than that gamma showers generate in the camera: electromagnetic showers images are elliptical, with the bigger axis oriented with the direction of arrival of the photons, while hadrons form larger and less aligned images. Other differences between the two regimes are the temporal dispersion, more pronounciated for hadronic showers, and the higher light density of the electromagnetic cascades. In order to obtain fairly clean gamma signals, suitable discrimination algorithms have been implemented, which are one of the topics discussed in the next chapter.

6.3.2 The IACT technique

IACTs are detectors for high-energy gamma quanta, installed on the surface of the Earth. The name *Imaging Atmospheric Čerenkov Telescope* contains most of the characteristics of this type of instrument:

- the detectors used have a light collection mirror and a camera, so they resemble optical telescopes at least superficially:

- these telescopes detect light produced by the Čerenkov effect;

- IACTs record many Čerenkov photons for a single original gamma; they are seen by the camera as an image whose characteristics allow to identify the recorded

particle as a gamma, and to specify its direction and energy;

- an advantage of these instruments, which makes them very competitive compared with spatial satellites, is their very large effective area: more than 10^4 m^2 instead of less than 1 m^2 (see also Fig. 6.11).

6.4 Characteristics of the MAGIC Telescope

Very high energy gamma astronomy with ground-based telescopes is a recent field of investigation in astroparticle physics instruments, and a lot of interesting subjects of observation are expected to be addressed to during the coming years. They are AGNs, PSRs and SNRs, GRBs and sources found at lower energies but not yet identified. Additionally, MAGIC is able to give other important contributions to cosmology and fundamental physics; among them, the observations of VHE gamma rays, if done systematically, will also allow to formulate constraints on stellar formation in the early Universe, by measuring the extragalactic infrared radiation field. Remarkably concluding this list, there are searches for the stable lightest supersymmetric particle, expected (if it exists) to annihilate with its own self-conjugate antiparticle into photons in areas of high gravitational field. Additionally, quantum gravity effects might become apparent if subtle time differences can be detected in the arrival of gammas from a given source, at different wavelengths. If they occur in nature, the MAGIC detector has the capability to record such phenomena. Finally, MAGIC will participate in multi-wavelength campaigns (simultaneous observations) wherever promising, and is also preparing for a close collaboration with several X-ray, optical, and radio experiments. The same relevance of simultaneous observations can be safely predicted for most future astrophysics observations. The correlation in time and in amplitude for expected signal fluctuations will give important clues to the mechanisms of production, acceleration, and transport through space.

In sight of such a promising perspective of investigation and discovery, we turn our attention to the aim of involving the reader into a deeper comprehension of the most important technical aspects of this telescope.

6.4.1 The frame and the driving system

The main mirror of the telescope rests on a rigid three layer space frame of carbon fiber-epoxy tubes, light and resistant to atmospheric conditions. Knots joining the tubes are made of aluminum. The weight of the frame, including the lower drive

ring for azimuthal movement, is about 9 tons, while the whole telescope and the undercarriage weights 64 tons. This frame structure allows the instrument to be repositioned within 22 s at any position in the sky, which makes this telescope very suitable to follow up GRBs, an extremely valuable and unique feature among current IACTs. The MAGIC Telescope is driven by high precision servo-motors, two 11 kW motors on the azimuthal axis and a single 11 kW motor on the elevation one. This alt-azimuth mounting lets an azimuthal wheeling of 400° and a zenith rolling between –80° and 100°. An accurated monitoring system is installed, in order to strongly reduce the oscillation effects, so that deformations can be held below 3.5 mm with respect to the nominal curvature at any position. The frame structure guarantees wind resistance up to $\sim$ 170 km/h and stability for complete ice coverage up to 3 cm thickness. The paraboloid shaped reflecting surface has a diameter of 17 m, a focal lenght-to-diameter ratio (f/D) set equal to 1 (in order to assure high optical quality images at the camera), and is doweled by 243 squared panels of one meter side, each hosting four squared aluminium mirrors of 49.5 m side. A high sensitivity CCD camera mounted on the reflector frame allows a high quality test of the precision of the tracking system, by monitoring both LEDs installed in the camera frame and stars from the celestial background (*Starguider System*).

6.4.2 The camera

The camera is the place where light received at the reflecting mirrors is collected and the conversion from Čerenkov photons to photo-electrons occurs. In the last decade, IACT cameras underwent a big development from a single photo-multiplier (PMT) version to cameras with a few hundred pixels. The more pixelized the camera, the better to resolve the differences between the background (hadron showers) and the signal (gamma showers). The MAGIC camera is equipped by 576 high quantum efficiency PMTs. Raising the mirror area permits to collect a larger number of photons, lowering the energy threshold of the IACT. As one of the main interests of any scientific collaboration is to investigate new and unknown phenomena, the observation of low energy showers ($\lesssim$ 100 GeV) is one of the main goal for MAGIC scientists. These showers are rather compact and close to the central part of the camera (due to trigger effects), so they are demanding a finer pixelization of the camera itself in order to properly resolve the images and to achieve a high efficiency on photon detectors. On the other side, the outer region of the camera has to record Čerenkov photons from the shower tails, where the statistical fluctuations in the shower development are larger. This implies more diffuse images in this region of the camera. In addition, the

optical quality is made worse by the coma aberration. For all these reasons, different kinds of PMTs are needed, in the inner and outer parts of the camera respectively. Fig. 6.9 shows a schematic picture of the MAGIC camera. The 576 exagonal shaped pixels, hosting different kind PMTs, are clearly shown: the 397 inner pixels have a 2.5 cm size, while those in the external region are double-sized. The trigger region is formed by the central 325 pixels from the inner zone. To avoid sagging, the camera in the telescope structure is supported on an aluminum arc reinforced with steel stressor cables. The total size of the camera is 1.5 m in diameter and its weight is 500 Kg.

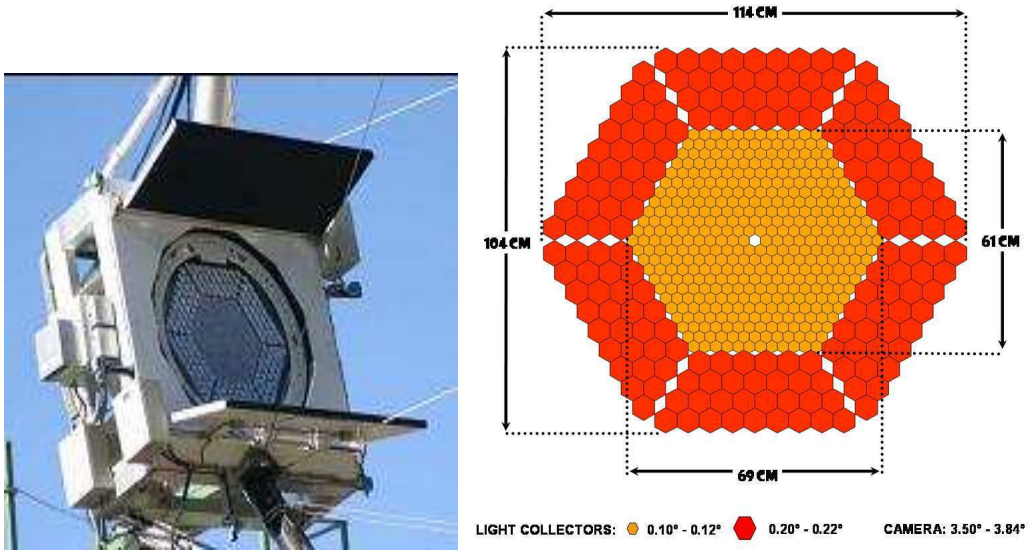

Figure 6.9: Schematic picture of the MAGIC camera.

The MAGIC camera has the following features:

- **fine granularity,** in order to resolve the features of low energy shower images and to permit an efficient gamma-hadron discrimination. Moreover, the E_{th} of the telescope is further reduced by lowering the integrated noise per pixel and the trigger threshold at the discriminator level.

- The **large Field of View (FOV)**, $3.5° - 3.8°$, assures recording of the greatest part of the shower images.

- **Low noise**: the detection of Čerenkov pulses suffers from a strong background of *Night Sky Background* (NSB) photons. The fast response of the whole system is able to reduce the width of the pulses at the trigger level to only a few nanoseconds.

- A **low gain operation** reduces the noise level recorded by the camera, making it suitable for observations also under strong moonlight.

6.4.3 The mirrors

The telescope reflector is composed by 964 mirror elements, each of them with an area of 49.5×49.5 cm^2. The overall curvature of the reflector is parabolic, in order to minimize the spread in the arrival time of the Čerenkov photons, while the curvature of the individual mirror tiles is spherical; moreover, because of the parabolic shape of the main reflector, their focal lengths are increased following their radial position on the dish: from 17 m at the center, to 18 m at the boundary. For the construction of the single mirror elements of the main reflector, MAGIC adopted a very innovative technology, consisting of using an aluminum honeycomb core to confer lightness and stiffness to the panel. The front mirror plate is made of a 5 mm thick AlMgSi 1.0 alloy, machined to spherical shape and polished by diamond milling to achieve the most adequate curvature radius for its position on the parabolic reflector. After the diamond milling, the mirror is coated with quartz, in order to protect it from ageing and scratches. The aluminum plate is glued together with an aluminum honeycomb inside a thin aluminum box and the final assembly weights only $\sim$ 4 Kg. Each mirror panel is equipped with a heating system to prevent ice and dew formation, and to dry them up from condensate water before data taking after periods of high humidity. The advantages of this mirror structure with respect to the conventional glass mirrors are numerous: less weight, the possibility of mirror heating, a fast production technique, lower cost and longer life. The reflecting surface achieved has a mean reflectivity of $\sim$ 85% in the wavelength range 300–650 nm and a roughness below 10 nm, which produces an excellent image quality: 90% of the light from a parallel beam is focused within a circle of 1.0 $\pm$ 0.2 cm diameter, less than half of the MAGIC pixel size. During the commissioning of the telescope, the light collection efficiency of the reflector was measured with a high-resolution large dynamic range CCD camera. The active mirror area at the time of measuring (including mirror imperfections, temporary defocusing and all effects of shadowing) was estimated to be 212 m^2. From several sources with a wavelength spectrum peaking at 500 nm, the average specular reflectivity was measured to be 0.77 $\pm$ 0.04.

6.4.4 The Active Mirror Control

As the MAGIC frame is not completely rigid, when the telescope is repositioned on different elevation angles the relecting surface turns aside from its ideal shape, due to weight redistribution. In order to avoid this disadvantage, a proper system of Active Mirror Control (AMC) has been developed to allow mirror adjustments and small corrections during telescope movements. MAGIC is the first IACT which makes use of such a technique, able to reduce mirror deformations and to raise the quantity of data taken. The AMC works over lightweight panels of four pre-adjusted mirror elements and with a switchable laser pointer. Each panel is tilted by two stepping motors, while being monitored by a CCD video camera that compares on demand the actual laser spot position on the casing of the camera with the nominal one. The 10^{-5} sr ($0.1^\circ \times 0.1^\circ$) *Point Spread Function* (PSF) of the reflector is extracted from the analysis of the width of muon particles rings and from the comparison of Hillas parameters in real and Montecarlo data (see next chapter). The reflector is focused at a distance of 10 km because this is the typical maximum distance to the shower at low zenith angle and for 100 GeV gamma rays. After AMC reflector adjustment, a point-like light source at this distance produces a gaussian image at the camera plane with $\sigma = 10.5$ mm, which corresponds to 0.035°.

6.4.5 The trigger system

After that analogical electrical signals are recorded, a trigger system works to subtract the greatest part of noise events. The trigger region in the camera, restricted to the innermost 325 pixels, is covered by 19 overlapping macrocells of 16 pixels each. There exist three stages or trigger levels.

- In the **level 0** trigger a predefined threshold for PMT pulses amplitude is established, in order to select whose pixels are to be considered swiched on (see Fig. 9.4). This threshold is set depending on the sky luminosity and may be modified during the data acquisition (for instance, when a luminous star is located in the field of view of the telescope and lights up part of the camera). The typical discriminator threshold is $\sim$ 10–12 phe per pixel.

- The **level 1** trigger looks for fast coincidences, less than 7 ns, of next-neighbor pixels. These coincidences are taken into account only for neighbor pixels, whose number (from 2 to 5) may be set by hand. If the multiplicity is larger than 2, an additional condition is required: each pixel contributing to the trigger must act

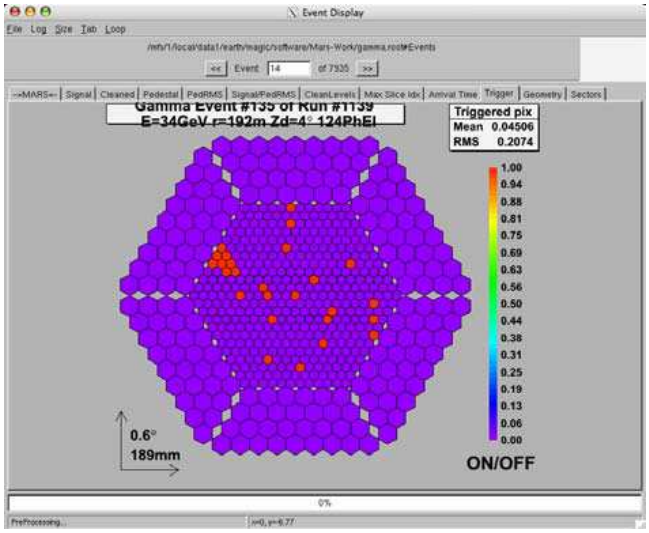

Figure 6.10: Level 0 trigger: red pixels are above threshold and swiched on.

at least two fired next-neighbors (the so-called *'closed-packed'* configuration). The effect of the many possible trigger configurations on the very low energy showers is still under investigation. The level 1 trigger in the MAGIC Telescope is typically set to coincidences of 4 closed packed pixels.

- The **level 2** trigger performs a more accurate discrimination of events, sending selected ones to the DAQ. It consists on a first stage of 19 programmable modules (the so-called SMART modules), where the level 1 information from each macrocell is divided into three 12-pixels regions, called LUT (*Look-Up-Tables*). The outputs from the 19 modules of the first stage are fed into a second and a third stage in a tree-like structure, in order to apply cuts on the event topology (number of pixels, shape and orientation). The level 2 allows MAGIC to perform a true online pattern recognition of the images, which increases the background rejection at the trigger level. The level 2 trigger directly communicates with the digital boards of the FADC system (see Fig. 6.12), enabling the acquisition of the data whenever an event triggers in the above mentioned three trigger levels. It must be pointed out that the level 2 trigger also contains a prescaler board, not to overcome the maximum acquisition rate allowed by the DAQ of 1 kHz. However, the level 2 trigger can handle trigger rates up to ~ 1 MHz and this might be a very valuable feature when performing observations at very low E_{th} (< 2 GeV), so it is planned for some gamma-ray emitting pulsars, as well as for AGNs in flare state and GRBs, where the trigger rate might go up to several tens of kHz.

The individual pixel rates of the channels included in the trigger region are monitored using 100 MHz scalers and these values are used to dynamically regulate the discriminator thresholds for each individual pixel. This *Individual Pixel Rate Control* (IPRC) acts only on pixels that are affected by stars brighter than 4 M. In normal observation, the global trigger rate is about 250 Hz for extragalactic sources (*standard pixel threshold*) and about 200 Hz for galactic sources (*increased pixel threshold*). According to the full MC simulation, this rate corresponds to a trigger threshold around 60 GeV.
Fig. 6.11 shows the MAGIC *effective area* as a function of energy. The saturation effect at high energies is mainly due to DIST and LEAKAGE cuts, whose effect is to lower trigger efficiency (for cuts' definitions, see next chapter).

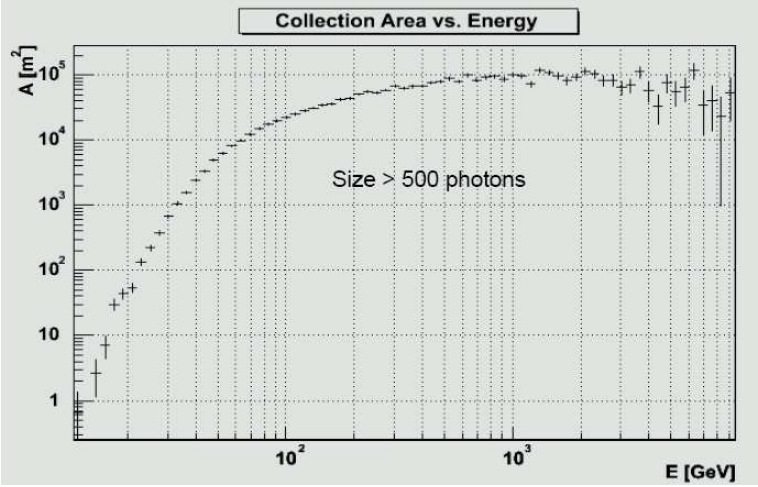

Figure 6.11: MAGIC effective area. (Courtesy of A. Moralejo, by the MAGIC Collab.).

6.4.6 The data acquisition system

In the DAQ, analogical PMT signals are amplified and transmitted to optical fibers before being broken into two parts, the first one going to the trigger and the other being further stretched and divided into two branches (high gain and low gain), in order to increase the dynamic range to $\sim$ 60 dB. It consists on 18 crates of 4 FADC boards, and a dual processor PC (the so-called DAQ PC), running a multithreaded C++ readout program in a Linux operative system. Each FADC board is prepared to digitalize the signals coming from 8 channels. The 576 8-bit FADC chips continuously digitalize the analogical PMT signals coming from the receiver boards at the frequency of 300 MHz and store them in the 32 kByte ringbuffers.

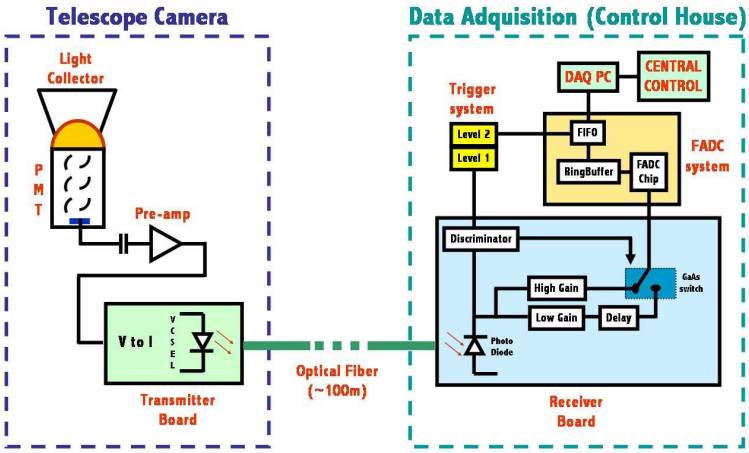

Figure 6.12: Scheme of the MAGIC data aquisition electronics.

The components of the DAQ for one of the channels are shown in Fig. 6.12. When a level 2 trigger arrives to the FADC modules within 100 μs, the FADC chip stops digitalizing, the position of the signal in the ringbuffer is determined, and 30 time slices (15 for high gain and 15 for low gain) are written into the *FiFo Buffer* for each pixel. This operation is performed at a maximum rate of 80 MBytes/s. The readout of the ring buffer results in a dead time of $\sim$ 20 μs, corresponding to the 2% at the design trigger rate of 1 kHz. The time and trigger informations for each event are recorded by dedicated digital modules, which are read out together with the FADC boards. As mentioned, during observations of AGNs in active state, low energy signals from strong pulsars and GRBs, the trigger rate could exceed the $\sim$ kHz data taking capability of the DAQ. Because of that, the DAQ is provided with a separated high frequency data stream which records only the time and trigger information of the events sent by the dedicated high frequency 2 level trigger, that can reach rates of up to $\sim$ MHz. The FADC data are reorganized and merged into a raw event data format. The data are then saved into a RAID0 disk system at a rate of up to 20 MBytes/s, which can amount to up to 800 Gbytes/night. Finally, during daytime the data are transformed into `.raw` format and written to tape. During normal telescope operation, the complete readout program running in the DAQ PC is controlled remotely via TCP/IP by the Central Control.

6.4.7 The MAGIC sensitivity

The MAGIC integral sensitivity curve is shown in Fig. 6.13. The error bars derive exclusively from the statistical uncertainty of the quality factor, dominated by the

low hadron statistics after cuts. For more details on the MAGIC sensitivity energy dependence, see [142].

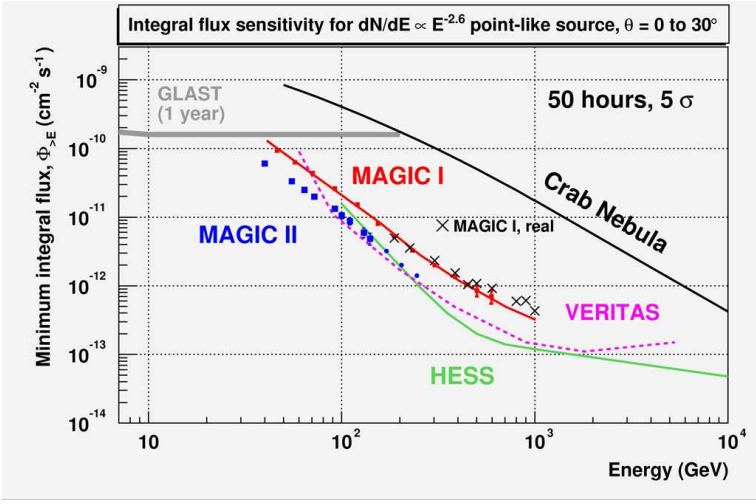

Figure 6.13: MAGIC integral flux sensitivity, assuming a PSF with projected σ around 0.041°. The curves for HESS (4–telescope setup) and VERITAS (7–telescope setup) are taken from [107, 190] respectively. Of course, MAGIC will be able to observe above 600 GeV: there, the estimate of sensitivity was simply not possible due to lack of MC hadron statistics. Crab flux comes from [14] and [128]. Note that the minimum on the y-axis refers to a hypothetical source with a pure power-law $E^{-2.6}$ differential energy spectrum, not to a source with a Crab-like spectral shape. Figure by [142].

Chapter 7

Data Analysis Methods for the MAGIC Telescope

This chapter describes the steps followed in this work for the analysis of the MAGIC Telescope data, from the checks to ensure the quality of the data to the data reduction chain: signal extraction, calibration, image cleaning and parameterization, gamma/hadron separation and final signal evaluation.

7.1 Sources of background

Subtraction of background is one of the major challenges of the IACT technique, which has to deal with two types of background:

Cosmic ray showers. As already mentioned in the previous chapter, high energy gamma-rays are relatively rare events to be detected from an IACT. Moreover, images produced in the camera by gamma-induced showers are similar to whose initiated by the much more abundant hadronic component of the cosmic rays. Additionally, cosmic-ray electrons develop an electromagnetic shower completely undistinguishable from gamma-induced showers, so they represent an irreducible background for the telescope. In order to discriminate between gamma and hadrons, several techniques have been developed, envolving the substantial differences of the respective processes.

Background light. Čerenkov photons produced in electromagnetic showers are far from being the only source of signal in the PMTs of an IACT: in fact, Čerenkov light has been estimated to only contribute a factor $\sim 10^{-4}$ to the total light of the night sky. There exist two kind of Night Sky Background (NSB): a diffuse component, the so-called LONS (*Light Of Night Sky*), both from arti-

ficial (human-made light pollution) and natural origin (like diffuse moonlight, sunlight scattered by interplanetary dust, zodiacal light, ionospheric fluorescence), and the background due to bright stars in the FOV of the instrument. Due to its excellent sky condition, 'El Roque de los Muchachos' is considered one the best sites for astronomical observation in the world, where the intensity of the LONS is estimated to produce an average of ~ 0.15 phe/ns for a 0.1° inner pixel of the MAGIC camera for moonless nights and pointing outside the Galactic plane [138]. This source of background seriously compromise the detection, increasing the contribution of lower-energy showers, then a proper evaluation and subtraction of this effect are essential for the data analysis. A detailed description of the different sources of natural background light is given in [74]. We only point out that although moonlight strongly affects the intensity of the signal, observations with the Moon are possible under appropriate conditions, consisting in avoiding observations during full Moon or Moon illuminated by more than 70% (not more than 30%, if haze layers of clouds are present), and never observing below 25° or above 130° angular distance to the Moon [1].

7.1.1 Run Classification

During data acquisition, all the events passing the trigger are digitalized by the FADC and stored by the DAQ into `.raw` data files, which contain for every pixel the information of the signal readout. Each raw-data file is called a run and a run number is assigned to it. There are three kinds of run:

Data runs. These are the collection of events passing all the trigger levels.

Calibration runs. In order to estimate the performances of every pixel in the camera, and in particular the conversion factor of the recorded signal to photoelectrons and to photons, light pulses of known wavelenght are produced to uniformly illuminate the camera and a calibration run is registered.

Pedestal runs. These runs contain informations on the NSB and other sources of noise and allow to determine the baseline of the signal and its fluctuations.

Alternatively, raw-data files can be classified according to the telescope pointing position respect to the source:

[1] The increase of the background light due to the presence of the Moon depends on various factors, including the source zenith angle, Moon phase, angular distance to the Moon, Moon zenith angle and atmospheric composition, as well as the aerosol content of the atmosphere. Direct moonlight during full Moon is about a few times 10^{15} ph m^{-2} s^{-1} sr^{-1}.

ON data runs. The telescope points directly to the source.

OFF data runs. The telescope points to a region where no known source is contained in the FOV and no signal is expected. ON data and OFF data are to be taken with similar background and zenith angle conditions.

Wobble mode data runs. The telescope swings from the ON-source position to a OFF-source position, at a distance of $\sim \pm 0.4^{\circ}$ from the center of the camera.

7.1.2 First run selection

A satisfactory analysis of a source would require as many hours of ON data as possible, and several times more OFF data, in order to reduce the effect of background fluctuations on the analysis results. Anyway, unless the data are taken in the Wobble mode, normally the quantity of OFF data available is lower than that of ON data, so their statistic is often enlarged by using also OFF data taken for other sources observed under similar conditions.

The first run selection is based on the quality of the data, depending on:

- the correct working of the trigger system;
- good atmospheric conditions;
- absence of technical problems at the telescope during data taking;
- sufficient quantity of events.

7.2 Monte Carlo data

Differently from other detectors, the IACT response can not be characterized with a controlled flux of known primary particles (the so-called *test beam*), so that realistic and detailed Monte Carlo (MC) simulations are crucial for testing the telescope performance. Many kinds of simulations may be performed, mainly:

- simulations of the shower developement in air, carried out by `Corsika`, a dedicate software package which has been developed by the KASKADE collaboration;
- simulations of the mirror dish, reproducing the atmospheric absorption of the Čerenkov photons and the telescope reflection, performed by `Reflector`;

- simulations of the FOV;

- simulations of the background, both diffuse and starlight;

- simulations of the camera response, carried out by the software `Camera`.

The detector simulation must reproduce all the effects that the different elements of the read-out chain produce on the signal. The mirror reflectivity, the effciency of light collection of all the parts involved, the gain of the PMTs, the noise introduced by the electronic chain, etc., all these parameters are adjusted to match the behavior of the telescope when the data were collected. A particular attention is given to the width of the PSF distribution of the light collected by the mirror dish and focused onto the camera, because mirror disalignment makes the Čerenkov photons focus into a wider region of the camera, the resulting image getting also wider. For that reason, whenever required, mirror panels that have deviated too much from their nominal position have to be adjusted.

The software package for data analysis developed by the MAGIC collaboration is called `Mars` (*MAGIC Analysis and Reconstruction Software*), it is written in `C++` and its classes work in the `Root` framework. The analysis discussed in the following of this Thesis has been performed with version `Mars V0-13-1` and `root 5.12f`.

7.3 Signal extraction and calibration

Once the first run selection is complete, the subsequent step of the analysis is the extraction of the signal from the FADC slices and its calibration. Different methods are implemented in the `Mars` package to extract the charge and the arrival time information of the signal, all of them with the aim of minimizing the effect of the NSB. The **digital filter** signal extractor calculates the signal as the weighted sum of N consecutive FADC slices, usually $N = 15$. The value of the weight depends on the signal shape, so a numerical fit is possible. The total charge Q is estimated from this sum, while the arrival time t depends on the peak position of the signal in the FADC slices. Due to its great efficiency, this filter is currently the most widely used in the MAGIC data analysis. The only disadvantage is that it can not efficiently extract pulses which are out of range of the FADC window. This can happen if the trigger and the FADCs are not well synchronized, a hardware problem which affected most of the 2005 data. In that case, another extractor has to be used: the **spline** method extrapolates the sample points with the common spline algorithm, and the total charge Q of the signal is simply proportional to the peak of the extrapolating

function, while the arrival time of the photons is deduced from its position. It has been demonstrated [93] that the two methods are equally effective, the only difference being that spline is faster and more powerful when above-like critical situations occur.

7.4 Pedestal subtraction

Shower signals are always inmersed in a background of NSB photoelectrons which alters the fluctuations size. Fluctuations are proportional to the square root of the NSB phe rate. Only pulses whose charge is significantly above the level of that noise, characterized through the pedestal RMS, are interpreted as a signal. This procedure is referred to as *'image cleaning'*.

7.5 Calibration

The integrated charge of the extracted signal is given in units of FADC counts, so it has to be converted to number of photoelectrons arriving at the first dynode of the PMTs. There are two different calibration levels: the **relative calibration**, a procedure that equalizes the response of different pixels to a same mean value, when subjected to the same input signal, and the **absolute calibration**, which is the estimation of the real number of photons producing the signal in every pixel. The number of phe arriving to the first dynode of each pixel can be derived as follows:

$$N_{phe} = \frac{(< Q > - < Q_{ped} >)^2}{\sigma^2} F^2, \tag{7.1}$$

where F is the excess noise introduced by the readout chain (~ 1.15 for the MAGIC PMTs), $< Q >$ is the mean charge in FADC counts of the pulse signal registered by the pixel, calculated from calibration pulses and to which the mean pedestal $< Q_{ped} >$ is subtracted, and σ^2 is defined as the reduced variance calculated from the charge distribution and corrected by the contribution of the pedestal variance $\sigma^2 \equiv \sigma_Q^2 \sigma_{ped}^2$. Then, the conversion factor from FADC counts to phe for each pixel is directly obtained from:

$$C_{phe}^{FF} = \frac{N_{phe}}{< Q > - < Q_{ped} >} = \frac{< Q > - < Q_{ped} >}{\sigma^2} F^2. \tag{7.2}$$

7.6 Identification of bad pixels

During the calibration procedure, some pixels can be affected by anomalous behavior and are to be rejected. These **bad pixels** are usually due to hardware problems

involving some elements of the readout chain. Another reason of pixel malfunctioning is the presence of a bright star in the FOV, which implies an increase of the pixel DC current and, subsequently, a higher pedestal RMS. The standard procedure is to substitute the value of pixels affected by fluctuations larger than five standard deviations (5σ) from the mean fluctuation with the value obtained from the interpolation of the neighbor pixels. Fig. 7.1 shows an example of the list of pixels identified as not suitable for further analysis, as resulted from the processing of a given calibration run of the Crab Nebula (see next chapter). Above the camera layout, conditions used to classify a pixel as 'bad' are listed.

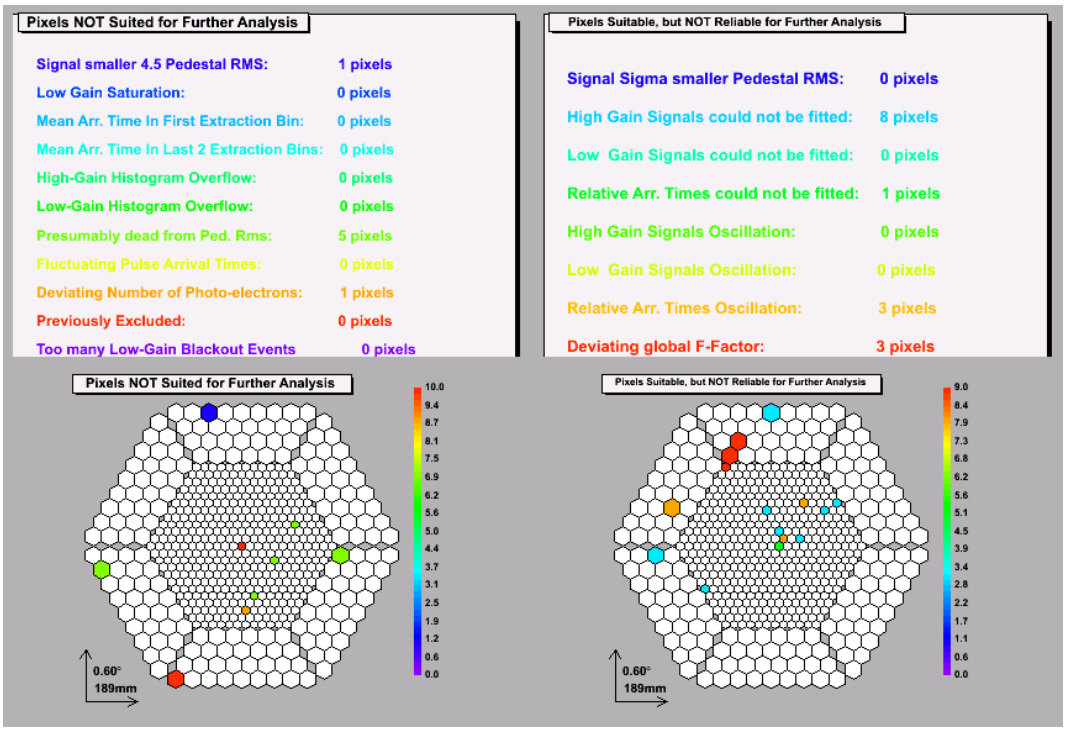

Figure 7.1: Example of bad pixels isolated during calibration of the Crab Nebula. (Data analysis in Chapter 8).

7.7 Image cleaning

After the signal calibration, the shower image is surrounded by diffuse background. The following step is therefore the selection of pixels which belong to the signal, a procedure called *image cleaning*. The pixel content is compared to two cleaning thresholds: a higher level selecting the pixels in the core, and a second loop for the surrounding ones. As a general rule, all isolated core pixels are excluded from the

image. In the standard MAGIC data analysis, the applied thresholds are 10 phe for the core pixels and 5 phe for the neighboring ones (*10:5 image cleaning*), but a more refined treatment of the core pixels is also possible. For instance, a *7:5 image cleaning* is preferred when analysing sources at low energy, as in the case of DM searches.

7.7.1 Parametrization of the shower image: the Hillas technique

Čerenkov photons produced in an atmospheric shower reach the telescope with different incident directions, thus they are focused into different pixels and form an image in the camera plane. Fig. 7.2 shows the process of image formation in the camera: Čerenkov photons distribute on an elliptical surface, with the head and the tail of the shower corresponding to the ellipse boundaries and the core filling the inner pixels.

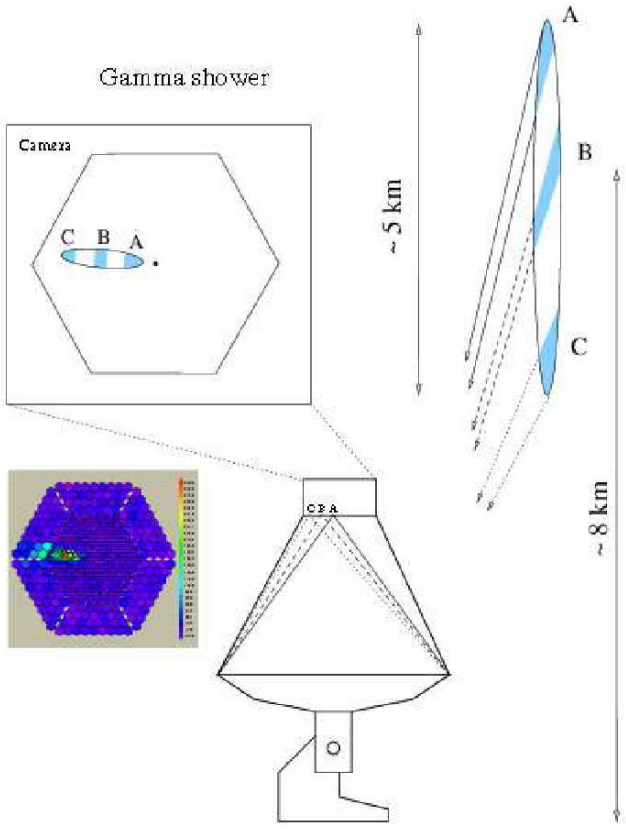

Figure 7.2: Formation of an image in an IACT.

The basic idea of the imaging technique is to use the image shape and orientation to extract physical informations about the primary particle. In 1985 Hillas proposed a

parametrization based on the first, second and third moments of the two-dimensional distribution of the signal along the image. For the moment calculation, the position of each pixel included in the image is weighted with the fraction of the image signal content in it. Moments are estimated with respect to a coordinate system centered at the image center of gravity (COG), with the x-axis along the major axis of the ellipse and the y-axis along the short one. Fig. 7.3 shows some of these moments, the so-called *Hillas parameters*. They can be grouped into two classes: those describing the shower shape (these are independent by any reference point), and those depending on a reference point. Hillas parameters are:

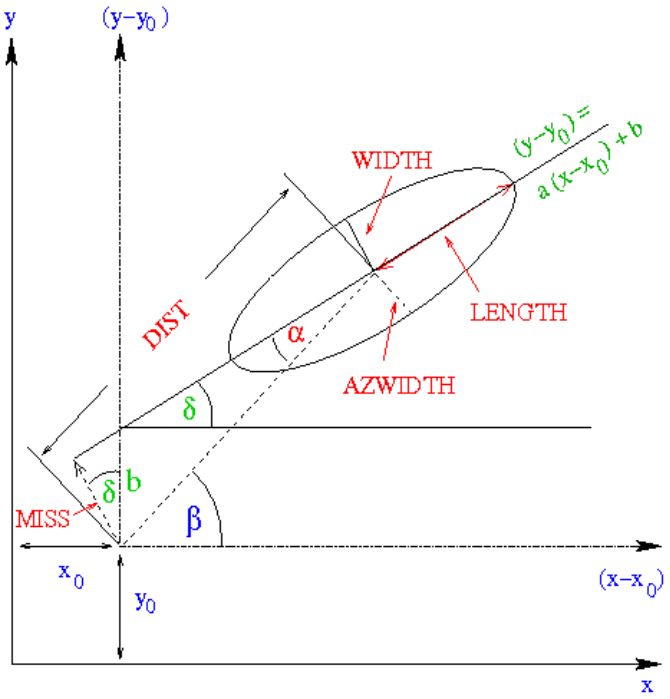

Figure 7.3: Image parameters as calculated according to the imaging technique.

SIZE – Total number of phe collected on the shower image. For a fixed zenith angle of observation and impact parameter value, it is nearly proportional to the energy of the primary particle.

LENGHT – Half length of the major axis of the shower ellipse. It is related with the longitudinal shower development in the atmosphere.

WIDTH – Half width of the minor axis of the shower ellipse. It provides information on the transversal shower development. As hadronic showers have

a larger transversal momentum with respect to the gamma ones, this parameter is used for discriminating the signal from the background.

CONCn – Fraction of phe contained in the n brightest pixels (n=1,...,7). It contains information about the shower core.

M3LONG – Third image moment along the ellipse major axis. It can help to distinguish which of the two ellipse ends represents the shower head and which one the shower end or tail. It is positive when the shower head is close to the camera center.

M3LONG – It is the third longitudinal image moment, weighted by the third power of the charge contained in each pixel.

ASYM – Vector between the image center of gravity and the brightest pixel. It informs about the asymmetry of the phe distribution along the major axis. It points to the part of the shower corresponding to the maximum development and helps to discriminate between the showers head and tail.

LEAKAGE – Fraction of the signal contained in the outer pixels of the camera. This is a crucial parameter for the reconstruction of the primary particle energy, especially for the highest energies, because it allows to estimate the fraction of the signal which is lost and to reject those images not properly parametrized.

LEAKAGE2 – The fraction of the signal contained in the two outermost pixel rings.

DIST – Distance between the shower COG and a reference point in the camera plane, normally its center. It provides information about the distance of the shower maximum and the impact parameter.

ALPHA – Angle between the major axis of the ellipse and the direction determined by the image COG and a reference point in the camera plane, normally the source position in the camera. ALPHA tells by which angle the main axis of the image misses the reference point. For images induced by primary gammas this parameter is close to zero, because of their preferential direction: on the contrary, hadrons directions are nearly isotropic, so corresponding images are characterized by random distributions in ALPHA. For this reason, this parameter is one of the most powerful tools to perform the signal/background separation.

ALPHAPOW – This parameter is the equivalent of the ALPHA, but with a value spanning from 0 to 180 degrees. It provides information about the head–tail structure of the shower.

7.8 Second run selection

Once Hillas parameters have been calculated for each image, their values allow to tag the image as background–like or gamma–like. Before starting with this procedure, anyway, further quality cuts have still to be applied in order to reject runs for which the analysis has failed. The main reasons to move a run out from the sample are:

- low rate, indicative of problems in the signal extraction or the calibration;
- inhomogeneities in the camera, whose main causes may be trigger macrocells misbehavior, dead pixels, etc. An analysis of the distribution of image COGs along the camera plane can clearly diagnose this problem. For instance, data taken for the starburst galaxy Arp 220 in June 2005 were affected by a problem of this kind (Fig. 7.4). Although the large inefficiency affecting the upper right region of the camera on May the 12^{th} was noticeably cured for the events on June the 7^{th}, some inhomogeneities still remained [74].

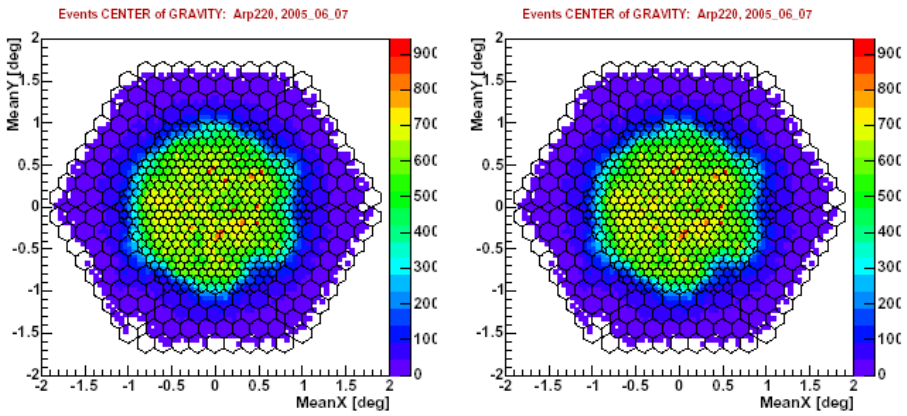

Figure 7.4: COG distribution of the shower images in the camera for the starburst galaxy Arp 220 in June 2005. It is easy to recognize some inefficiencies, especially for the night of May the 12^{th}, as well as the flower shape feature of the trigger macrocells configuration. Figure by [74].

Another case of data taking affected by a problem of this kind concerns the Draco dwarf spheroidal, and will be discussed in Sec. 10.6.

- Bad quality data, showing anomalous Hillas parameters distribution. The comparison can be made both among different data sequences, corresponding to different observation nights, and between the ON and OFF data samples recorded during the same period (ON-OFF compatibility).

- Events associated with sparks in the camera, probably caused by discharges between the PMTs shielding and some other metallic element, easily recognizable by a logarithmic SIZE versus CONC graph [74].

7.8.1 Gamma/hadron separation

This is the very crucial point of the analysis: the images induced by gamma rays emitted by the observed astrophysical source have to be distinguished from those produced by the cosmic background, i.e. hadrons (mainly protons, nuclei of helium and lighter elements), electrons and isolated muons. Among all these particles, hadrons are by far the most important ones because of the very large ratio, 10^4, between their quantity with respect to the expected amount of gamma rays coming from a typical point source.
The basic idea is to select those parameters which strongly depend on the electromagnetic or hadronic nature of the events, and classify them into a scheme allowing a sharp rejection of the background contribution.
In order to determine the features that distinguish the two kinds of events, a sample of pure gamma-ray events is necessary. As previously mentioned, the impossibility of having a controlled flux of known primary particles makes the appeal to MC simulations a need. For training the gamma-hadron separation method, a proper amount of hadron-like data runs is also required. In that case, OFF data are usually treated as an appropriate sample.
Many different methods have been implemented to pursue this purpose:

Static cuts or 'supercuts'. In the $n-$dimensional Hillas space, there exist a number of appropriate parameters which allow a realistic discrimination between gammas and hadrons based on the *shape* (WIDTH and LENGHT) or the *orientation* of the shower (ALPHA). The incoming direction of a particle is a point on the camera that lies on the straight line described by the major axis of the shower image. This means that the gamma–showers point to the position in the camera which corresponds to the expected provenience direction of the photons when the telescope points to the source (in the ON/OFF mode), whereas background showers are randomly oriented

in the camera. Therefore, the ALPHA parameter should peak around ALPHA= 0° for gamma–showers and exibit a uniform ALPHA distribution for background events. Due to its unique discrimination faculty, it is straightforward to produce an ALPHA distribution (the so–called *alpha plot*) with all the events surviving the cuts on the other parameters, and then to tag as gamma–like those events producing the peak at small angles α.

Dynamic cuts. Being the shape of the shower images dependent also on other variables, as the energy of the showers (represented by SIZE), the impact parameter (associated to DIST) and the zenith angle of observation, cuts of dynamical kind can be applied in order to improve the gamma/hadron separation performance.

Random Forest. More recently, a very powerful method was developed to attribute to a single global parameter the faculty of measuring the probability that a set of parameters characterizing an event belongs to a hadronic shower. This parameter, intuitively defined as HADRONNESS, is estimated through one of the more sophisticated classification methods used in high energy physics, that of the *Random Forest* (RF). This separation method is trained with two data samples, each of them belonging to one of the two categories that need to be classified: a sample of pure gamma showers (simulated with MC data) and a sample of hadron showers (taken from OFF real data). A detailed description of this method is given in [74]. We only mention here that this is a multidimensional iterative classification system, where a certain number of image parameters, at least partially independent, is selected for the training so that RF compare the values of the selected parameters for the two data sample. After training, RF is applied to the data adding to each event a new information about its HADRONNESS, which is a real number from 0 to 1. Strictly speaking, if an event has a HADRONNESS 1, then it is considered a hadron–like shower, while HADRONNESS 0 means that we are dealing with a gamma. The HADRONNESS is a monothonic function of the probability for an event of being an hadron, but it is not linear. It is possible, then, to reject the major part of the background events just applying a HADRONNESS cut.
A recent study [198] demonstrates that RF gives comparable results as neural networks in terms of gamma/hadron separation capability, and improved results compared to static and dynamic cuts, particularly at low energies.

7.9 Signal detection

There exist several methods to derive the primary paramters of a shower and complete the analysis chain. In this section we will discuss how to reconstruct the arrival direction and the energy of the primary gamma-ray.

7.9.1 Source position reconstruction

The basic idea is that the source position in the sky can be reconstructed starting from the image parameters. In its standard ON/OFF operation mode, the IACT directly points to the source under consideration, and if the source is point-like, it is assumed that its position coincides with the camera center. This means that to reconstruct the source position it is sufficient to check for a possible mispointing of the telescope and tracking precision, and in case to correct it. Thanks to the *Starguider System*, the pointing of the telescope is computed with a precision better than 0.01° from the position of the many stars in the FOV of the CCD camera [166].
At this point, the analysis is performed in terms of an ALPHA plot with respect to the center of the camera. In this case, the DIST parameter, i.e. the distance between the image COG and the camera center, is also the true distance between the image COG and the source position in the camera. This standard analysis, based on the ALPHA parameter, may be used also for very well known point-like sources observed in the Wobble mode, but is in general a very bad task when studying signals emitted from extended objects, as Galactic SNRs, DM searches, or sources whose position is not known, as for UES or GRBs. Another situation when a source independent analysis is needed is the search of new sources in the camera FOV, as when doing a sky survey, or the treatment of the signal coming from a new discovered object, a very lucky and good omen task!
In order to deal with these tricky situations, methods for position reconstruction based on source independent parameters have been developed, as discussed in the next section.

In the following of this Thesis, we will discuss two different analysis, a test oriented one we have performed on a Crab Nebula sample, and the study of the Unidentified EGRET Source $3EG\_J1835+5918$ carried out by the Padova working group. In each case, both a source dependent and a source independent analysis have been performed, being in any case the ALPHA-based study an useful chance of understanding and comparison.

7.10 The DISP method

The DISP method has been developed by the MAGIC Collaboration taking note of its successful application to the WHIPPLE experiment, motivating a great interest into its improvement and adapting to our telescope. A very important and crucial role in that sense has been carried out by the Barcelona working group.
In this framework, the source position is assumed to lie on the major axis of the shower ellipse that parametrizes the shower image in the camera and, by definition, the DISP is defined as the distance between the *unknown* source position and the image COG. For point-like sources, the DISP parameter is expected to be nearly proportional to the DIST one. In 1994, Fomin et al. proposed the following way to estimate the DISP:

$$\mathrm{DISP} = \zeta \left(1 - \frac{\mathrm{WIDTH}}{\mathrm{LENGHT}}\right), \tag{7.3}$$

where ζ is a parameter dependent on the telescope performances and the image SIZE and has to be determined from MC simulation of electromagnetic showers.
The basic idea is that shower images which are closer to the source position in the camera, and therefore have WIDTH/LENGHT (*elongation*) values near to 1, have a DISP value lower than showers which are further away from the camera position. In other words, low-value DISP showers are more roundish, whereas high-value DISP showers are elliptical (see Fig. 7.5). As it is clearly visible on the right side of the

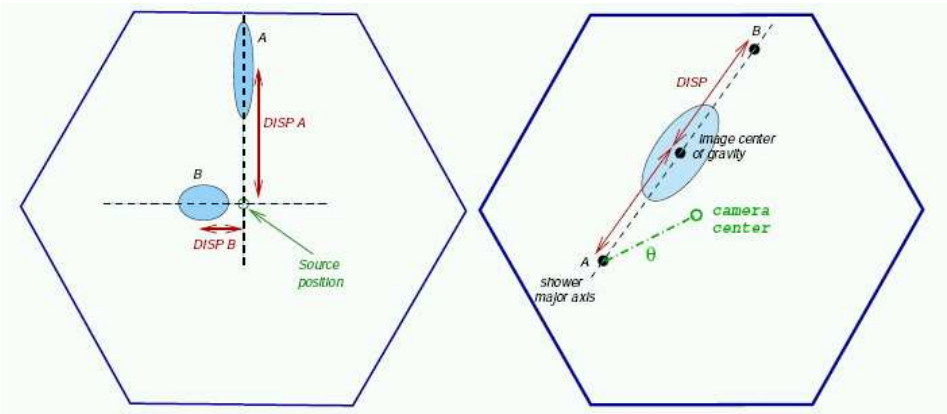

Figure 7.5: Schematic representation of two images with the same estimated source position, but with different DISP values. The angle θ is also shown, being A the correct source position. Figure by [160].

picture, two possible source position solutions along the shower major axis are possible. As already mentioned, images in the camera contain information about the

longitudinal development of the shower in the atmosphere. Čerenkov photons from the upper part of the shower create a narrower section of the image with a higher photon density (*head*), while photons from the shower tail normally generate a much more fussy and spread image end (*tail*). Therefore, asymmetries in the charge distribution of the images can indicate to which image edge the source position is closer. The choice between the two ones may be made by using another Hillas parameter as a discriminator, commonly the ASYM (very suitable for high energy showers) or the M3LONG.

In the framework of source position indipendent analysis, an other parameter may be of help when evaluating the excess detection, alternatively to the ALPHA approach. In the so-called THETA-SQUARED approach, the angle θ is the distance between the nominal and the reconstructed source position, in other words from the camera center to the DISP-reconstructed position (Fig. 7.5). Arguing from geometrical considerations that the square of the θ angle is proportional to the number of backgroung events, the differential distribution of the number of events may be plotted againt θ^2 ($\theta^2 - plot$).

Finally, the result of the DISP analysis may be plotted on a bidimensional map, the so-called *skymap-plot* (see Fig. 8.7 and 8.8 of the next chapter). In this map, what is of great interest is the distribution of the excess events, i.e. whose obtained subtracting normalized OFF from ON ones, after a HADRONNESS cut. We point out that, for the reasons previously discussed in this section, *two HADRONNESS estimations* have to be made, and different results to be used for source position dependent and independent analysis respectively. Results from DISP analysis have been used to compare the angular resolution of the telescope with that reached with other methods, demonstrating a very remarkable and promising improvement [74].

7.10.1 Energy estimation

At a first appoximation, the number of photoelectrons can be considered proportional to the energy of the shower, so that the Hillas paramter SIZE may be used for a first rough estimation of the shower energy. Anyway, many other parameters have to be considered for a more precise estimation of the energy. Among them, the shower *Impact Parameter* (IP), i.e. the distance between the shower axis and the detection point, as well as the zenith angle of observation, play a role of primary plane. For instance, if showers incide with large zenith angles, they distribute on a larger area, and the resulting photon energy decreases.
In standard MAGIC analysis, the energy reconstruction is performed by training the

Random Forest on a set of selected paramters, whose information content is related to the primary particle energy.

7.11 Signal evaluation

Let us enter now into the final steps of the analysis chain. The probability that the excess count rate is due to the real photons emitted from the gamma-ray source, rather than to background fluctuation, is the most important information we need at this stage.

7.11.1 Significance calculation

In the standard Hillas analysis and after that cuts in HADRONNESS have been applied, from α and θ^2 plots for ON and OFF data it is possible to derive the **excess**:

$$N_{exc} = N_{ON} - \beta\, N_{OFF}, \tag{7.4}$$

where the OFF data are supposed to have been correctly normalized to the ON ones and β is the normalization factor. If the source under observation is bright enough, positive values of the excess appear at low ALPHA values. The signal region corresponds to ALPHA values below the predefined ALPHA cut and the background region to the remaining ALPHA values.
Different methods have been developed by the many experimental collaborations to estimate the statistical significance of the signal. Among them, one of the most commonly used is that due to Li & Ma, who in 1983 performed an historical work which demonstrates that many of the previous procedures gave an overestimate of the significance [126]. As a conclusion, they proposed the following formula, also adopted in the MAGIC standard analysis chain:

$$N_\sigma = \sqrt{2}\left\{ N_{ON}\, ln\Big[\frac{1+\alpha}{\alpha}\Big(\frac{N_{ON}}{N_{ON}+N_{OFF}}\Big)\Big] + ln\Big[(1+\alpha)\Big(\frac{N_{OFF}}{N_{ON}+N_{OFF}}\Big)\Big]\right\}^{1/2}. \tag{7.5}$$

The best strategy is then to estimate the significance for a well-known source, so that optimal HADRONNESS cuts may be selected, and apply them to the analysis of the unknown source under investigation.
It is a general prescription in gamma-ray astronomy to accept as 'detected' those sources which exibit a significance greater than 5.

7.12 Flux sensitivity

The sensitivity of an IACT is defined as the gamma-ray flux that a source should emit in a given range of energies (or above a given energy for an integral flux sensitivity), to achieve a 5 sigma detection in 50 hours of observation, and is given by the following expression (in per cent) [74]:

$$S = \frac{1}{2\,N_{exc}}\left[\frac{T_{obs}(\mathrm{h})}{2} + \sqrt{\frac{T_{obs}(\mathrm{h})^2}{4} + 2\,T_{obs}(\mathrm{h})\,(1+\beta)\,\beta\,\mathrm{N_{OFF}}}\right] \times 100, \tag{7.6}$$

while its error is:

$$\Delta\,S = \sqrt{\frac{(S/100)^2}{N_{exc}} + \frac{T_{obs}(\mathrm{h})^2\,(1+\beta)^2\,\beta^2\,\mathrm{N_{OFF}}}{4\,N_{exc}^2\left[\frac{T_{obs}(\mathrm{h})^2}{4} + 2\,T_{obs}(\mathrm{h})\,(1+\beta)\,\beta\,\mathrm{N_{OFF}}\right]}} \times 100, \tag{7.7}$$

where T_{obs} is the observation time for ON (and OFF) data taking.

7.13 Upper limits

If an unwanted feature of the source under investigation is the total absence of a signal, as it occurred for the source discussed in Chapter 9, it is at least desirable to establish an upper limit (U.L.) to the flux emitted by the source. A way to compute the upper limit appeals to the sensitivity of a standard candle previously analyzed. Following [74], the 5σ U.L., i.e. the upper limit with a confidence level (C.L.) of 99.9999 % for the flux emitted from a source during T_{obs} hours, is given by:

$$F_{\mathrm{u.l.}\,|5\,\sigma} = \sqrt{\frac{50}{T_{obs}(\mathrm{h})}}, \tag{7.8}$$

where $F_{\mathrm{u.l.}\,|5\,\sigma}$ is expressed in Crab Units, i.e. in units of per cent of the flux of the Crab Nebula. It may occur that the U.L. is relaxed, requiring only a C.L. of 95.45%:

$$F_{\mathrm{u.l.}\,|2\,\sigma} = \frac{2}{5}\,F_{\mathrm{u.l.}\,|5\,\sigma}. \tag{7.9}$$

To convert the estimated upper limits at a given energy into flux units, we may use the differential Crab spectrum extracted by MAGIC data from 2004 and 2005 [132]:

$$\frac{dF}{dE} = (1.50 \pm 0.18)\cdot 10^{-3}\frac{E}{\mathrm{GeV}}^{-2.58\pm0.16}\ \mathrm{ph\ cm^{-1}\ s^{-1}\ TeV^{-1}}. \tag{7.10}$$

Part III

Possible Observations of Galactic DM Sources with MAGIC

Chapter 8

Evaluating the MAGIC Sensitivity with Crab

This chapter contains results for the data analysis of a MAGIC data sample of the Crab Nebula, with the aim to test the analysis chain and performances before its application to an unknown source.

8.1 Introduction

In VHE experiments, the Crab Nebula is usually treated as a 'standard candle'. Actually, up to now there does not exist any indication of variability in the flux of gamma-rays from this source above a few hundred GeV up to several tens of TeV. This makes the Crab an excellent candidate to understand and carefully test telescope performances. In the present study, we perform the analysis of more than two hours sample of data ON and OFF for the Crab Nebula, collected in January 2005. As a result, the selected sample allow a satisfactory measure of the Crab flux at energies from 100 GeV up to 1 TeV. In the present study, we refer to errors as purely statistic, unless differently specified.

8.2 Definition of the data sample

The main features of the sample of data used in the present analysis are summerized in Tab. (8.1). For the ON sequence, the 2.5 hours of data have been registered during the night between 3 and 4 January 2005, while the 2.6 hours of OFF data refer to the night between 7 and 8 January 2005.
The first step of the analysis has been the check of the compatibility beween ON and OFF data. In order to perform that, some testing parameters have been chosen:

Crab Nebula Data Sample

sequence type	number	Zd mean [°]	data rate [Hz]	Ped RMS	PSF [mm]	Inhomogeneity
ON – Crab	46693	14	180	1.14	19	8.7
OFF – Crab	47403	16	173	1.15	18.3	8.9
ON/OFF ratio	–	0.875	1.04	0.99	1.03	0.97

Table 8.1: Testing parameters for the ON and OFF Crab Nebula data samples used in the preliminary analysis.

- the zenith angle of observation (Zd);
- the event rate;
- the pedestal RMS, containig informations about the FOV of the telescope;
- the reflector point spread function (PSF);
- the inhomogeneity parameter.

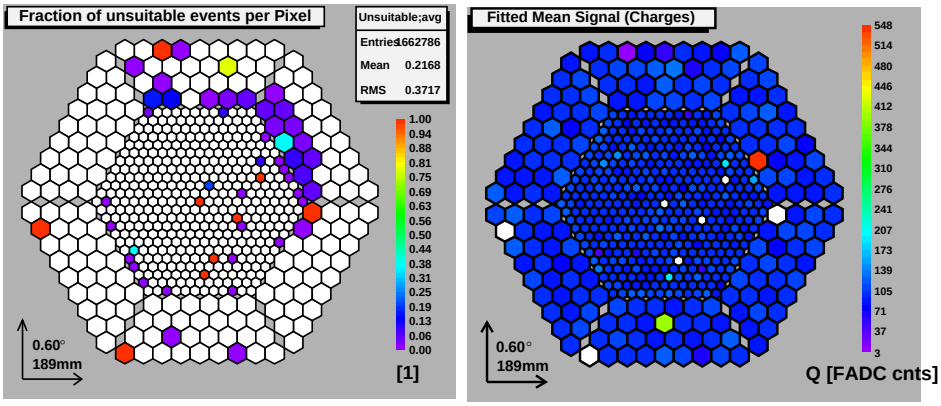

Figure 8.1: *Left side:* pixels not suited for further analysis of the selected data sample for the Crab Nebula. *Right side:* mean charge for each pixel as reconstructed by the extractor.

8.3 Extraction and Calibration of the Signal

As during the Period 25, when all the data have been taken, the camera was affected by some problems of synchronization between the FADCs and the trigger, in calibrating data we used the *spline extractor*. Additionally, some care has been

taken in the selection of the MC data in order to be tuned with the actual spot of the telescope. After the calibration procedure, some pixels have been considered bad and rejected, as it is possible to see in the left side of Fig. 8.1 (see also Fig. 7.1), while the right side of the same plot shows the mean charge for each pixel as reconstructed by the extractor.

8.4 Image cleaning

At this stage we have rejected all the pixels lighted by NSB. We set a level of 10 photoelectrons for the core pixels, and 5 for the external ones (*Absolute 10:5*). The results of the image cleaning are presented in Fig. 8.2.

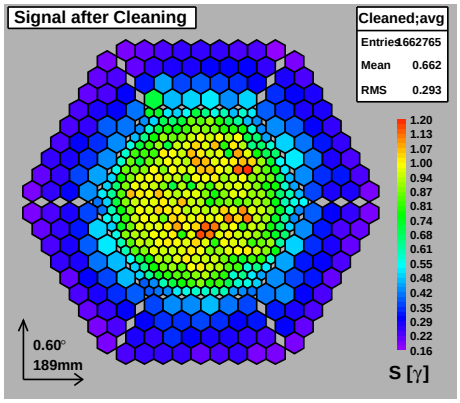

Figure 8.2: Signal after cleaning.

As a result of this step, only 76%, 74% and 70% of the events survived for the ON, OFF and MC data respectively.

Current versions of `Mars` allow an authomatic correction of all the systematic effects seriously compromising the image parametrization. As our data were quite old, however, we did not set these prescriptions in the cleaning program. Additionally, both the ON and the OFF data of our sample were in culmination. From the comparison between the ON and OFF rates after cleaning, we saw that there were an anoumalous run, which had to be moved out by hand (Fig. 8.3).

8.5 Image parametrization

The image parameters were then calculated from the cleaned data. In Fig. 8.4 we show the distributions of two interesting parameters for the ON and OFF samples

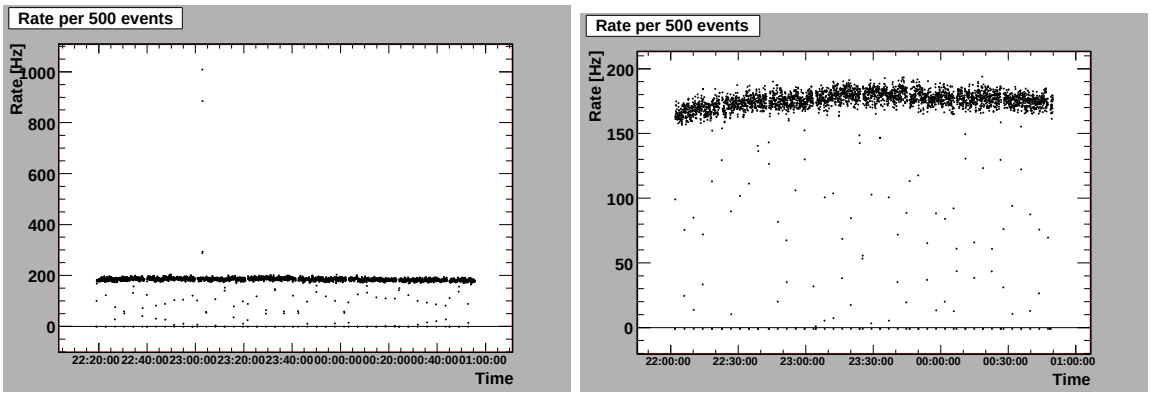

Figure 8.3: Plots of rate versus time for the ON and OFF data. The ON run 46693 has been moved out by hand.

respectively. As we can see, the distributions for the two kinds of data are similar, as aspected because of the very small signal to noise ratio.

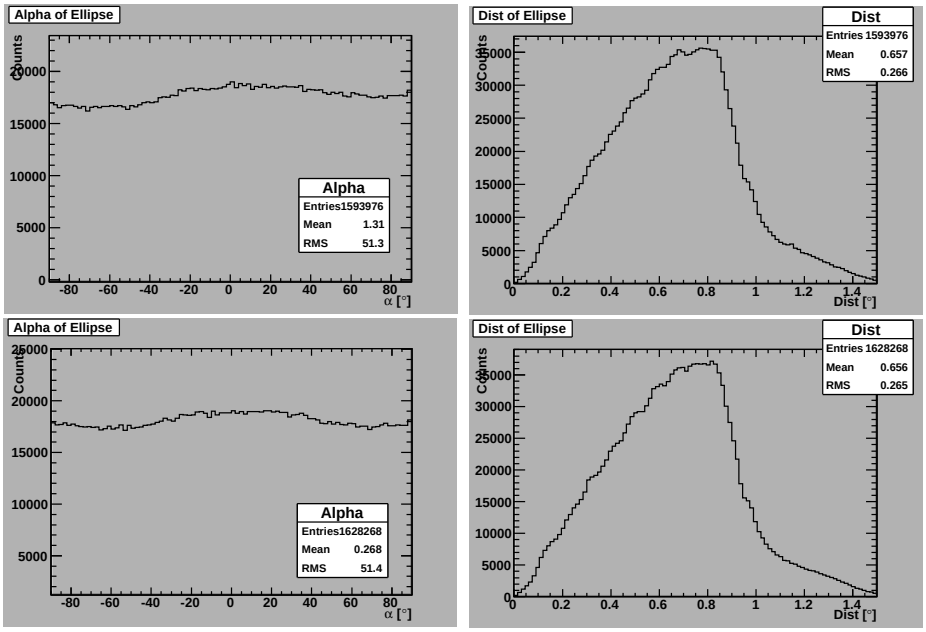

Figure 8.4: α and *dist* distributions for the ON and OFF data.

8.6 Hadronness calculation

For the calculation of the HADRONNESS parameter, very important for the gamma/hadron separation, the Random Forest method was applied. For the training

phase, a sample of gamma–like and one of hadron–like events is needed, together with a set of image parameters, as discussed in the previos chapter. The gamma events selected were a subsample of the MC data, while the hadrons were a subsample of the ON data. The reason why it were used the ON data instead the OFF data for the hadronic subsample is that in this way the hadronness is optimized, in order to recognize the hadronic showers in the ON data sequence, that is our main goal. The number of gamma events is, at this stage, negligible respect to the total number of events of the sequence, so also the error committed is negligible. The parameters chosen for the training are:

- SIZE
- WIDTH
- LENGTH
- CONC
- CONC7
- M3LONG

After the training, RF was applied to the ON, to the OFF and to the sample of MC data not used for the training, and each event was enriched with the parameter HADRONNESS.

8.7 Detection of the signal

Source independent analysis: the α–plot.
As already mentioned, the α–plot allow the claim for detection of the source, if the significance of the signal after cuts is higher than 5 σ. The Crab Nebula is a well established source, and at least 15σ/hour of significance above 100 GeV is expected, in order to demonstrate the correctness of the analysis chain. The upper part of Fig. 8.5 shows the α–plot in the energy bin [120–300], and for an applied HADRONNESS cut at 0.1.

Source independent analysis: the θ^2–plot.
It is interesting to investigate the shape of the shower independently on its shape and orientation in the camera. Fig. 8.6 shows results for this kind of analysis.

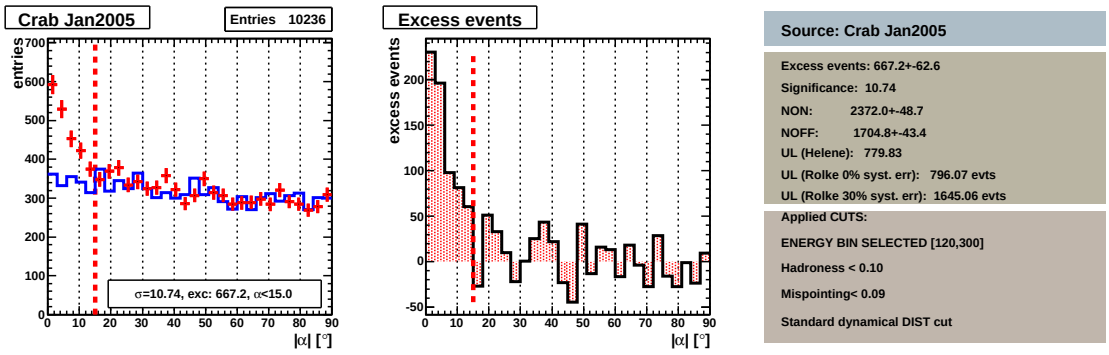

Figure 8.5: α–plot in the energy bin [120–300], and with the HADRONNESS cut at 0.1, for the ON and OFF data samples in analysis.

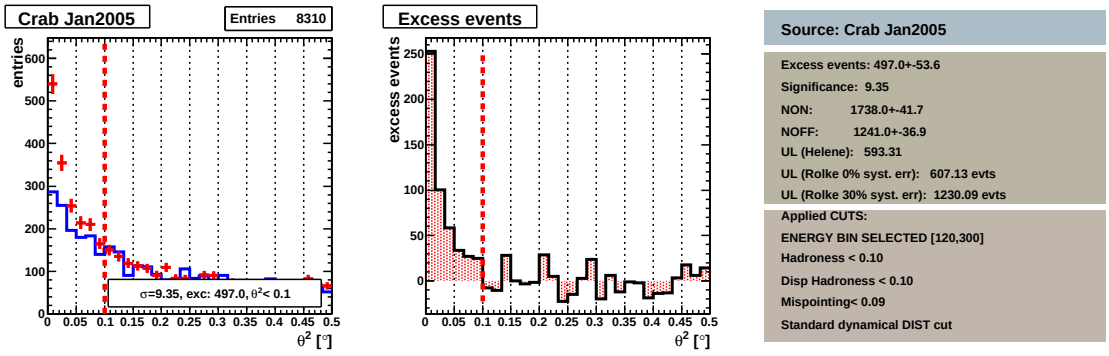

Figure 8.6: θ–plot in the energy bin [120–300], and with the HADRONNESS cut at 0.1, for the ON and OFF data samples in analysis.

8.8 Sky Map of the Crab Nebula region

For the sky map projection, a dedicated RF training was done with the following source independent parameters:

- SIZE
- WIDTH
- LENGTH
- CONC
- CONC7

The number of excess events detected (after a HADRONNESS cut of 0.2 and with the discriminator parameter M3LONGPOW3) as a function of the incoming direction

is drawn in Fig. 8.7 and 8.8. The emission is peaked at the center of the map, where the telescope pointed, which is the same galactic position related to the Crab Nebula TeV emission detected by other experiments. This also means that this step of the was correctly performed.

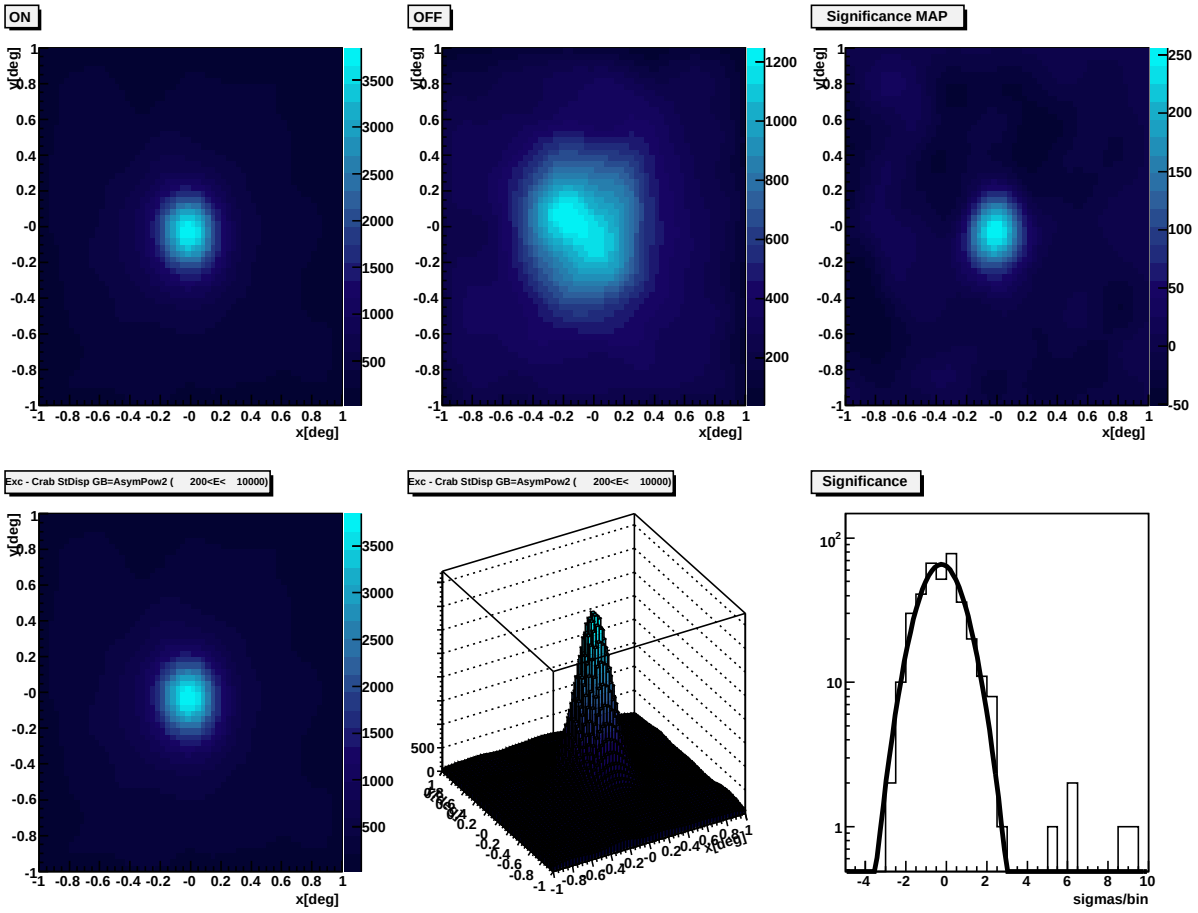

Figure 8.7: Skymap in energy bin.

8.9 Energy reconstruction and flux estimation

The energy reconstruction was performed with a subsample of MC data, trained by RF with the following parameters:

- SIZE
- DIST
- WIDTH

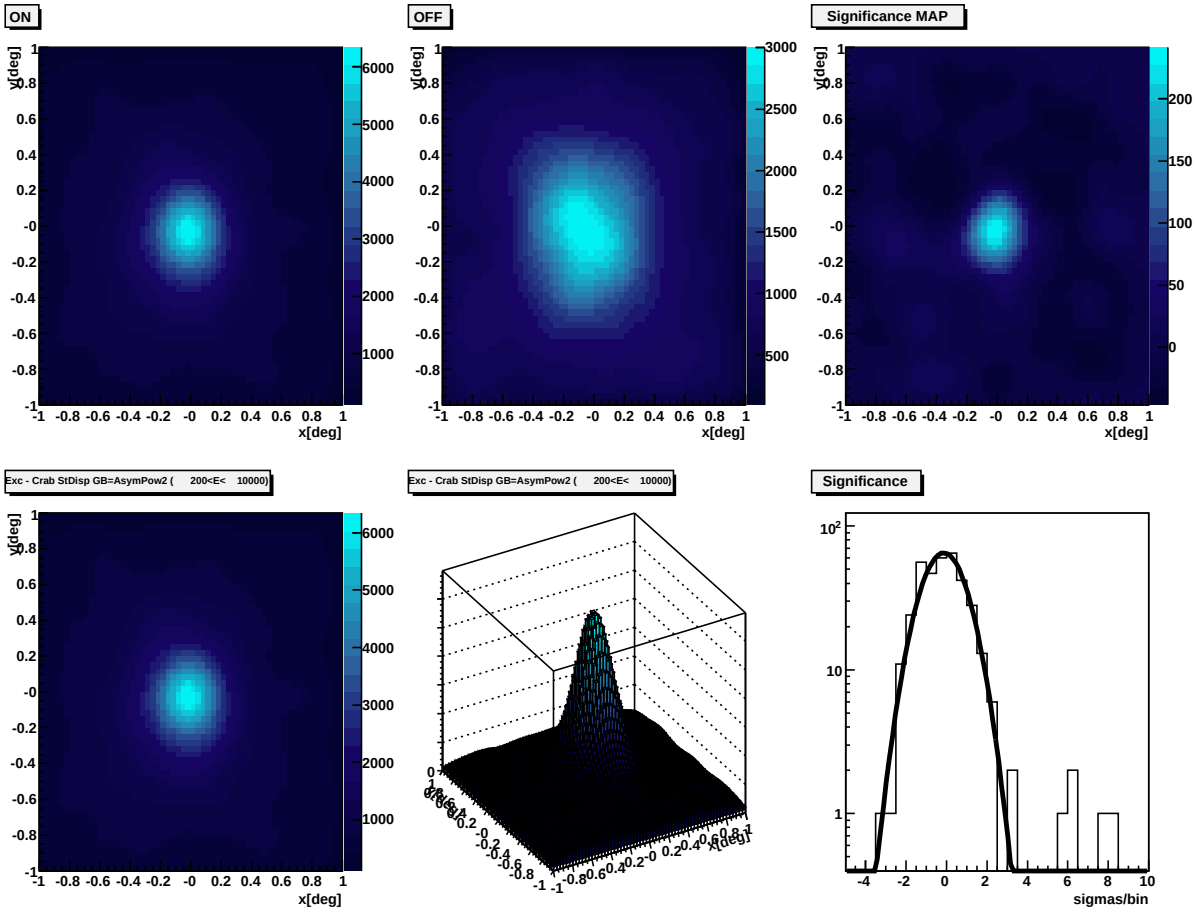

Figure 8.8: Skymap in bin of size.

- LENGTH
- CONC
- CONC7
- LEAKAGE
- ZENITH ANGLE
- ENERGY

For the flux evaluation, we divided samples into 11 energy bins and applied dedicated cuts in HADRONNESS and ALPHA, in order to calculate the effective area and the excess for each bin. The former values were calculated from MC data, the latter

from the ALPHA distributions, after the ON/OFF normalization. An HADRONNESS cut of 0.9 was deduced from the HADRONNESS versus estimated energy mean distribution of the MC subsample. The ALPHA distribution for each energy bin is reported in Fig. 8.9, while the distribution of the excess events detected from the α–plots is drawn in Fig. 8.9. The effective area distribution, in Fig. 8.9, exibits a quite low value at low energies ($\sim$ 100 GeV), which rapidly increases reaching a value of 10^5 m^2 at energies around 300 GeV.

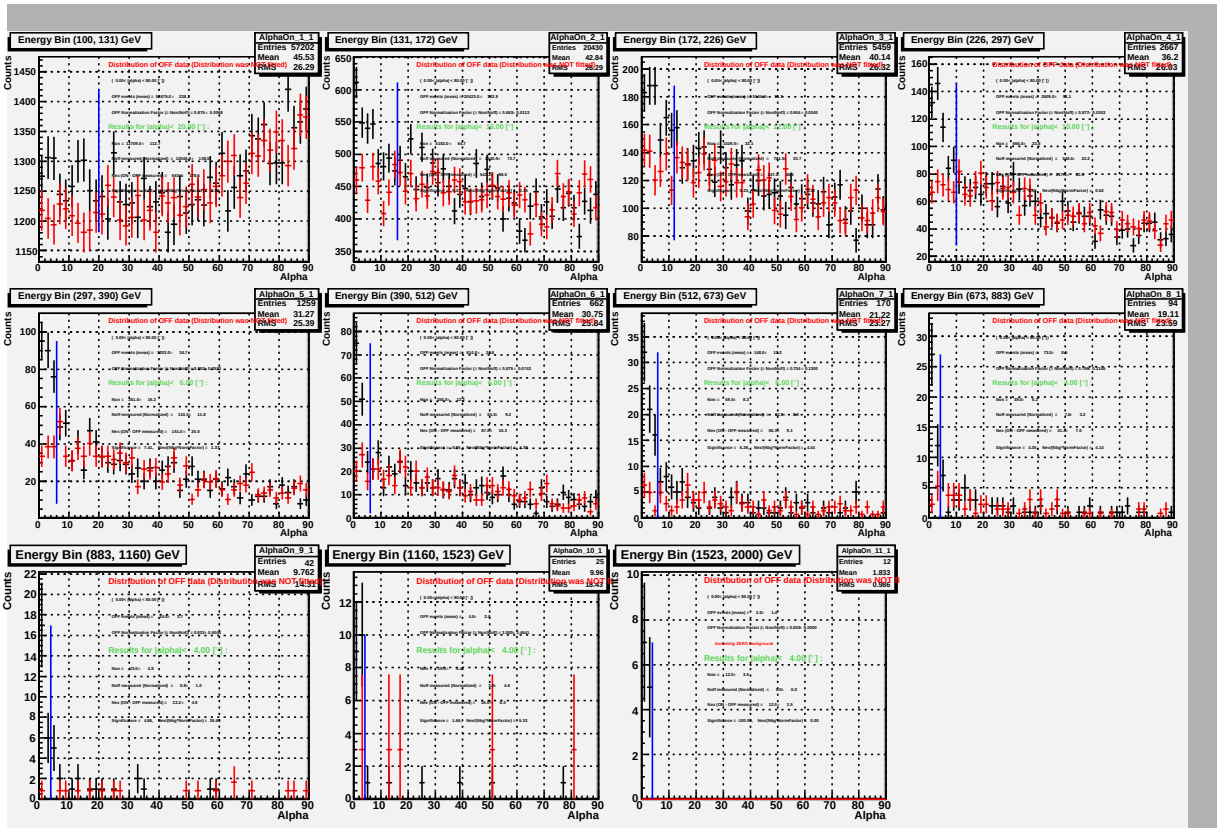

Figure 8.9: ALPHA distributions for selected energy bins for the estimation of the flux from the Crab Nebula.

Fig. 8.9 shows the differential spectrum obtained for the Crab Nebula. The data points are fitted by a power law function:

$$\frac{dN}{dE} = (2.48 \pm 0.42_{stat} \cdot e^{-11}) \Big(\frac{E}{\mathrm{TeV}} \Big)^{-2.59 \pm 0.14_{stat}} \ \mathrm{ph\,cm^{-2}\,s^{-1}\,TeV^{-1}}. \qquad (8.1)$$

This results satisfactory matches, within the errors, with the spectral parameters obtained from other measurements of the Crab spectrum [133, 132].

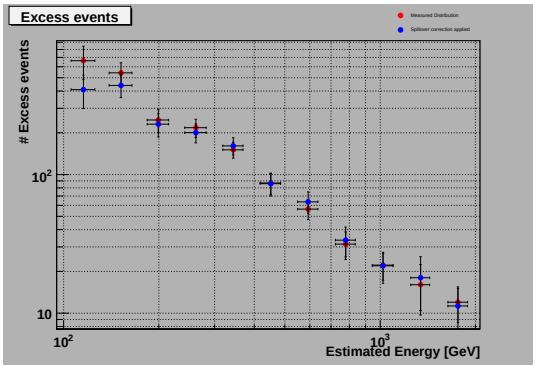

Figure 8.10: Distribution of the excess events calculated from the α–plots.

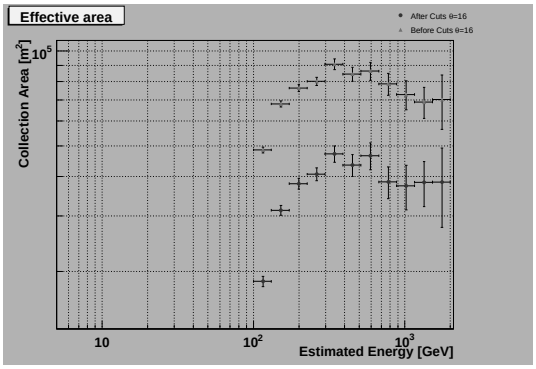

Figure 8.11: Effective area.

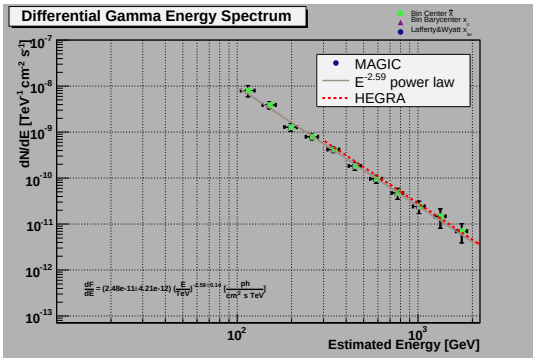

Figure 8.12: Differential spectrum of the Crab Nebula. The data points can be fitted with a power low.

8.10 Conclusions from the test analysis

After having tested the analysis chain and performances of the telescope on a selected data sample of the Crab Nebula, obtained results allow to draw the following

considerations:

1) our sample exibits a significance in good agreement with previous MAGIC results;

2) the sky map projection confirms the coordinates of the source;

3) the differential flux can be fitted with a power law whose parameters are, within the errors, in agreement with previous estimations;

4) the energy interval accessible within the reach of this analysis ranges from 100 GeV to 1 TeV,

making us confident that all the selection of both OFF and MC samples, as well as the extraction of the signal with the Spline method and the selected 7:5 cleaning, the choice of the parameters for the RF training and the applied final cuts are very consistent and give satisfactory results at energies between 100 GeV and 1 TeV.

Chapter 9

Search for Very High Energy Gamma-Rays from the Unidentified EGRET Source 3EG_J1835+5918

This chapter contains a review of the main results of the preliminary data analysis of the Unidentified EGRET Source 3EG_J1835+5918, carried out by the Padova MAGIC working group. This source has been selected as the best target for observation of gamma rays from DM annihilation inside mini-spikes near Intermediate Mass Black Holes (IMBH) [38]. Nevertheless, being this source also one of the main subjects of this Thesis, it has been very interesting and fair to come into discussions with the analyzers and to understand the main steps of the analysis. Unfortunately, in the period of the data taking the telescope was suffering for great instabilities due to important modifications in the hardware setup, with very bad effects on the data quality. Nevertheless, a standard analysis of the source has been possible, and led to physically reasonable results.

9.1 The observational proposal

In spring 2006, the MAGIC Dark Matter Working Group (DMWG) required to partecipate to a proposal of observation for Unidentified EGRET Sources (UES). After a preliminary selection of candidates based on the same criteria outlined in Chapter 5, it was recognized that the UES 3EG_J1835+5918 was representing the best target to search a signal from neutralino annihilation. However, any of the selected sources would constitute a potential candidate for detection.
As a preliminary step, people asked which was the expected flux in the MAGIC en-

ergetic regime. Althought the DM annihilation gamma-ray spectrum features differently in different ranges, the extrapolation of the measured EGRET fluxes to MAGIC energies may be of some help. Fig. 9.1 shows results obtained for the whole sample of proposed sources. In the upper plot, extrapolation is performed by mean of the spectral index, as supplied by the 3EG Catalog [103]; in the lower part of the picture, we show more accurate calculations, including the exponential cut-off at the neutralino mass in the representative cases of $m_\chi = 400$ GeV and $m_\chi = 1.5$ TeV. As one can see from that plot, assuming a mass of 1.5 TeV all sources should become visible within 20 hours. Note however that the integral EGRET fluxes are affected by considerable errors (30%).

9.2 Introduction to the analysis

The analysis was done in the environment of `Mars V0-13-1` compiled with `root 5.12f`. The following steps have been followed:

- data were downloaded already standard-calibrated (Digital Filter extractor), apart from a small data subsample downloaded as `.iso` files;

- the need of pushing the analysis to the lowest energies moved analyzers not to stick with the standard MAGIC cleaning method (*absolute 10-5*), and try two different configurations:

  Absolute 7-5. Each core pixel must have more than 7 phes, so that all pixels with more than 4 phes close to them contribute to the shower. In the following of this dissertation, this method will be called the *cleanabs* method.

  Time and relative cleaning. The selection between core and neighbor pixels does not refer to the absolute number of phes, but to the relative charge signal to an average pedestal signal for that pixel. The method will be recalled as the *cleantime* method.

- When calculating the Random Forest matrices for the image and energy reconstruction, the program has been run sequence by sequence, both to take into account the spread in zenith angle and the fact that different sequences taken in different days could have different features in the problematic observation period. At the same time, the DISP parameter has been estimated using a source-dependent analysis.

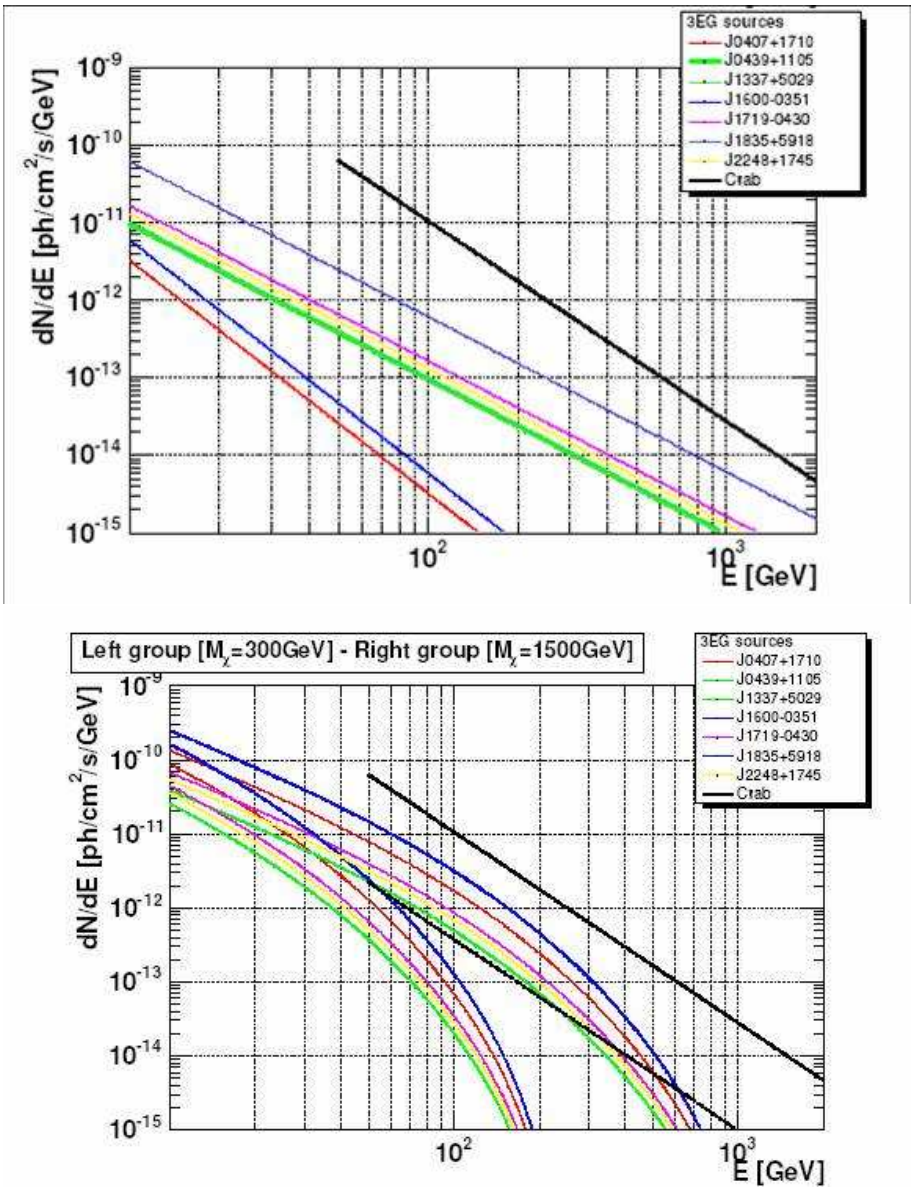

Figure 9.1: *Upper panel:* Extrapolation of proposed Unidentified EGRET Sources, spectral index as given in the 3EG [103]. *Lower panel:* Same spectra as above, calculated by mean of a spectral index of -1.5 and an exponential cut-off for two different DM mass values. The Crab differential flux is also shown for comparison (black line), while the dotted line indicates the 1/20 Crab flux, corresponding to an ideal source that, according to MAGIC integral sensitivity, can be observed in 10 hours with 3σ significance. (Courtesy of the MAGIC Collab.).

9.3 Data Sample

The entire data sample is reported in Table 9.1.

Data have been subsequently grouped into sequences according to zenith angle,

	ON	OFF
2006/06/22	93871-93916	
2006/06/24	94104-94124	
2006/06/25	94245-94272	
2006/06/26	94391-94421	
2006/06/27		94519-94550
2006/06/28	94591-94680	94578-94588
2006/06/29	94707-94800**	
2006/06/30	94829-94915*	
2006/07/01	94953-95027	
2006/07/02	95109-95140	95068-95106*
2006/07/03	94150-95220	95179-95203*

Table 9.1: Initial data sample of the source 3EG_J1835+5918, collected between June and July 2006. (*) Data initially not transferred at PIC and only subsequently downloaded as `.iso` files. (**) Data partially missing and found at a second stage. (Courtesy of the MAGIC Collab.).

in order to have a homogeneous sample. Table 9.3 shows these sequences. The zenith angle of the data through the night of observation can be also seen in Figure 9.2. The conversion between zenith angles and zenith bins is reported in Table 9.2.

Zenith angles	Zenith bin (zbin)
29.0–36.4	13–19
32.3–40.1	16–23
40.1–44.4	24–28
40.1–47.6	24–32

Table 9.2: Conversion between zenith angles and zbins. (Courtesy of the MAGIC Collab.).

9.4 Data Check

Data were downloaded already calibrated with standard digital filter extractor. Only in the case of the missing data (*) in Table 9.1, data have been downloaded in `.raw` format and calibrated with the digital filter yet. For each sequence, a first quality check have been manually performed. A data check is always preferable before starting an analysis. With this aim, people observed that:

- some files showed huge bumps in the rate and had to be rejected without further checks;

		ON		OFF	
Zbin	Date	Runs	Eff.Time [h]	Runs	Eff.Time [h]
13–19	2006/06/22	93871-93916	2.35		
	2006/06/29	94722-94775	3.00		
	2006/06/30	94829-94894	3.76		
	2006/07/01	94954-95005	2.81		
	2006/07/02			95068-95106	1.97
	2006/07/03	95150-95176	1.35		
Total			**13.27**		**1.97**
16–23	2006/06/24	94104-94124	1.04		
	2006/06/25	94245-94260	0.74		
	2006/06/26	94391-94410	1.08		
	2006/06/27			94519-94542	1.20
	2006/06/28	94591-94620	1.63	94578-94588	0.06
		94623-94669	2.68		
	2006/06/29	94707-94721	0.79		
		94776-94789	0.85		
	2006/06/30	94895-94902	0.52		
	2006/07/01	95006-95016	0.76		
	2006/07/02	95109-95130	1.00		
	2006/07/03			95179-95191	0.66
Total			**11.09**		**1.92**
24–28	2006/06/25	94260-94272	0.47		
	2006/06/26	94410-94421	0.67		
	2006/06/27			94543-94550	0.86
	2006/06/28	94670-94680	0.72		
	2006/07/03			95192-95203	0.61
Total			**1.86**		**1.47**
24–32	2006/06/29	94790-94800	0.62		
	2006/06/30	94903-94914	0.81		
	2006/07/01	95017-95027	0.67		
	2006/07/02	95133-95140	0.50		
	2006/07/03	95206-95220	0.74		
Total			**3.34**		**-**
Total			**29.56**		**5.36**

Table 9.3: Sequences of ON and OFF data ordered and grouped according to zenith angles and date. (Courtesy of the MAGIC Collab.).

- the plot showing the rejected/unsuitable pixels had to be checked and a certain number of unreliable pixels to be ruled out.

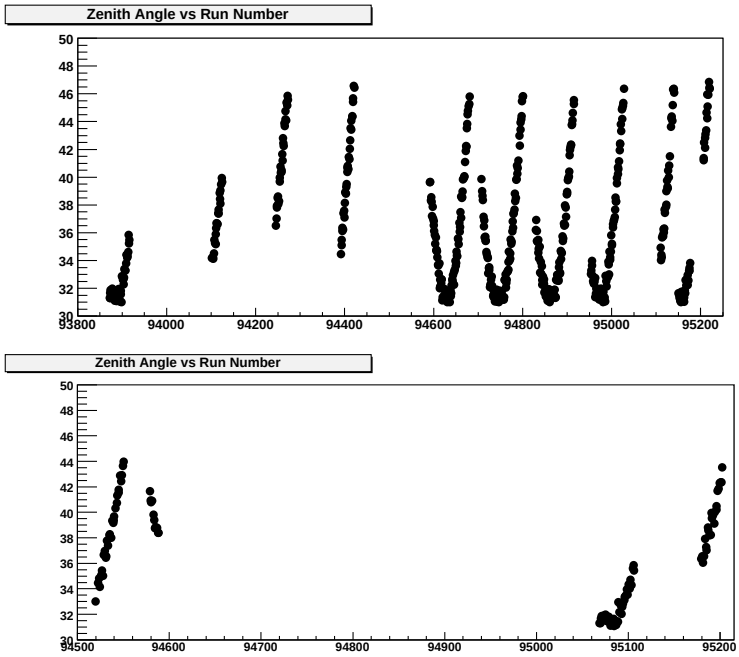

Figure 9.2: The zenith angle of the data vs run number for ON and OFF data. (Courtesy of the MAGIC Collab.).

9.4.1 Run Selection

A first result of the mentioned checks allowed a run by run selection. As a result, a certain number of files has been rejected, as shown in Table 9.4.

9.4.2 Bad Pixels

As a second result, *bad pixels* was individuated, recovering their charge content by interpolation of the adjacent ones. Results on bad pixels are shown in Table 9.5. After the image cleaning, for each sequence, analyzers considered the task of doing a manual check an important step, in order to ensure that the used runs were suitable for the analysis. This decision has been above all justified by the many hardware problems MAGIC was suffering in the data taking period.

9.4.3 Strong camera inhomogeneity

In Fig. 9.3 one can see the distribution over the camera COG of the triggering ellipses. In a normal operating situation, the distribution is expected to be almost flat in the variable PHI, i.e., in the angle between the COG and a chosen axis. A perfect flatness is undoubtly unreachable, due to the finite acceptance of the camera

Sequence	Rejected Runs	Percentage
93871–93916	93874, 93876	2/46
94104–94124	-	0/21
94245–94260	94251, 94258	2/16
94260–94272	-	0/8
94391–94410	94407-09	3/20
94410–94421	94420	1/12
94519–94542	94519,94520,94521	3/25
94543–94550	94546-7	2/8
94578–94588	-	0/11
94591–94620	-	0/29
94623–94669	94634,94641,94650,95657	4/47
94670–94680	-	0/10
94707–94721	-	0/16
94722–94775	-	0/54
94776–94789	-	0/14
94790–94800	-	0/11
94829–94894	-	0/66
94895–94902	-	0/8
94903–94915	-	0/13
94954–95005	-	0/46
95006–95016	-	0/11
95017–95027	-	0/11
95068–95106	-	0/38
95109–95130	95114,95120-21,95126,95129,95130	6/22
95133–95140	-	0/8
95150–95176	-	0/17
95179–95191	-	0/13
95192–95203	-	0/12
95206–95220	95213	1/15
	Total	21/628 (3%)

Table 9.4: Rejected runs. (Courtesy of the MAGIC Collab.).

trigger region which has a non-round shape, as one can see in Fig. 9.4. Nevertheless, strong inhomogeneities are visible in two regions in the upper part of the camera. These parts correspond to two units (cells) in the trigger hardware pattern, well recognizable in the mentioned figure.

The reason for this inhomogeneities must be connected with the installation of the new *MuX* readout system, and in particular with the related installation of a signal splitter just before the FADCs line doubling. Due to a still unclear overheating, a certain number of cells in the trigger configuration fused, so that a high number of pixels lost the capability to provide a trigger signal. This fact does not mean that

Sequence	Bad pixels (calib)
93870	65,458,509,514,537
94103	65,458,509,537
94244	65,297,458,509,514,537
94390	457,458,509,514,537
94518	23,65,509,514,537
94577	65,458,509,514,537 (48,69,206,249,291)
94590	65,458,509,510,514,537
94622	48,65,69,206,291,458,509,510,514,537
94952	65,509,514
95108	65,509,514
95132	65,503,505,509,514
95149	65,69,297,503,505,509,537
95205	19,65,69,503,505,509,514,522,537

Table 9.5: Results on bad pixels. (Courtesy of the MAGIC Collab.).

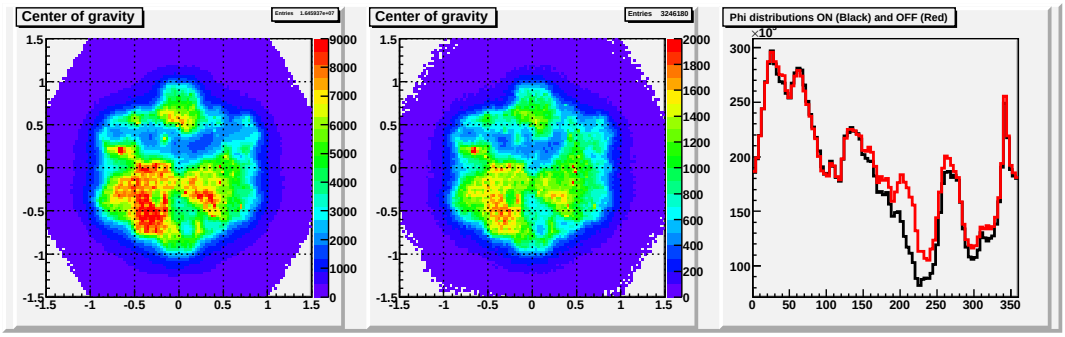

Figure 9.3: Distribution of the ellipse COGs in the camera for a sample run of 3EG_J1835+5918. (Courtesy of the MAGIC Collab.).

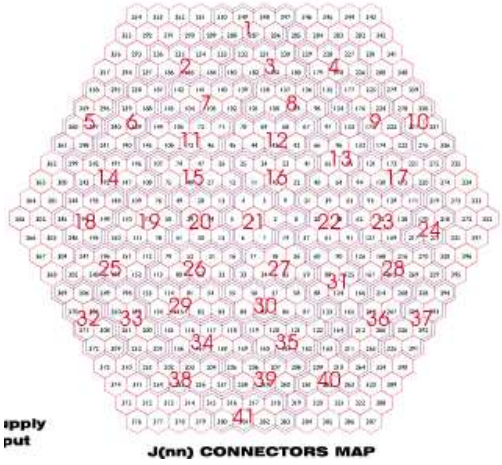

Figure 9.4: Trigger cells in the MAGIC camera. (Courtesy of the MAGIC Collab.).

the pixels themselves were dead – they were yet giving normal signal readout – but only that no-trigger was coming from them. The effect of the missing trigger region can be seen in Figure 9.3. What people tried to do was to see if it was possible to recover anyway the analysis for such data, the first operation being to take out the corresponding part of the camera, as is graphically explained in Fig. 9.5. The region excluded from the analysis is:

$$30^\circ < \phi < 63^\circ \text{ and } 103^\circ < \phi < 146^\circ.$$

One can see that even after the cut in the trigger region, a discrepancy between the

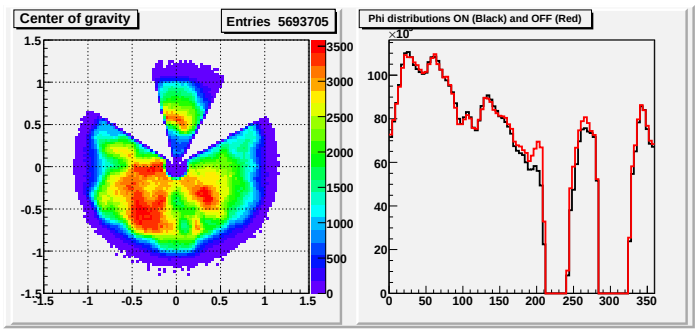

Figure 9.5: First rejection of part of the camera. (Courtesy of the MAGIC Collab.).

remaining ON and OFF samples still occurred. For this reason, an additional cut in PHI was added:

$$180^\circ < \phi < 210^\circ,$$

i.e. an additional 8% of the camera was lost, for a total of 26%. As a final result, Fig. 9.6 illustrates the part of the camera preserved in the analysis. After this latter cut, the agreement between ON and OFF data became reliable.

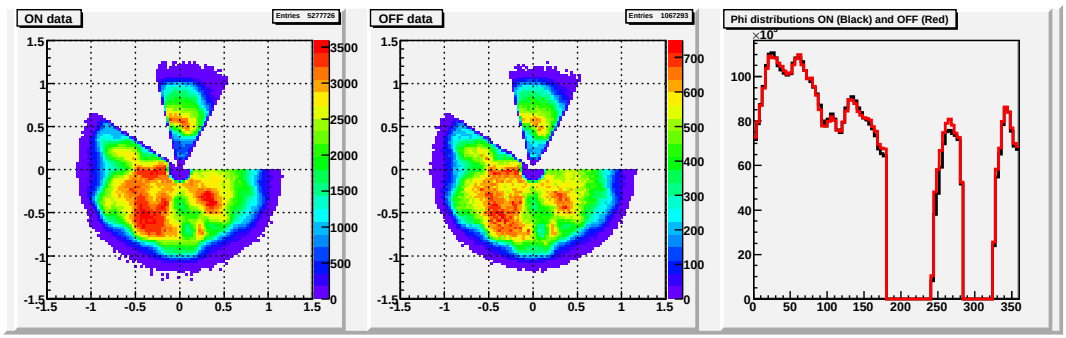

Figure 9.6: Final situation of the camera after rejection. (Courtesy of the MAGIC Collab.).

9.4.4 PHI–cut check with a Crab sample

In order to understand what happened to detection efficiency when taking out part of the camera, a test on a couple of hours of Crab data has been used. In order to understand the role of the introduced PHI–cut in the camera, the analysis has been tested both with and without the mentioned cut. On both analysis, only the *time* image cleaning has been performed. Table 9.6 shows the used sample.

Source	Date	Runs	Effective Time [h]
Crab ON	2006/01/04	46695-46746	2.09
Crab OFF	2006/01/08	47417-47459	2.13

Table 9.6: Data sample used foe PHI-cut check. (Courtesy of the MAGIC Collab.).

As one can see, cuts introduce a significant decrease in the effective observation time (estimated about the 25%).

Effective time and number of events

In the case of Crab, the PHI–cut in the camera has the main effect to decrease the number of events. Of course, this is related to the rejection of part of the camera. In Table 9.7 one can clearly see that this effect amounts about 20%. For the effective observation time, instead, no difference is present (this is intuitively due to that we are borrowing events 'here and there', the total observation time being to remain the same). This effect had to be included in the flux calculation, because the effective time directly enters in the flux evaluation formula and the artificial effect of excluding a part of the camera should be taken into account there.

	Eff.time [h]	Eff.Time *cuts* [h]	Nr.Evts	Nr.Evts *cuts*
Crab ON	1.32	1.32	415k	328k (-20%)
Crab OFF	1.73	1.73	519k	410k (-21%)

Table 9.7: Effective time and number of events for the Crab sample with and without the PHI–cut in the camera. (Courtesy of the MAGIC Collab.).

For this reason, an artificial cut of 20% is applied in the analysis of 3EG_J1835+5918.

Energy threshold

The MC distributions of estimated energy with and without the PHI–cut are plotted in Fig. 9.7. Both series of plots are based on a 0.15 HADRONNESS cut. The energy threshold for the *normal Crab* is 50 GeV, while for the *cut Crab* it corresponds to 60 GeV. In principle, the PHI–cut should not change this parameter – in fact the modification is not so relevant. Nevertheless, a slight discrepancy in the parameter is probably due to different HADRONNESS significance in the two samples.

Effects on the Alpha and Theta-squared plots

The effect of the camera cut is evident in the α and θ^2 plots. Here the difference between *normal Crab* and *cut Crab* is of great interest. Fig. 9.8 and 9.9 show the Alpha and Theta-squared distributions for *normal Crab* and *cut Crab*, for two energy bins: the 120–300 GeV bin (which is the same used for 3EG_J1835+5918) and the 120–1000 GeV bin. Additionally, a HADRONNESS cut of 0.15 is used. Both series of plots show a significant decrease in the sensitivities in the *phicut*. Table 9.8 resumes the results.

		Alpha plot		Theta-squared plot	
Energy [GeV]	Source	Excess	Significance	Excess	Significance
120-300	*Normal Crab*	273±34	8.1	234±41	5.7
	Cut Crab	208±30 (-24%)	7.2 (-12%)	159±36 (-32%)	4.5 (-21%)
120-1000	*Normal Crab*	410±38	11.0	346±46	7.7
	Cut Crab	309±33 (-25%)	9.70 (-35%)	239±32(-31%)	6.2(-20%)

Table 9.8: Alpha and Theta-squared plots results. (Courtesy of the MAGIC Collab.).

We notice the following things:

- the efficiency loss is more remarkable for the Alpha plot than for the Theta-squared plot. The reason of this may be related to the HADRONNESS cut. This is also confirmed by the different number of entries in Alpha and Theta-squared plots.
- The significance decrease due to the cut is somehow similar to the percentage of rejected camera ($\sim 25\%$) and is higher in case of the excess events.

As a consequence of these results, one can conclude that **the analysis is possible and give reliable results in the case of Crab, consistently with a 25% camera loss.** Provided this information, the MAGIC Collaboration decided to proceed with the analysis of 3EG_J1835+5918 data.

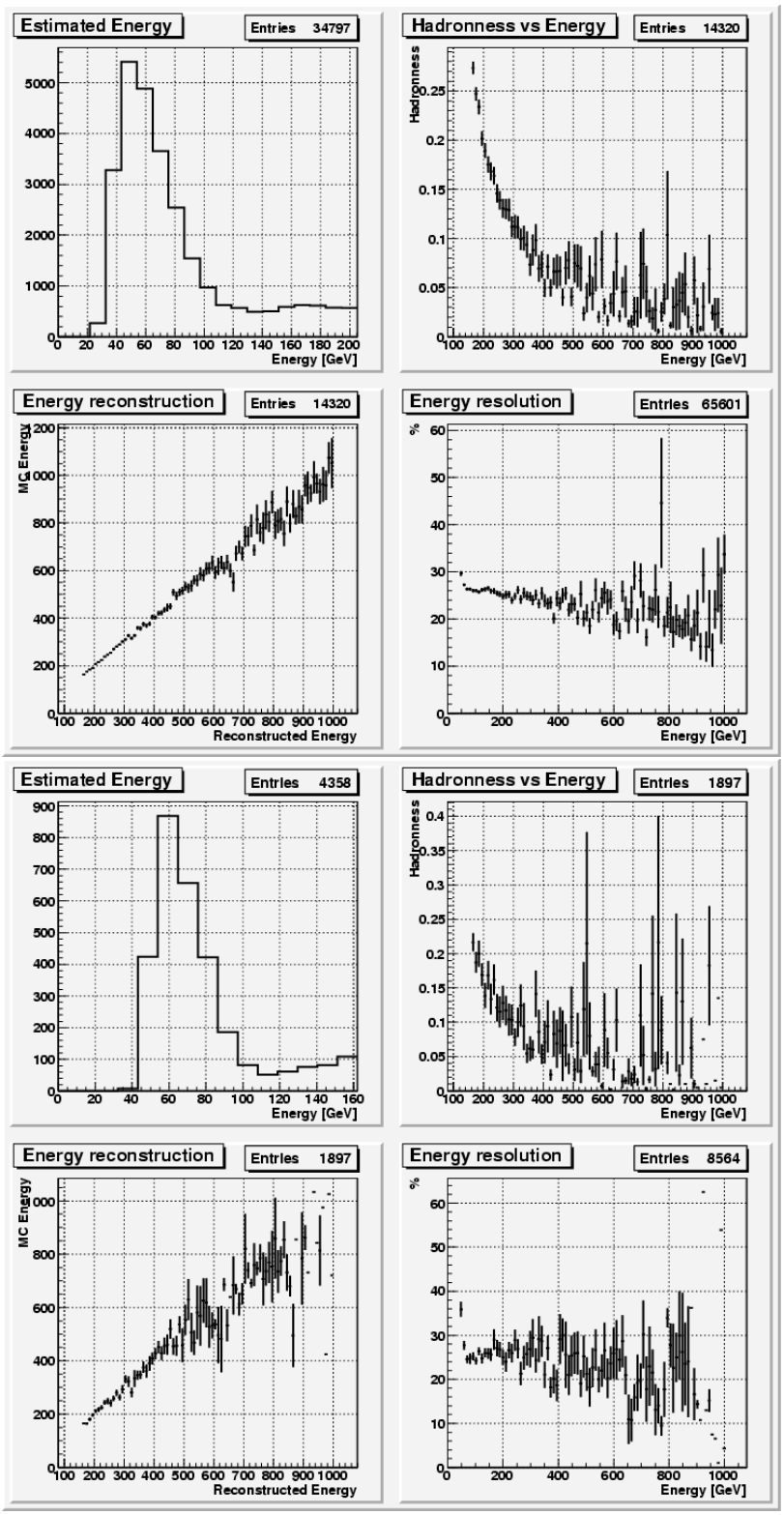

Figure 9.7: MC estimated energy distributions for the *normal Crab*. (Courtesy of the MAGIC Collab.).

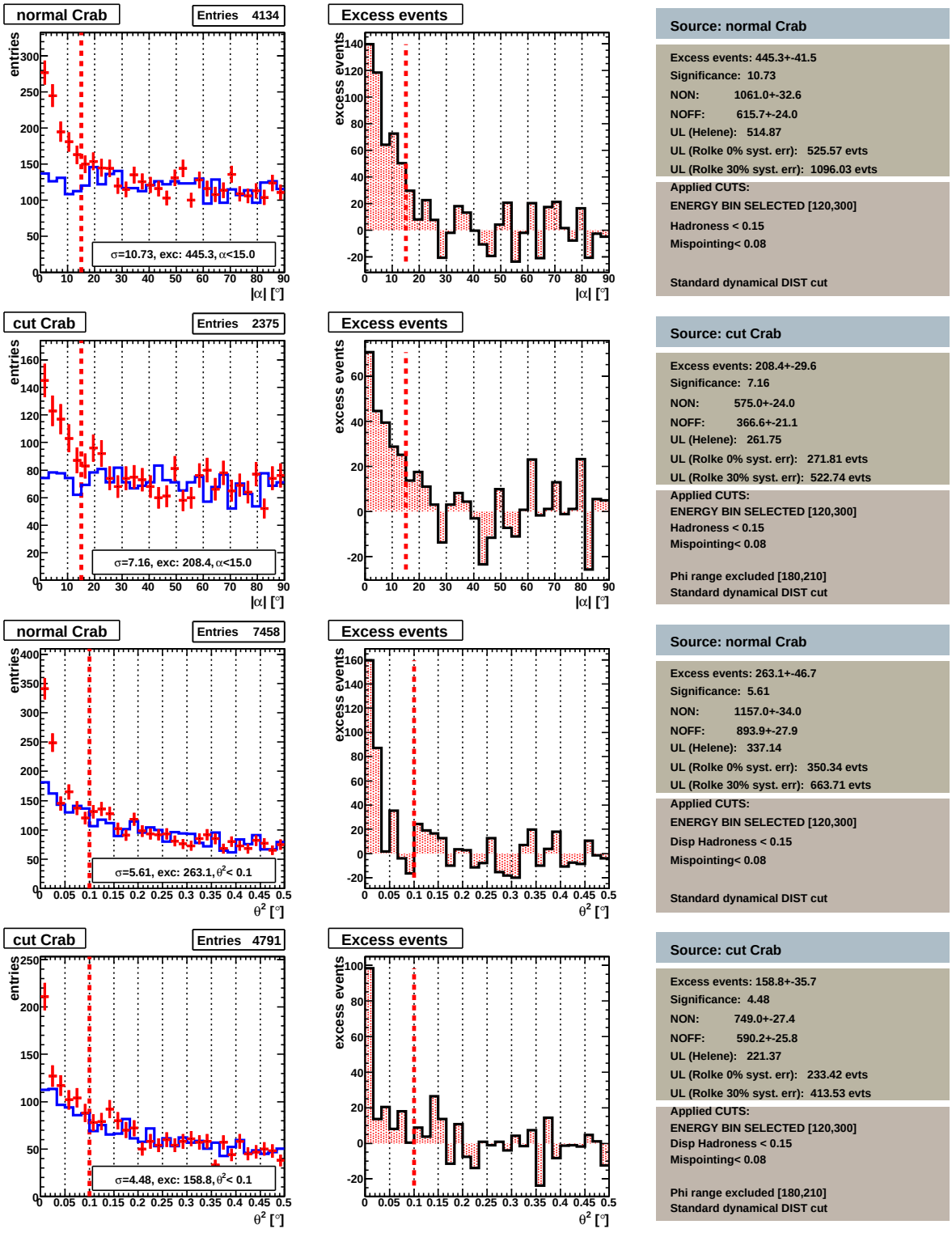

Figure 9.8: Alpha and Theta-squared plots for the *normal Crab*. (Courtesy of the MAGIC Collab.).

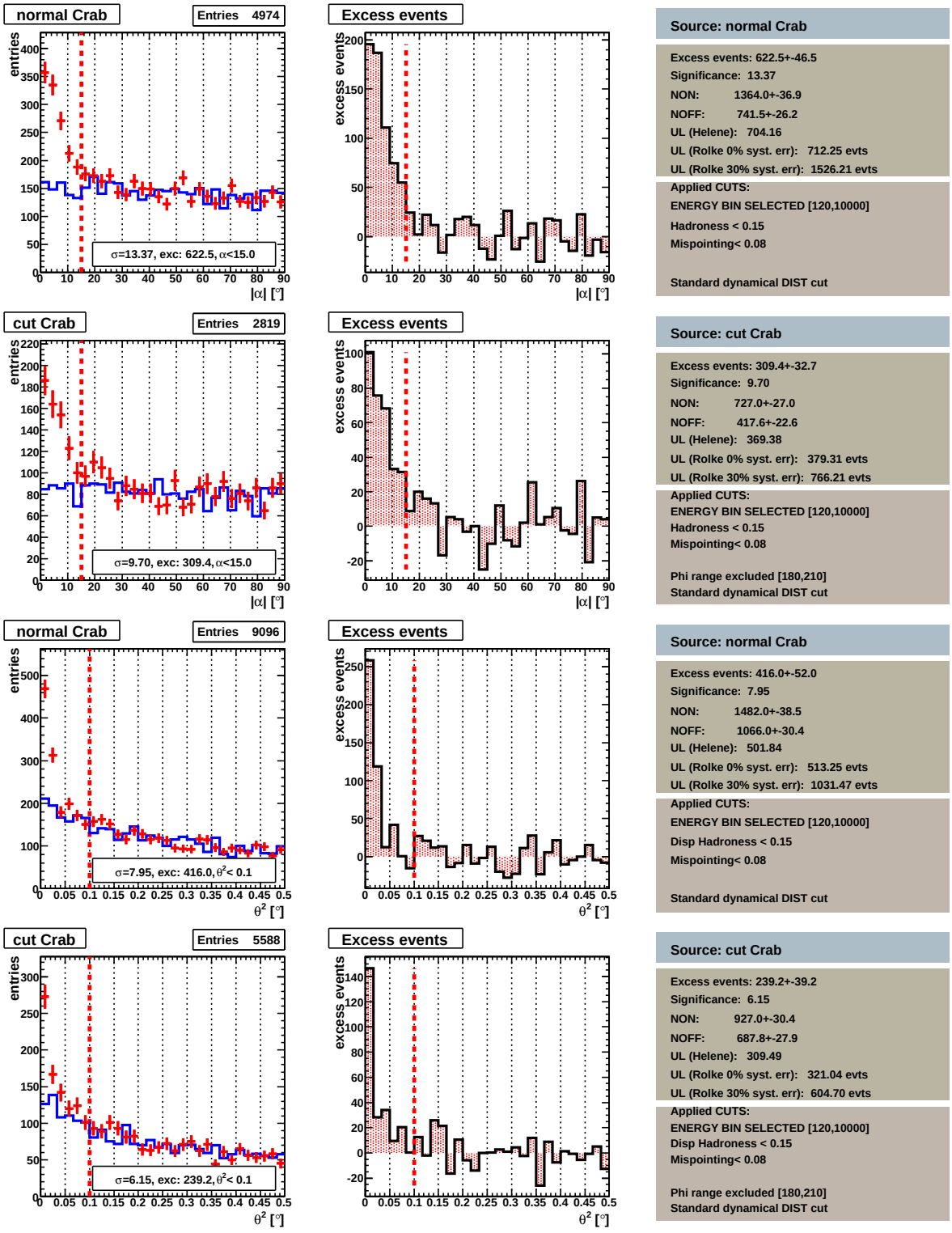

Figure 9.9: Alpha and Theta-squared plots for the *normal Crab*. (Courtesy of the MAGIC Collab.).

9.5 Random Forest training

No PHI–cuts have been applied at this stage, because the trigger problem was not altering the data quality, but simply reducing camera counts in a non-homogeneous way. Fig. 9.10 shows some results. In particular, the so-called *dynamic cuts* are shown for the variable WIDTH, LENGHT and DIST. In the upper left pad of the figure, one can see the best polynomial fit for the MC data. In real data, a SIZE-dependent cut could thus be performed, by excluding the data which shifted from the best-fit polynom. In the other two pads, the standard quality cuts are shown, excluding the WIDTH known sparks events (the so-called *car* events).

9.6 ON-OFF compatibility

At this stage, analyzers were left with a larger set of information for each event. A comparison between ON and OFF was possible and desirable, in hope to observe an event excess on the ON sample as to the OFF one. Depending on the considered energy range, not applying a strict cut in the HADRONNESS parameter – i.e. below 0.4–0.5 – made the Hillas parameters distributions for ON and OFF to perfectly overlap, for data taken under homogeneous conditions. In the following analysis, the HADRONNESS < 0.9 distributions – in presence of a confidential cut able to leave out some marginal data that would not be used – have been checked.

9.6.1 Cleaning method

The reconstructed energy has then compared to the simulated one. In Fig. 9.11 one can see a comparison between the two used cleaning techniques: the *absolute 7:5* and the *relative* cleaning.
Here we list some differences found in the two methods:

- the energy threshold is 120 GeV for the *cleantime* cleaning and 150 GeV for the *cleanabs* method;
- the energy reconstruction is finer for the *cleantime* method;
- also the energy resolution is improved in the *cleantime* case.

Taking note of this, analyzers decided to choose the TIME cleaned data for further considerations. (The same effect had been found for the Crab.)

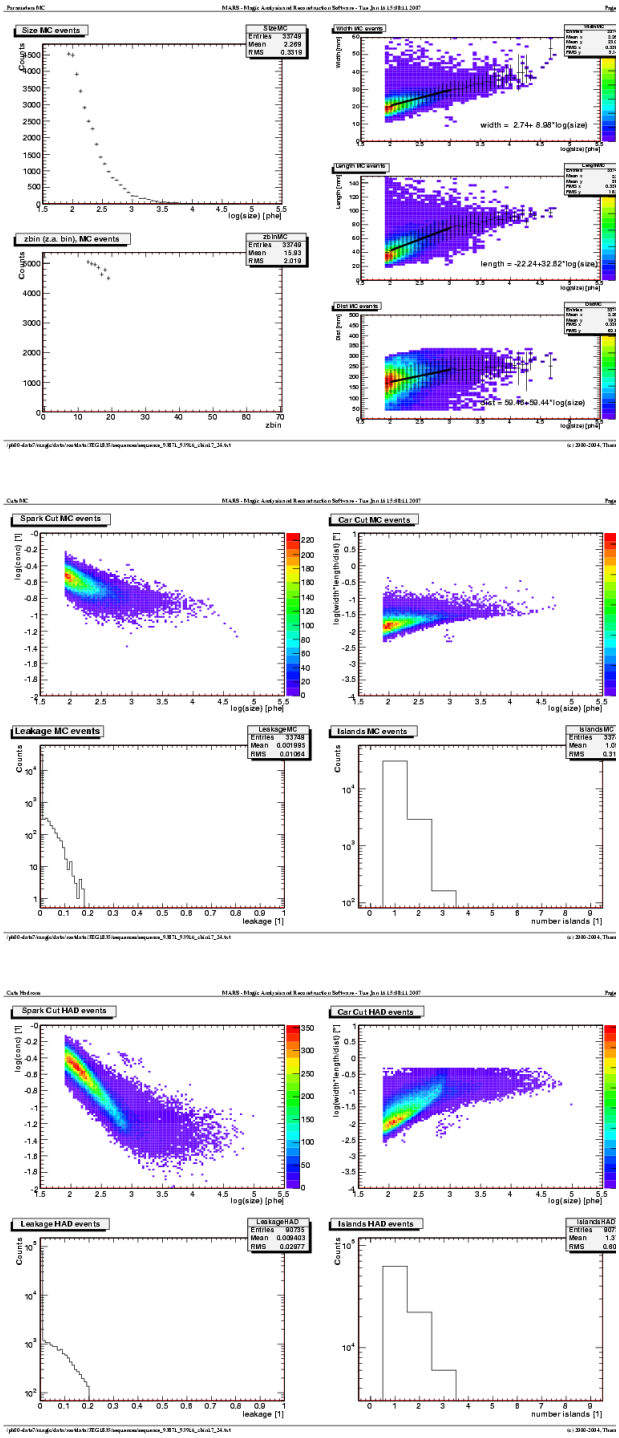

Figure 9.10: Some plots from the Random Forest training status-display. *Upper pad:* the WIDTH, LENGHT and DIST dynamical cuts are shown as a function of SIZE. *Middle pad:* other quality cuts for gammas. *Lower pad:* same quality cuts for hadrons. (Courtesy of the MAGIC Collab.).

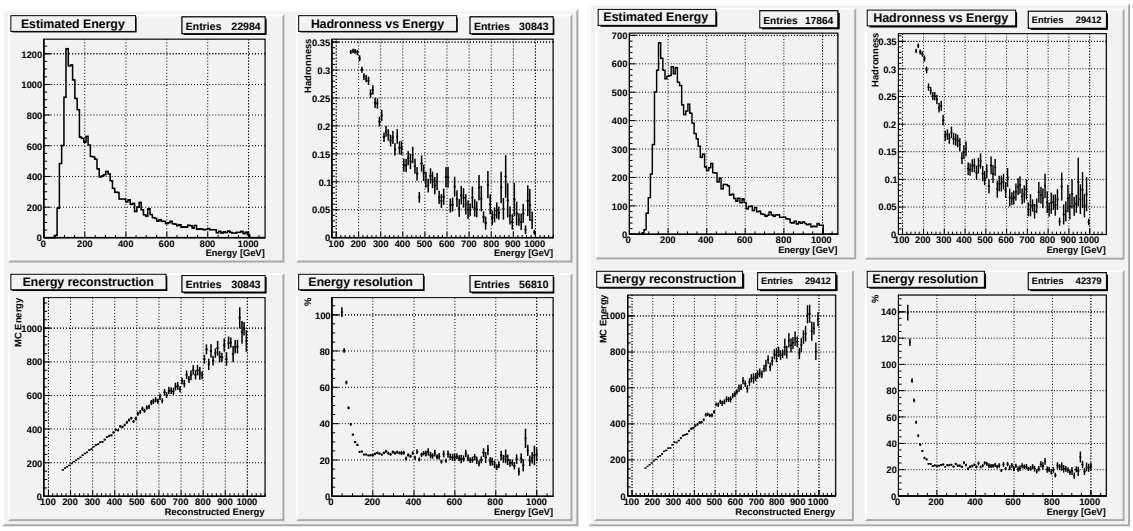

Figure 9.11: Energy reconstruction for the MC gamma sample. *Upper set of plots:* temporal relative cleaning. *Lower set of plots:* absolute 7:5 cleaning. (Courtesy of the MAGIC Collab.).

9.7 Alpha plots and Theta-squared plots

As mentioned above, the data sample has been divided into smaller subsamples with homogeneous zenith angles. An energy-bin dependent analysis has also been performed:

Bin 1: 120 GeV $< E <$ 300 GeV; **Bin 2:** 300 GeV $< E <$ 1000 GeV.

Let us concentrate first on the first energy bin. The Alpha and Theta-squared plots for the first zenith angle bin (30–36 deg) is shown in Fig. 9.12. One can draw the following conclusions:

- **in the first energy bin, both plots do not show any hint of signal. This is a clear indication that the source has not been observed above 120 GeV by MAGIC.**

- **The comparison between ON and OFF data gives better results for the θ^2 analysis.**

- **The agreement between ON and OFF data is very good, demonstrating that the exclusion of a part of the camera has satisfactory corrected the problem and that both the cleaning method and performed checks show high quality.**

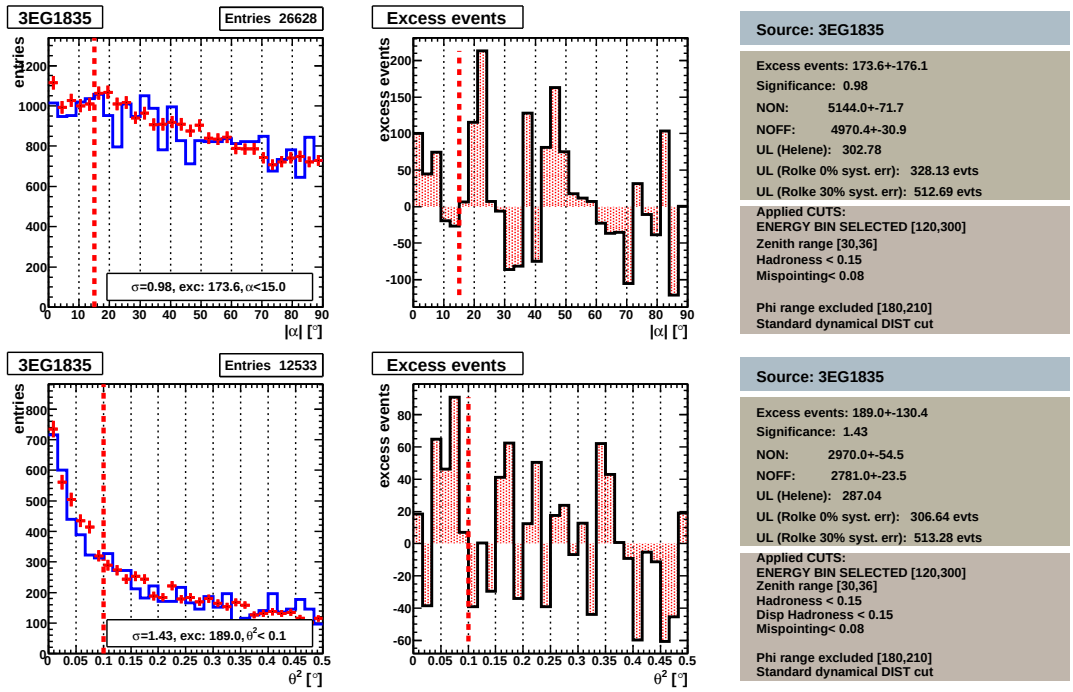

Figure 9.12: Alpha and Theta-squared plots for 3EG_J1835+5918 for the first zenith angle bin (30–36 deg). (Courtesy of the MAGIC Collab.).

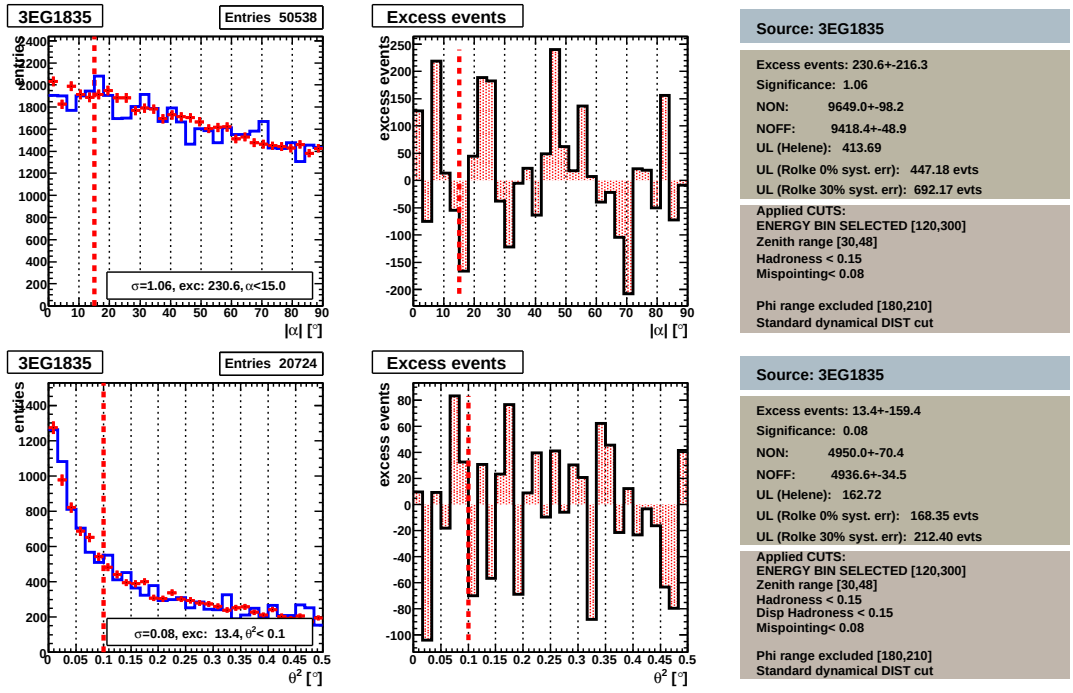

Figure 9.13: Alpha and Theta-squared plots for 3EG_J1835+5918 for the second zenith angle bin (30–48 deg). (Courtesy of the MAGIC Collab.).

In case one make up together the entire data sample over all the zenith angles, similar results are obtained, as shown in Fig. 9.13.

9.8 Conclusions and future work

Given the negative results in this hard analysis task, no flux can be estimated from this source. It is nevertheless possible to calculate upper limits for the gamma emission as a function of the energy bin. At now, some different working groups are involved in this purpose, as well as in a deeper study aimed to improve some crucial steps followed in the analysis of 3EG_J1835+5918. In particular, the Padova working group is training a more sophisticated cleaning method, and we can anticipate here that new promising results have already been obtained and will appear on an incoming MAGIC internal note.

Part IV

Extragalactic Sources of TeV Gamma-Rays

Chapter 10

Detection of a Possible DM Signal from the Draco Dwarf Spheroidal

"The dragon, slain by Heracles during one of his labours, guarded the precious tree on which grew the golden apples."

(Johann Bode, "Uranographia")

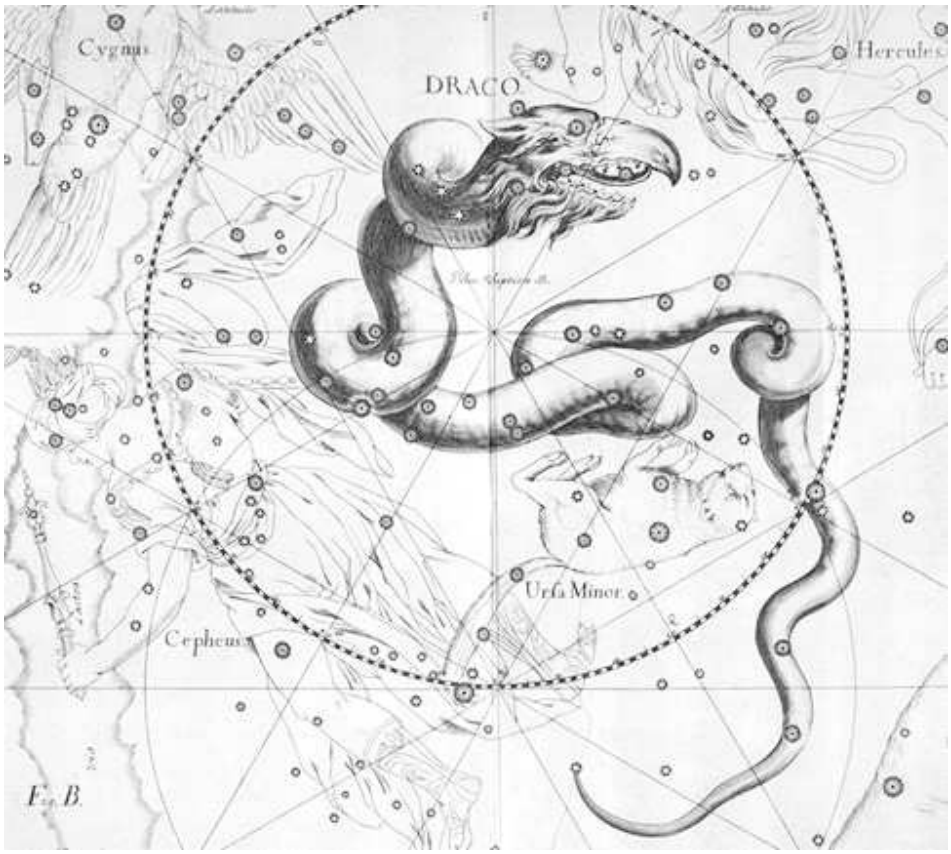

10.1 Extragalactic sources of dark matter

Although the Galactic Center is the most promising target for detection of WIMP annihilation signals, a suspected DM source has to compete, there, with a plethora of thermal and non-thermal multi-GeV and TeV emitters (pulsars, supernova remnants and molecular clouds, just to name a few). The same consideration applies to the center of nearby spiral galaxies. In this sense, then, galaxy centers are likely not the best places where to unambiguously identify DM annihilation signals.

Dwarf spheroidals (dSph) galaxies are ideal astrophysical systems to probe of the nature of dark matter: they are DM dominated, their stellar population is old with negligible ongoing star-formation activity, their gas content is very small, and they are close enough to produce reasonably high fluxes. Several dSph galaxies populate the region around the Milky Way and M31, and some of them seem to be dynamically stable and featuring high concentrations of DM. Among these systems, the Draco dSph galaxy (hereafter 'Draco' for short) is one of the most interesting cases. This object has already been considered as a possible gamma-ray source fed by DM annihilations in recent studies [32], to explain a tentative detection from the direction of Draco reported by the CACTUS collaboration ('TAUP', Zaragoza, Spain, September 2005; 'Cosmic Rays to Colliders 2005', Prague, Czech Republic, September 2005; 'TeV Particle Astrophysics Workshop', Batavia, USA, July 2005; 'PANIC 05', Santa Fe, USA, October 2005).

10.2 The Draco dwarf spheroidal galaxy

The Draco dwarf galaxy (Fig. 10.1) was discovered by Albert G. Wilson of Lowell Observatory in 1954. It is a member of the Local Group (Fig. 10.2, upper panel) and is a satellite of the Milky Way (Fig. 10.2, lower panel). Recent studies indicate that this galaxy may contain a large DM fraction [185]. It is also one of the faintest dwarf galaxies known. It only contains an old population of stars and insignificant amounts of interstellar matter. The main properties of Draco are listed in Tab. 10.2.

10.3 Modeling the halo of Draco

Modeling the DM distribution in dwarf spheroidals is not a straightforward task. For isolated CDM halos numerical simulations provide a universal shape for density

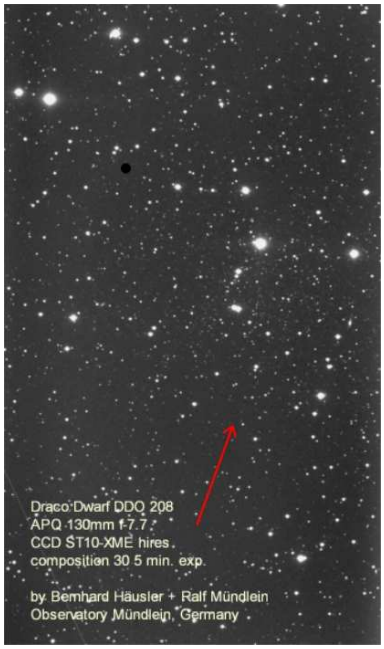

Figure 10.1: The Draco dwarf galaxy.

profiles and a correlation between the object's mass and its concentration parameter (see Chapter 2). However, the picture is less clear for satellites which, being located deep inside the potential well of the host halo, have been strongly remodeled by tidal forces, as a function of their merging histories. Therefore, in order to predict gamma-ray fluxes from neutralino annihilation from Draco, we will not resort the correlation between mass and concentration parameters used for the Milky Way. Recently, Colafrancesco et al. 2006) have investigated the mass models for Draco in the light of available observational data, achieving more realistic DM density profiles [66]. More specifically, for a given functional form for the profile consistent with the picture outlined in Section 2.2.1, the density profile $\rho(r)$ is mapped into:

Tab. 10.2. Main properties of Draco (observation data epoch J2000.0).

Type	dE0 pec, dwarf
Right Ascension	$17^{\mathrm{h}}\ 20.1^{\mathrm{m}}$
Declination	$57^{\circ}\ 55'$
Distance	80 kpc
Apparent Magnitude	+9.9
Apparent Dimension	$51' \cdot 31'$

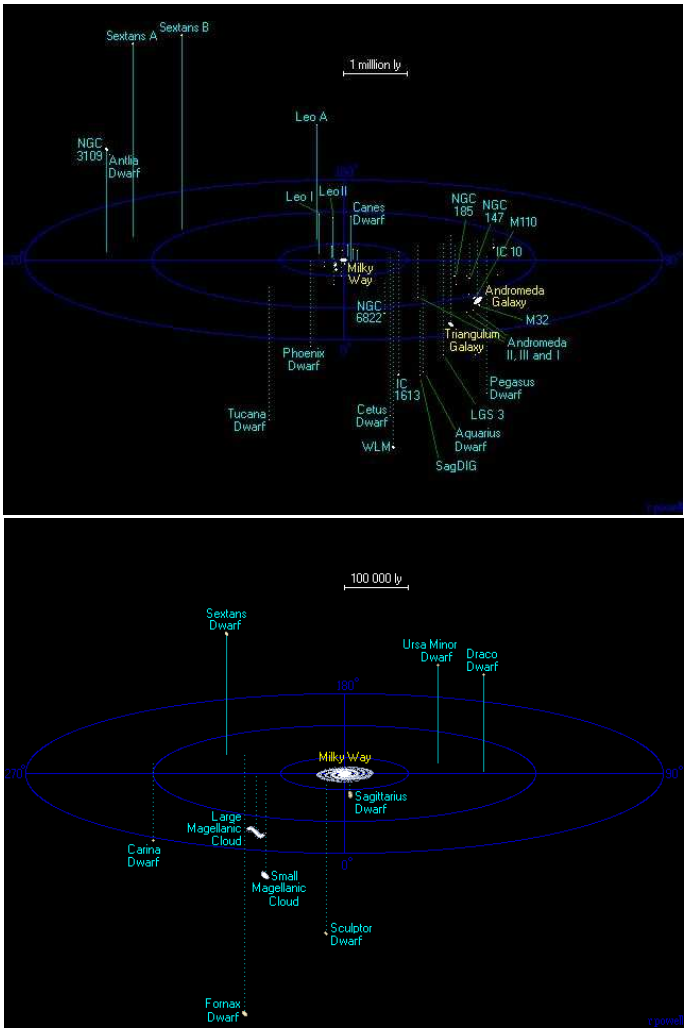

Figure 10.2: *Upper panel:* The Local Group of galaxies. *Lower panel:* The satellites of the Milky Way.

$$\rho(r) \rightarrow \rho(r)\exp(-r/r_{\rm tid}), \tag{10.1}$$

where r_{tid} is determined by:

$$\frac{M(r_{\rm tid})}{r_{\rm tid}^3} = \left[2 - \frac{r}{M_{MW}(r)}\frac{\partial M_{MW}}{\partial r}\right]\frac{M_{MW}(r)}{r^3}\bigg|_{r=r_p-r_{\rm tid}} \tag{10.2}$$

being $M(r_{\rm tid})$ the mass of Draco within the tidal radius and $M_{MW}(r) = 10^{12}$ M$_\odot$ the mass of the Milky Way within the galactocentric distance r; the expression on the right hand side is computed for the orbital radius of Draco r_p at its latest pericenter passage, $r_p = 20$ kpc.

In order to derive the normalization and lenght scale for the three DM profiles

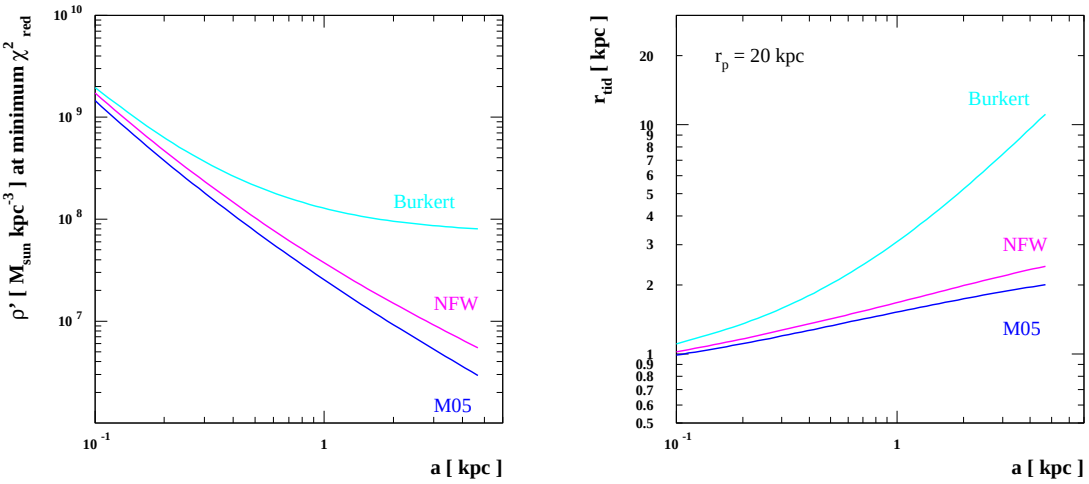

Figure 10.3: *Left panel:* profile normalization factor ρ' versus the scale lenght a, best fit models for the NFW, M05 and Burkert density profiles. *Right panel:* Tidal radius versus the scale lenght a. Datapoints kindly provided by P. Ullio.

adopted in this work, namely the NFW, the M05 and the Burkert profiles, the main dynamical constraint considered in [66] is the observed line-of-sigth velocity dispersion of Draco stellar population. Comparing its theoretical expression [41, 127] with the Munoz et al. and Wilkinson et al. datasets [143, 193], the following best fit-models are derived:

i) **NFW profile:** $a = 1$ kpc, $\rho' = 3.7 \cdot 10^7$ $M_\odot$ kpc^{-3}, $r_{tidal} = 1.7$ kpc;

ii) **M05 profile:** $a = 1$ kpc, $\rho' = 2.54 \cdot 10^7$ $M_\odot$ kpc^{-3}, $r_{tidal} = 1.5$ kpc;

iii) **Burkert profile:** $a = 0.5$ kpc, $\rho' = 2.1 \cdot 10^8$ $M_\odot$ kpc^{-3}, $r_{tidal} = 2.0$ kpc.

The dataset does not allow us to discriminate among the three models.

In the left panel of Fig. 10.3, we plot the value of ρ' corresponding to the model with minimum χ^2, for the three DM density profiles and as a function of the scale factor a; note the huge span in the range of values of the logarithmic vertical scale. In the right panel we show the tidal radii as determined assuming for the radius at the last pericenter passage 20 kpc.

Once the two parameters a and ρ' are known, it is easy to derive the virial mass and concentration M_{vir} and c_{vir} corresponding to the best-fit models. Following this approach, results in Colafrancesco et al.'s results suggest that models with a mass $M_{vir} = 10^9$ $M_\odot$ are preferred.

Assuming a spherically symmetric halo profile, the total annihilation rate in Draco within the radius r_{tidal} is given by Eq. 4.2 and 4.3. Adopting a Draco distance of $d = 80$ kpc [22], in Fig. 10.4 we plot the range of expected values of $\langle J(l,b)\rangle(\Delta\Omega)$ within the minimum-χ^2 halo models selected before, setting $\Delta\Omega$ equal to the MAGIC point-spread-function (PSF), $\Delta\Omega = 10^{-5}$ sr. As just observed by Colafrancesco et al., there is a very small spread in the predicted $\langle J(l,b)\rangle$, even considering significantly different DM halo shapes, in contrast to what one finds in the analogous situation when estimating the DM annihilation VHE flux from the Galactic Center. Infact, in the case of Draco the distance to the source is much larger than in the case of the Galactic Center, and the l.o.s. integral involves an average over a large volume, smoothing out the effect of a singularity in the density profile; at the same time, however, the mean DM density is on average fairly large for any profile, since the dark halo concentration parameter is large.

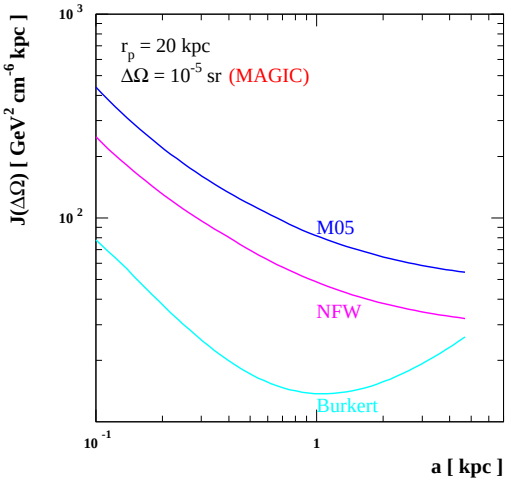

Figure 10.4: l.o.s. integral towards the center of Draco, versus the scale factor a, for the best configurations of the NFW, M05 and Burkert profiles.

For neutralino masses below 700 GeV the leptonic channel (bino-like neutralino), especially the annihilation into $\tau^+\tau^-$, produces most of the photons. At the same time, there is a possibility to produce VHE gamma-rays, above the threshold of 100 GeV, involving pure-wino and pure-higgsino final states in the dominant channels W^+W^- and ZZ. In Fig. 10.5 we show the gamma-ray fluxes from the center of Draco for some sample WIMP models, respectively dominant annihilation final state into $b\bar{b}$ and mass $M_\chi = 50$ GeV or 100 GeV in the left panel, and annihilation modeled into a pure higgsino and a pure wino in the right one. In both figures, fluxes

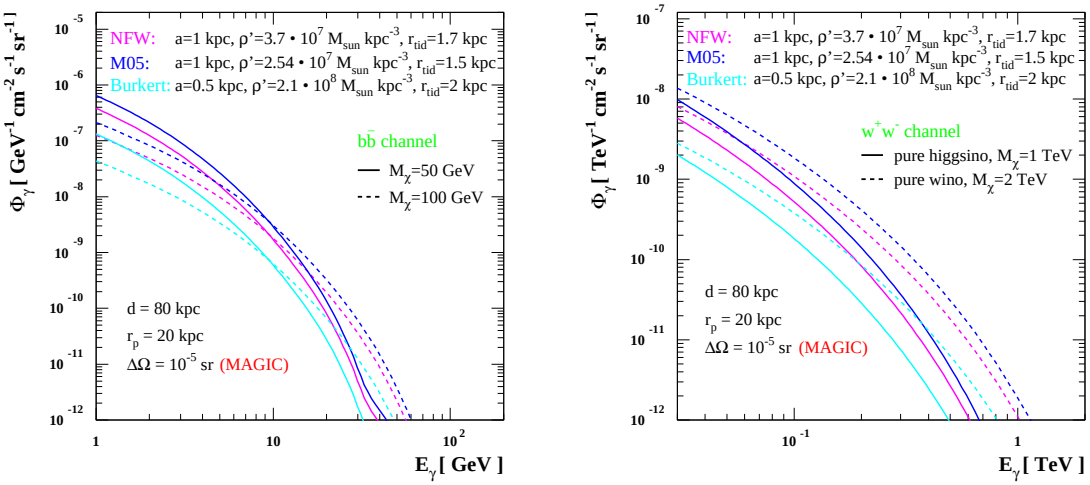

Figure 10.5: *Left panel:* gamma-ray fluxes from the center of Draco for some sample WIMP models, dominant annihilation final state into $b\bar{b}$ and mass $M_\chi = 50$ GeV or 100 GeV. *Right panel:* annihilation modeled into a pure higgsino and a pure wino.

are evaluated for the three best-fit models itemized above.

10.4 Prospects for the MAGIC experiment

Of the currently operating IACTs, MAGIC is the best suited for observations of Draco, thanks to its northern hemisphere location. Furthemore, MAGIC has a lower energy threshold (∼50 GeV for overhead sources) than other IACTs (∼200 GeV for HESS or VERITAS). At the latitude of MAGIC (22° north), Draco reaches zenith angles as small as 29°. At this latitude, an energy threshold of E_0 ∼100 GeV should be possible. Above this energy only WIMPs considerably massive can produce a large number of gamma photons.

The primary background for ACTs is generated by hadronic cosmic rays. Fortunately, most of these showers can be identified and removed from the signal. In the energy range we are interested in, we use the following estimates for the ACT cosmic ray background [66]:

$$\frac{\mathrm{d}N_{\mathrm{had}}}{\mathrm{d}\Omega}(E > E_0) = 6.1 \times 10^{-3} \epsilon_{\mathrm{had}} \left(\frac{E_0}{1\ \mathrm{GeV}}\right)^{-1.7} \mathrm{cm}^{-2}\ \mathrm{s}^{-1}\ \mathrm{sr}^{-1}, \quad (10.3)$$

$$\frac{\mathrm{d}N_{\mathrm{el}}}{\mathrm{d}\Omega}(E > E_0) = 3.0 \times 10^{-2} \left(\frac{E_0}{1\ \mathrm{GeV}}\right)^{-2.3} \mathrm{cm}^{-2}\ \mathrm{s}^{-1}\ \mathrm{sr}^{-1}, \quad (10.4)$$

where ϵ is the fraction of hadronic showers which are misidentified as electromagnetic, which is on the order of 1% for MAGIC. Integrating this above the 100 GeV threshold of the telescope, and considering an effective area of $\sim 5 \times 10^8$ cm^2, this background accumulates at a rate of $\sim 100 \times \epsilon$ photons per hour over a 10^{-5} sr solid angle (approximately a 0.1° by 0.1° circle).

In Fig. 10.6 we show the sensitivity of MAGIC to DM annihilations in Draco for three representative annihilation modes ($b\bar{b}, \tau^+\tau^-$ and W^+W^-) and our three choices for the halo profile. As also noted in [32], for the case of a NFW profile, MAGIC will observe Draco with 5σ significance only if DM particles annihilation cross sections estimate $\sim 10^{-25}$ cm^3 s^{-1} or higher, a value somewhat larger than that required to agree with the measured thermal relic density. However, non-thermally generated relics, allowing larger annihilation cross sections, are not forbidden. Both the MSSM and the mSUGRA scenarios are considered. Note that all models accounting for the WMAP boundary of the relic density ($\Omega_\chi h^2 < 0.094$) lead to χ_1^0 masses from 70 GeV up to 700 GeV, approximately. The gamma yield per annihilation ranges between 10^{-4} and 1, for an assumed energy threshold of 100 GeV (see Fig. 4.2).

10.5 The observation of the CACTUS experiment

CACTUS is a ground based Čerenkov telescope located near Barstow, California. Its large sensitivity to gamma-rays above ∼50 GeV and effective area of up to $\sim 5 \times 10^4$ m^2 for $\sim$ TeV gamma-rays compensate for its main disadvantage of using due a dish array that were designed for solar observations.

At several conferences, the CACTUS collaboration announced that with 7 hours of observation in the direction of Draco a 30.000 events excess had been detected – roughly 7000 and 4000 above, respectively, 100 and 125 GeV (see Fig. 10.7). Unfortunately, the CACTUS Telescope has a relatively poor angular resolution (0.3 degrees in the direction of the Crab Nebula and even worse in the direction of Draco), so no spatial properties can be derived by this observation. Although the CACTUS result is still preliminary and has been very recently replaced by an upper limit, it is interesting to consider the implications of such a detection if it will be confirmed as such. To compare the CACTUS result with the predicted DM annihilation spectrum, the injected spectrum has to be convolved with the energy dependent effective area of the telescope:

$$A_{\rm eff} = 5.69 \cdot 10^4 \left[1 - e^{-0.94(E_\gamma - 48.5)}\right] + 11.9 \times E_\gamma, \tag{10.5}$$

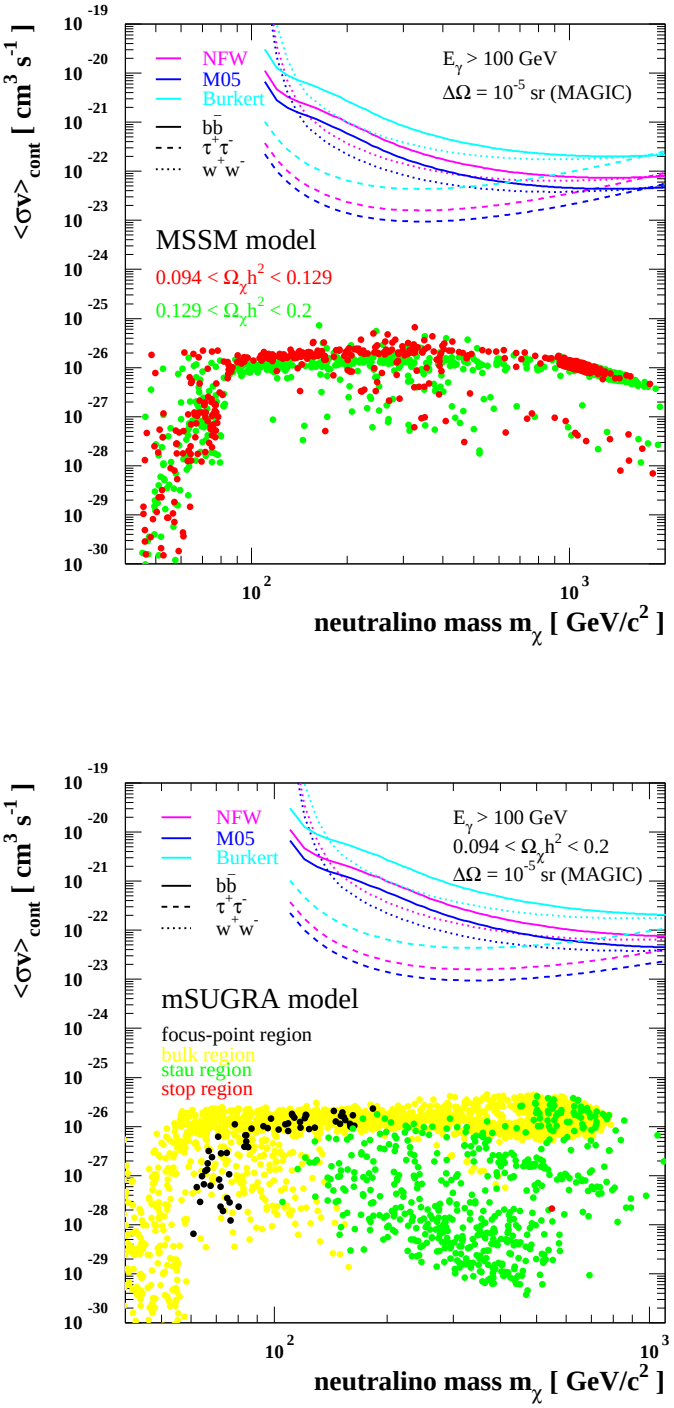

Figure 10.6: The sensitivity of MAGIC to DM annihilation radiation from Draco in the MSSM (*upper panel*) and mSUGRA (*lower panel*) scenarios. We have considered a 5×10^8 cm^2 effective area, a solid angle of 10^{-5} sr, 20 hours of observation time, and 99% hadronic separation ($\epsilon = 0.01$). The solid, dashed and dotted lines correspond to annihilations to $b\bar{b}$, $\tau^+\tau^-$ and W^+W^-, respectively. All contours represent the cross section and mass required to generate a detection at the 5σ level. Datapoints for the mSUGRA scan kindly provided by S. Profumo.

where A_{eff} is parametrized as in [60] and the photon energy E_γ is measured in GeV. For low energetic photons (~ 100 GeV), the resulting effective collection area is about $5 \cdot 10^4$ m^2. A rough estimate of the observed flux into the CACTUS PSF ($\Delta\,\Omega = 10^{-3}$ sr) gives:

$$F(E_\gamma > 50\,\mathrm{GeV}) = \frac{N_\gamma}{A_{eff}\,t} \sim 2.4 \cdot 10^{-9}\mathrm{cm}^{-2}\mathrm{s}^{-1}. \tag{10.6}$$

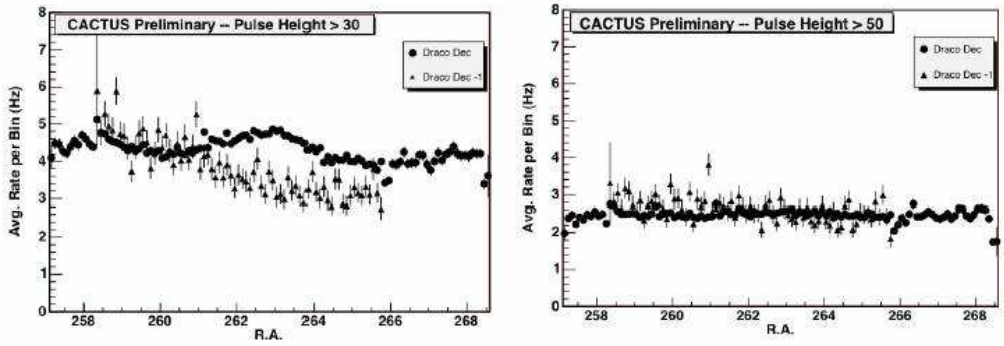

Figure 10.7: Average rate observed by the CACTUS Telescope in the direction of Draco; pulse hight cuts of 30 (*left panel*) and 50 (*right panel*) have been applied. A pulse hight of 50 is of the order of 100 GeV. Figure by [28].

Reporting final considerations in [32], we observe that normalizing to the total rate seen by CACTUS and comparing the energy distribution of events to that expected from annihilating DM, the excess reported by CACTUS appears to be consistent with the following cases:

- a $\sim$500 GeV DM particle annihilating to $b\bar{b}$,

- a $\sim$300 GeV DM particle annihilating to W^+W^-,

- a $\sim$200 GeV DM particle annihilating to $\tau^+\tau^-$.

Anyway, systematic uncertainties in CACTUS's energy determination and understanding of backgrounds might rule out these conclusions. Despite these concerns, Bergström et al. (2006) conclude that DM annihilation appears to be consistent with the limited spectral information contained in the CACTUS signal from Draco, if its mass ranges between 150 and 1000 GeV.
However, each of these scenarios require very high annihilation rates, which leads to some potential problems. First of all, this rate would require a very cusped or spiked halo distribution – roughly 10^3 to 10^4 times larger than for the maximal NFW model.

To accommodate this, either a very large annihilation cross section (still compatible but in the high end of models with a thermal relic density), or a very dense DM distribution (perhaps involving an intermediate mass black hole in the center of Draco). Secondly, as large annihilation cross sections give enhanced signals for any indirect detection technique, a check for compatibility with the antimatter flux measured at Earth is a must. Colafrancesco et al. estimate the induced flux of antiprotons and positrons, within the diffusive convective model for the propagation of charged particles implemented in the '*DarkSUSY*' package, probing that models in such region of the parameter space should be testable with higher precision antimatter data. Furthemore, the limit placed by the EGRET satellite on the gamma-ray flux from the Draco region is violated for most scenarios. More in detail, after imposing angular cuts of 1.71°, 1.18° and 0.82° for gamma-rays between respectively 1–2 GeV, 2–4 GeV and 4–10 GeV, EGRET actually detected 6 events, with an expected background of 4.1. The only exception occurs for DM which annihilates to tau pairs. In this case, only a few events are expected to have been seen in EGRET, and the rate expected for DM annihilation to $\tau^+\tau^-$ is of the same order of magnitude as the excess of $\sim$2 events observed by EGRET. This annihilation mode may dominate, for example, in the case of a bino-like neutralino which annihilates through the exchange of a light stau.

All the estimates given above are quite uncertain, however, as the CACTUS data have not been published yet. Moreover, a reasonable instance is to consider the effect of the integrated starlight from the background and the Draco stars, the intrinsic background by electron induced showers, as well as the implications of a suitable noise treatment.

If the CACTUS measurements are correct, one should expect that signal would be either confirmed or disproved with a few hours.

10.6 The observation of Draco with MAGIC

Observation proposal.

The Draco dwarf spheroidal galaxy has been observed by the MAGIC Telescope, after the CACTUS collaboration's claim of a high signal from the direction to this galaxy. As there were severe concerns about that observation, an independent measurement was needed to confirm or disprove it. In spring 2007, MAGIC was the best suited ACT for such a kind of obervation, as the photons observed by CACTUS were mainly low energetic ($E_\gamma < 150$ GeV) and no other VHE measurements towards Draco had

been planned till then. As already mentioned, with a mass to luminosity ratio $M/L \lesssim 300$, Draco is the most DM dominated dwarf and the 'cleanest' object for a dedicated DM observation campaign (there are no known 'conventional' VHE emitters in its field of view).
Draco was proposed for a MAGIC observation with the following requirements:

- 20 hours observation time from May to June 2006:
- zenith angles from 30 to 40 degrees (as low zenith angle observations preserve the MAGIC nominal (low) energy threshold);
- moonless time;
- 5 hours OFF data.

Data analysis.
The MAGIC collaboration is carrying out the analysis of the Draco data. As the work is still in progress, time is not ripe yet for strong statements. As a preliminary result, we only mention that a first analysis of the distribution of centers of gravity (COG) of the images along the camera plane diagnosed a hard camera inhomogeneity problem in a consistent run sample, making data strongly incompatible.

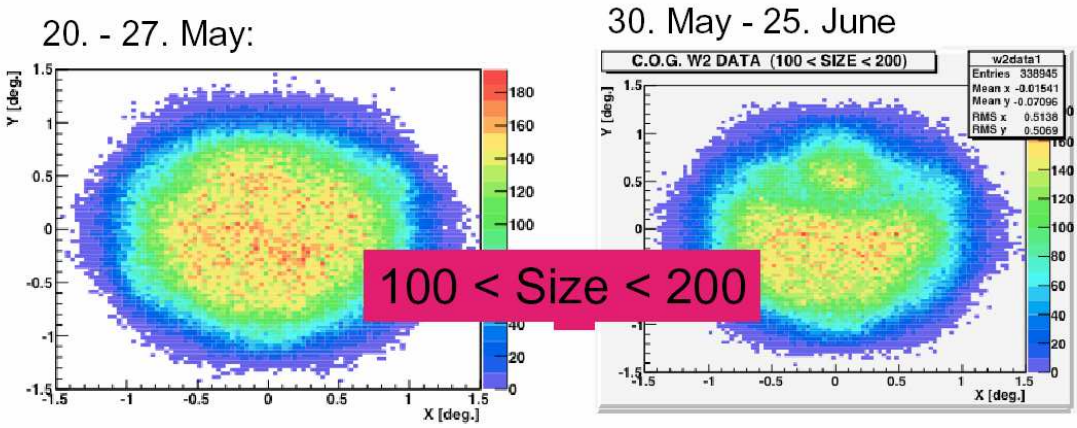

Figure 10.8: Preliminary results of the analysis of the Draco dwarf spheroidal. As clearly shown, data taken in different observation periods look very different, yielding no normalization possible. (Courtesy of the MAGIC Collab.).

As clearly shown in Fig. 10.8, two different data sets exist, both taken in wobble mode (contrary to that required in the proposal): a first one, comprising data taken before May the 30$^{\text{th}}$ 2007, where a major hardware crash had occurred, and a second

data set, taken after these hardware problems had been fixed. While the first sample seems not to be affected by severe camera inhomogeneity, the other set shows a very inhomogeneous distribution of the COG in the camera.
Two different MAGIC groups are presently working on improving Draco data analysis, their main aim being to understand if the best effort is to move out part of the camera and, above all, to find an efficient way to match the apparently incompatible data groups together.

Chapter 11

The Baryonic versus Dark Matter VHE Gamma-Ray Luminosity of Star-Forming Galaxies

Using recent data on emission at energies higher than 0.2 TeV from a complete sample of point sources in the central Galactic region, we estimate the Galaxy's luminosity in this band due to the collective point-source luminosity. Arguing that such sources are related to ongoing star formation activity and assuming a hadronic origin for their gamma-ray emission, their main spectral and luminosity properties can be explained assuming that cosmic ray acceleration and interaction with ambient matter occurs inside the parent sites of star formation (i.e., molecular clouds). Using the star-formation rate (or its proxy, the far-infrared luminosity) as a scaling variable, we generalize our estimate of the Galaxy's TeV point-source luminosity to star-forming galaxies – suggesting a quite steep dependence on SFR.

11.1 Introduction

Star formation (SF) leads to gamma-ray emission through the production of SN-accelerated proton cosmic rays (up to energies $\sim 10^{14}$ eV), which by interaction with the ambient gas produce neutral pions that in turn (on timescales $\sim 10^{-16}$ s) decay into very-high-energy (VHE) gamma-rays (with energy 30 GeV $\lesssim \epsilon \lesssim$ 30 TeV). In a given galaxy, the higher the SF rate (SFR) the more frequent the SN explosions, hence the more intense the gamma-ray emission. Reversing the argument, gamma-ray emission gauges SFR. The basic notion is that the ongoing SFR can be measured based on stellar end-products which are both sufficiently gamma-ray-bright for their collective emission to be unambiguously identified, and sufficiently short-lived so that

they trace the 'instantaneous' SFR.

The plan of this chapter is as follows. In Section 11.2 we review the properties of the TeV sources in our Galaxy and compute their star formation-related TeV luminosity; in Sec. 11.3 we discuss Galactic TeV point sources as cosmic-ray accelerators; in Sections 11.4, 11.5 and 11.6 we estimate the three main contributions to the TeV emission in a star-forming galaxy, i.e., (i) the two baryonic components due to the collective emission from TeV point sources and the diffuse radiation produced by hadronic illumination of interstellar gas, plus (ii) the non-baryonic contribution originated from the radiation of annihilating dark matter. Our aim is to provide a recipe to estimate the respective strenghts of these different contributions for promising nearby candidates, which might be proposed for observations by present or future gamma-ray telescopes. Specifically, in the second part of this work we apply our scheme to the nearby galaxy M 31.

11.2 VHE gamma-ray point sources in the Galaxy

In a survey of the Galactic plane in the region $|l| \leq 30°$, $|b| \leq 3°$, HESS detected 14 sources at energies higher than 0.2 TeV (see Tab. 11.1 and [1]). Proposed counterparts are supernova remnants (SNRs), pulsar wind nebulae (PWNs) and X-ray binaries (XRBs), while the nature of the other sources is unknown (see [1, 10]). Whatever their detailed nature, a reasonable expectation is that all of these TeV sources are related to stellar endproducts, either single (like SNRs) or binary (like pulsars (PSRs) or black holes (BHs) accreting from a close massive main-sequence companion star). In either case, the progenitors are supposed to be massive, bright, short-lived stars. Hence, these Galactic-plane TeV sources are immediate products of the ongoing star-formation activity. Although seen extended by HESS (e.g., SNR shells, nebulae surrounding XRBs), by origin and location the TeV emission of these Galactic-plane sources is anyway closely related to point-like objects proper, i.e. stellar remnant: hence we will dub these sources 'TeV point sources' (TPs). (Of course, these TPs would appear point-like if seen in external galaxies.)

These 14 sources constitute a complete sample (hereafter: Sample 1) of Galactic TeV sources down to a lower flux limit of 3×10^{-12} ph cm^{-2} s^{-1}. This notion allows us to estimate the portion of Galactic TeV emission [1] that arises from ongoing star formation. In the Galaxy, these sources are distributed on the plane ($< b >= -0.23° \pm 0.08°$) symmetrically around the center ($< l >= -5.68° \pm 5.23°$). The superposed emission

[1] By 'TeV emission' in this chapter we mean 'emission at energies $\epsilon \geq 0.2$ TeV'.

of the 14 sources is $f_{\geq 0.2\,\mathrm{TeV}} = 3.6 \times 10^{-10}$ ph cm^{-2} s^{-1}. Because the distances to the sources are unknown, and the outer radius of the HESS survey is much smaller than the Sun's Galactocentric distance (the former is 4.3 kpc if the latter is 7.5 pc – see [165]), we assume that all our TPs are located in the Galactic Center so their implied collective (photon) luminosity is $L^{\mathrm{TP}}_{\geq 0.2\,\mathrm{TeV}} = 2.45 \times 10^{36}$ ph s^{-1}.

We now extrapolate this luminosity from the fraction of Galactic disk surveyed by HESS to the entire disk. To do this we assume (with some simplification) a **thin exponential disk model,** where the surface stellar mass density (that follows the surface brightness through a constant stellar mass-to-light ratio) is described by $\sigma(R) \propto e^{-R/R_d}$ with $R_d = 2.25$ kpc [69]. Assuming a constant TeV light-to-mass ratio, extrapolating the above exponential disk from 4.3 kpc to infinity we obtain a 1.75 factor increase for the luminosity. The extrapolated Galactic TP photon luminosity is then estimated to be:

$$L_{\geq 0.2\,\mathrm{TeV}} \;=\; 4.27 \times 10^{36} \quad \mathrm{ph\ s^{-1}}\,. \tag{11.1}$$

How does this extrapolation compare with current observations of Galactic TPs? We searched the refereed literature for Galactic TPs that are not in Sample 1: we found 10 such sources (Sample 2; see Tab. 11.2 for their main data). Because $< b >= -0.43^\circ \pm 0.31^\circ$, these sources too lie on the Galactic disk. Several of them are known to be stellar endproducts, such as SNRs and XRBs. By the nature of their members, Samples 1 and 2 are then homogeneous. In order to compare the respective luminosities, we bring the luminosities of Sample 2 objects into consistency with those of Sample 1: for each object, using the measured flux $f_{\geq \epsilon_{\mathrm{min}}}$ and spectral index Γ, we compute $f_{\geq 0.2\,\mathrm{TeV}}$ (see Tab. 11.2). The estimated [2] collective (photon) luminosity of Sample 2 turns out to be $L^{\mathrm{TP}}_{\geq 0.2\,\mathrm{TeV}} \sim 5.75 \times 10^{35}$ ph s^{-1}. This value is much lower than the extrapolation for Sample 1. Hence we can deduce that the value in Eq. 11.1, which was extrapolated from a complete inner-disk sample to the entire disk, safely accomodates the contribution from all known Galactic TPs – and perhaps hints at the presence of yet-undetected TeV sources, akin to those in Sample 1, in the outer disk.

We conclude this section by noting that the typical systematic error on the photon index is $\sim$0.2. As the total error is derived by adding in quadrature the systematic and statistical errors, the mean luminosity-weighted spectral index for Sample(s) 1

[2]The distance to HESS J1303−631 is known only with large uncertainty, and that to TeV J2032+4130 is unknown. For the former case we used the mean luminosity implied by the distance limits, while to the latter object we attributed the mean luminosity defined by the other 9 objects of Sample 2.

(and 2) is $< \Gamma > \simeq 2.4 \pm 0.3$. Furthermore, the typical systematic error in the absolute flux is $\sim$30%. We can then summarize the results obtained so far by expressing the differential photon spectrum as:

$$\Phi^{\rm TP}_{\geq 0.2\,{\rm TeV}}(\epsilon) \;\sim\; 6.3 \times 10^{35} \Big(\frac{\epsilon}{\rm TeV}\Big)^{-2.4} \quad {\rm ph\ s^{-1}\,TeV^{-1}}\,. \tag{11.2}$$

11.3 TeV point sources as CR accelerators

The Galactic TeV emission from stellar endproducts can be assessed in terms of a basic model that incorporates the standard features of the hadronic channel of VHE gamma-ray emission between accelerated protons and diffuse ambient matter.

We start by assuming that the observed gamma-ray photons are all of hadronic origin, i.e. they are produced by the interaction of energetic CR protons with ambient matter [3]. As for the astrophysical setting, we assume that CR protons are accelerated by SN explosions (see [61]) which, marking the death of massive ($> 8\,M_\odot$) hence short-lived stars, occur in the same environment in which the progenitor stars were born, i.e. in within giant molecular clouds (GMCs). These clouds (typically, with $M \sim 10^5 M_\odot$; e.g., [175]) are structured (e.g., [50]) as a lower-density ($n_{\rm H_2} \sim 10$ cm^{-3}) medium embedding a distribution of higher-density ($n_{\rm H_2} \sim 10^3$ cm^{-3}), low-filling-factor ($\sim$ 5%) clumps. In the relevant mass range ($1 \lesssim M/M_\odot \lesssim 3 \times 10^4$), clump shapes vary from spherical (with radii $r \sim 0.2 - 2.4$ pc) to highly irregular, and the clump mass spectrum, $dN(M) \propto M^{-q}$ with $q \sim 1.7$, ensures that most of the clumps are small but most of the mass is in large clumps. Active star formation occurs in the high density peaks ($n_{\rm H_2} \gtrsim 10^4$ cm^{-3}; e.g., [92]) within the clumps.

After a SN explosion, the circumstellar material is swept by a shock wave with compression ratio $s \equiv (\gamma + 1)/(\gamma - 1 + 2\,\beta^2/M^2)$ (being $\gamma \equiv C_P/C_V = 5/3$ the specific-heat ratio, $\beta \equiv (c_s/V_A)$ the plasma beta, and $M \equiv u_1/V_A$ the Alfvénic Mach number of the shock; with, in turn, u_1 the upstream background plasma speed, c_s the sound speed in plasma, and V_A the Alfvén speed). When a distribution of particles, initially with momentum distribution $n \propto \delta(p - p_0)$, is overtaken by the shock wave, the resulting momentum distribution of the downstream particles is $dn/dp \propto p^{-\alpha}$ (for $p > p_0$), where $\alpha = 3s/(s-1) = 3/2M^2(\gamma+1)/(M^2-1)$ [49]. The corresponding integral gamma-ray emissivity (normalized to the ambient CR energy density) by pp

[3] Following [184], we neglect additional (hadronic) contribution to TeV gamma-ray emission from proton illumination of the inner winds of massive stars [167], and the (leptonic) contribution from inverse Compton interaction of energetic electrons with the strong ambient FIR field (this simiplification is well-justified above 100 MeV, see [152]).

interaction via π^0 decay is $g^{[\alpha]}_{\geq\epsilon} = g^{[\alpha]}_{1\ \mathrm{TeV}}(\epsilon/\mathrm{TeV})^{3-\alpha}$ ph s^{-1} erg^{-1} cm^3 (H-atom)$^{-1}$ [75]. Assuming for simplicity strong shocks ($M >> 1$), leads to $\alpha = 4$. From [75], where values of $g^{[\alpha]}$ are reported for several values of α, we then choose $\alpha = 4.1$: this leads to $g_{\geq E} = 10^{-17}(E/\mathrm{TeV})^{-1.1}$ ph s^{-1} (erg cm^{-3})$^{-1}$ (H-atom)$^{-1}$.

The integral gamma-ray luminosity of a source with gas number density n and CR energy density U_{CR} in a volume V is given by:

$$L_{\geq\epsilon} \ = \ \int_V g_{\geq\epsilon}\, n\, U_{\mathrm{CR}}\, dV \ \ \mathrm{ph\ s^{-1}}\,. \tag{11.3}$$

According to our assumption, VHE gamma-ray emission is produced by pp interaction (via π^0 decay) in the same environment where the massive progenitor stars were born, i.e. inside GMCs. Some care is in order to pick realistic values for the physical quantities. From the typical densities and filling factors of the clumps and the inter-clump medium (see above), one obtains a GMC density of $n^{\mathrm{GMC}}_{\mathrm{H_2}} \sim 0.05{\times}10^3{+}0.95{\times}10$ cm^{-3} = 60 cm^{-3}: for simplicity, in numerical estimates we'll take $n^{\mathrm{GMC}}_{\mathrm{H_2}} = 50$ cm^{-3}. A typical GMC mass of $M^{\mathrm{GMC}} \sim 10^4 M_\odot$ implies, for such a density, a radius $r^{\mathrm{GMC}} \sim 10$ pc: it should be noticed that, if it were located in the Galactic center, this GMC size would be viewed under an opening angle of 0.1°, which is similar to the typical angular radii of Sample-1 sources (defined as σ in gaussian surface-brightness fits, $I(r) \propto \exp(-r^2/\sigma^2)$, see [1]). Next, for the ambient CR energy density within the cloud we take $E^{\mathrm{GMC}}_{\mathrm{CR}} \sim 10^2$ eV cm^{-3}, which is about two orders of magnitude higher than the local (i.e., solar) Galactic value [4] and similar to the value inferred for the central starburst of M 82 (see [189]). Using these values for the physical parameters in Eq. 11.4, we obtain that each CR-illuminated GMC has a photon luminosity $L^{\mathrm{TP}}_{\geq 0.2\,\mathrm{TeV}} \sim 2\times10^{35}$ ph s^{-1}. A galaxy similar to the Milky Way, with (say) 25 such sources, will then have an integral photon luminosity $L^{\mathrm{TP}}_{\geq 0.2\,\mathrm{TeV}} \sim 5\times10^{36}$ ph s^{-1}. This value is in fair agreement with our Galaxy's estimated luminosity in Eq. 11.1.

The differential VHE gamma-ray emissivity corresponding to a strongly-shocked particle distribution is $dg/d\epsilon \propto \epsilon^{-\Gamma}$ with $\Gamma = \alpha - 2 \sim 2$. Although quite rough, the agreement of this value of Γ with the measured spectral indexes reported in Tab. 11.1 and Tab. 11.2 (for which $<\Gamma> \simeq 2.4 \pm 0.3$) suggests the basic validity of the shock-acceleration mechanism in interpreting the VHE gamma-ray emission of Galactic sources. Our basic shock-acceleration hypothesis also leads to straightforwardly predicting the slope of the CR spectrum. The shocked particles distribution

[4] The CR proton flux measured at Earth is $J(\epsilon) = 2.2\times(\epsilon/\mathrm{GeV})^{-2.75}$ ph s^{-1} cm^{-2} sr^{-1} GeV^{-1}. It implies an energy density of $\frac{1}{c}\int_{1\,\mathrm{GeV}}^{\infty}\epsilon\, J(\epsilon)\, d\epsilon \sim 1$ eV. Such a local value is generally *assumed* to be representative of the Galactic mean value (e.g., [1]).

function can be recast in terms of energy: $dn/d\epsilon \propto \epsilon^{-\theta}$, with $\theta = \alpha/2$. If $\alpha = 4$ as assumed here (and appropriate for a strong shock), then $\theta = 2$. This value of θ is (broadly) comparable with that measured for the spectrum of CRs at energies below the 'knee' at 10^{15} eV, which is thought to be the highest attainable energy for protons accelerated in SN-driven shocks via the second-order Fermi mechanism (e.g., [163]): this suggests that the 'sea' of CRs measured at Earth is the superposed emission of the CRs produced by several (Galactic) accelerators.

11.4 TeV point emission from starburst galaxies

Given its basic character, our simple model is remarkably successful in explaining the spectral and luminosity properties of the observed Galactic TP sources. In particular, our assumption that the emission of these sources is immediately related to the death, and hence to the birth, of massive ($> 8\ M_\odot$) stars gets some important support. Consequently, we may surmise that in star-forming galaxies the collective TP emission is an indicator of the current SFR. (A similar situation holds for the 2–10 KeV emission: e.g., [157].)

A first assumption is that the various terms in Eq. 11.3 scale with SFR as: $U_{\rm CR} \propto$ SFR, and $n \propto {\rm SFR}^{1/\eta}$, with $\eta \sim 1.5$. (The latter scaling reproduces the standard Schmidt [1959] law between SFR and density of the ambient medium; see [117].) As our Galaxy has SFR $\sim 2\,M_\odot\,{\rm yr}^{-1}$, Eq. 11.1 can then be parameterized as:

$$L^{\rm TP}_{\geq 0.2\,{\rm TeV}} \;=\; 4.27\times 10^{36}\Big(\frac{\rm SFR}{2\,M_\odot\,{\rm yr}^{-1}}\Big)^{1+\frac{1}{\eta}} \quad {\rm ph\ s}^{-1}\,. \tag{11.4}$$

We wish to recast Eq. 11.4 in terms of observables. In a galaxy, the ongoing SFR is effectively measured by the FIR luminosity [5]. This emission mostly originates from the warm dust clouds that harbor sites of star formation: the UV radiation, emitted by massive stars, is absorbed by such placental clouds which then get heated up and emit thermal FIR radiation. A suitable conversion formula,

$${\rm SFR}(\geq 0.1\,M_\odot) \;=\; \frac{L_{\rm FIR}}{2.2\times 10^{43}\ {\rm erg\,s}^{-1}} \quad M_\odot\ {\rm yr}^{-1} \tag{11.5}$$

(Kennicutt, 1998 [117] – assuming a Salpeter [1955] stellar initial mass function defined as $dN/dM \propto M^{-2.35}$ in the mass range $0.1 \geq M/M_\odot \geq 100$), allows Eq. 11.4 to be transformed into:

[5] The FIR flux is defined in [105] as a combination of the *IRAS* 60 μm and 100 μm fluxes according to $f_{\rm FIR} \equiv 1.26\times 10^{-11}(2.58\,f_{60} + f_{100})$ erg s^{-1} cm^{-1}, where f_{60} and f_{100} are expressed in Jy.

$$L^{\rm TP}_{\geq 0.2\,{\rm TeV}} \sim 4.3\times 10^{36}\Big(\frac{L_{\rm FIR}}{4.4\times 10^{43}\ {\rm erg\ s^{-1}}}\Big)^{1+\frac{1}{\eta}} \quad {\rm ph\ s^{-1}}, \tag{11.6}$$

with $\eta \sim 1.5$; in view of Eq. 11.2, we summarize all these concepts into:

$$\Phi^{\rm TP}_{\geq 0.2\,{\rm TeV}}(\epsilon) \sim 6.3\times 10^{35}\Big(\frac{\epsilon}{\rm TeV}\Big)^{-2.4}\times \tag{11.7}$$

$$\times\Big(\frac{L_{\rm FIR}}{4.4\times 10^{43}\ {\rm erg\ s^{-1}}}\Big)^{1.7} \quad {\rm ph\ s^{-1}\,TeV^{-1}}\,.$$

When VHE gamma-ray data become available for a sample of galaxies, the relation proposed in Eq. 11.6 will be tested. Lacking such data, in Sections 11.7 and 11.8 we will check how our prediction fits available luminosity limits for the very nearby star-forming Andromeda galaxy.

Once a VHE gamma-ray photon is produced in a star-forming GMC, it still has to cross – and leave unscathed – both its placental GMC and parent galaxy to reach Earth (e.g., [167]). During its travel, a VHE gamma-ray photon can interact with ambient photons (which, especially at FIR and UV energies, are plentiful in a star-forming environment) and produce e^+e^- pairs. To check the strength of this effect, let us evaluate the optical depth to pair production, $\tau_{\gamma\gamma} = n_\gamma \sigma_{\gamma\gamma} r$ (where n_γ is the target photon number density, $\sigma_{\gamma\gamma} \sim 2\times 10^{-30}$ cm^2 in the range 1 eV – 1 TeV (see [123]) is the photon-photon cross section, and r is the distance travelled), which measures how transparent the medium is to VHE gamma-ray photon propagation. We evaluate $\tau_{\gamma\gamma}$ first for crossing the placental GMC, then for crossing the parent galaxy. For the purpose of this estimate we set $n_\gamma \equiv U_{\rm FIR}/(h\nu_{\rm FIR})$, where $U_{\rm FIR}$ is the local FIR luminosity density and $\nu_{\rm FIR} = 3\times 10^{12}$ s^{-1} is the frequency of a 100 μm photon. In the first case, if the local placental starburst field has $U_{\rm FIR} \sim 200$ eV (e.g., [152]), we obtain $n_\gamma \sim 1.6\times 10^4$ ph cm^{-3}; since $r^{\rm GMC} \sim 10$ pc, we finally get $\tau^{\rm GMC}_{\gamma\gamma} \sim 10^{-6}$. In the second case, setting (see [97]) $U_{\rm FIR} \sim 10\,U_{\rm CMB}$ (being $U_{\rm CMB} = 4.18\times 10^{-13}$ erg cm^{-3} the local energy density of the cosmic microwave background radiation) as a mean value in the star-forming galaxy, we obtain $n_\gamma \sim 200$ ph cm^{-3}; since $r^{\rm gal} \sim 10$ kpc, we finally get $\tau^{\rm GMC}_{\gamma\gamma} \sim 10^{-5}$. In both cases the optical depth to pair production is small enough (for a wide range of realistic values of the relevant physical parameters) to ensure that, once they are produced by hadronic illumination of the star-forming GMCs, the TeV gamma-ray photons emitted by SF-related stellar endproducts can safely reach Earth.

11.5 Diffuse TeV radiation in starburst galaxies

We have computed our Galaxy's superposed TeV emission from point sources, arguing it to be an indicator of star formation activity. We have next proposed a simple, but astrophysically motivated, scaling relation – calibrated on our Galaxy – that allows one to estimate the TeV point-source luminosity of a star-forming galaxy as a function of its (FIR luminosity which is a proxy for its) global SFR.

In addition to such integrated emission, truly diffuse TeV radiation can be produced by hadronic illumination of interstellar gas. The bombarding CR protons, once they have been accelerated to energies $\lesssim 10^{14}$ eV during SN explosions in star-forming regions, can leave the GMCs that harbor the SF sites and diffuse into the galaxy's general interstellar medium. In fact, the dense GMC material is transparent to proton diffusion: the total pp-interaction cross section is $\sigma_{\rm pp} \sim 10^2$ mb $= 10^{-25}$ cm^{-2} (see [79]), hence the optical depth to pp interaction while crossing the GMC is $\tau_{\rm pp} \sim \sigma_{\rm pp} n_{\rm p} r \sim 3 \times 10^{-4}$ (where $n_{\rm p} \sim 10^2$ cm^{-3} is the assumed average density of the target protons in the cloud, and $r \sim 10$ pc is the assumed cloud radius – see above). This ensures that the galaxy's ISM can be efficiently illuminated by such SN-accelerated, GMC-escaping CR protons. (This conclusion is experimentally quite obvious given the detection at Earth – i.e. outside a GMC – of CR protons in the appropriate energy range.) From Eq. 11.3 the expected level of this diffuse gas emission is:

$$L^{\rm gas}_{\geq \epsilon} = 2 \times 10^{37} (\epsilon/{\rm TeV})^{-1.1} (U_{\rm CR}/{\rm eV\,cm^{-2}}) (M^{\rm gas}/10^9 M_\odot) \text{ ph s}^{-1}. \quad (11.8)$$

For our Galaxy, if $M^{\rm gas} \sim 10^9 M_\odot$, the expected diffuse hadronic-channel TeV luminosity is $L^{\rm gas}_{\geq 0.2\,{\rm TeV}} \sim 1.2 \times 10^{38}$ ph s^{-1}, more than an order of magnitude higher than the collective luminosity from individual sources. Although the point-source and diffuse-gas emission share the same physical origin, i.e. SN-accelerated CR protons interacting with ambient atoms, the reason for the latter being higher is that the pp cross section is small enough that the whole Galaxy is transparent to CR protons, so the main variable for hadronic TeV emission is the total mass of target gas – which is relatively high in our Galaxy. At 1 Mpc, the corresponding flux would be $f^{\rm gas}_{\geq 0.2\,{\rm TeV}} \sim 10^{-12}$ ph cm^{-2} s^{-1}, i.e. within detectability by current imaging atmospheric Čerenkov arrays. The scaling of this diffuse emission with SFR can be thought of as being conceptually similar to the TP emission case. Since $U_{\rm CR} \propto \dot{\rho}_{\rm SFR}$ and $n \propto (\dot{\rho}_{\rm SFR})^{1/\eta}$ with $\eta \sim 1.5$, integration over galaxy volume yields $L^{\rm gas}_{\geq \epsilon} \propto {\rm SFR}^{1+1/\eta}$. So, if star-forming galaxies constitute a homologous sequence, then the TP-to-gas TeV emission ratio is expected to be (roughly) constant with SFR (or FIR luminosity, or gas mass).

Table 11.1: Data I: Sample 1

Source[a]	l, b[b]	$f^{(c)}_{\geq 0.2\,\mathrm{TeV}}$	Γ[d]	Notes[e]	Offset[f]	D[g]
HESS J1614-518	331.52, −0.58	57.8	2.46 ± 0.20			
HESS J1616-508	332.39, −0.14	43.3	2.35 ± 0.06	PSR J1617−5055 (PWN)	10.4	6.5
HESS J1632-478	336.38, +0.19	28.7	2.12 ± 0.20	IGR J16320−4751 (XRB)	3	
HESS J1634-472	337.11, +0.22	13.4	2.38 ± 0.27	IGR J16358−4726 (XRB) / G337.2+0.1 (SNR)	13 / 10	... / 14
HESS J1640-465	338.32, −0.02	20.9	2.42 ± 0.15	G338.3−0.0 (SNR) / 3EGJ1639−4702 (UID)	0 / 34	8.6
HESS J1702-420	344.26, −0.22	15.9	2.31 ± 0.15			
HESS J1708-410	345.67, −0.44	8.8	2.34 ± 0.11			
HESS J1713-381	348.65, −0.38	4.2	2.27 ± 0.48	G348.7+0.3 (SNR)	0	10.2
HESS J1745-303	358.71, −0.64	11.2	1.82 ± 0.29	3EGJ1744−3011 (UID)	10	...
HESS J1804-216	8.40, −0.03	53.2	2.72 ± 0.06	G8.7−0.1 (SNR) / PSR J1803−2137 (PWN)	21 / 10.8	6 / 3.9
HESS J1813-178	12.81, −0.03	14.2	2.09 ± 0.08	G12.82−0.02 (SNR)	0	4
HESS J1825-137	17.78, −0.74	39.4	2.46 ± 0.08	PSR J1826−1334 (PWN) / 3EGJ1826−1302 (UID)	11 / 43	3.9 / ...
HESS J1834-087	23.24, −0.32	18.7	2.45 ± 0.16	G23.3−0.3 (SNR)	0	4.8
HESS J1837-069	25.18, −0.11	30.4	2.27 ± 0.06	AXJ1838.0−0655 (UID)	6	...

[a] Source name. [b] Galactic coordinates (l: longitude; b: latitude), in degrees and fractions of a degree. [c] Measured photon flux above 0.2 TeV, in 10^{-12} ph cm^{-2} s^{-1}. [d] Photon spectrum power-law index. [e] Possible identifications (and class) of source. Class codes are: PWN, pulsar wind nebula; XRB, massive X-ray binary; SNR, supernova remnant; UID, unidentified. [f] Offset between HESS source and proposed identification, in arcmin. [g] Distance (from the Sun) of proposed identification, in kpc. All data are from Aharonian et al., 2005a [1].

Table 11.2: Data II: Sample 2

Source[a]	b[b]	D[c]	$\epsilon_{\rm min}$[d]	$f_{\geq\epsilon_{\rm min}}$[e]	Γ[f]	$f_{\geq 0.2\,\rm TeV}$[g]	$L_{\geq 0.2\,\rm TeV}$[h]	Notes[i]	References[j]
HESS J1826−148	−0.8	3.2	0.25	5.1E−12	2.12	6.4E−12	7.9E+33	LS 5039	[3]
PSR B1259−63	−1	1.5	0.38	4.0E−12	2.7	1.2E−11	3.2E+33		[4]
RX J0852.0−4622	−1.2	0.5	1	2.0E−11	2.1	1.2E−10	3.5E+33	G266.2−1.2	[5]
HESS J1303−631	0	2.1−7.7	0.38	1.2E−11	2.44	3.0E−11	(1.6−21.6) E+34		[6]
MSH 15−52	−1.2	5.2	0.28	2.3E−11	2.27	3.5E−11	1.2E+35	G320.4−1.2	[7]
TeV J2032+4130	1.5		1	7.0E−13	2.0	3.5E−12			[8]
G0.9+0.1	0.1	8.5	0.20	5.7E−12	2.4	5.7E−12	5.0E+34		[9]
SNR RXJ1713.7−3946	−0.5	1	1	1.5E−11	2.2	1.0E−10	1.3E+34	G347.3−0.5	[12]
Sagittarius A*	0	7.5	0.165	1.8E−11	2.2	1.4E−11	9.7E+34		[13]
Crab (pulsar, nebula)	−1.3	2	0.316	1.1E−10	2.6	2.3E−10	1.1E+35	M 1	[14]

[a] Source name. [b] Galactic latitude, in degrees and fractions of a degree. [c] Distance (from the Sun), in kpc. [d] Lower energy threshold, in TeV. [e] Measured photon flux above $E_{\rm min}$, in ph cm^{-2} s^{-1}. [f] Measured spectral photon index. [g] Derived photon flux above 0.2 TeV, in ph cm^{-2} s^{-1}. [h] Derived photon luminosity above 0.2 TeV, in ph s^{-1}. [i] Other names, or identifications, of source. [j] References: [2] Aharonian et al., 2005b; [3] Aharonian et al., 2005c; [4] Aharonian et al., 2005d; [5] Aharonian et al., 2005e; [6] Aharonian et al., 2005f; [7] Aharonian et al., 2005g; [8] Aharonian et al., 2005h; [11] Aharonian et al., 2004a; [12] Aharonian et al., 2004b; [13] Aharonian et al., 2004c.

11.6 Neutralino annihilation induced TeV emission in star-forming galaxies

A further source of diffuse emission might be the annihilation radiation by non-baryonic dark matter (DM). The continuum spectrum of gamma-rays produced by neutralino annihilation in galatic halos extends from some tens of GeV to a few TeV, so it may significantly contribute to the VHE gamma-ray emission of star-forming galaxies.

As discussed in the previous chapter, the production of VHE gamma-rays above 100 GeV is allowed for massive WIMPs. In the case of a bino-like neutralino which annihilates through the exchange of a light stau, the dominant annihilation channel is $\tau^+\tau-$, while in the case light squarks are involved the final states are $b\bar{b}$ and $t\bar{t}$. Moreover, for the pure-wino and pure-higgsino models the dominant channels are W^+W^- and ZZ.

Again, the normalization of the gamma-ray spectrum of star-forming galaxies depends on the halo mass profile and concentration. Considering a spherically symmetric, smooth halo mass distribution, the isotropic gamma-ray flux from a generic galaxy located at a distance d from the Milky Way is given by Eq. 4.2, 4.3 and 4.4. In Section 11.8 we will calculate the TeV flux of the local star-forming galaxy M 31 (the Andromeda galaxy).

11.7 Star-forming galaxies: a nearby example

Star formation, which mostly occurs in disk and irregurar galaxies, can proceed over a vast range of rates ($0.1 \lesssim \mathrm{SFR} \lesssim 1000\ \mathrm{M_\odot\ yr^{-1}}$). As a reference, our Galaxy has $\mathrm{SFR} \sim 2\ \mathrm{M_\odot\ yr^{-1}}$. Starburst galaxies and ultraluminous IR galaxies ($L_{\mathrm{IR}} \gtrsim 10^{12}\, L_\odot$) are dominated by star-formation activity [156].
The very nearby Andromeda galaxy, M 31, is in many ways akin to our Galaxy: in particular, $\mathrm{SFR} \sim 1\ \mathrm{M_\odot\ yr^{-1}}$.

11.7.1 The Andromeda galaxy

General morphological and structural properties.
Andromeda is the largest member of the Local Group of galaxies, which includes the Milky Way and its satellite galaxies. This galaxy is also frequently referred to as M 31 or NGC 224 and its own satellites include M 32, at center left of Fig. 11.1, and M 110, at lower right. This is a large spiral type Sb galaxy with two arms and a bright disk

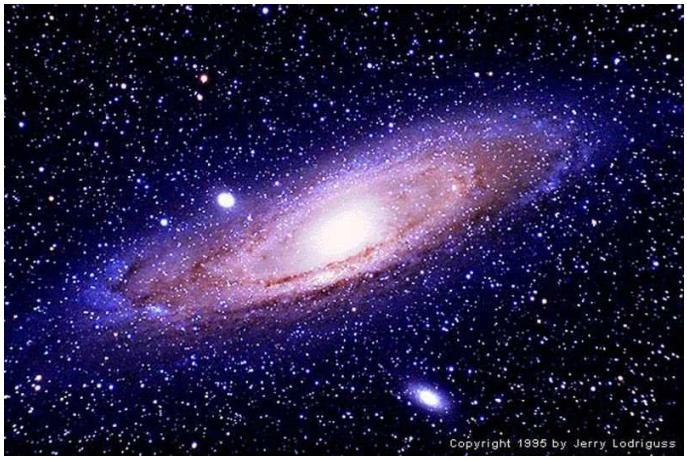

Figure 11.1: The Andromeda galaxy.

that is now believed to span as much as 69.9 kpc in width [58]. In 2005, astronomers announced that Andromeda's disk actually extends far further out, so that the disk spans at least 79.7 kpc [111]. The outer disk emits nearly 10 percent of the galaxy's total light and may be comprised of metal-poor stars stripped from smaller galaxies that strayed too close. Careful estimates of obtained Andromeda's angular diameter indicated that its disk had a diameter of over 61.3 kpc. Hence, Andromeda's spiral disk may be as much as twice as large as the Milky Way's. Although Andromeda was long thought to be the most massive galaxy in the Local Group, recent data suggest that Andromeda's visible mass may be $M_{bar} \sim 3 - 4 \cdot 10^{11}$ $M_\odot$. This is considerably less than recent estimates suggest for the Milky Way's visible mass, which then would be much denser than Andromeda's. These results apparently have been confirmed by recent estimates of the total halo masses of the two spirals, which suggest that Andromeda has a $M_{halo} \sim 0.7 - 1.2 \cdot 10^{12}$ $M_\odot$, while our Galaxy has $M_{halo} \sim 10^{12}$ $M_\odot$. [86, 87]. A summary of the main properties of M 31 is given in Tab. 11.7.1.

Demography.

M 31 has a bright yellowish nucleus, dark winding dustlanes, and bluish spiral arms and star clusters. Young stars are probably being born in many dusty regions of Andromeda that are bright in infrared wavelengths, with many short-lived, but massive, blue stars. Furthemore, star formation in M 31 is largely concentrated in an annulus about 10 kpc from the center, where the cosmic-ray rate is expected to be enhanced. The star formation rate range from 0.5 to 1 solar masses per year, and the supernova rate is estimated to be about 1.2 per century, leading to the discovery of a significant number of supernova remnants − more than 200 − by optical searches. So far, only

one supernova has been recorded in the Andromeda Galaxy, but it was the first to be detected outside the Milky Way. Known as *Supernova* 1885 for the year of its appearance, it has also been designated as *SAndromedae*. The supernova reached a magnitude of 6 between August 17th and 20th, but then faded to magnitude 16 by February 1890. M 31 has been observed in the X rays by ROSAT, leading to the discovery of 560 new sources, and in the inner part by XXM, which located 116 sources [15].

The active galactic nucleus.

In the 1990s, the Hubble Space Telescope and subsequent ground-based observations found that Andromeda has a nucleus with a double structure, with the 'nuclear hotspots' located close together, moving with respect to each other, and one nucleus slowly disrupting the other through tidal forces. This suggests that the great spiral consumed a major galactic companion whose substance has been mostly merged except for its central core. In 2005, astronomers using the Hubble Space Telecope announced that the two bright blobs are actually composed of an elliptical ring of older red stars and a smaller, brighter and denser disk of young blue stars around 200 million years old around the galaxy's central black hole [NASA press release]. Andromeda's core has a supermassive central black hole of around 140 million solar masses [latest NASA press release]. Recent observations with the Chandra X-Ray Observatory also revealed numerous other bright X-ray sources, most of which are probably due to binary systems where a star is feeding gas into a neutron star and a black hole.

Tab. 11.7.1. Main properties of M 31 (observation data epoch J2000.0).

Type	Sb
Right Ascension	$00^{\mathrm{h}}\ 42.7^{\mathrm{m}}$
Declination	$41^\circ\ 16'$
Zenith distance at culmination	13°
Distance	700–889 kpc
Radius	33.7 kpc
Redshift	-0.001
Apparent magnitude	$+3.4$
Absolute magnitude	-21.4
Total mass	$1.2 \cdot 10^{12}\ \mathrm{M}_\odot$
Mass/Luminosity ratio	12 ± 1
Apparent Dimension	$3.2^\circ \cdot 1.0^\circ$

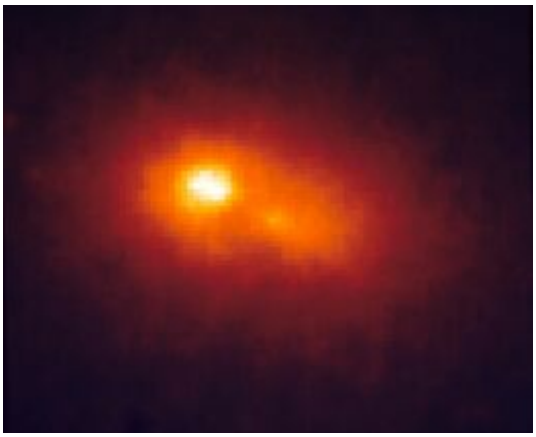

Figure 11.2: The galactic nucleus of M 31.

An unusually young galactic halo.
Unlike the Milky Way, Andromeda's halo includes many younger stars around 6 to 13 billion years old, which may have been stripped from companion galaxies or created from a galactic collision. In addition, a giant stream of metal-rich stars was recently detected in Andromeda's halo [112]. The presence of younger stars in Andromeda's halo may be the result of a more violent phase of the galaxy past involving mergers with smaller satellite galaxies. Furthermore, numerical simulations of the movements of Andromeda and the Milky Way suggest that the two big spiral galaxies themselves may eventually collide and merge within 5 to 10 billion years.

An old but bright globular cluster.
A small and compact satellite of Andromeda, G 1 is the brightest globular star cluster in the Local Group. Also known as Mayall II, G 1 contains at least 300.000 old stars. G 1 may have at least 10 to 18 million solar masses [134] and is located around 39.8 to 52.1 kpc from Andromeda's nucleus. It appears to be nearly as old as the oldest of the roughly 250 known globulars in the Milky Way and so probably was formed shortly after the birth of the first stars at the beginning of the Universe. Recently, some astronomers claimed to have discovered a 20.000 solar mass black hole in G 1's core [94].

According to the Greek mythology, Andromeda, the daughter of Orpheus king of Ethiopia and Cassiopeia, was rescued from Cetus, the Whale, by Perseus who later married her.

11.7.2 TeV gamma rays from M 31

Between August and September 2001, for the first time a survey for gamma-ray emission from TeV point-like sources in the Andromeda galaxy was performed by the HEGRA system of imaging atmospheric Čerenkov telescopes [15]. After data cleaning and a selection of good observation time of 20.1 hours, the greatest part of which taken at zenith angles below 25°, no excess of signal events was detected at levels over a few percent of the Crab flux. In spite of the lack of a real detection from this object, it has been possible to extract the upper limits of 3.3% of the Crab flux at the center of M 31 and about 30% at its periphery, referring to an energy of 1 TeV. Although this observation ruled out the discovery of a new population of VHE in the Andromeda starburst galaxy, the HESS survey of the Galactic plane in the region $|l| \geq 30°$, $|b| \geq 3°$, with the discovery of the 14 new sources at energies higher than 0.2 TeV listed in Tab. 11.1, probed the existence of such a class of sources in star-forming galaxies. While the survey of the whole Galactic sky with a Čerenkov telescope may be hardly possible, it is relatively easy to cover all of M 31 in searching of new TeV sources.

On this basis, we address the expectation concerning the visibility of VHE sources from Andromeda with the MAGIC telescope, in relation to the improved sensitivity of this instrument. Assuming a point-like source with a spectral index of 2.6, viewed at 0–30 zenith angle, and according to recent estimates of the MAGIC flux sensitivity (see Fig. 6.13 and [142]), we find the following **upper limits in 30 h at 5 sigma**:

E > 1 TeV: 0.029 Crab $= 5.2 \times 10^{-13}$ ph cm^{-2} s^{-1};

E > 200 GeV: 0.022 Crab $= 5.2 \times 10^{-12}$ ph cm^{-2} s^{-1}.

The first aim of this observation is to use the improved sensitivity of the telescope to obtain a more constrained upper limit on the collective Galactic point sources flux. It is manifest that if the caracteristics of VHE gamma-ray sources in other star-forming galaxies are similar to those in the Milky Way, the availability of observational data for the TeV flux from collective point sources in M 31, or better still for a sample of nearby galaxies, might permit to test the model proposed in Section 11.4, as well to gauge the star formation rate in the galaxy under study.

11.8 Different contributions to the TeV emission

The VHE gamma-ray emission from a star-forming galaxy is due to mainly three contributions:

- a non-baryonic contribution originating from the radiation of self-annihilating DM, consisting of two separate components: the signal from the smooth distribution, and the enhanced signal from the halo substructures;

- a first baryonic component due to the collective emission from TeV-point sources - which are evolutionary end-products of massive, bright, short-lived progenitor stars: these TeV sources are immediate products of the ongoing star formation activity;

- a second baryonic component which mainly results from the hadronic illumination of interstellar gas by the SN-accelerated cosmic-ray protons.

Baryonic component.
For an assumed distance of 770 kpc and a central area of radius 1.4 kpc, ∼10 times smaller than that surveyed by HESS in the Galactic Center, HEGRA-based upper limits [15] imply $L_{\geq 0.2\,\mathrm{TeV}} < 3.1 \times 10^{38}$ ph s^{-1} (for an assumed photon index of 2.5), well above the predicted value of 1.3×10^{36} ph s^{-1} based on Eq. 11.4 for SN rate that is estimated to be about half the Galactic value (see [15] and references therein). Furthermore, the HEGRA TeV survey found no indications for TPs in the Andromeda galaxy [15]: if the characteristics of such sources are similar in Andromeda and in the Milky Way, then typical fluxes $f_{\geq 0.2\,\mathrm{TeV}} \sim 2.5 \times 10^{-15}$ ph cm^{-2} s^{-1} should be expected from individual Andromeda TPs, i.e. signals which are only $\mathcal{O}(-3)$ of the sensitivity of current imaging atmospheric Čerenkov arrays such as HESS or MAGIC.
The level of diffuse emission from the hadron-illuminated gas in M 31 can be estimated from Eq. 11.8 and considering that, within our set of assumptions, $L^{\mathrm{gas}}_{\geq \epsilon} \propto \mathrm{SFR}^{1+1/\eta}$ with $\eta \sim 1.5$ and SFR being approximately half the Milky Way's. This leads to $f^{\mathrm{gas}}_{\geq 0.2\,\mathrm{TeV}} \sim 0.4 \cdot 10^{38}$ ph s^{-1}.

Non-baryonic component.
The dark matter contributions to the TeV gamma-ray flux from the Andromeda starburst galaxy are modeled as follows: for what the subhalo component is concerned, we assume that substructures follow the distribution function described in Chapter 2, modeling the dark matter distribution in both the host halo and the subhalos with a

NFW profile, with concentration parameter following Bullock et al. According with very recent results [95], we adopt for M_{100} the value of 7.5×10^{11} $M_\odot$ [6]. We evaluate the two dark matter signals by mean of Eq. 4.2, 4.3 and 4.4, where the integration is performed on the line of sight and the flux in mediated on the MAGIC point spread function (PSF), assuming an inner and outer truncation radius for the profile of 10^5 kpc and equal to the virial radius respectively.

In order to correctly model the dynamics of the galaxy, a **realistic mass model** is needed. In principle, a detailed mass model of M 31 ought to comprise of several components: the central black hole, the nucleus, the bulge, the bar, the spheroid, the thick and thin stellar disks and the thin gaseous disk. Following [95], we restrict the description of the baryonic component to only three contributions: the central BH, the bulge and the disk.

* **The Central Black Hole.** The very central region of M 31 is comprised of a central BH and a distinct small-scale stellar nuclear component that is photometrically and dynamically separate from the bulge and the large-scale galactic disk. The most recent estimate of the BH mass is $M_\bullet = (5.6 \pm 0.7) \times 10^7$ $M_\odot$, while the mass of the stellar component is estimated to be $\lesssim 2\times10^7$ $M_\odot$ within ~ 10 pc. In terms of the total M 31 potential, the two nuclear components are only relevant on scales $r < 20$ pc and, for all practical purposes, can be ignored in the context of the calculations of interest to us. However, to facilate wider use of the present M 31 model, we include the dynamically more important of the two, the BH component, in the form of a point mass located at the center of the galaxy, and fix its mass to the value quoted above.

* **The Galactic Bulge.** The bulge of M 31 is modeled as the spherically symmetric mass distribution represented by a Hernquist profile:

$$M_b(r) = \frac{M_b\, r^2}{(r_b + r)^2}, \tag{11.9}$$

where $M_b = 3.3 \times 10^{10}$ $M_\odot$ is the total mass of the bulge, $r_b = 0.61$ kpc is its scale radius and all parameters are assigned here by adopting their best fit values, as given in [95].

[6] We define M_Δ as the mass enclosed with the sphere of radius R_Δ such that the mean density inside is $\Delta\rho_c$, where $\Delta = 100$ or 200 and $\rho_c = 277.72\ h^2$ $M_\odot$ kpc^2 is the present-day critical density.

∗ **The Galactic Disk.** In order to model the M 31 galactic disk, we begin by assuming that the disk mass distribution can be described by an exponential surface density profile:

$$\sigma_d(R) = \sigma_0 e^{-R/R_d}, \tag{11.10}$$

where $\sigma_0 = 4.6 \times 10^8$ $M_\odot$ kpc^{-2} is the central surface density, $R_d = 5.4$ kpc is the scale length of the disk, and R is the distance from the centre of M 31 in the plane of the disk (best fit values in [95].) This corresponds to a disk mass within a sphere of radius r of

$$M_d(r) = 2\pi\sigma_0 R_d^2 \left[1 - (1 + r/R_d)e^{-r/R_d}\right]. \tag{11.11}$$

Here, $r = \sqrt{R^2 + z^2}$ is the distance from the centre of M 31 and z is the distance perpendicular to the plane of the disk.

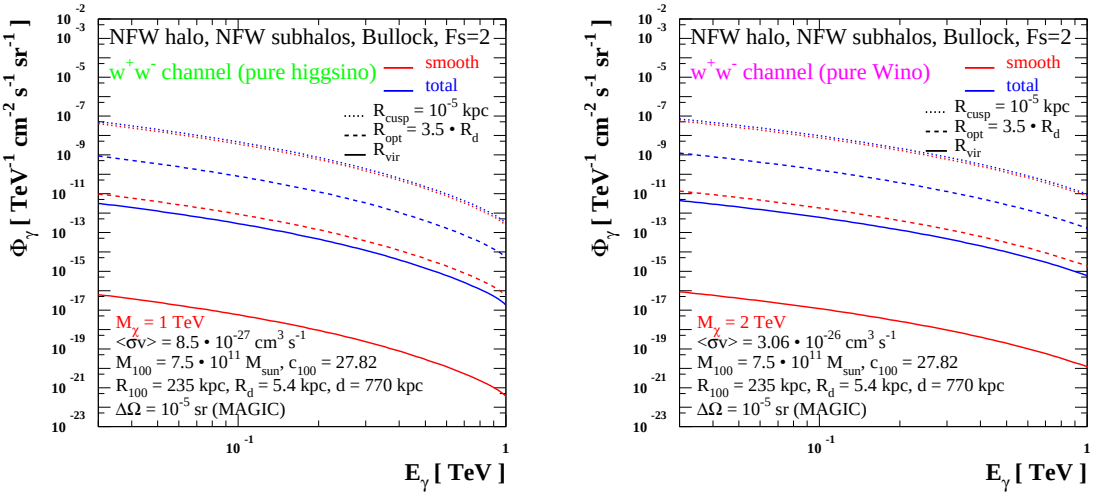

Figure 11.3: Differential spectra from neutralino TeV gamma-ray emission from the Andromeda galaxy. A NFW universal shape profile is assumed, with concentration parameter in substructures being equal to the concentration in halos of equal mass (parameter $F_s = 2$), as extrapolated with the Bullock et al. prescription. Annihilation is modeled into pure higgsino (*left panel*) and pure wino (*right panel*) final states. Rates from the center of the halo, from the optical and the virial radius are evaluated. Baryons data are taken from [95]. (Figure by Bisesi & Persic, 2007 [43]).

Fig. 11.3 shows results for three different distances from the center of Andromeda, respectively the inner truncation radius supposed to be corresponding to the central

cusp of the halo, the optical radius $R_{opt} = 3.5\, R_d$, and the virial radius. Moreover, the two extreme cases of neutralino annihilation into pure higgsino and pure wino final states are considered, showing remarkable differences in the differential gamma-ray spectrum up to 0.1 TeV, with the wino channel being the stronger.

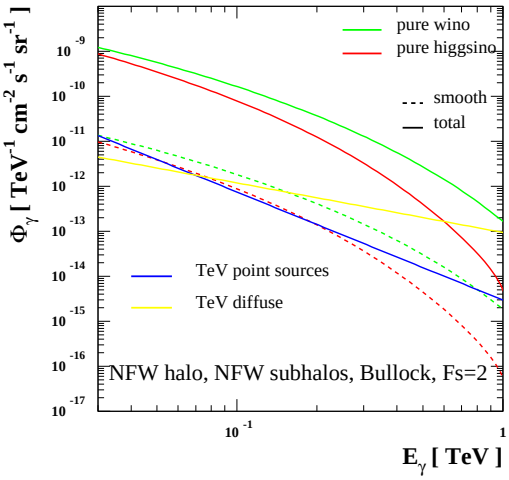

Figure 11.4: Non baryonic dark matter, baryonic point sources and baryonic diffuse TeV emission from the Andromeda galaxy, evaluated at the optical radius $R_{opt} = 3.5\, R_d$. For the dark matter component, a NFW universal shape profile is assumed, with concentration parameter in substructures being equal to the concentration in halos of equal mass (parameter $F_s = 2$), as extrapolated with the Bullock et al. prescription. Baryons data are taken from [95]. (Figure by Bisesi & Persic, 2007 [43]).

Fig. 11.4 shows the superimposed three emissions at the optical radius, where a very interesting feature seems to occur. We point out that this represents the most promising region where to try separating the signal coming from subhalos from that emitted by the smooth component: in fact, in the innermost part of the galaxy the cusp largely dominates over any other contribution, while at the boundaries of the source the baryonic fluxes are very much suppressed, due to the very small amount of matter in that region. Getting deeply into investigation about the role of baryonic contributions at the optical radius, we seek for the opportunity to treat them as a reducible background to be subtracted from the total signal. As we can see in the figure, up to energies of 0.1 TeV the diffuse TeV component overcomes the TPS one, dominating it by more than one order of magnitude at energies of 1 TeV. Anyway, the very remarkable fact is that at lower energies both components are comparable or slightly lower than the smooth dark matter signal, becoming fully comparable

with it and even largely predominant in the upper part of the spectrum. This would turn the task of separating a purely smooth dark matter signal from the baryonic background a very hard one: that points to the role of substructures as a unique feature to overcome the problem.

11.9 Conclusions

In this conclusive work, we have considered the effect of the superimposition of the baryonic component to the dark matter signal in external starburst galaxies. For the former, we have generalized our knowledge of the Milky Way to other star-forming galaxies using the star-formation rate as a scaling variable, estimating the differential specrum for both the TeV point sources contribution and the diffuse TeV background. Finally, the dynamical evolution model for substructures proposed in the first part of this Thesis has been applied to a specific case of star-forming galaxy different than the Milky Way, the Andromeda galaxy, to predict the TeV emission from neutralino annihilation (into pure higgsino and pure wino final states). The results seem very promising at the optical radius, where the chance to separate the two dark matter components are quite good, because the spectral signature of baryons is very different from those of the two dark matter distributions: the baryonic signal would act as an undesired background of comparable strenght if only the smooth halo component is considered, but it becomes a (sub)tractable background when, more realistically, the subhalo component, too, is considered.

Chapter 12

Conclusions and Outlook

The main aim of this work, as well as of the whole journey of my Ph.D. training, has been to try to understand some features of the current cosmological picture of the Universe. One of the most powerful opportunities offered by contemporary cosmology is the availability of observational data able to provide essential constraints to theoretical and phenomenological models (*precision cosmology*). Moreover, the recent extraordinary developements in computer science allow scientists to build progressively more realistic, and hence complex, models. For the ambitious goal to learn as much as possible in the various areas covered in my Thesis, I carried a work that turned out to be both theoretical and experimental. I thought this interdisciplinary effort was really fascinating!

A summary of this work may be as follows:

- great importance was given to studying and understanding the main properties of dark matter in galaxies, focusing on its role in the evolution of cosmic structures (Chapter 2);

- an estimate was given of the enhancement, due to the halo's clumpy structure, of the gamma and cosmic-ray signals produced by the neutralino annihilation in the Galaxy (Chapter 4);

- the proposal that some unidentified EGRET sources may be DM clumps in the Galactic halo was quantitatively evaluated, and the structural properties of such sources were constrained based on observational data (Chapter 5);

- my Ph.D. training included learning several aspects involved in operating the MAGIC Telescope, including the data taking at the Roque de Los Muchachos Observatory and the acquisition of data processing techniques during bootcamps. As a consequence of this, I participated in a proposal of observation,

followed by data analysis of the Crab Nebula and 3EG_J1835+5918 (Chapters 7 to 9);

- I provided a review of current structure models and neutralino-annihilation flux predictions highlighted the role of the Draco dwarf spheroidal galaxy as the current leading candidate for DM detection by Cherenkov techniques (Chapter 10);

- the final part of the work gave me the opportunity to make a foray into extragalactic astrophysics, dealing with the issue of the simultaneous presence of different types, baryonic and non-baryonic, of TeV emitters. (Chapter 11).

"Alles Vergängliche
Ist nur ein Gleichnis;
Das Unzulängliche,
Hier wird's Ereignis;
Das Unbeschreibliche,
Hier ist's getan;
Das Ewigweibliche
Zieht uns hinan."

(Faust, Ch. Myst.)

Acknowledgements

I am grateful to my supervisor, Prof. Alessandro De Angelis, without whose help and support the present work could not even get started. A grateful thank to the two persons, Piero Ullio and Massimo Persic, who followed me in reaching the main results of this Thesis.

I am endebted to all the many people who so kindly and friendly helped me in learning and performing the MAGIC data analysis: Hendrik Bartko, Michele Doro, Saverio Lombardi, Pratik Majumdar, Mosè Mariotti, Abelardo Moralejo, Elisa Prandini, Villi Scalzotto, Nadia Tonello, Robert Wagner, Wolfgang Wittek, Fabio Zandanel. Being a member of the MAGIC Collaboration has offered me a memorable opportunity to work in an experimental group. Thanks to all you! In particular, I cherish a very good memory of my first observational experience at the Roque de Los Muchachos, where Dorota Sobczynska introduced me to the secrets of telescope operations. And thanks also to the Zürich's Dark Matter Working Group friends, Adrian Biland and Sabrina Stark, who organized annual meetings at ETH.
Many thanks to all people who dedicated time to discussions and contribute in some way to the technical aspects of this work: among them, Gianfranco Bertone, Stefano Borgani, Josè Flix, Andrea Lapi, Francesco Longo, Stefano Profumo, Paolo Salucci, Francesco Shankar.
During my PhD training, I spent some time abroad. I thank Prof. Lars Bergström for kindly hosting and supporting me at Stockholm University, and Joachim Edsjö for very useful discussions.
This work would not have been possible without the help of the Udine Department of Physics and SISSA Informatics staffs. I feel a particular care for Oriana Mansutti and Federico Onofrio, for the patience and generosity demonstrated in the final stages of this way.

This Thesis work is dedicated with gratitude to the most important persons of my life, so indispensably participating in the many steps (not always easy!) which led my PhD experience to this conclusion.

Gazie papà, grazie mamma: credo che senza la fiducia che avete saputo trasmettermi lungo tutto il percorso della mia vita questa, nè altre imprese, sarebbero potute essere più che un sogno. E soprattutto grazie a te, David, per avermi dato una dimostrazione di affetto così sincera e profonda.

Bibliography

[1] Aharonian, F.A. & al. (HESS Collab.): A Low Level of Extragalactic Background Light as Revealed by Gamma-Rays from Blazars. *Nature* **440**, 1018 (2006).

[2] Aharonian, F.A. & al. (HESS Collab.): The HESS Survey of the Inner Galaxy in Very High-Energy. *ApJ* **636**, 777 (2006).

[3] Aharonian, F.A. & al. (HESS Collab.): Discovery of Very High Energy Gamma Rays Associated with an X-ray Binary. *Science* **309**, 746 (2005).

[4] Aharonian, F.A. & al.: Discovery of the Binary Pulsar PSR B1259-63 in Very-High-Energy Gamma Rays around Periastron with HESS. *A&A* **442**, 1 (2005).

[5] Aharonian, F.A. & al. (HESS Collab.): Detection of TeV γ-Ray Emission from the Shell-Type Supernova Remnant RX J0852.0-4622 with HESS. *A&A* **437**, 7 (2005).

[6] Aharonian, F.A. & al. (HESS Collab.): Serendipitous Discovery of the Unidentified Extended TeV γ-Ray Source HESS J1303-631. *A&A* **439**, 1013 (2005).

[7] Aharonian, F.A. & al. (HESS Collab.): Discovery of Extended VHE Gamma-Ray Emission from the Asymmetric Pulsar Wind Nebula in MSH 15-52 with HESS. *A&AL* **435**, 17 (2005).

[8] Aharonian, F.A. & al. (HEGRA Collab.): The Unidentified TeV Source (TeV J2032+4130) and Surrounding Field: Final HEGRA IACT-System Results. *A&A* **431**, 197 (2005).

[9] Aharonian, F.A. & al. (HESS Collab.): Very High Energy Gamma Rays from the Composite SNR G 0.9+0.1. *A&AL* **432**, 25 (2005).

[10] Aharonian, F.A. & al. (HESS Collab.): A Possible Association of the New VHE Gamma-Ray Source HESS J1825-137 with the Pulsar Wind Nebula G18.0-0.7. *A&AL* **442**, 25 (2005).

[11] Aharonian, F.A. & al. (HESS Collab.): A Search for Very High Energy γ-Ray Emission from the Starburst Galaxy NGC 253 with HESS. *A&A* **442**, 177 (2005).

[12] Aharonian, F.A. & al. (HESS Collab.): High-Energy Particle Acceleration in the Shell of a Supernova Remnant. *Nature* **432**, 75 (2004).

[13] Aharonian, F.A. & al. (HESS Collab.): Very High Energy Gamma Rays from the Direction of Sagittarius A. *A&AL* **425**, 13 (2004).

[14] Aharonian, F.A. & al. (HEGRA Collab.): The Crab Nebula and Pulsar between 500 GeV and 80 TeV: Observations with the HEGRA Stereoscopic Air Čerenkov Telescopes. *ApJ* **614**, 897 (2004).

[15] Aharonian, F.A. & al. (HEGRA Collab.): Search for TeV Gamma-Ray Emission from the Andromeda Galaxy. *A&A* **400**, 153 (2003).

[16] Aharonian, F.A.: Gamma Rays From Molecular Clouds. *Space Sci. Rev.* **99**, 187 (2001).

[17] Akerib, D.S. & al.: Limits on Spin-Independent Interactions of Weakly Interacting Massive Particles with Nucleons from the Two-Tower Run of the Cryogenic Dark Matter Search. *Phys. Rev. L* **96**, 011302 (2006).

[18] Alam, S.M.K., Bullock, J.S. & Weinberg, D.H.: Dark Matter Properties and Halo Central Densities. *ApJ* **572**, 34 (2002).

[19] Albert i Fort & al. (MAGIC Collab.): MAGIC Observations of Very High Energy Gamma-Rays from HESS J1813-178. *ApJL* **637**, 41 (2006).

[20] Albert i Fort & al. (MAGIC Collab.): The MAGIC Project, Part 3. MAGIC Detector and Analysis Details. In: *Contributions to the 29th ICRC 2005*, Pune, India (2005). Preprint: astro-ph/0508274.

[21] Alcock, C. & al.: The MACHO Project: Microlensing Results from 5.7 Years of Large Magellanic Cloud Observations. *ApJ* **542**, 281 (2000).

[22] Aparicio, A., Carrera, R. & Martinez-Delgado, D.: The Star Formation History and Morphological Evolution of the Draco Dwarf Spheroidal Galaxy. *AJ* **122**, 252A (2001).

[23] Atkins, R.W. & al. (MILAGRO Collab.): Milagrito, a TeV Air-Shower Array. *Nucl. Instrum. Meth.* **A449**, 478 (2000).

[24] Baer, H. & Balazs, C.: χ^2 Analysis of the Minimal Supergravity Model Including WMAP, $g(\mu) - 2$ and $b \to \gamma$ Constraints. *JCAP* **0305**, 006 (2003).

[25] Baltz, E.A. & Wai, L.: Diffuse Inverse Compton and Synchrotron Emission from Dark Matter Annihilations in Galactic Satellites. *Phys. Rev. D* **70**, 023512 (2004).

[26] Baltz, E.A. & Edsjö, J.: Positron Propagation and Fluxes from Neutralino Annihilation in the Halo. *Phys. Rev. D* **59**, 3511 (1999).

[27] Bardeen, J.M., Keiser, J.R. & Szalay, A.S.N.: The Statistics of Peaks of Gaussian Random Fields. *ApJ* **304**, 15 (1986).

[28] Bartko, H. & al.: Dark Matter Observations in Draco. *Proposal of observation for the MAGIC Telescope* (2006).

[29] Battaglia, M. & al.: Updated Post-WMAP Benchmarks for Supersymmetry. *EPJC* **33**, 273 (2004).

[30] Benson, A.J. & al.: Heating of Galactic Discs by Infalling Satellites. *MNRAS* **351**, 1215 (2004).

[31] Benson, A.J. & al.: The Effects of Photoionization on Galaxy Formation - II: Satellites in the Local Group. *MNRAS*, **333**, 177 (2002).

[32] Bergström, L. & Hooper, D.: Dark Matter and Gamma-Rays From Draco: MAGIC, GLAST and CACTUS. *Phys. Rev. D* **73**, 3510 (2006).

[33] Bergström, L.: Non-Baryonic Dark Matter: Observational Evidence and Detection Methods. *Rep. Prog. Phys.* **63**, 793 (2000).

[34] Bergström, L., Edsjö, J. & Ullio, P.: Cosmic Antiprotons as a Probe for Supersymmetric Dark Matter? *ApJ* **526**, 215 (1999).

[35] Bergström & al.: Clumpy Neutralino Dark Matter. *Phys. Rev. D* **59**, 043506 (1999).

[36] Bergström, L., Ullio, P. & Buckley, J.H.: Observability of Gamma-Rays from Dark Matter Neutralino Annihilations in the Milky Way Halo. *Astropart. Phys.* **9**, 137 (1998).

[37] Bergström, L. & Snellman, H.: Observable Monochromatic Photons from Cosmic Photino Annihilation. *Phys. Rev. D* **37**, 3737 (1988).

[38] Bertone, G. & al.: New Signature of Dark Matter Annihilations: Gamma Rays from Intermediate-Mass Black Holes. *Phys. Rev. D* **72**, 103517 (2005).

[39] Bertone, G., Hooper, D. & Silk, J.: Particle Dark Matter: Evidence, Candidates and Constraints. *Phys. Rep.* **405**, 279 (2005).

[40] Binney, J. & Tremaine, S.: Galactic Dynamics, 428. Princeton Univ. Press, Princeton (1987).

[41] Binney, J. & Mamon, G.A.: M/L and Velocity Anisotropy from Observations of Spherical Galaxies, or Must M87 Have a Massive Black Hole. *MNRAS* **200**, 361 (1982).

[42] Bisesi, E. & Ullio, P.: Substructures in the Milky Way and Prospects to Detect Dark Matter, to be submitted (2007).

[43] Bisesi, E. & Persic, M.: Point-Source TeV Luminosity of Starbursts, to be submitted (2007).

[44] Bisesi, E.: Populations of Subhalos in Cold Dark Matter Halos. In: De Angelis, A. & Mansutti, O., *Proceedings of the Third Workshop on Science with the New Generation of High Energy Gamma-Ray Experiments*, Cividale del Friuli (Italy), May 30$^{\text{th}}$ - June 1$^{\text{st}}$, 2005, p. 125, World Scientific Publishing Co.Pte.Ltd. (2006).

[45] Bisesi, E.: The Impact of Subhalos on the Gamma-Ray Signal from Dark Matter Annihilation. In: *Astrophysics and Space Science volume 'The Multi-Messenger Approach to High-Energy Gamma-Ray Sources (Third Workshop on the Nature of Unidentified High-Energy Sources)'*, Barcelona, July 4-7$^{\text{th}}$, 2006, in press.

[46] Bisesi, E., Mariotti, M. & Scalzotto, V.: Dark Matter Detection in Gamma Astroparticle Experiments. In: *Proceedings of the 6$^{\text{th}}$ International Symposium 'Frontiers of Fundamental and Computational Physics' (FFP6)*, Udine (Italy), Sep. 26-29$^{\text{th}}$, 2004, p. 315. Preprint: astro-ph/0503535.

[47] Blais-Ouellette, S., Amram, P. & Carignan, C.: Accurate Determination of the Mass Distribution in Spiral Galaxies. II. Testing the Shape of Dark Halos. *AJ* **121**, 1952 (2001).

[48] Blais-Ouellette, S. & al.: Accurate Parameters of the Mass Distribution in Spiral Galaxies. I. Fabry-Perot Observations of NGC 5585. *AJ* **118**, 2123 (1999).

[49] Blandford, R.D. & Ostriker, J.P.: Particle Acceleration by Astrophysical Shocks. *ApJL* **221**, 29 (1978).

[50] Blitz, L.: Giant Molecular Clouds. In: Levy, E.H. & Lunine, J.I.: *Protostars and Planets III*, 125 University of Arizona, Tucson (1993).

[51] Blom, J.J., Paglione, T.A.D. & Carramiñana, A.: Diffuse Gamma-Ray Emission from Starburst Galaxies and M31. *ApJ* **516**, 744 (1999).

[52] Bonanos, A.Z. & al.: The First DIRECT Distance to a Detached Eclipsing Binary in M33. *Astrophysics and Space Science* **304**, 207 (2006).

[53] Bottino, A. & al.: Antiproton Fluxes from Light Neutralinos. *Phys. Rev. D* **72**, 083518 (2005).

[54] Brunthaler, A. & al.: The Geometric Distance and Proper Motion of the Triangulum Galaxy (M33). *Science* **307**, 1440 (2005).

[55] Bullock, J.S. & al.: Profiles of Dark Haloes: Evolution, Scatter and Environment. *MNRAS* **321**, 559 (2001).

[56] Bullock, J.S., Kravtsov, A.V. & Weinberg, D.H.: Reionization and the Abundance of Galactic Satellites. *ApJ* **539**, 517 (2000).

[57] Burkert, A.: The Structure of Dark Matter Halos in Dwarf Galaxies. *ApJL* **447**, 25 (1995).

[58] Chapman, S.C. & al.: The Accretion Origin of a Vast Extended Stellar Disk Around the Andromeda Galaxy: Discovery of a New Component of Galaxies? *AAS* **226**, 2101 (2005).

[59] Chen, X.L., Kamionkowski M. & Zhang, X.M.: Kinetic Decoupling of Neutralino Dark Matter. *Phys. Rev. D* **64**, 021302 (2001).

[60] Chertok, A.: Search for Dark Matter Annihilation in Draco with CACTUS. *http://ucdcms.ucdavis.edu/solar2/results/Chertok.PANIC05.pdf.*

[61] Chevalier, R.A.: Supernova Remnants in Molecular Clouds. *ApJ* **511**, 798 (1999).

[62] Chiba, T. & Nakamura, T.: Feasibility of Reconstructing the Quintessential Potential Using Type Ia Supernova Data. *Phys. Rev. D* **62**, 121301 (2000).

[63] Chiba, T., Okabe, T. & Yamaguchi, M.: Kinetically Driven Quintessence. *Phys. Rev. D* **62**, 023511 (2000).

[64] Choi, K.: String or M Theory Axion as a Quintessence. *Phys. Rev. D* **62**, 043509 (2000).

[65] Colafrancesco, S., Profumo S. & Ullio, P.: Detecting Dark Matter WIMPs in the Draco Dwarf: a Multi-Wavelength Perspective (2006). Preprint: astro-ph/0607073.

[66] Colafrancesco, S., Profumo S. & Ullio, P.: Multi-Frequency Analysis of Neutralino Dark Matter Annihilations in the Coma Cluster. *A&A* **455**, 21 (2006).

[67] Côté, S., Carignan, C. & Freeman, K.C.: The Various Kinematics of Dwarf Irregular Galaxies in Nearby Groups and Their Dark Matter Distributions. *AJ* **120**, 3027 (2000).

[68] de Blok & al.: Mass Density Profiles of Low Surface Brightness Galaxies. *ApJL* **552**, 23 (2001).

[69] Dehnen, W. & Binney, J.: Local Stellar Kinematics from Hipparcos Data. *MNRAS* **298**, 387 (1998).

[70] Dehnen, W. & Binney, J.: Mass Models of the Milky Way. *MNRAS* **294**, 429 (1998).

[71] De Lucia, G. & al.: Substructures in Cold Dark Matter Haloes. *MNRAS* **348**, 333 (2004).

[72] Diemand, J., Moore, B. & Stadel, J.: Earth-Mass Dark-Matter Haloes as the First Structures in the Early Universe. *Nature* **433**, 389 (2005).

[73] Diemand, J. & al.: Cusps in Cold Dark Matter Halos. *MNRAS* **364**, 665 (2005).

[74] Domingo Santamaría E.: γ-Ray Emission from Regions of Star Formation. Theory and Observations with the MAGIC Telescope. *Ph.D. Thesis, University of Barcelona* (2006).

[75] Drury, L.O'C., Aharonian, F.A. & Volk, H.J.: The Gamma-Ray Visibility of Supernova Remnants. A Test of Cosmic Ray Origin. *A&A* **287**, 959 (1994).

[76] Dwek, E. & al.: Morphology, Near-Infrared Luminosity, and Mass of the Galactic Bulge from COBE DIRBE Observations. *ApJ* **445**, 716 (1995).

[77] Edsjö, J. & al.: Accurate Relic Densities with Neutralino, Chargino and Sfermion Coannihilations in mSUGRA. *J. Cosm. Astropart. Phys.* **04**, 001 (2003).

[78] Edsjö, J.: *Ph.D. Thesis, University of Uppsala* (1997). Preprint: astro-ph/9704384.

[79] Eidelman, S. & al.: Pion Form Factor Phase, $\pi\,\pi$ Elasticity and New e^+e^- Data. *Phys. Lett. B* **582**, 27 (2004).

[80] Eke, V.R., Navarro, J.F. & Steinmetz, M.: The Power Spectrum Dependence of Dark Matter Halo Concentrations. *ApJ* **554**, 114 (2001).

[81] Ellis, J.R. & al.: Likelihood Analysis of the CMSSM Parameter Space. *Phys. Lett. D* **69**, 095004 (2004).

[82] Ellis, J.R. & al.: Supersymmetric Dark Matter in Light of WMAP. *Phys. Lett. B* **565**, 176 (2003).

[83] Enomoto, R. & al.: Constraints on Cold Dark Matter in the Gamma-Ray Halo of NGC 253. *ApJ* **596**, 216 (2003).

[84] Esposito, J.A. & al.: In-Flight Calibration of EGRET on the Compton Gamma-Ray Observatory. *ApJS* **123**, 203 (1999).

[85] Evans, N.W.: No Need for Dark Matter in Galaxies? In: Spooner, N.J.C. & Kudryavtsev, V., *Proceedings of the 3rd International Workshop on the Identification of Dark Matter*, p. 85, World Scientific Publishing Co.Pte.Ltd. (2001).

[86] Evans, N. & al.: Dynamical Mass Estimates for the Halo of M31 from Keck Spectroscopy. *ApJ* **540**, 9 (2000).

[87] Evans, N. & Wilkinson, M.I.: The Mass of the Andromeda Galaxy. *MNRAS* **316**, 929 (2000).

[88] Falvard, A. & al.: Supersymmetric Dark Matter in M31: Can One See Neutralino Annihilation with CELESTE? *Astropart. Phys.* **20**, 467 (2004).

[89] Flores, R.A. & Primack, J.R.: Observational and Theoretical Constraints on Singular Dark Matter Halos. *ApJL* **427**, 1 (1994).

[90] Freudenreich, H.T.: A COBE Model of the Galactic Bar and Disk. *ApJ* **492**, 495 (1998).

[91] Fujita, Y. & al.: Analytical Approach to the Mass Distribution Function of Subhalos and Cold Fronts in Galaxy Clusters. *ApJ* **577**, 11 (2002).

[92] Gao, Y. & Solomon, P: The Star Formation Rate and Dense Molecular Gas in Galaxies. *ApJ* **606**, 271 (2004).

[93] Gaug, M.: Calibration of the MAGIC Telescope and Observation of Gamma-Ray Bursts. *Ph.D. Thesis, University of Barcelona* (2006).

[94] Gebhardt, K., Rich, R.M. & Ho, L.C.: A 20.000 $M_{\odot}$ Black Hole in the Stellar Cluster G1. *ApJ* **578**, 41 (2002).

[95] Geehan, J.J. & al.: Investigating the Andromeda Stream: I. Simple Analytic Bulge-Disk-Halo Model for M31. *Nature* **404**, 363 (2000).

[96] Gehrels, N. & al., *MNRAS* **366**, 996 (2006).

[97] Goldshmidt, O. & Rephaeli, Y.: Compton X-Ray Emission from NGC 253. *ApJ* **444**, 113 (1995).

[98] Gondolo, P. & al.: DarkSUSY: Computing Supersymmetric Dark Matter Properties Numerically. *JCAP* **07**, 008 (2004).

[99] Green, A.M., Hofmann, S. & Schwarz, D.J.: The First WIMPy Halos. *J. Cosm. Astropart. Phys.* **08**, 003 (2005).

[100] Grenier, I.A.: Gamma-Ray Sources as Relics of Recent Supernovae in the Nearby Gould Belt. *A&AL* **364**, 93 (2000).

[101] Häfner, R. & al.: A Dynamical Model of the Inner Galaxy. *MNRAS* **314**, 433 (2000).

[102] Hanna, D.S.: The STACEE-32 Ground Based Gamma-Ray Detector. *Nucl. Instrum. Meth.* **491**, 126 (2002).

[103] Hartman, R.C. & al.: The Third EGRET Catalog of High-Energy Gamma-Ray Sources. *ApJ* **123**, 79 (1999).

[104] Hayashi E. & al.: The Structural Evolution of Substructure. *ApJ* **584**, 541 (2003).

[105] Helou, G., Soifer, B.T. & Rowan-Robinson, M.: Thermal Infrared and Nonthermal Radio - Remarkable Correlation in Disks of Galaxies. *ApJL* **298**, 7 (1985).

[106] Hinton & al. (HESS Collab.): The Status of the HESS Project. *New Astron. Rev.* **48**, 331 (2004).

[107] Hofmann, W.: The Universe Viewed in Gamma Rays. In: *The HESS project* (2002).

[108] Hofmann, S., Schwarz, D.J. & Stoecker, H.: Damping Scales of Neutralino Cold Dark Matter. *Phys. Rev. D* **64**, 083507 (2001).

[109] Holder, J. & al., 2006 (VERITAS Collab.): Status and Performance of the First VERITAS Telescope. In: *Contributions to the 29th ICRC 2005*, Pune, India (2005). Preprint: astro-ph/0507451.

[110] Hughes, E.B. & al.: Characteristics of the Telescope for High Energy Gamma-Ray Astronomy Selected for Definition Studies on the Gamma Ray Observatory. *IEEE Trans. Nucl. Sci.* **27**, 364 (1980).

[111] Ibata, R. & al.: On the Accretion Origin of a Vast Extended Stellar Disk around the Andromeda Galaxy. *ApJ* **634**, 287 (2005).

[112] Ibata, R. & al.: A Giant Stream of Metal-Rich Stars in the Halo of the Galaxy M31. *Nature* **412**, 49 (2001).

[113] Kanbach, G.: The Project EGRET (Energetic Gamma-Ray Experiment Telescope) on NASA's Gamma-Ray Observatory (GRO). *Space Sci. Rev.* **49**, 69 (1989).

[114] Kanbach, G. & al., in Johnson, W.N., *Proceedings of the Gamma Ray Observatory Science Workshop*. Greenbelt, NASA (1988).

[115] Kane, G.L., Kolda, C.F., Roszkowski, L. & Wells, J.D.: Study of Constrained Minimal Supersymmetry. *Phys. Rev. D* **49**, 6173 (1994).

[116] Kawachi, A. & al.: The Optical Reflector System for the CANGAROO-II Imaging Atmospheric Čerenkov Telescope. *Astropart. Phys.* **14**, 261 (2001).

[117] Kennicutt, R.C., Jr.: The Global Schmidt Law in Star-Forming Galaxies. *ApJ* **498**, 541 (1998).

[118] Kent, S.M., Dame, T.M. & Fazio, G.: Galactic Structure from the Spacelab Infrared Telescope. II - Luminosity Models of the Milky Way. *ApJ* **378**, 131 (1991).

[119] Kitayama, T. & Suto, Y.: Semianalytic Predictions for Statistical Properties of X-Ray Clusters of Galaxies in Cold Dark Matter Universes. *ApJ* **469**, 480 (1996).

[120] Klypin, A., Zhao, H.S. & Somerville, S.: ΛCDM-Based Models for the Milky Way and M31 I: Dynamical Models. Preprint: astro-ph/0110390.

[121] Klypin & al.: Galaxies in N-Body Simulations: Overcoming the Overmerging Problem. *ApJ* **516**, 530 (1999).

[122] Klypin, A. & al.: Where Are the Missing Galactic Satellites? *ApJ* **522**, 82 (1999).

[123] Lang, K.R.: Astrophysical Formulae, Vol.1, 434. Springer, Berlin (1999).

[124] Lasserre, T. & al.: Not Enough Stellar Mass Machos in the Galactic Halo. *A&AL* **355**, 39 (2000).

[125] Lee, J.: The Formalism for the Subhalo Mass Function in the Tidal-Limit Approximation. *ApJL* **604**, 73 (2004).

[126] Li, T.P. & Ma, Y.Q.: Analysis Methods for Results in Gamma-Ray Astronomy. *ApJ* **272**, 317 (1983).

[127] Lokas, E.L. & Mamon, G.A.: Dark Matter Distribution in the Coma Cluster from Galaxy Kinematics: Breaking the Mass-Anisotropy Degeneracy. *MNRAS* **343**, 401 (2003).

[128] Lucarelli, E. & al.: Observations of the Crab Nebula with the HEGRA System of IACTs in Convergent Mode Using a Topological Trigger. *Astropart. Phys.* **19**, 339 (2003).

[129] Lucarelli, E. & al.: Limits on the TeV Flux of Diffuse Gamma Rays as Measured with the HEGRA Air Shower Array. *Astropart. Phys.* **17**, 459 (2002).

[130] Malhotra, S.: The Vertical Distribution and Kinematics of HI and Mass Models of the Galactic Disk. *ApJ* **448**, 138 (1995).

[131] Mashchenko, S., Couchman, H.M.P & Sills, A.: Modeling Star Formation in Dwarf Spheroidal Galaxies: a Case for Extended Dark Matter Halos. *ApJ* **624**, 726 (2005).

[132] Masterson, C. & al.: Observations of the Crab Nebula with the MAGIC Telescope. In: *Contributions to the 29th ICRC 2005*, Pune, India (2005).

[133] Masterson, C. & al.: Observations of the Crab Nebula with the H.E.S.S. In: *Contributions to the 29th ICRC 2005*, Pune, India (2005).

[134] Meylan, G. & al.: Mayall II = G 1: A Giant Globular Cluster in M31. *http://www.aas.org/publications/baas/v29n5/aas191/abs/S098004.html*

[135] Mirabal, N. & Halpern, J.P.: A Neutron Star Identification for the High-Energy Gamma-Ray Source 3EG J1835+5918 Detected in the ROSAT All-Sky Survey. *ApJL* **547L**, 137 (2001).

[136] Mirabal, N. & al.: Search for the Identification of 3EG J1835+5918: Evidence for a New Type of High-Energy Gamma-Ray Source. *ApJ* **541**, 180 (2000).

[137] Mirabal, N. & Halpern, J.P.: A Neutron-Star Identification for the High-Energy Gamma-Ray Source 3EG J1835+5918: The Next Geminga. *AAS* **32**, 1506 (2000).

[138] Mirzoyan, R. & al., *NIMA* **351**, 513 (1994).

[139] Moore, B. & al.: Dark Matter Substructure within Galactic Halos. *ApJL* **524**, 19 (1999).

[140] Moore, B. & al.: Cold Collapse and the Core Catastrophe. *MNRAS* **310**, 1147 (1999).

[141] Moore, B.: Evidence Against Dissipationless Dark Matter from Observations of Galaxy Haloes. *Nature* **370**, 629 (1994).

[142] Moralejo, A.: Monte Carlo Estimate of Flux Sensitivity of MAGIC for Point-Like Sources. In: *Internal MAGIC Documents*, MAGIC:TDAS 04-04-040824 (2004).

[143] Munoz, R.R. & al.: Exploring Halo Substructure with Giant Stars: The Velocity Dispersion Profiles of the Ursa Minor and Draco Dwarf Spheroidal Galaxies at Large Angular Separations. *ApJ* **631**, 137 (2005).

[144] Muñoz, C.: Dark Matter Detection in the Light of Recent Experimental Results. *Int. J. Mod. Phys. A* **19**, 3093 (2004).

[145] Nagano, M. & Watson, A.A.: Observations and Implications of the Ultrahigh-Energy Cosmic Rays. *Rev. Mod. Phys.* **72**, 689 (2000).

[146] *NASA/IPAC Extragalactic Database.* Results for NGC 598 (2006).

[147] Navarro, J.F., Frenk, C.S. & White, S.D.: A Universal Density Profile from Hierarchical Clustering. *ApJ* **490**, 493 (1997).

[148] Nolan, P. L. & al.: Variability of EGRET Gamma-Ray Sources. *ApJ* **597**, 615 (2003).

[149] Oguri, M. & Lee, J.: A Realistic Model for Spatial and Mass Distribution of Dark Halo Substructures: An Analytic Approach. *MNRAS* **355**, 120 (2004).

[150] Okamoto T. & Habe A.: Formation and Evolution of Galactic Halos in Clusters of Galaxies. *ApJ* **516**, 591 (1999).

[151] Ong, R.: Rapporteur Talk OG1. In: *Contributions to the 29th ICRC 2005*, Pune, India (2005).

[152] Paglione, T.A.D. & al.: Diffuse Gamma-Ray Emission from the Starburst Galaxy NGC 253. *ApJ* **460**, 295 (1996).

[153] Peacock, J.A.: Cosmological Physics. Cambridge University Press, Cambridge (1999).

[154] Peale, S.J.: On Microlensing Event Rates and Optical Depth Toward the Galactic Center. *ApJ* **509**, 177 (1998).

[155] Peebles, P.J.E.: Principles of Physical Cosmology. Cambridge University Press, Cambridge (1993).

[156] Persic, M. & Rephaeli., Y.: Galactic Star Formation Rates Gauged by Stellar End-Products. *A&A* **463**, 481 (2007).

[157] Persic, M. & al.: 2-10 keV Luminosity of High-Mass Binaries as a Gauge of Ongoing Star-Formation Rate. *A&A* **419**, 849 (2004).

[158] Persic, M. & Rephaeli, Y.: Starburst Galaxies and the X-Ray Background. *A&A* **399**, 9 (2003).

[159] Persic, M., Salucci, P. & Stel, F.: The Universal Rotation Curve of Spiral Galaxies - I. The Dark Matter Connection. *MNRAS* **281**, 27 (1996).

[160] Prandini, E.: Observation of VHE Gamma Emission from the AGN 1ES1218+304 with the MAGIC Telescope. *Diploma Thesis, University of Padova* (2006).

[161] Press, W.H. & Schechter, P.: Formation of Galaxies and Clusters of Galaxies by Self-Similar Gravitational Condensation. *ApJ* **187**, 425 (1974).

[162] Profumo, S.: Neutralino Dark Matter, Where Particle Physics Meets Cosmology. *Ph.D. Thesis, SISSA* (2004).

[163] Protheroe, R.J. & Clay, R.W.: Ultra High Energy Cosmic Rays. *PASA* **21**, 1 (2004).

[164] Reed, D. & al.: Evolution of the Mass Function of Dark Matter Haloes. *MNRAS* **346**, 565-572 (2003).

[165] Reid, M.J.: The Center of Our Galaxy. In: M. Morris, *Proceedings of IAU Symposium*, p. 136 Kluwer, Boston (1989).

[166] Riegel, B. & al.: A Tracking Monitor for the MAGIC Telescope. In: *Contributions to the 29th ICRC 2005*, Pune, India (2005),

[167] Romero, G.E. & Torres, D.F.: Signatures of Hadronic Cosmic Rays in Starbursts? High-Energy Photons and Neutrinos from NGC 253. *ApJL* **586**, 33 (2003).

[168] Romero, G.E., Benaglia, P. & Torres, D.F.: Unidentified 3EG Gamma-Ray Sources at Low Galactic Latitudes. *A&A* **348**, 868 (1999).

[169] Roszkowski, L., Ruiz de Austri, R. & Nihei, T.: New Cosmological and Experimental Constraints on the CMSSM. *JHEP* **0108**, 024 (2001).

[170] Rudaz, S. & Stecker, F.W.: Cosmic-Ray Antiprotons, Positrons, and Gamma Rays from Halo Dark Matter Annihilation. *ApJ* **325**, 16 (1988).

[171] Salpeter, E.E.: The Luminosity Function and Stellar Evolution. *ApJ* **121**, 161 (1955).

[172] Salucci, P.: The Distribution of Dark Matter in Spirals. In: Mamon, G. & al.: Dark Matter in Spiral Galaxies, EAS Publications Series (2005). Preprint: astro-ph/0603449.

[173] Salucci, P. & Burkert, A.: Dark Matter Scaling Relations. *ApJL* **537**, 9 (2000).

[174] Salucci, P. & Persic, M.: Maximal Halos in High-Luminosity Spiral Galaxies. *A&A* **351**, 442 (1999).

[175] Sanders, D.B. & al.: Luminous Infrared Galaxies. *ARA&A* **34**, 749 (1996).

[176] Seljak, U. & al.: Cosmological Parameter Analysis Including SDSS Ly-Alpha Forest and Galaxy Bias: Constraints on the Primordial Spectrum of Fluctuations, Neutrino Mass, and Dark Energy. *Phys. Rev. D* **71**, 3515 (2005).

[177] Somerville, R.: Can Photoionization Squelching Resolve the Substructure Crisis? *ApJL* **572**, 23 (2002).

[178] Spergel, D.N. & al.: Wilkinson Microwave Anisotropy Probe (WMAP) Three Year Results: Implications for Cosmology (2006). Preprint astro-ph/0603449.

[179] Spergel, D.N. & al.: First-Year Wilkinson Microwave Anisotropy Probe (WMAP) Observations: Determination of Cosmological Parameters. *ApJS* **148**, 175 (2003).

[180] Tasitsiomi, A. & Olinto, A.V.: Detectability of Neutralino Clumps via Atmospheric Čerenkov Telescopes. *Phys. Rev. D* **66**, 083006 (2002).

[181] Thompson, D.J. & al.: The Second EGRET Catalog of High-Energy Gamma-Ray Sources. *ApJ* **101**, 259 (1995).

[182] Thompson, D.J. & al.: Calibration of the Energetic Gamma-Ray Experiment Telescope (EGRET) for the Compton Gamma-Ray Observatory. *ApJ* **86**, 629 (1993).

[183] Tormen G., Diaferio A. & Syer D.: Survival of Substructure within Dark Matter Haloes. *MNRAS* **299**, 728 (1998).

[184] Torres, D.F. & al.: Luminous Infrared Galaxies as Plausible Gamma-Ray Sources for the Gamma-Ray Large Area Space Telescope and the Imaging Atmospheric Čerenkov Telescopes. *ApJL* **607**, 99 (2004).

[185] Tyler, C.E.: Particle Dark Matter Constraints from the Draco Dwarf Galaxy. *Ph.D. Thesis, University of Chicago. Phys. Rev. D* **66**, 023509 (2002).

[186] van den Bosch, F.C., Tormen G. & Giocoli, C.: The Mass Function and Average Mass-Loss Rate of Dark Matter Subhaloes. *MNRAS* **359**, 1029 (2005).

[187] van den Bosch, F.C. & Swaters, R.A.: Dwarf Galaxy Rotation Curves and the Core Problem of Dark Matter Halos. *MNRAS* **325**, 1017 (2001).

[188] Völk, H.J.: New Results from High Energy Gamma-Ray Astronomy. In: Meurs, E.J.A. & Fabbiano, G., *Populations of High Energy Sources. Proceedings of the 230th Symposium of the International Astronomical Union*, Dublin (Ireland), Aug. 15-19$^{\rm th}$, 2005, p. 95, Cambridge University Press, Cambridge (2006).

[189] Völk, H.J. & al.: The Nonthermal Energy Content and Gamma-Ray Emission of Starburst Galaxies and Clusters of Galaxies. *SSR* **75**, 279 (1996).

[190] Weekes, T.C. & al.: VERITAS: the Very Energetic Radiation Imaging Telescope Array System. *Astropart. Phys.* **17**, 221 (2002).

[191] Weiland, J.L. & al.: COBE Diffuse Infrared Background Experiment Observations of the Galactic Bulge. *ApJL* **425**, 81 (1994).

[192] Weller, J. & al.: Fast Identification of Bound Structures in Large N-Body Simulations. *MNRAS* **364**, 823 (2005).

[193] Wilkinson, M.I. & al.: *ApJ* **611**, 21 (2004).

[194] Yano, T., Nagashima, M. & Gouda, N.: Limitations of the Press-Schechter Formalism. *ApJ* **466**, 1 (1996).

[195] Zhao, H. & Evans, N.W.: The So-Called 'Bar' in the Large Magellanic Cloud. *ApJL* **545**, 35 (2000).

[196] Zhao, H.S.: A Steady-State Dynamical Model for the COBE-Detected Galactic Bar. *MNRAS* **283**, 149 (1996).

[197] Zhao, H. & Mao, S.: On the Microlensing Optical Depth of the Galactic Bar. *MNRAS* **283**, 1197 (1996).

[198] Zimmermann, J.: Statistical Learning in High Energy and Astrophysics (2005). *Ph.D. Thesis, University of München* (2005).